THE QUANTUM DYNAMICS OF ATOM PLUS DIATOM CHEMICAL REACTIONS

Thesis by

George Chappell Schatz

In Partial Fulfillment of the Requirements
For the Degree of
Doctor of Philosophy

California Institute of Technology
Pasadena, California
1976
(Submitted September 8, 1975)

To my wife Margaret and to my parents.

Acknowledgements

I would like to acknowledge the guidance, insight and assistance of my research advisor Prof. Aron Kuppermann. His close cooperation and constant encouragement throughout my years of graduate study has made my work tremendously fulfilling. Many of the research projects described in this thesis might never have been successful without a number of brilliant suggestions and ideas made by him at crucial points in their development.

I thank Prof. Joel Bowman for his collaboration on several papers and for many interesting and fruitful discussions.

I thank my theoretical dynamics colleagues Dr. Michael Baer, Dr. Rung Ling, Dr. Bjarne Andresen and John Dwyer for their helpful interest in my research. I also thank the present and former members of the Kuppermann research group for providing a broadening and enlightening environment in which to share the research experience. I would also like to express my appreciation to Prof. William A. Goddard, Prof. Vincent McKoy and the members of their respective research groups for their interest in my research. I thank Prof. S. I. Chan for his valuable guidance in many important decisions.

I thank my friends in the astronomy department, Richard Green, Steve Willner and Paul Hickson for many years of enjoyable social and scientific interchange.

I wish to express my deepest appreciation to my dear relatives Cynthia and Don McCleary for their kind hospitality during my stay in southern California.

I thank the National Science Foundation for a fellowship, and the Air Force Office of Scientific Research for financial support. I wish to express deep gratitude to the kind people at Ambassador College for providing generous amounts of computer time for many of the projects described in this thesis.

I thank Linda Bryant and Henriette Wymar for their expert and painstaking typing of this thesis.

I thank Jon Burke for assistance on several of the projects in this thesis.

Most of all, I thank my wife Margaret and my parents George and Dorothy, to whom this thesis is dedicated, for constant love and understanding.

Abstract

The results of accurate quantum dynamical calculations on one, two and three dimensional atom plus diatomic molecule electronically adiabatic chemical reactions are presented.

In papers 1 and 2, comparisons between quantum, quasi-classical and semi-classical results for the collinear $F + H_2$ and $F + D_2$ reactions, are examined. Paper 3 discusses the role of reactive and nonreactive collisions in producing vibrational deactivation in the collinear H + FH, D + FD, H + FD and D + FH systems.

The extension of reactive scattering calculational methods to atom diatom collisions on a plane and in three dimensions is presented in papers 4 and 6, respectively. In both applications, the Schrödinger equation is solved by a coupled equation method in each of the three arrangement channel regions. This is followed by a matching procedure in which the wave function is made smooth and continuous at the boundaries of these regions. In the three dimensional case, the use of body fixed coordinates is crucial to obtaining an efficient coordinate transformation between arrangement channels.

Applications of these 2D and 3D methods to the $H + H_2$ exchange reaction are presented in papers 5 and 7. Integral and differential cross sections, reaction probabilities, product and reagent state rotational distributions, and other dynamical information are discussed in the papers, and these results are extensively compared with those of previous quasi-classical, semi-classical and approximate quantum calculations. The results of a very simple angular momentum decoupling approximation are considered in paper 7.

In papers 8 and 9 the relative importance of direct versus resonant (shape or Feshbach) mechanisms for several atom diatom reactions is examined. A number of techniques for characterizing both mechanisms are discussed, including time delays, eigenphase shifts, Argand diagrams and the collision lifetime matrix. Extension of these 1D resonances to the 2D and 3D reactions is examined in paper 10 for the simple case of $H + H_2$.

Table of Contents

INTRODUCTION

Introduction

In the 10 papers which comprise this thesis, we are interested in the dynamics of electronically adiabatic atom plus diatom chemical reactions. We shall concentrate almost exclusively on a quantum description of the collision processes as obtained from the Schrödinger equation. Only very recently has it become possible to solve this equation accurately for three dimensional reactions. Therefore, fully 2/3 of this thesis is devoted to the study of the considerably simpler dynamical models which are obtained by accurately solving the Schrödinger equation for an atom diatom system of reduced collision dimensionality. Although the results of these 1D and 2D calculations cannot be directly compared with experiment, we can compare them with the results of approximate dynamical methods such as the quasi-classical and semi-classical methods. These comparisons should give us some indication of how accurate the approximate theories should be when applied to three dimensional reactions. In addition, the use of 1D and 2D models enables us to characterize the nature and importance of quantum dynamical effects such as tunnelling, interferences and resonances. In papers 1 and 2 we examine the collinear $F + H_2$ and $F + D_2$ reactions within the context of the above considerations. These strongly exothermic reactions produce highly inverted product vibrational distributions, so the primary emphasis of these two papers is towards characterizing the distributions obtained from accurate quantum, quasi-classical and semi-classical methods. In paper 3, the role of reactive and nonreactive collisions in producing vibrational deactivation in the collinear H + FH, D + FD, H + FD and

D + FH systems is examined. For many of the reactions studied in papers 1 - 3, 3D classical trajectory results are available for comparison, and these comparisons reveal both similarities and differences between comparable results with different collision dimensionality.

Papers 4 and 5 are concerned with the theory and results for the coplanar (2D) atom diatom reaction dynamics. In many respects, the 2D and 3D worlds are very closely related for atom diatom collisions. In both cases, the full interaction potential is sampled, and the concept of reaction path bifurcation, which is so crucial to an application to H + H_2, is common to both calculations (but not to the 1D calculation). This makes the 2D application a very realistic attempt to describe the reaction dynamics, and the 2D-3D comparisons given in paper 7 support this contention.

Papers 6 and 7 deal with the three dimensional collision dynamics. Paper 6 describes the theoretical procedure used for accurately solving the Schrödinger equation. The internal variables are treated in a manner very analogous to the 2D treatment of paper 4 while the external variables are treated through the use of a rotating body fixed coordinate system. In the application of this theoretical method to 3D H + H_2 (paper 7), we examine the dynamical information (cross sections, transition probabilities, rotational distributions) from a number of different viewpoints in an attempt to characterize the results as completely as possible. Comparisons are made between our accurate quantum results and those of a number of earlier approximate calculations, and many of the strengths and weaknesses of the approximate theories are revealed.

Finally, in papers 8 - 10, we concentrate on the role of direct and resonant processes in atom diatom chemical reactions. Papers 8 and 9 include studies of collinear systems, using such quantities and time delays, Argand diagrams, eigenphase shifts and the lifetime matrix to characterize the resonant and direct mechanisms and their interferences. Paper 10 includes an extension to the 2D and 3D reactions using the methods of papers 4 and 6, and presents the important discovery of a resonance in 3D H + H_2.

1. EXACT QUANTUM, QUASI-CLASSICAL, AND SEMI-CLASSICAL REACTION PROBABILITIES FOR THE COLLINEAR $F + H_2 \rightarrow FH + H$ REACTION [*]

---

[*] This paper appeared in the Journal of Chemical Physics 63, 674 (1975).

Exact Quantum, Quasi-Classical and Semi-Classical reaction Probabilities for the Collinear $F + H_2 \rightarrow FH + H$ Reaction.*

George C. Schatz,[†] Joel M. Bowman[†§] and Aron Kuppermann
Arthur Amos Noyes Laboratory of Chemical Physics**
California Institute of Technology, Pasadena, California 91125

(Received

Exact quantum, quasi-classical and semi-classical reaction probabilities and rate constants for the collinear reaction $F + H_2 \rightarrow FH + H$ are presented and compared. The exact quantum results indicate a large degree of population inversion in the FH product with P_{02}^R and P_{03}^R being the dominant reaction probabilities. The energy dependence of these two probabilities at low translational energies are quite different. P_{02}^R shows an effective threshold of 0.005eV which can largely be interpreted as resulting from tunnelling through a vibrationally adiabatic barrier. P_{03}^R has a much larger effective threshold (0.045eV) apparently resulting from dynamical effects. Quasi-classical probabilities for the collinear $F + H_2$ reaction were calculated by both the forward (initial conditions chosen for reagent $F + H_2$) and reverse (initial conditions for product $H + FH$) trajectory

---

[*] Work supported in part by the United States Air Force Office of Scientific Research.

[†] Work performed in partial fulfullment of the requirements for the Ph. D. degree in Chemistry at the California Institute of Technology.

[§] Present address: Department of Chemistry, Illinois Institute of Technology, Chicago, Ill. 60616

[**] Contribution No. 4988.

methods. The results of both calculations correctly indicate that P_{03}^{R} and P_{02}^{R} should be the dominant reaction probabilities. However, the threshold behavior of the quasi-classical forward P_{03}^{R} disagrees strongly with the corresponding exact quantum threshold energy dependence. By contrast, there is good agreement between the reversed trajectory results and the exact quantum ones. The uniform semi-classical results also agree well with the corresponding exact quantum ones indicating that the quasi-classical reverse and the semi-classical methods are preferable to the quasi-classical forward method for this reaction. The important differences between the threshold behavior of the exact quantum and quasi-classical forward reaction probabilities are manifested in the corresponding rate constants primarily as large differences in their activation energies. Additional exact quantum results at higher total energies indicate that threshold effects are no longer important for reactions with vibrationally excited H_2. Resonances play an important role in certain reaction probabilities primarily at higher relative translational energies.

1. Introduction

The reactions $F + H_2$ (D_2, DH) → FH (FD) + H (D) have recently been the subject of several experimental studies in which very detailed rate constants and cross sections for these reactions have been measured. Relative rate constants into specific vibrational (and sometimes vibrational-rotational) states of the products have been measured by both infrared chemiluminescence[1] and chemical laser[2] techniques and, quite recently, both methods have been used to study the temperature dependences of these relative rates.[1f, 2d] Angular distributions for specific product vibrational states of the $F + D_2$ reaction have been studied at several incident energies by a crossed molecular beam apparatus.[3] In addition, there exist several (usually indirect) determinations of the overall bulk rate constants for the $F + H_2$ reaction[4] and more recently studies of isotope effects for the $F + H_2$, $F + D_2$, F + HD and F + DH series.[5] A very important application of these reactions has been to the fluorine-hydrogen chemical lasers[2a,6], where $F + H_2 \rightarrow FH + H$ serves as the main pumping reaction.

Complementing these experimental studies have been several quasi-classical trajectory studies on $F + H_2$[7,8,9], $F + D_2$[7,10,11] and F + DH (HD)[7,9] and one recent semi-classical study on collinear $F + D_2$.[12] The results of the quasi-classical studies have generally been in reasonably good agreement with the detailed rate constants obtained by infrared chemiluminescence and chemical laser experiments but in much poorer agreement with the angular distributions obtained by the molecular beam experiments. There also exists some disagreement between experiment and the classical calculations on the rotational distribution of the detailed rate constants,[7b] and on isotope effects.[5] Additional theoretical developments have been the characterization of the product state distributions by temperature-like parameters,[13] and the establishment of a relationship between these parameters and certain details of the potential energy surface.[14] All of the classical theoretical studies have employed semi empirical potential energy surfaces.[7-11] An ab initio potential energy surface has also been calculated[15] and the semi-empirical surfaces are in reasonable agreement with it.

Aside from possible defects in the potential energy surface used, the most important sources of disagreement between the quasi-classical trajectory calculations and experiment are: (a) electronically non-adiabatic effects, and (b) quantum dynamical effects. The first problem has been discussed by various investigators[16,17,18] but its importance is not completely understood at present and we shall not consider it here.

In this paper, we study the importance of quantum dynamical effects in the $F + H_2 \rightarrow FH + H$ reaction by comparing the results of accurate quantum mechanical solutions to the Schrödinger equation for the collinear collisions to the results of the corresponding quasi-classical and semi-classical calculations. In the following paper (hereafter referred to as II), we make the analogous study for the $F + D_2$ reaction and also examine exact quantum results for F + HD(DH). Results of our preliminary studies[19,20] indicated that quantum effects were quite important in the collinear $F + H_2$ reaction[19] and, in fact, the disagreement between the quasi-classical and exact quantum reaction probabilities at low reagent relative translational energies was quite large. In the present paper, we give a more detailed analysis of the reaction probabilities for F + H_2 as calculated by four different methods: an exact quantum mechanical solution, the quasi-classical forward and quasi-classical reverse trajectory methods and the uniform semi-classical method. We also present and compare the corresponding rate constants obtained from the results of these four methods. In addition, we examine resonances, tunnelling and energy partitioning in this reaction, and examine the results of exact quantum calculations at total energies for which two vibrational states of the reagent H_2 are accessible.

In all cases, we restrict our considerations to collinear collisions of a fluorine atom with a hydrogen molecule where the two hydrogen atoms are considered to be distinguishable. The resulting cross sections are in the form of dimensionless probabilities of reaction between specific vibrational states of the reagents to form products in specific states and are not directly comparable with experiment (although certain other quantities such as final state distributions can, with caution, be subject to such a comparison). Our justification for studying collinear dynamics lies mainly in its use as a predictive model for the energy release behavior in actual three dimensional collisions[21] and as a testing ground for approximate theories of chemical dynamics.[22] Exact quantum dynamics is currently feasible for many types of collinear reactions and thus the importance of quantum effects in chemical reactions can readily be established within the collinear restriction. How these quantum effects will be modified in two or three dimensional systems has not yet been fully established but some progress has been made towards obtaining exact quantum solutions to these problems[23] and quite recently accurate converged results have been obtained for the $H + H_2$ coplanar and 3-D exchange reaction.[24]

In section 2 the potential energy surface used in our calculations is described. In section 3 we compare the quantum, quasi-classical and semi-classical reaction probabilities for $F + H_2$ and in section 4 we compare the corresponding rate constants. Reaction probabilities for $F + H_2$ in the higher total energy range where two reagent vibrational states are open are discussed in section 5 and in section 6 is a short summary.

2. Potential Energy Surface

We used the semi-empirical LEPS potential energy surface of Muckerman[12, 25] (his surface 5). This surface is intermediate in character between his surfaces 2 and 3 of reference 7b and was chosen to optimize agreement between his three dimensional trajectory results and experiment.[7b, 12] Using Muckerman's notation, the parameters describing the extended LEPS surface are D_e (HF) = 6.1229eV, β_e (HF) = 2.2187 Å^{-1}, R_e (HF) = .9170 Å, Δ (HF) = 0.167, D_e (H_2) = 4.7462eV, β_e (H_2) = 1.9420 Å^{-1}, R_e (H_2) = 0.749 Å and Δ (H_2) = 0.106. The exothermicity is 1.3767eV (31.76 kcal/mole) and the barrier height 0.0461eV (1.06 kcal/mole). Fig. 1 shows an equipotential contour plot of the collinear surface along with the minimum energy path. The coordinate system for the plot (and for all calculations) is chosen to diagonalize the kinetic energy with a single reduced mass and is defined by:[26]

$$x_1' = \left(\frac{\mu_{F,HH}}{\mu_{HH}}\right)^{\frac{1}{4}} \left(r_{HF} + \frac{\mu_{HH}}{m_H} r_{HH}\right)$$

$$x_2' = \left(\frac{\mu_{HH}}{\mu_{F,HH}}\right)^{\frac{1}{4}} (r_{HH})$$

where r_{HF} is the shorter of the two HF bond distances in the H - H - F linear geometry. The analogous coordinate system appropriate for the product arrangement channel (FH + H) is:

$$z_1' = \left(\frac{\mu_{H,FH}}{\mu_{FH}}\right)^{\frac{1}{4}} \left(r_{HH} + \frac{\mu_{FH}}{m_H} r_{HF}\right)$$

$$z_2' = \left(\frac{\mu_{HF}}{\mu_{H,FH}}\right)^{\frac{1}{4}} \left(r_{HF}\right)$$

These coordinate systems have the advantage over others[27] in that the transformation between the (x_1', x_2') coordinate system appropriate for reagents and the (z_1', z_2') system appropriate for the products, is orthogonal.

Since the vibrational spacing in H_2 is about 12 kcal/mole and that in HF is 11 kcal/mole, four vibrational states of HF are normally accessible for thermal distributions of reagent H_2 due to the exothermicity of the reaction.

3. Quantum, Quasi-Classical and Semi-Classical Reaction Probabilities for Collinear $F + H_2 \rightarrow FH + H$

3. 1 Exact Quantum Reaction Probabilities

3. 1. 1 Numerical Method

We used the close coupling propagation method of Kuppermann[28] to solve the Schrödinger equation for the collinear system $F + H_2$. The method involves dividing the configuration space depicted in Fig. 1 into different regions and then propagating though a given region in a coordinate system appropriate to that region. In particular, rectangular coordinates were used in the near asymptotic regions appropriate to reagents and products and polar coordinates in the strong interaction region with the origin of the coordinate system chosen in the classically inaccessible plateau area corresponding to dissociation. A basis set of pseudo vibrational eigenfunctions describing motion transverse to the direction of propagation was used for expanding the wave functions. These eigenfunctions were calculated by a finite difference procedure,[29] and the basis set was changed often during the propagation to insure an efficient representation of the wave function. Contributions from continuum vibrational channels are not included in this method. The integration of the coupled Schrödinger equation was done with an Adams-Moulton 4th order predictor -- 4th order corrector method (with a 4th order Runge-Kutta-Gill initiator). The procedure for extracting the probability matrices from the asymptotic solutions is similar to that used by Truhlar and Kuppermann.[22] Convergence of the final reaction probabilities was carefully checked by observing the effect of varying the location of the origin of the polar coordinate system, location of the end point of the integration,[30] number of closed vibrational channels, number of integration steps, and number of grid points in the finite difference eigenfunction determination. Using 12 to 15 vibrational channels throughout the integration, we obtained a scattering matrix for which unitarity and symmetry were deemed adequate (flux conservation to 0.5% and symmetry to 5% or better) in the reagent translational energy range (relative to $\nu = 0$) $E_0 = 0.0$ to 1.10eV. The computation time for a 13 channel calculation on an IBM 370-158 computer was approximately 32 min. for the initial calculation in which a large amount of energy independent information was stored on disk for subsequent use and 5 min. per energy thereafter.

3. 1. 2. Results

We define the probability of reaction from an initial state ν (of the reagent H_2) to a final state ν' (of the product HF) by the symbol $P_{\nu\nu'}^R$. (This symbol will also be used as a shorthand notation for the phrase "$\nu \rightarrow \nu'$ reactive collision.") The total reaction probability P_ν^R from a given incident state ν is the sum of $P_{\nu\nu'}^R$ over all accessible ν'. The exact quantum (EQ) reaction probabilities P_{02}^R, P_{03}^R and P_0^R for $F + H_2$ in the translational energy range $E_0 = 0.0$ to 0.4eV are presented in Fig. 2. The reaction probabilities for the transitions P_{00}^R and P_{01}^R, which are also allowed in this E_0 range, are plotted in Fig. 3. We see that P_{00}^R and P_{01}^R have an energy dependence very similar to P_{02}^R, but with much smaller values ($P_{00}^R \simeq 6x10^{-5}\ P_{02}^R$, $P_{01}^R \simeq 1x10^{-2}\ P_{02}^R$). As a result, only P_{02}^R and P_{03}^R contribute appreciably to P_0^R in the energy range considered. As was pointed out previously,[19] P^R_{02} and P^R_{03} have remarkably different threshold behaviors. We shall define the effective threshold energy E_T for the $\nu\rightarrow\nu'$ transition as the difference between the (lowest) energy for which the corresponding $P^R_{\nu\nu'}$ is equal to, say, 1% of the maximum value attained by this quantity and the energy at which the $\nu\rightarrow\nu'$ process becomes energetically possible. With this definition, P^R_{02} has an effective threshold of 0.005eV while for P^R_{03} (which is energetically forbidden until E_0=0.013eV) E_T is 0.045. Note that while the barrier height is 0.0461eV, the zero point energy of H_2 is 0.268eV, so the transition P^R_{02} is classically allowed even at zero translational energy. Likewise the $0\rightarrow3$ reactive transition is classically allowed as the HF (3) channel opens up at E_0 = 0.013eV. One possible explanation for why the effective threshold of P^R_{02} is greater than zero is that the exchange of energy between motion transverse to the reaction coordinate and that along the reaction coordinate is not efficient (at least in the entrance channel region of configuration space where the saddle point lies). Truhlar and Kuppermann have shown[22] that a more realistic estimate of the effective barrier height in $H + H_2$ is obtained from vibrationally adiabatic theory. The vibrationally adiabatic barrier (for zero curvature and using the harmonic approximation) for $F + H_2$ is 0.26eV which is still appreciably larger than the effective quantum threshold energy for P^R_{02} (0.005eV) although it is quite close to the P^R_{02} quasi-classical threshold energy (.025eV) (see section 3.2.2). This difference between the quantum and quasi-classical threshold energies could in part be due to tunnelling through the one dimensional adiabatic barrier, within the framework of an adiabatic description of the quantum dynamics in the neighborhood of the saddle point. In II we shall see that the results for $F + D_2$, F+ HD and F + DH support this conclusion. The high threshold energy for P_{03}^R is not easily explained as resulting from one dimensional adiabatic barrier tunnelling and is probably due to a dynamical effect as will be discussed in section 3. 2. 2.

The sharp spike in the P_{02}^R curve at energies slightly above threshhold is reminiscent of the Feshbach type internal excitation resonances observed in the collinear $H + H_2$ reaction.[31] A discussion of other resonances in the $F + H_2$ reaction is presented in section 5.

Simultaneously with the reactive transition probabilities, we have calculated the nonreactive ones corresponding to the collisions $F + H_2(0) \rightarrow F + H_2(0)$ and $FH\ (\nu) + H \rightarrow FH(\nu') + H$. The probabilities for the first of these nonreactive processes are simply the difference between unity and the total reaction probability P_0^R (as long as $\nu = 1$ of H_2 is closed). The transition probabilities for the $H + HF(\nu')$ inelastic $(\nu' \neq \nu)$ processes are all quite small (generally less than 0.01) up to $E_0 = 0.4$eV and vary relatively slowly with energy. Unitarity of the scattering matrix then forces the elastic probabilities for $H + HF(\nu)$ collisions to be roughly equal to the difference between unity and the probability for the $F + H_2\ (0) \rightarrow FH(\nu) + H$ reactive process. The behavior of the inelastic transition probabilities for nonreactive H + HF collisions contrasts strongly with the corresponding inelastic transition probabilities for collinear H + FH collisions.[32] In the latter case we find that the probability of an inelastic collision is comparable in magnitude to the elastic transition probabilities and, in addition, the probabilities of multiquantum jump transitions are often greater than the probabilities of single quantum jump transitions. A more complete discussion of the results for collinear H + FH will be given in ref. 32.

3. 2 Quasi-Classical Reaction Probabilities

3. 2. 1 Method

The classical trajectory calculations were carried out in the same way as in a previous $H + H_2$ study.[33, 34] The initial phase angle variable for the vibration of the ground state of H_2 was varied uniformly over a grid of typically 100 points in the interval 0 to 2π. The final action number of the product HF was computed for each reactive trajectory and assigned a quantum number by rounding off the action number to the nearest integer. Thus, the transition probability $P^R_{0\nu'}$ was defined as the fraction of reactive trajectories with final quantum number ν'.

When this procedure is carried out in the direction $F + H_2\ (\nu=0) \rightarrow FH\ (\nu') + H$ we term the quasi-classical transition probabilities "Quasi-Classical Forward" (QCF). For the reverse reaction the quasi-classical transition probabilities are termed "Quasi-Classical Reverse" (QCR). Quantum mechanically, the forward and reverse probabilities are rigorously equal at the same total energy, but quasi-classically they are not.[20] Therefore, either of the two quasi-classical results, QCF or QCR, could be used to represent the probabilities for the (forward) reactive collisions. Since there is presently no a priori way of deciding which of these two procedures will give results closer to the EQ ones, we have used them both and corresponding results are presented below.

3.2.2 Results

In Fig. 4 we plot the QCF and EQ reaction probabilities P_{02}^R, P_{03}^R and P_0^R versus the translational energy E_0, as well as the corresponding exact quantum ones given in Fig. 2. Out of the 100 trajectories, none yielded HF with $\nu = 0$ or 1 (i.e., $P_{01}^R = P_{00}^R = 0$ probably to within 0.01 or less). There are two important points to be noted in comparing the EQ and QCF results. First, both the exact quantum and the quasi-classical results predict roughly the same amount of vibrational excitation in the HF product on the average. Indeed, if we define f_V as the fraction of the total energy which ends up as vibrational energy in the product HF, then in Fig. 5 we see that f_V is roughly 0.81 and nearly independent of E_0 in the QCF results, and fluctuates between 0.66 and 0.89 with an average value of 0.79 in the EQ results. From this, we conclude that the quantum and quasi-classical dynamics agree (on the average) with respect to partitioning of product energy between translational and vibrational degrees of freedom. Second, despite this average agreement, there are very significant differences between the EQ and QCF reaction probabilities particularly with respect to the P_{03}^R threshold and the P_{03}^R / P_{02}^R ratio. In Fig. 6 this ratio is displayed as a function of E_0 for both the EQ and QCF results. As has been pointed out previously,[19] the lack of agreement between the individual transition probabilities P_{02}^R and P_{03}^R can be partially explained as arising from the reasonable but nevertheless arbitrary way of assigning a discrete quantum number to a continuous product vibrational energy. However, the large differences in the energy dependence of the EQ and QCF $P^R_{0\nu}(\nu = 2,3)$ suggests that this is probably not the whole explanation and that other significant differences exist between the classical and quantum dynamics in this system. In addition, this arbitrariness in the definition of a product quantum number is not present in the total reaction probabilities P^R_0, yet the differences in magnitude and energy dependence of the EQ and QCF results are still very significant.

It is also of interest to analyze the EQ and QCF reaction probabilities by an information theoretic approach.[13] In order to include a study of isotope effects in this analysis, we defer a discussion of this to paper II.

In Fig. 7 are plotted the QCR and EQ reaction probabilities P^R_{02}, P^R_{03} and P^R_0 versus E_0. The transition probability P^R_{02} is non zero at zero reagent translational energies. This can occur because of the convention of rounding classical vibrational quantum numbers to the nearest integer.[20,33,34]

The QCR results in Fig. 7 are in much better agreement with the quantum probabilities than are the QCF results in Fig. 4. This is true not only of the total reaction probabilities P^R_0, but also of the individual transition probabilities especially P^R_{03}. The fact that the threshold behavior of the P^R_{03} transition can be described correctly by a quasi-classical method suggests that the 0.045 eV effective threshold energy in P^R_{03}(EQ) is a dynamical effect related to motion through classically accessible regions of configuration space. The fact that the reverse rather than the forward trajectory method produces the best agreement with the exact quantum results must be regarded as an empirical observation at present. It would be interesting to further analyze the quasiclassical results from the viewpoint of what regions of configuration space are being sampled by the QCR and QCF trajectories and with what velocities, and how well the current density fields derived from these trajectories agree with the corresponding exact quantum current densities.[35] The good agreement between the QCR and EQ results suggests that the QCR procedure should be applied to a three dimensional trajectory calculation. If the differences between the one dimensional QCR and QCF results are also found in three dimensional calculations, this could be indicative of the presence of important quantum dynamical effects in the three dimensional reaction. Wilkins[36] has completed a three dimensional QCF study of the reaction FH (ν) + H $\rightarrow H_2(\nu')$ + F (ν varying from 1 through 6). His results can be considered to be QCR calculations for the reaction F + H_2 (ν') $\rightarrow$ FH (ν) + H. He has also published QCF rate constant calculations[9a] for the latter reaction with $\nu' = 0$. It would be very interesting to compare the corresponding (QCR and QCF) cross sections. Perry et al[37] have recently published a three dimensional comparison of the QCR and QCF cross sections for the endothermic I + H_2 $\rightarrow$ HI + I reaction at one total energy. They found that microscopic reversibility was approximately obeyed at this energy but made no detailed study of the energy dependence of the cross sections and did not investigate threshold effects.

3.3 Semi-Classical Reaction Probabilities

3.3.1 Method

For most energies, uniform semi-classical reaction probabilities were calculated according to the procedure described in reference 34. However, for translational energies E_0 greater than 0.10 eV the transition P^R_{02} was computed by a simple analytical continuation technique,[38] similar in spirit to that of Miller.[39] This was necessary in order to obtain a non-vanishing value of this transition probability since in the above energy range, although energetically allowed, it is dynamically forbidden.[34, 39] In addition, it was found that P^R_{03} was ill-determined near threshold in that a plot of final FH vibrational action number m_f versus initial H_2 vibrational phase angle (q_0) revealed "raggedness" (i.e., very rapid variation of m_f with q_0) for m_f near the value 3.[40] Raggedness was also observed over a range of energies for the $F + D_2$ $(\nu = 0) \rightarrow FD$ $(\nu' = 4) + D$ reaction by us (see following paper II) and by Whitlock and Muckerman.[12] We managed to overcome this difficulty at several energies by doing the semi-classical analysis for the reverse reaction, i.e., $H + HF$ $(\nu = 3) \rightarrow H_2$ $(\nu = 0) + F$.[41] For this reaction, the results were considerably less "ragged" for m_f approximately equal to 0 than they were for the forward reaction around $m_f = 3$. A more complete discussion of this procedure is given in paper II for the $F + D_2$ reaction.

3. 3. 2 Results

The semi-classical reaction probabilities P_{02}^{R} and P_{03}^{R} for $F + H_2$ are presented in Fig. 8 along with the corresponding exact quantum probabilities. In the absence of considering complex-valued trajectories (in complex phase space at complex times), vanishing quasi-classical reaction probabilities implies that the corresponding semi-classical ones also vanish. Therefore, P_{01}^{R} (USC) = P_{00}^{R} (USC) = 0. From the appearance of the reaction probabilities in Fig. 8, we see that the qualitative agreement between the EQ and USC results is quite good. There are large differences between the magnitudes of the USC and EQ probabilities at certain energies, but such differences are not usually too important for the resulting collinear rate constants (see section 4). Of more serious consequence for such rate constants is the small difference between the threshold energies of the P_{02}^{R} curves. As pointed out in section 3. 2. 1., this threshold difference of about 0.020eV could be partly due to an adiabatic tunnelling effect and it may be possible to improve the agreement between the EQ and USC results by using complex trajectories.[42, 43]

3.4 Comparison of EQ, QCF, QCR and USC Reaction Probabilities

In Figs. 9 and 10 we compare the exact quantum, quasi-classical forward, quasi-classical reverse and semi-classical reaction probabilities P_{02}^{R}, P_{03}^{R} and P_{0}^{R} for $F + H_2$ as a function of the reagent translational energy. Note that the QCR results resemble the USC ones much more than the QCF results do. Obviously, the USC threshold energy must be larger than or equal to both the QCF and QCR threshold energies. However, we cannot presently put forward an a priori reason that would have permitted us to predict which of the latter two energies is greater nor which of the quasi-classical reaction probabilities should be closer to the USC ones. It is also very interesting to note that the QCR results resemble the EQ ones more than the USC ones do. One should, however, be cautious not to generalize this observation. As shown in paper II, the reverse behavior is found for the $F + D_2$ reaction.

4. EQ, QCF, QCR and USC Rate Constants for $F + H_2$

The detailed $\nu \rightarrow \nu'$ rate constant for a one-dimensional bimolecular reaction such as $F + H_2(\nu) \rightarrow FH(\nu') + H$ is defined as

$$\begin{aligned} k^{R}_{\nu\nu'}(T) &= \langle V_{\nu}\, P^{R}_{\nu\nu'}(V_{\nu}) \rangle_{T} \\ &= \int_{0}^{\infty} f_{T}(V_{\nu})\, V_{\nu}\, P^{R}_{\nu\nu'}(V_{\nu})\, dV_{\nu} \ , \end{aligned}$$

where V_{ν} is the initial relative velocity of the reagents $F + H_2(\nu)$ and $f_T(V_{\nu})$ is the one-dimensional Boltzmann relative velocity distribution function. Changing the integration variable from V_{ν} to the initial relative reagent translational energy E_{ν} this expression becomes[22]

$$k^{R}_{\nu\nu'}(T) = \frac{1}{(2\pi\mu_{F,HH}kT)^{\frac{1}{2}}} \int_{0}^{\infty} P^{R}_{\nu\nu'}(E_{\nu})\, e^{-E_{\nu}/RT}\, dE_{\nu}.$$

Note that for one-dimensional systems, number densities are expressed in molecule/cm so that a bimolecular rate constant has the units cm/(molecule · sec.).

Using the reaction probabilities presented in Fig. 7, we have calculated the rate constants k_{03}^{R} and k_{02}^{R} from the EQ, QCF, QCR and USC reaction probabilities. Arrhenius plots of these rate constants are presented in Fig. 11. We see that for k_{03}^{R} all plots are nearly linear at high temperatures. Because of the extremely small effective threshold energies of P_{02}^{R}, the Arrhenius plots of k_{02}^{R} are only linear at low temperature (< 500 K). At high temperature, the temperature dependence of k_{02}^{R} approaches $T^{\frac{1}{2}}$ which is characteristic of a reaction with zero activation energy. Arrhenius activation energies E_a^{02} and E_a^{03} and pre-exponential factors A_{02} and A_{03}, which were determined by a least squares fit to the 200-400 K results and to the 900-1200 K results, are given in Table I. It is clear from Fig. 11 and Table I that k_{03}^{R} (QCF) has an activation energy which is significantly lower than the activation energies of k_{03}^{R} (EQ, QCR or USC). This is an obvious consequence of the different effective threshold energies of the reaction probabilities (Fig. 9) and illustrates how these threshold differences can affect the detailed rate constants. As might be expected from Fig. 9, k_{03}^{R} (QCR) and k_{03}^{R} (USC) are in quite good agreement with k_{03}^{R} (EQ).

The relative agreement among the corresponding three k_{02}^{R} rate constants is much less satisfactory at low temperatures, the difference between k_{02}^R (EQ) and k_{02}^R (USC) is mainly determined by the 0.02 eV difference in the threshold energies of the P_{02}^R reaction probabilities. Since P_{02}^R (QCR) has its effective threshold at zero translational energy, k_{02}^R (QCR) has a smaller activation energy than k_{02}^R (EQ) which in turn has a smaller activation energy than k_{02}^R (QCF or USC). The total rate constant k_0^R which is essentially due to the contributions of k_{03}^R and k_{02}^R does not exhibit simple Arrhenius behavior because it is the sum of two Arrhenius expressions which are of equal magnitude near T = 1000 K, but which have quite different activation energies. Note that the experimental activation energy (which is 1.71 kcal/mole)[44] seems to represent an average of the present EQ values of E_a^{02} and E_a^{03}.

In Fig. 10 we plot the ratio k_{03}^R / k_{02}^R as a function of temperature. The large difference between the temperature variation of the QCF ratio and that of the EQ, QCR or USC ratios is again a consequence of the difference in the reaction probabilities in Fig. 9. It is interesting to note that the three dimensional quasi-classical forward trajectory method yields a rate constant ratio which is nearly independent of temperature,[9a] in agreement with the one dimensional QCF results presented here. An experimental measurement of the temperature dependence of k_{03}^R / k_{02}^R[2e] seems to agree reasonably well with the three dimensional QCF result[9a] and consequently disagrees with our EQ result. This may indicate that the strong difference between the activation energies of k_{03}^R and k_{02}^R observed here is largely averaged out in three dimensions. On the other hand, for the $F + D_2$ reaction, the agreement between experiment and the quasi-classical results is not as consistent as it is for $F + H_2$ (to be discussed in paper II), so it is possible that the averaging process in three dimensions does not completely destroy the important differences between the results of quantum and classical mechanics as reported in this paper.

In contrast to the k_{03}^R / k_{02}^R ratio, k_{02}^R (EQ) / k_{01}^R (EQ) is nearly constant in the temperature range considered here. This agrees with the temperature variations of both the experimental[2d] and three dimensional QCF[9a] results, although the absolute magnitudes of the ratios are quite different (~90 for 1-D versus ~3 for 3-D). We also found that k_{01}^R (EQ) / k_{00}^R (EQ) is nearly independent of temperature with a value of roughly 210. Therefore k_{01}^R (EQ) and k_{00}^R (EQ) are respectively about 2 and 4 orders of magnitude smaller than k_{02}^R (EQ).

5. Exact Quantum Reaction Probabilities for Vibrationally Excited Reagents

In order to observe the effect of vibrational excitation of the reagent H_2 on the resulting reaction probabilities, we extended the range of our exact quantum calculations to total energies of 1.4 eV. In Fig. 13 we plot P_{02}^R, P_{03}^R and P_{14}^R, the three largest reaction probabilities for $F + H_2$ in this energy range, as a function of energy. There are several important points to note about this figure.

First, the transition P_{14}^R has virtually zero effective threshold energy but otherwise has a similar translational energy dependence to that of P_{03}^R (which has the same $\nu' - \nu$ value as P_{14}^R). The absence of a significant threshold energy in P_{14}^R indicates that the dynamical effects responsible for the appearance of a significant effective energy threshold in P_{03}^R are no longer significant in P_{14}^R. This will lead to lower activation energies and higher rates of reaction for reagents which are initially vibrationally excited. The similarity between P_{14}^R and P_{03}^R implies that for the most significant reaction probabilities, an increase in the vibrational energy of the reagent results in a corresponding increase in the vibrational energy of the product. This agrees with experimental observations for $F + D_2$.[1f]

Second, the reaction probabilities P_{03}^R and P_{14}^R have sharp peaks at $E_0 = 0.425$eV and 0.823eV respectively. An analysis of the energy dependence of the scattering matrix elements corresponding to similarly shaped reaction probability curves in the $H + H_2$ collinear reaction[31,45] and in several other model reactions[46] showed that narrow peaks (or dips) in the reaction probabilities were the result of the presence of internal excitation

(Feshbach) resonances. These resonances are associated with excitations of virtual states of the intermediate triatomic complex (FHH in the present case). From Fig. 13 we see that the contributions of the direct processes seem to be rather small in regions of energy where the resonance processes are important. This results in only small interference effects between direct and compound state contributions to the scattering amplitude and the resulting reaction probabilities have nearly symmetrical peaks as a function of energy near the resonance energies. The resonance widths are about .01eV and only one non-negligible reaction probability seems to show resonant behavior at either of the two resonance energies. There seems to be a correlation between the appearance of an internal excitation resonance and the opening of a specific vibrational state of the product (as in the resonance at 0.823eV, which is close to the opening of the $\nu = 5$ channel in HF at 0.839eV). This indicates a correlation of the resonance state with the reaction products rather than with the reagents or with the transition state. We shall analyze this phenomenon further in paper II when we examine the high energy $F + D_2$ reaction probabilities.

Although the total E in Figure 13 extends to 1.16eV only, we have done calculations up to E = 1.4eV but found all reaction probabilities in this higher energy range to be less than 0.01. This behavior seems to be related to "centrifugal" effects associated to the angle between the x_1', and z_1' axes (i.e., the skew angle between the asymptotic portions of the minimum energy path for the potential of Fig. 1) and will be further discussed in paper II.

6. Summary

Many of the dynamical effects presented in this paper will be further examined in paper II to where we will relegate a more extensive summary of quantum effects in the F + H_2 reaction. In this paper we have seen that there are very serious differences between the results of quantum and standard quasi-classical mechanics for collinear F + H_2, most notably in the energy dependence of the reaction probability P^R_{03} near threshold. These differences in the behavior of the reaction probabilities result in important differences in the detailed thermal rate constants. The fact that the quasi-classical forward reaction probabilities and rate constants disagree quite strongly with the exact quantum results is of great significance since nearly all the trajectory studies done to date on this reaction have been of the quasi-classical forward type. For the present reaction, both the quasi-classical reverse and uniform semi-classical methods provide us with more accurate ways of approximating the exact quantum results. This suggests that it might be of interest to use these methods in three dimensions. Indeed, it may be possible to use the results of collinear calculations such as the ones presented here as a guide line when choosing an approximate method for doing three dimensional calculations.

Additional exact quantum results for F + H_2 show that threshold effects are no longer important when the reagent H_2 is initially vibrationally excited. The dominant transitions appear to be those which channel additional vibrational energy in the reagents into additional vibrational energy in the products. Internal excitation resonances are found to play an important role in the reaction probabilities at certain translational energies. There seems to be a one to one correspondence between the energy at which a resonance occurs and the energy at which a related product vibrational channel opens.

Acknowledgement

We thank Ambassador College for the use of their computational facilities in most of the work reported here.

TABLE I. Arrhenius Rate Constant Parameters for $F + H_2 \rightarrow FH + H^{(a)}$

	Temp. Range	EQ	QCF	QCR	USC
E_a^{02}	200-400 K	.411	.791	.230	.766
E_a^{02}	200-400	2.279	.853	2.596	2.495
A_{02}	200-400	1.620×10^4	2.424×10^4	1.669×10^4	1.486×10^4
A_{03}	200-400	2.667×10^4	2.492×10^4	3.377×10^4	4.621×10^4
E_a^{02}	900-1200	.223	.750	.086	.390
E_a^{03}	900-1200	2.628	1.444	2.869	2.368
A_{02}	900-1200	1.459×10^4	2.558×10^4	1.628×10^4	1.182×10^4
A_{03}	900-1200	4.433×10^4	4.464×10^2	4.689×10^4	4.499×10^4

(a) $k_{oi}(T) = A_{oi} \exp(-E_a^{oi}/RT)$ where E_a^{oi} is in kcal/mole and A_{oi} is in cm/ (molec · sec).

Footnotes

1. (a) J.C. Polanyi and D.C. Tardy, J. Chem. Phys. 51, 5717 (1969); (b) K.G. Anlauf, P.E. Charters, D.S. Horne, R.G. MacDonald, D.H. Maylotte, J. Polanyi, W.J. Skrlac, D.C. Tardy and K.B. Woodall, J. Chem. Phys. 53, 4091 (1970); (c) N. Jonathan, C.M. Melliar-Smith and D.H. Slater, Mol. Phys. 20, 93 (1971); (d) N. Jonathan, C.M. Melliar-Smith, D. Timlin, and D.H. Slater, Appl. Optics 10, 1821 (1971); (e) N. Jonathan, C.M. Melliar-Smith, S. Okuda, D.H. Slater and D. Timlin, Mol. Phys. 22, 561 (1971); (f) J.C. Polanyi and K.B. Woodhall, J. Chem. Phys. 58, 2298 (1973); (g) H.W. Chang, and D.W. Setser, J. Chem. Phys. 58, 2298 (1973).

2. (a) K.L. Kompa and G.C. Pimentel, J. Chem. Phys. 47, 857 (1967); (b) K.L. Kompa, J.H. Parker and G.C. Pimentel, J. Chem. Phys. 51, 91 (1969); (c) O.D. Krogh and G.C. Pimentel, J. Chem. Phys. 51, 5717 (1969); (d) R.D. Coombe and G.C. Pimentel, J. Chem. Phys. 59, 251 (1973); (e) W.H. Green and M.C. Lin, J. Chem. Phys. 54, 3222 (1971); (f) M.J. Berry, J. Chem. Phys. 59, 6229 (2973).

3. (a) T.P. Schaefer, P.E. Siska, J.M. Parson, F.P. Tully, Y.C. Wong and Y.T. Lee, J. Chem. Phys. 53, 3385 (1970); (b) Y.T. Lee, invited talk at the VII International Conference on the Physics of Electronic and Atomic Collisions, Amsterdam, 1971.

4. See compilations by N. Cohen, Report No. TR-0073(3430)-9, The Aerospace Corporation, El Segundo, Calif. (1972) and Report No. TR-0074(4530)-9, The Aerospace Corporation, El Segundo, Calif. (1974).

5. A. Persky, J. Chem. Phys. 59, 5578 (1973).

6. (a) D.J. Spencer, T.A. Jacobs, H. Mirels and R.W. F. Gross, Int. J. Chem. Kinetics 1, 493 (1969); (b) T.F. Deutsch, Appl. Phys. Lett, 10, 234 (1967); (c) S.N. Suchard, R.L. Kerber, G. Emanuel and J.S. Whittier, J. Chem. Phys. 57, 5065 (1972) and references therein.

7. (a) J.T. Muckerman, J. Chem. Phys. 54, 1155 (1971); (b) *ibid.*, 56, 2997 (1972).

8. (a) R.L. Jaffe and J.B. Anderson, J. Chem. Phys. 54, 2224 (1971); (b) *ibid*., 56, 682 (1972), (c) R.L. Jaffe, J.M. Henry and J.B. Anderson, J. Chem. Phys. 59, 1128 (1973).

9. (a) R.L. Wilkins, J.Chem. Phys. 56, 912 (1972); (b) R.L. Wilkins, J. Phys. Chem. 77, 3081 (1973).

10. N.C. Blais and D. G. Truhlar, J. Chem. Phys. 58, 1090 (1973).

11. A. Ding, L. Kirsch, D. Perry, J. Polanyi, J. Schreiber, Disc. Far. Soc., 55, 252 (1973).

12. P.A. Whitlock and J.T. Muckerman, J. Chem. Phys. 61, 4618 (1975).

13. (a) A. Ben-Shaul, R.D. Levine, and R.B. Bernstein, Chem. Phys. Lett. 15, 160 (1972); (b) A. Ben-Shaul, R.D. Levine, R.B. Bernstein, J. Chem. Phys. 57, 5427 (1972);

(c) A. Ben-Shaul, G.L. Hofacker, and K.L. Kompa, J. Chem. Phys. 59, 4664 (1973).

14. G.L. Hofacker and R.D. Levine, Chem. Phys. Lett. 15, 165 (1972), also unpublished results.

15. (a) C. F. Bender, S.V. O'Neil, P.K. Pearson and H.F. Schaefer III, Science, 176, 1412 (1972); (b) C.F. Bender, P.K. Pearson, S.V. O'Neil and H.F. Schaefer III, J. Chem. Phys. 56, 4626 (1972).

16. D.G. Truhlar, J. Chem. Phys. 56, 3189 (1972).

17. J.T. Muckerman and M.D. Newton, J. Chem. Phys. 56, 3191 (1972)

18 J.C. Tully, J. Chem. Phys. 60, 3042 (1974).

19. G.C. Schatz, J.M. Bowman and A. Kuppermann, J. Chem. Phys. 58, 4023 (1973).

20. J.M. Bowman, G.C. Schatz, A. Kuppermann, Chem. Phys. Lett. 24, 378 (1974).

21. (a) P.J. Kuntz, E.M. Nemeth, J.C. Polanyi, S.D. Rosner, and C.E. Young, J. Chem. Phys. 44, 1168 (1966); (b) J.C. Polanyi and W.H. Wong, J. Chem. Phys. 51, 1439 (1969).

22. D. Truhlar and A. Kuppermann, J. Chem. Phys. 56, 2232 (1972).

23. (a) R. Saxon and J. Light, J. Chem. Phys. 56, 3874 (1972); (b) ibid., 56, 3885 (1972); (c) G. Wolken and M. Karplus, J. Chem. Phys. 60, 351 (1974); (d) A. B. Elkowitz and R. E. Wyatt, J. Chem. Phys., in press (15 March 1975 issue).

24. (a) A. Kuppermann, G. C. Schatz and M. Baer, J. Chem. Phys. 61, 4362 (1974); (b) A. Kuppermann and G. C. Schatz, J. Chem. Phys., in press (15 March 1975 issue).

25. J.T. Muckerman (private communication).

26. L.M. Delves, Nuclear Phys. 20, 275 (1960).

27. G. Glasstone, K. Laidler and H. Eyring, *Theory of Reaction Rates*, McGraw Hill, 1941, p. 101; M. Karplus and K. Tang, J. Chem. Phys. 50, 1119 (1970).

28. (a) A. Kuppermann, Potential Energy Surfaces in Chemistry, ed. W.A. Lester (University of California at Santa Cruz, August 1970) pp. 121-129; (b) Abstracts of papers, VII International Conference on the Physics of Electronic and Atomic Collisions, Amsterdam, 1971.

29. D.G. Truhlar, J. Comp. Phys. 10, 123 (1972).

30. The reaction probabilities were found to be independent of the location of the endpoints of the integrations in each arrangement channel before the potential had completely reached its asymptotic value. However, the translational energies computed at the points of termination of the integrations were slightly smaller than their correct asymptotic values. The results reported here have been corrected by the difference (less than .0002eV).

31. G.C. Schatz and A. Kuppermann, J. Chem. Phys. 59, 964 (1973).

32. G.C. Schatz and A. Kuppermann, to be published.

33. J.M. Bowman and Aron Kuppermann, Chem Phys. Lett. 12, 1 (1972).

34. J.M. Bowman and Aron Kuppermann, J. Chem. Phys. 59, 6524 (1973).

35. A. Kuppermann, J.T. Adams and D.G. Truhlar, Abstracts of Papers, Eighth International Conference on the Physics of Electronic and Atomic Collisions, edited by B.C. Cobic and M.V. Kurepa, Belgrade (1973) p. 149.

36. R.L. Wilkins, J. Chem. Phys. 58, 3038 (1973).

37. D.S. Perry, J.C. Polanyi and C.W. Wilson, Chem. Phys. Lett. 24, 484 (1974).

38. J.M. Bowman, unpublished Ph.D. Thesis, California Institute of Technology, 1974.

39. W.H. Miller, Chem. Phys. Lett. 4, 431 (1970); J. Chem Phys. 53, 3578 (1970).

40. C.C. Rankin and W.H. Miller, J. Chem. Phys. 55, 3150 (1971).

41. This procedure is obviously valid if the function $m_f(q_0)$ is "smooth" (i.e., non-ragged) for both the forward and reverse trajectories since under these conditions, semi-classical reaction probabilities (contrarily to quasi-classical ones) rigorously obey microscopic reversibility.[34] As a result, when one of these $m_f(q_0)$ is smooth and the other not, it is reasonable to associate the semi-classical reaction probability of both the forward and reverse reactions to the smooth $m_f(q_0)$.

42. W.H. Miller and T.F. George, J. Chem. Phys. 56, 5668 (1972); J. Chem. Phys. 57, 2458 (1972).

43. For the H + H_2 reaction, the complex trajectory method yields reaction probabilities differing by less than 30% from the exact quantum results for energies less than the barrier (ref. 32).

44. G.C. Fettis, J.H. Knox and A.F. Trotman-Dickenson, J. Chem. Soc. 1064 (1960).

45. R.D. Levine and S.F. Wu, Chem. Phys. Lett. 11, 557 (1971).

46. S.F. Wu, B.R. Johnson and R.D. Levine, Mol. Phys. 25, 839 (1973).

Figure Captions

1. Equipotential contour plot of the FH_2 collinear potential energy surface used in all calculations reported here. Energies given are relative to the minimum in the H_2 diatomic potential curve. Coordinate system is defined in text. Heavy line denotes the minimum energy path with saddle point indicated by a cross.

2. Exact quantum reaction probabilities for collinear $F + H_2$ as a function of relative translational energy E_0 and total energy E (relative to minimum in H_2 diatomic potential energy curve). (a) Total reaction probability P_0^R from $\nu = 0$ of H_2 (b) Reaction probabilities P_{02}^R and P_{03}^R (defined in text). Vertical arrow in abscissa indicates the energy at which $\nu = 3$ of HF becomes accessible.

3. Exact quantum reaction probabilities P_{01}^R and P_{00}^R (similar to Fig. 2).

4. Quasi-classical forward and exact quantum reaction probabilities for $F + H_2$: (a) P_0^R, (b) P_{02}^R and P_{03}^R. Dashed line indicates QCF results with their associated statistical errors indicated by vertical bars. Solid line indicates EQ results (as in Fig. 2).

5. Fraction (f_V) of the total reagent energy (in excess of product zero point energy) which ends up as vibrational energy in the product HF as a function of the reagent translational energy E_0 and total energy E. Solid line indicates EQ results and dashed line QCF results. Other notation analogous to Fig. 2.

6. Ratio of reaction probabilities P_{03}^R / P_{02}^R versus translational energy E_0 and total energy E. Solid line indicates EQ results and dashed line QCF results. Other notation analogous to Fig. 2.

7. Quasi-classical reverse and exact quantum reaction probabilities for $F + H_2$: (a) P_0^R, (b) P_{02}^R and P_{03}^R. Dashed line indicates QCR results with their associated statistical errors indicated by vertical bars. Solid line indicates EQ results (as in Fig. 2).

8. Uniform semi-classical and exact quantum reaction probabilities for $F + H_2$: (a) P_0^R, (b) P_{02}^R and P_{03}^R. Dashed line indicates USC results, solid line EQ results as in Fig. 2.

9. EQ (solid), QCF (short dash), QCR (dash dot) and USC (long dash) reaction probabilities P_{03}^R (a) and P_{02}^R (b) for $F + H_2$ (from Figs. 2, 4, 7-8).

10. EQ (solid), QCF (short dash), QCR (dash dot) and USC (long dash) total reaction probability P_0^R for $F + H_2$ (from Figs. 2, 4, 7-8).

11. Arrhenius plot of EQ (solid), QCF (short dash), QCR (dash dot) and USC (long dash) rate constants for $F + H_2$: (a) k_{02}^R, (b) k_{03}^R.

12. Ratios of rate constants k_{03}^R / k_{02}^R for $F + H_2$ as a function of temperature. EQ (solid), QCF (short dash), QCR (dash dot), and USC (long dash).

13. Exact quantum reaction probabilities P_{02}^R, P_{03}^R and P_{14}^R for $F + H_2$ at translational energies higher than those in Fig. 2. Arrows near $E_0 = 0.44$eV and 0.84eV indicate the opening of $\nu = 4$ and 5 respectively of HF while that at 0.51eV indicates the energy E_0 at which $\nu = 1$ of H_2 becomes accessible.

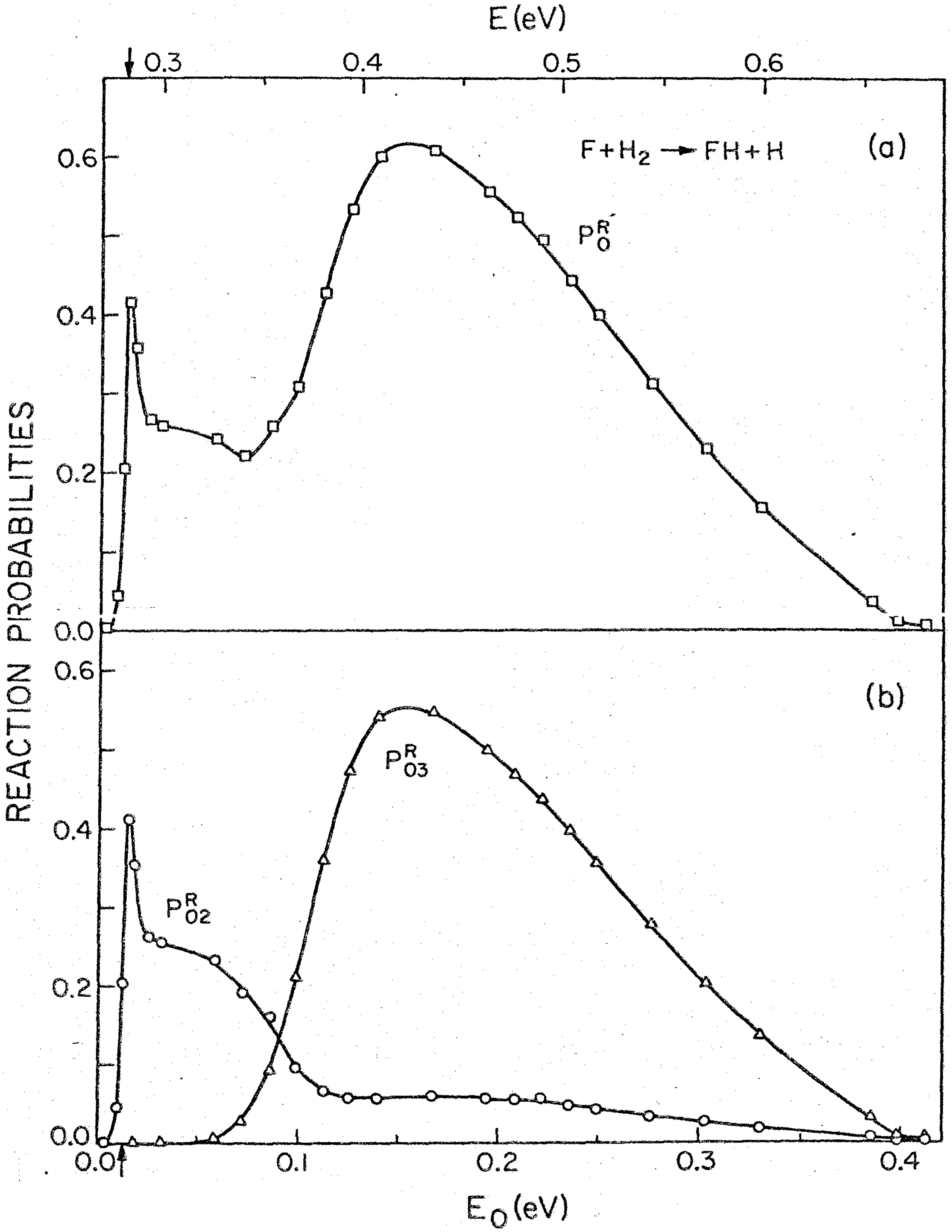
E (eV)
0.3
0.4
0.5
0.6
$F + H_2 \rightarrow FH + H$
(a)
P_0^R
(b)
P_{03}^R
P_{02}^R
REACTION PROBABILITIES
0.0
0.2
0.4
0.6
0.0
0.1
0.2
0.3
0.4
E_0 (eV)

Figure 2

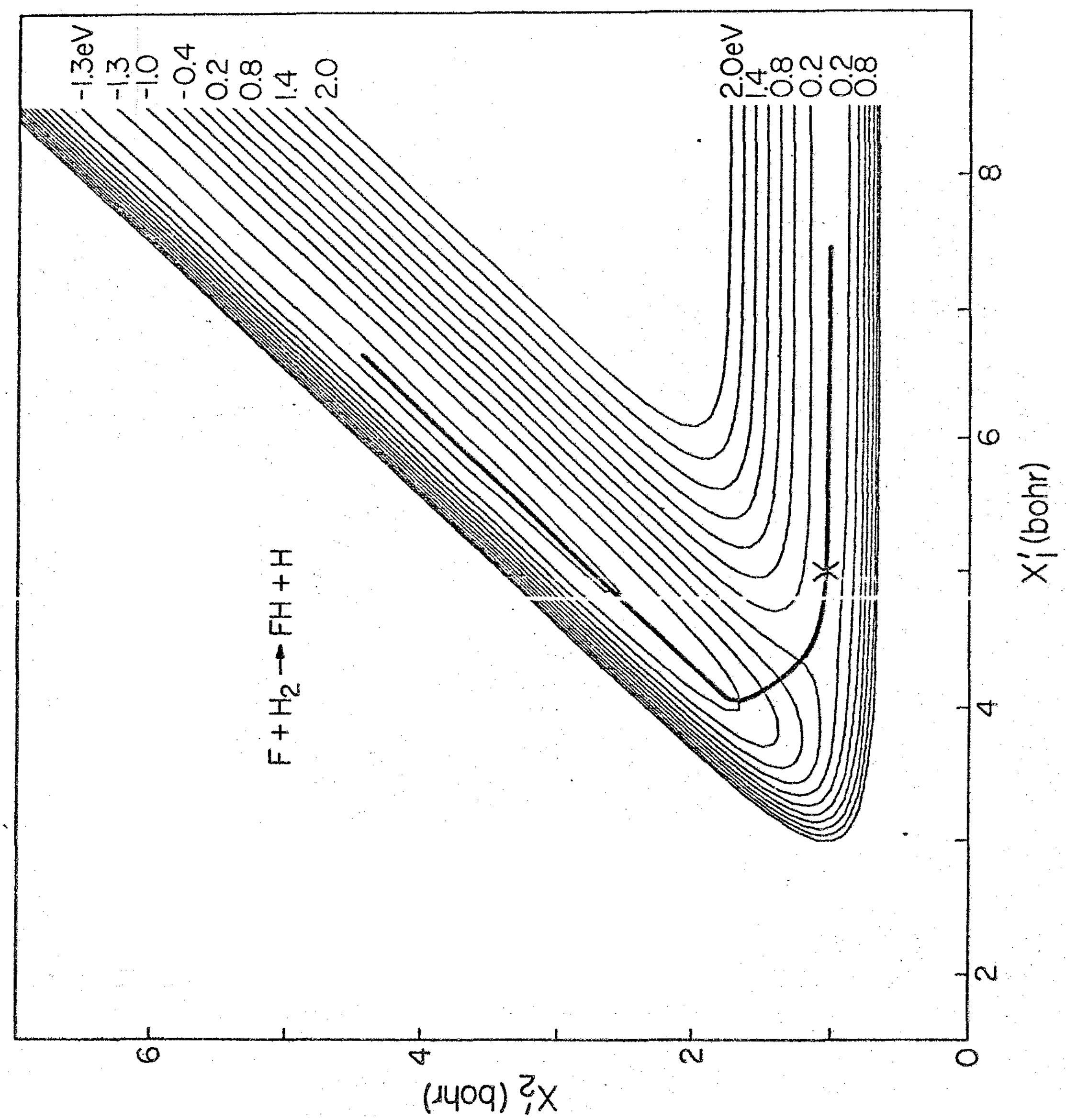
F + H$_2$ → FH + H
-1.3eV
-1.3
-1.0
-0.4
0.2
0.8
1.4
2.0
2.0eV
1.4
0.8
0.2
0.2
0.8
2
4
6
8
X$'_1$ (bohr)
0
2
4
6
X$'_2$ (bohr)

Figure 1

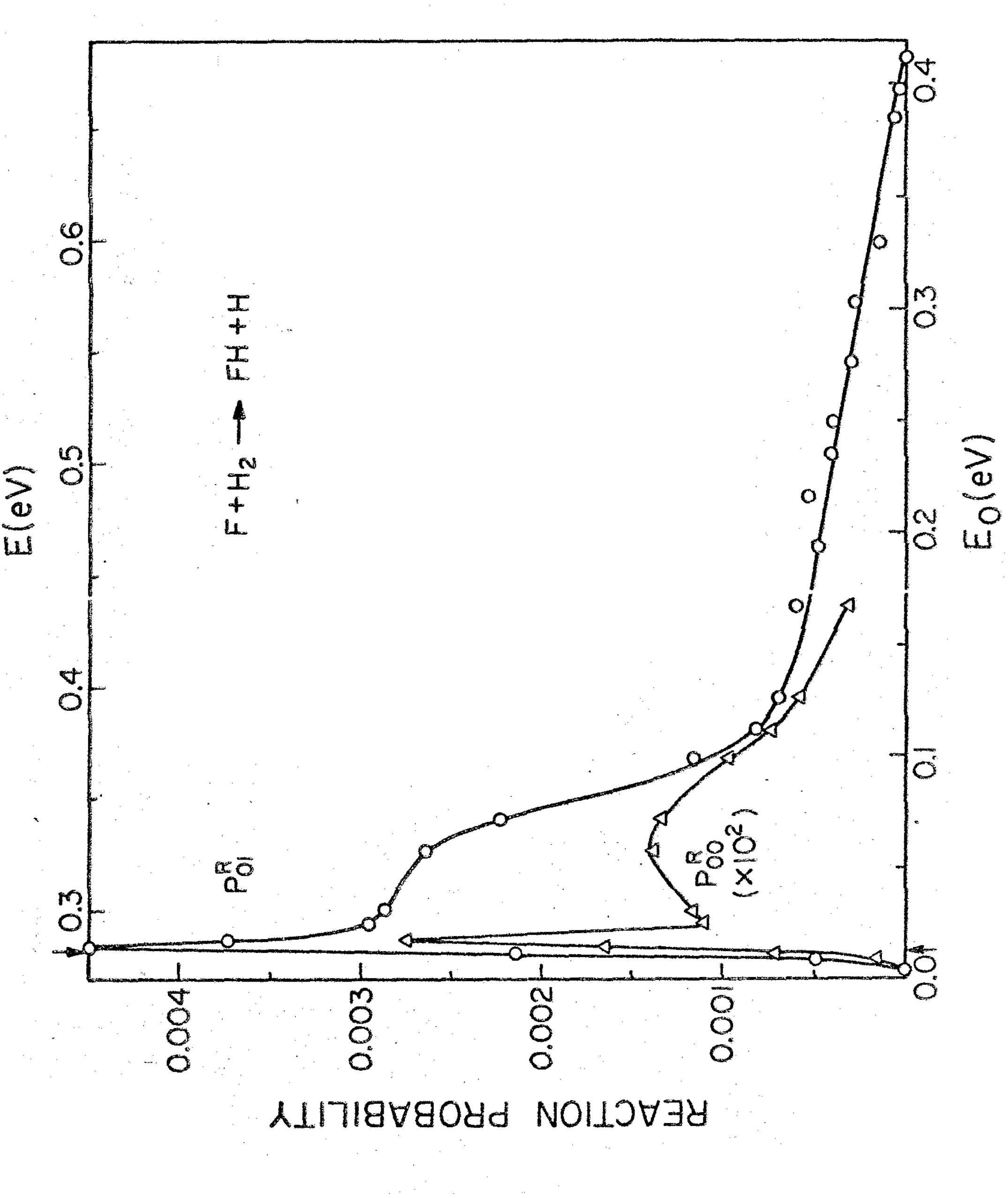
E(eV)
0.3
0.4
0.5
0.6
F + H$_2$ → FH + H
P^R_{01}
P^R_{00} (×10^2)
REACTION PROBABILITY
0.004
0.003
0.002
0.001
0.0
0.1
0.2
0.3
0.4
E$_0$(eV)

Figure 3

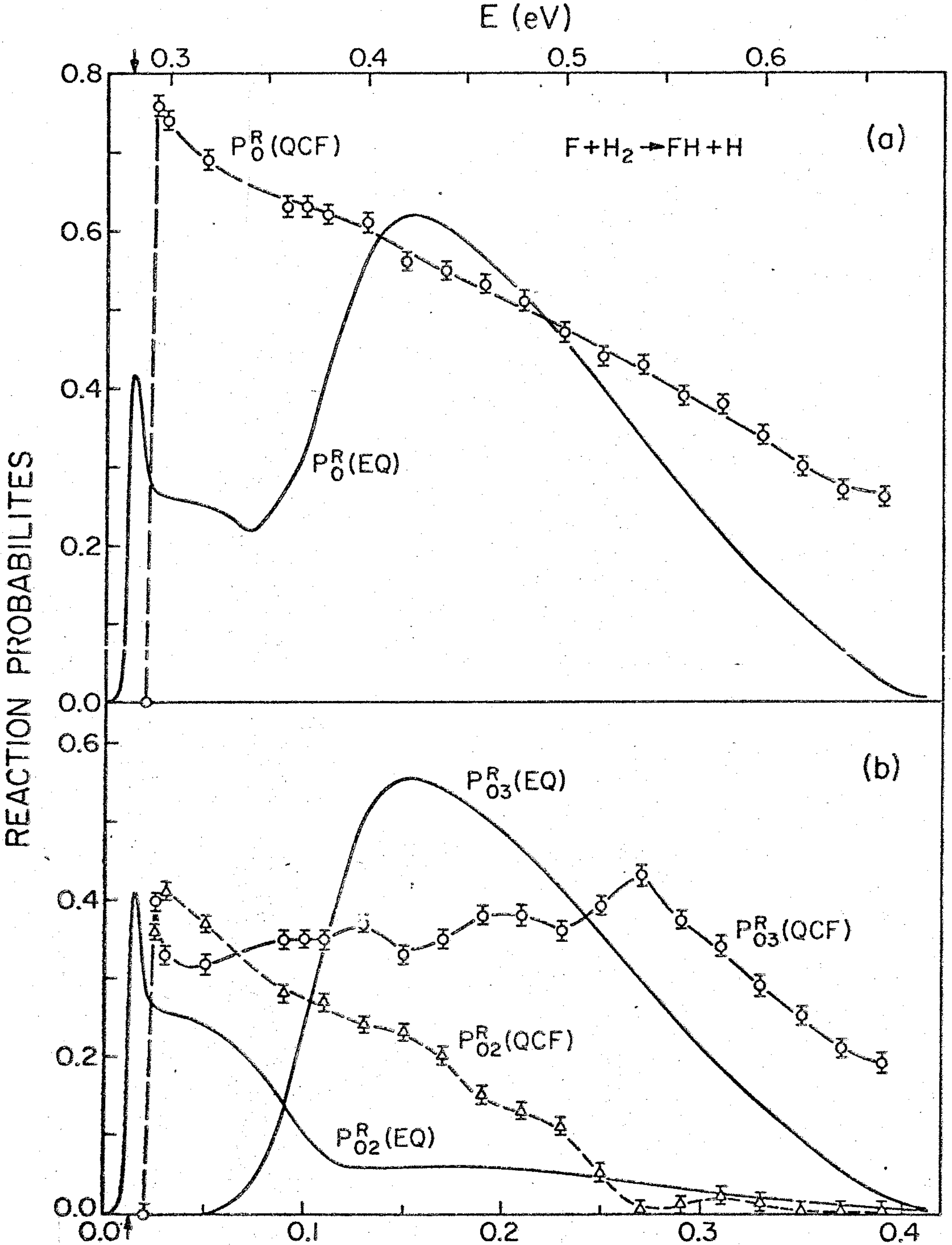
E (eV)
0.3
0.4
0.5
0.6
0.8
0.6
0.4
0.2
0.0
(a)
P_0^R(QCF)
$F+H_2 \rightarrow FH+H$
P_0^R(EQ)
REACTION PROBABILITES
0.6
0.4
0.2
0.0
(b)
P_{03}^R(EQ)
P_{03}^R(QCF)
P_{02}^R(QCF)
P_{02}^R(EQ)
0.01
0.1
0.2
0.3
0.4
E_0(eV)

Figure 4.

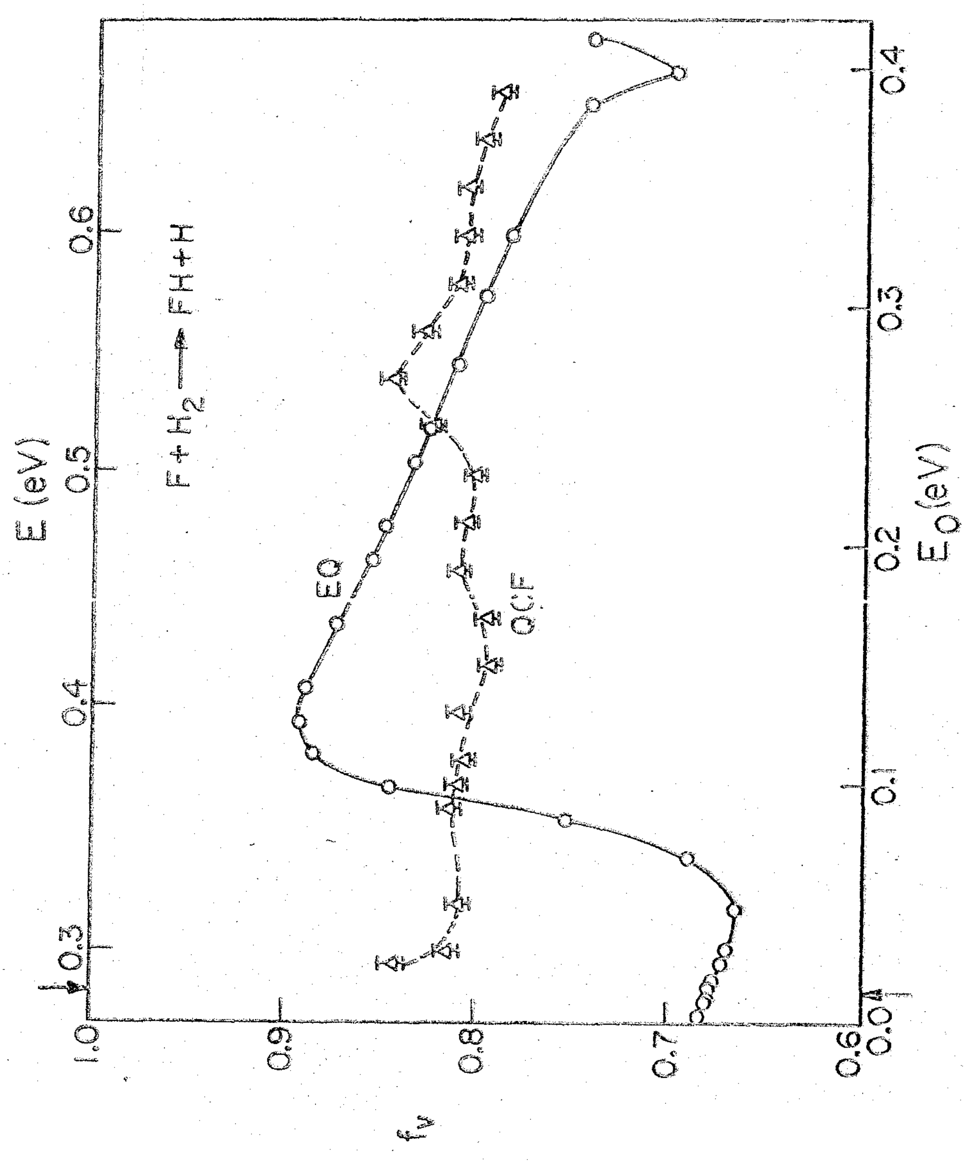

Figure 5

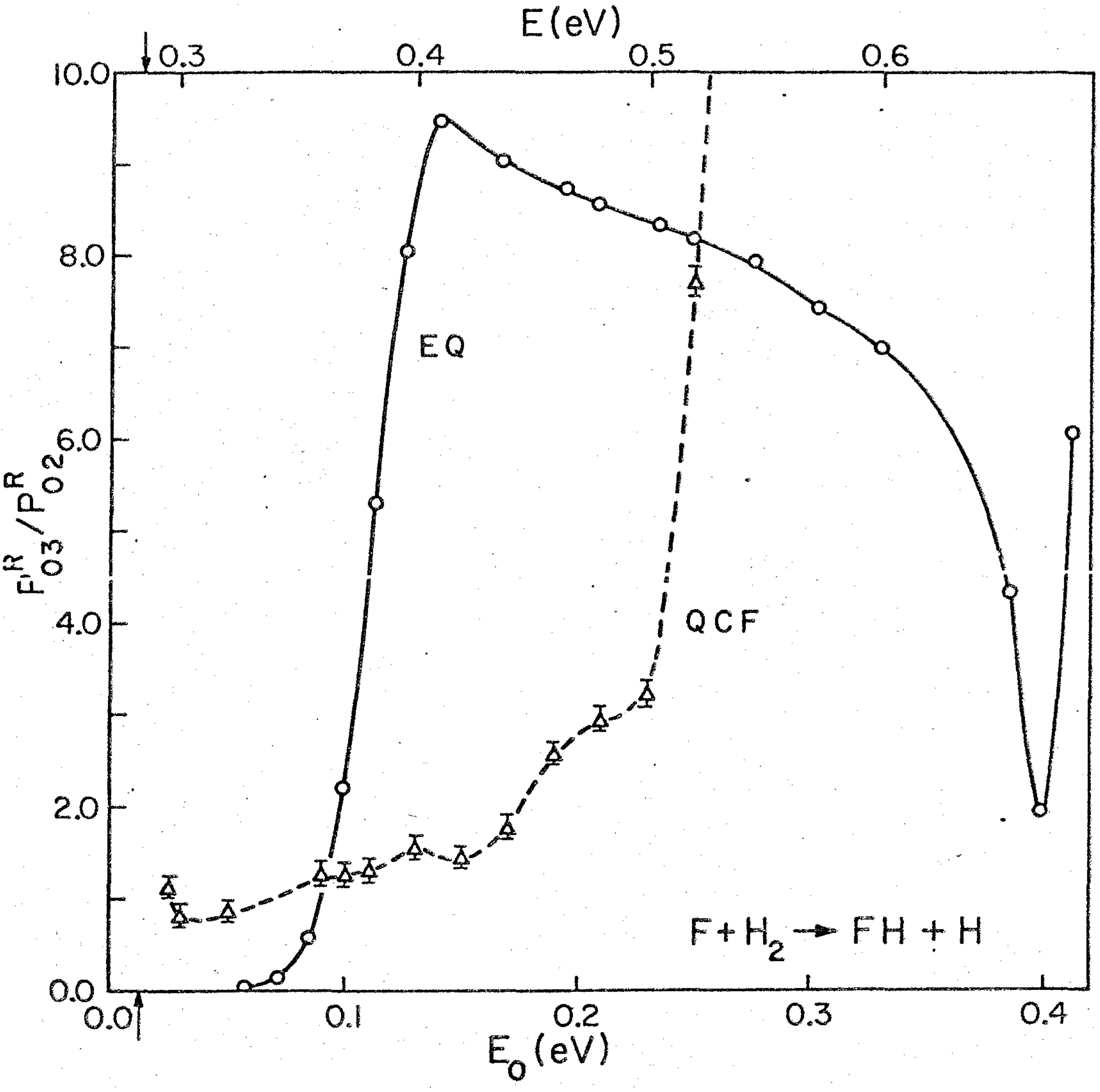
E(eV)
0.3
0.4
0.5
0.6
10.0
8.0
6.0
4.0
2.0
0.0
F^{R}_{03}/P^{R}_{02}
EQ
QCF
$F + H_2 \rightarrow FH + H$
0.0
0.1
0.2
0.3
0.4
E_0 (eV)

Figure 6

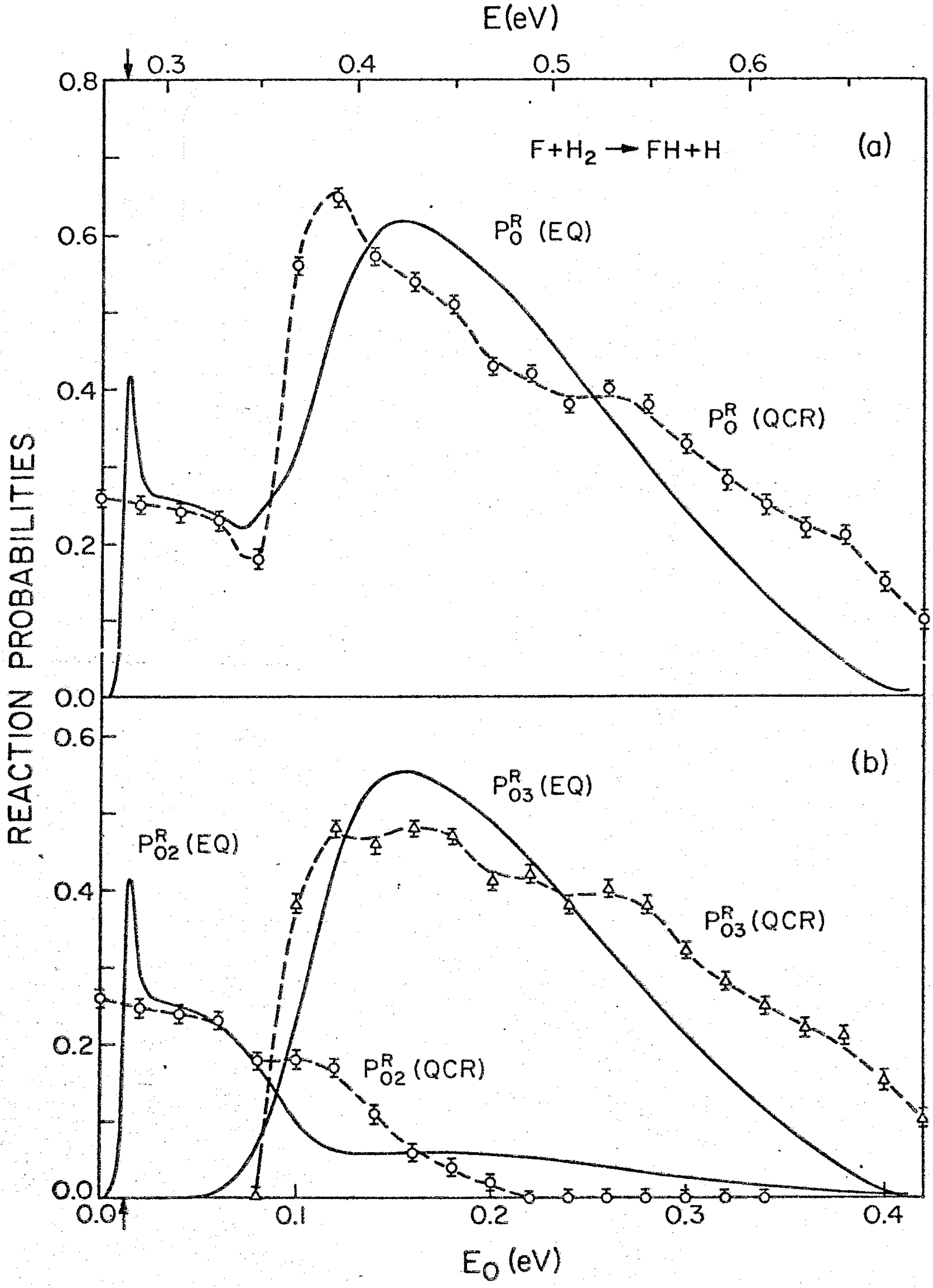
E(eV)
0.3
0.4
0.5
0.6
0.8
0.6
0.4
0.2
0.0
F+H$_2$ → FH+H
(a)
P$^R_0$ (EQ)
P$^R_0$ (QCR)
REACTION PROBABILITIES
0.6
0.4
0.2
0.0
(b)
P$^R_{03}$ (EQ)
P$^R_{02}$ (EQ)
P$^R_{03}$ (QCR)
P$^R_{02}$ (QCR)
0.0
0.1
0.2
0.3
0.4
E$_0$ (eV)

Figure 7

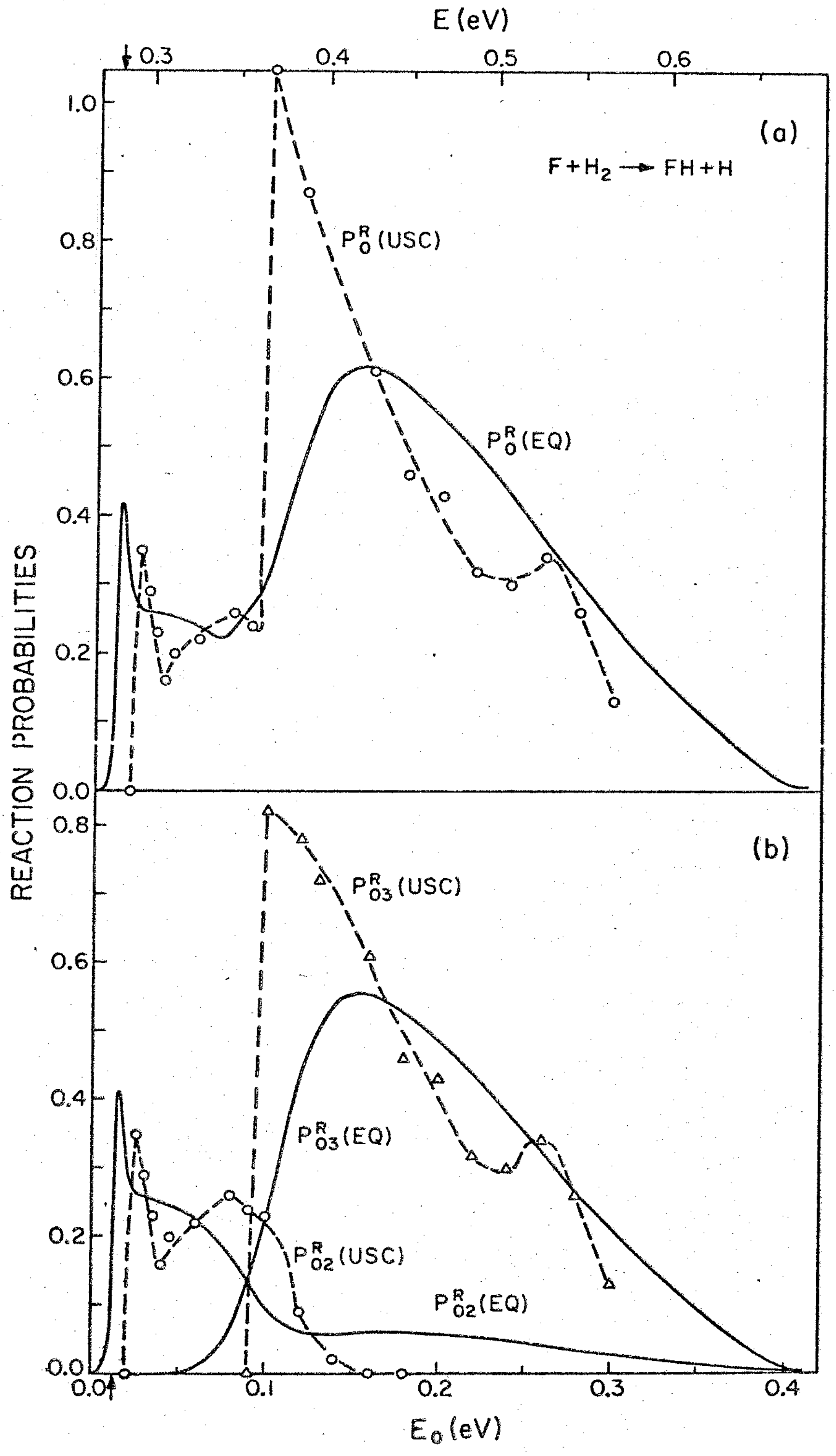
E (eV)
0.3
0.4
0.5
0.6
1.0
0.8
0.6
0.4
0.2
0.0
(a)
F + H2 → FH + H
P$^R_0$ (USC)
P$^R_0$ (EQ)
REACTION PROBABILITIES
0.8
0.6
0.4
0.2
0.0
(b)
P$^R_{03}$ (USC)
P$^R_{03}$ (EQ)
P$^R_{02}$ (USC)
P$^R_{02}$ (EQ)
0.0
0.1
0.2
0.3
0.4
E0 (eV)

Figure 8

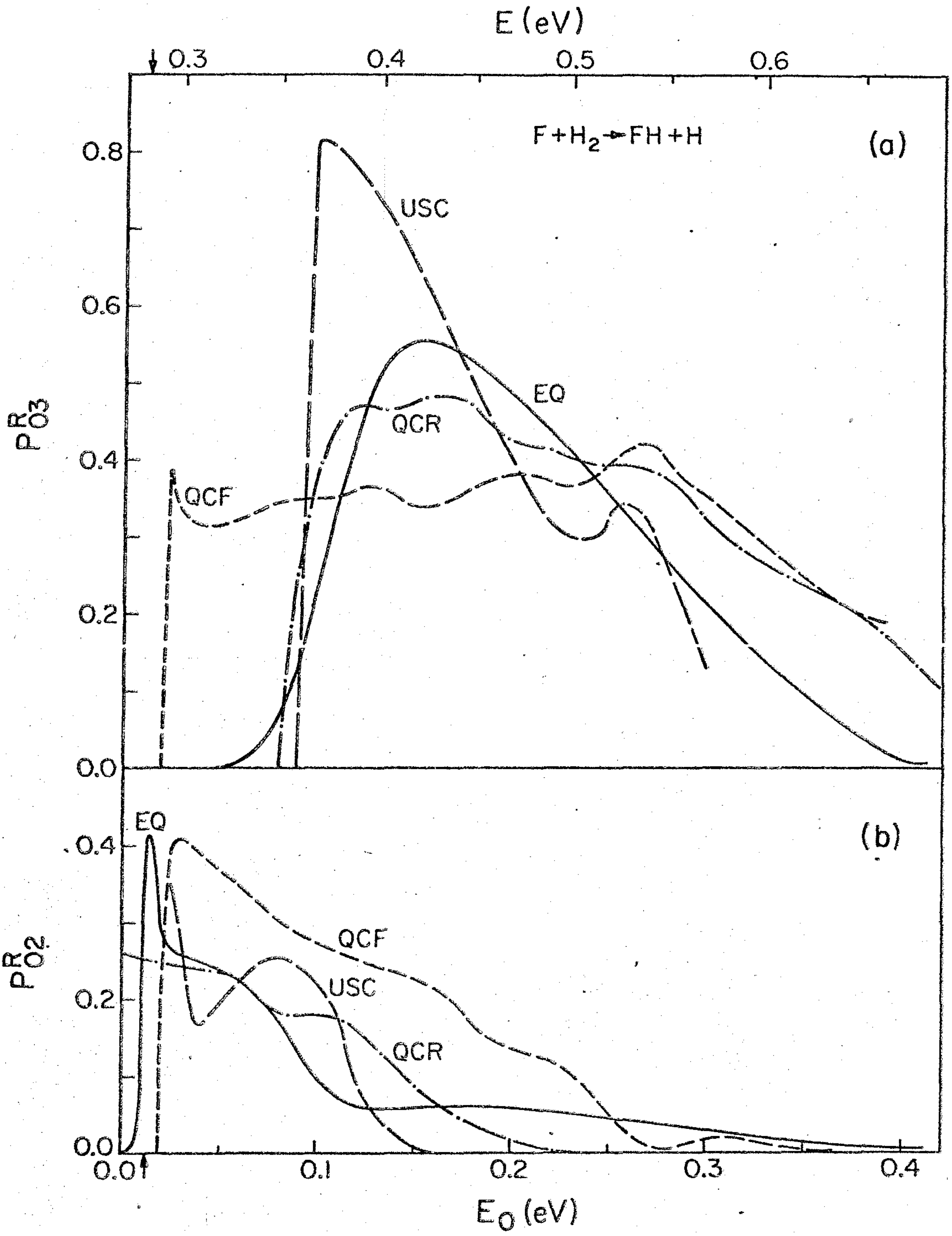
E (eV)
0.3
0.4
0.5
0.6
F+H$_2$→FH+H
(a)
P^R_{03}
0.8
0.6
0.4
0.2
0.0
USC
EQ
QCR
QCF
(b)
P^R_{02}
0.4
0.2
0.0
EQ
QCF
USC
QCR
0.01
0.1
0.2
0.3
0.4
E$_0$ (eV)

Figure 8

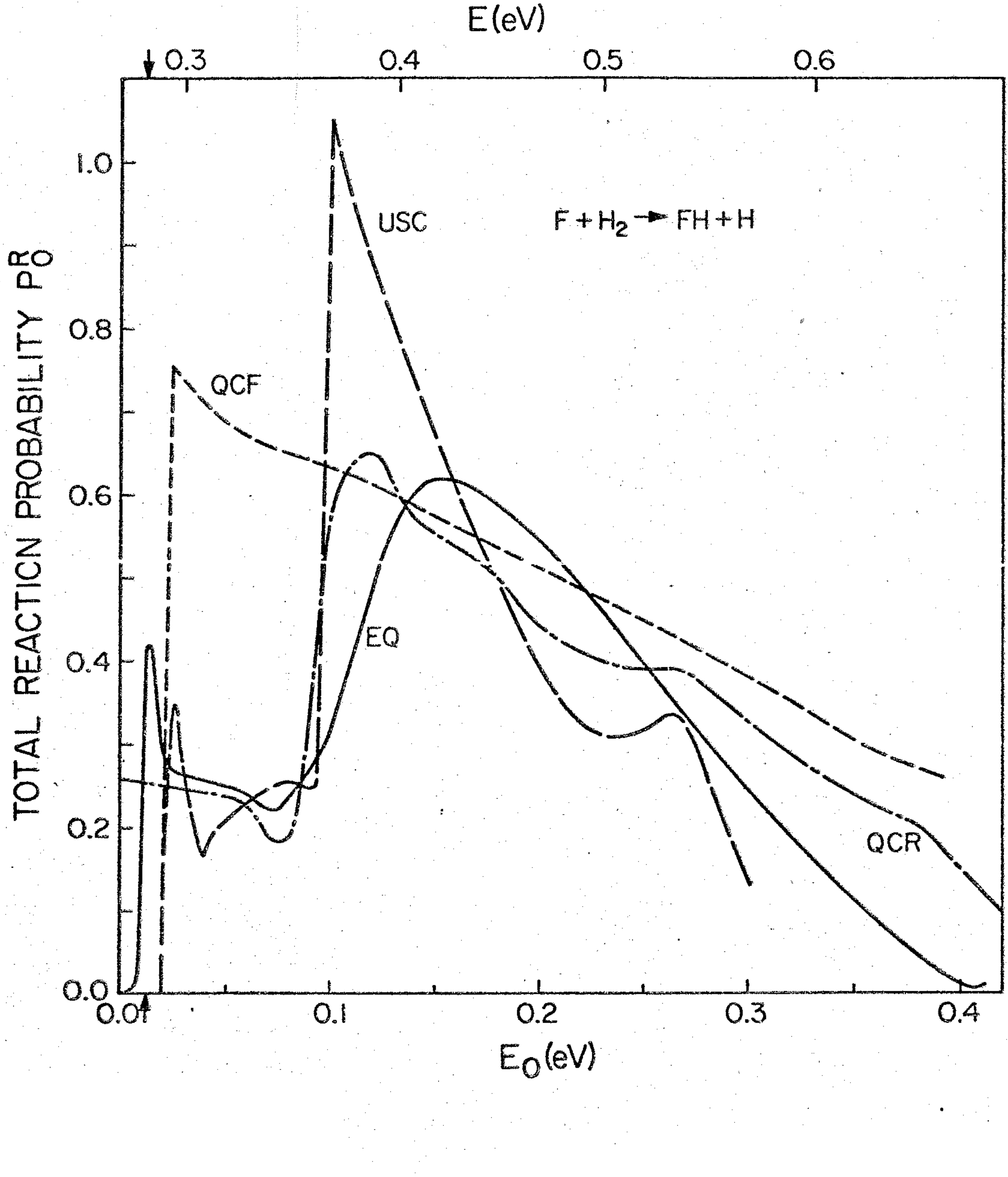
E(eV)
0.3
0.4
0.5
0.6
1.0
0.8
0.6
0.4
0.2
0.0
0.01
0.1
0.2
0.3
0.4
E_0(eV)
TOTAL REACTICN PROBABILITY P_0^R
USC
$F + H_2 \rightarrow FH + H$
QCF
EQ
QCR

Figure 10

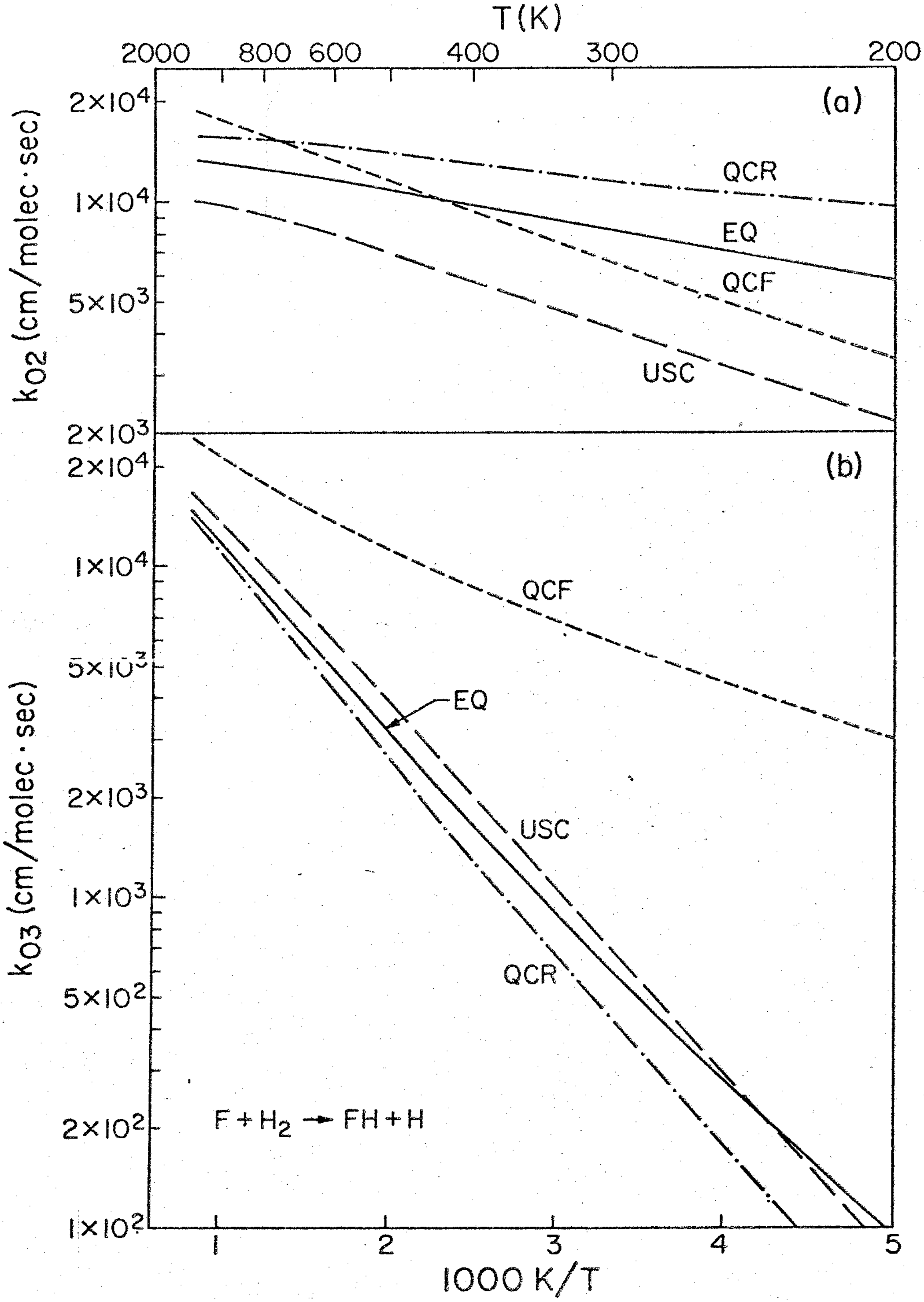
T(K)
2000
800
600
400
300
200
(a)
2×10^4
1×10^4
5×10^3
2×10^3
k_O2 (cm/molec·sec)
QCR
EQ
QCF
USC
(b)
2×10^4
1×10^4
5×10^3
2×10^3
1×10^3
5×10^2
2×10^2
1×10^2
k_O3 (cm/molec·sec)
QCF
EQ
USC
QCR
F + H2 → FH + H
1
2
3
4
5
1000 K/T

Figure 11

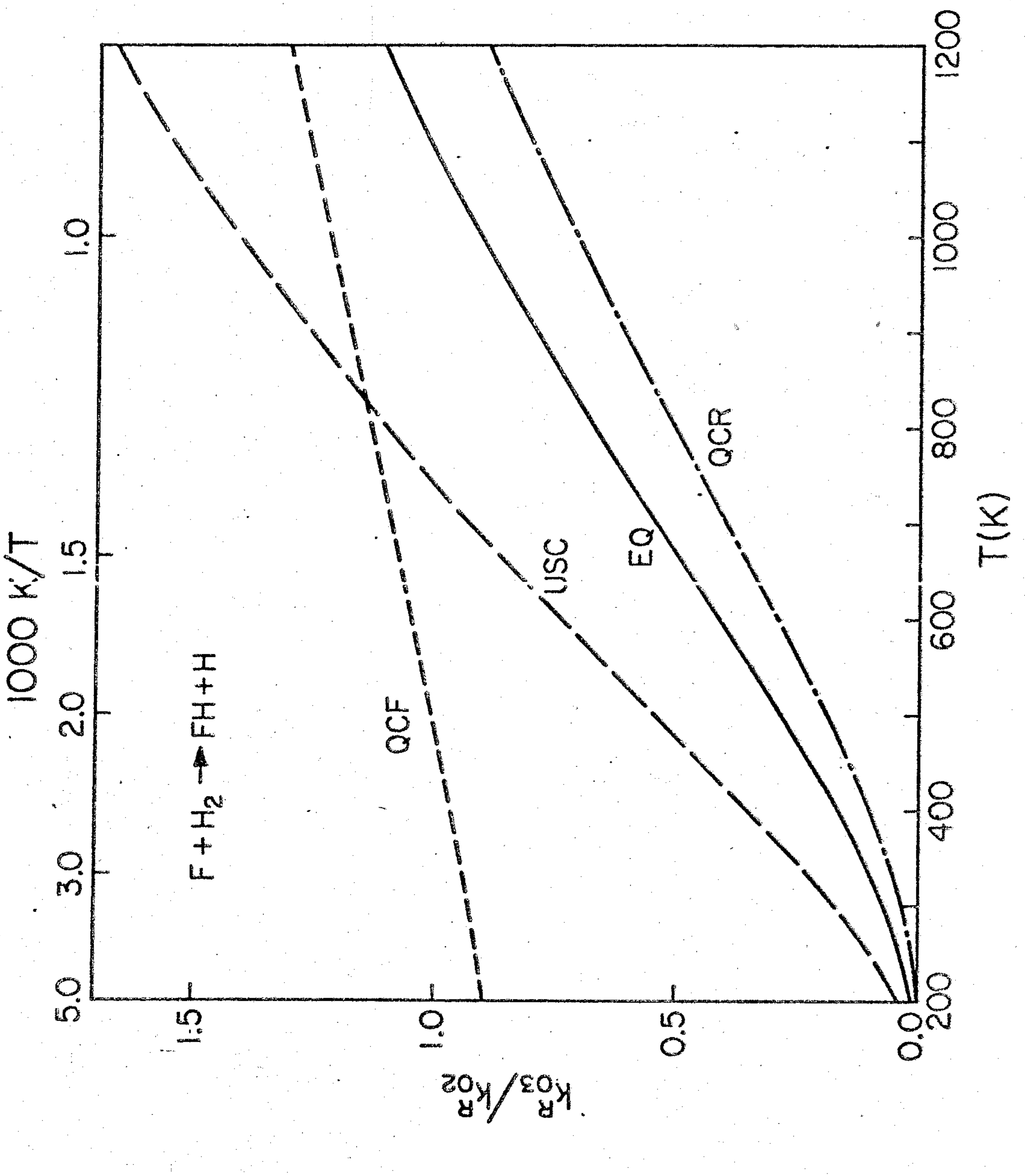
1000 K/T
5.0
3.0
2.0
1.5
1.0
F + H₂ → FH + H
QCF
USC
EQ
QCR
k^R_03/k^R_02
0.0
0.5
1.0
1.5
200
400
600
800
1000
1200
T(K)

Figure 12

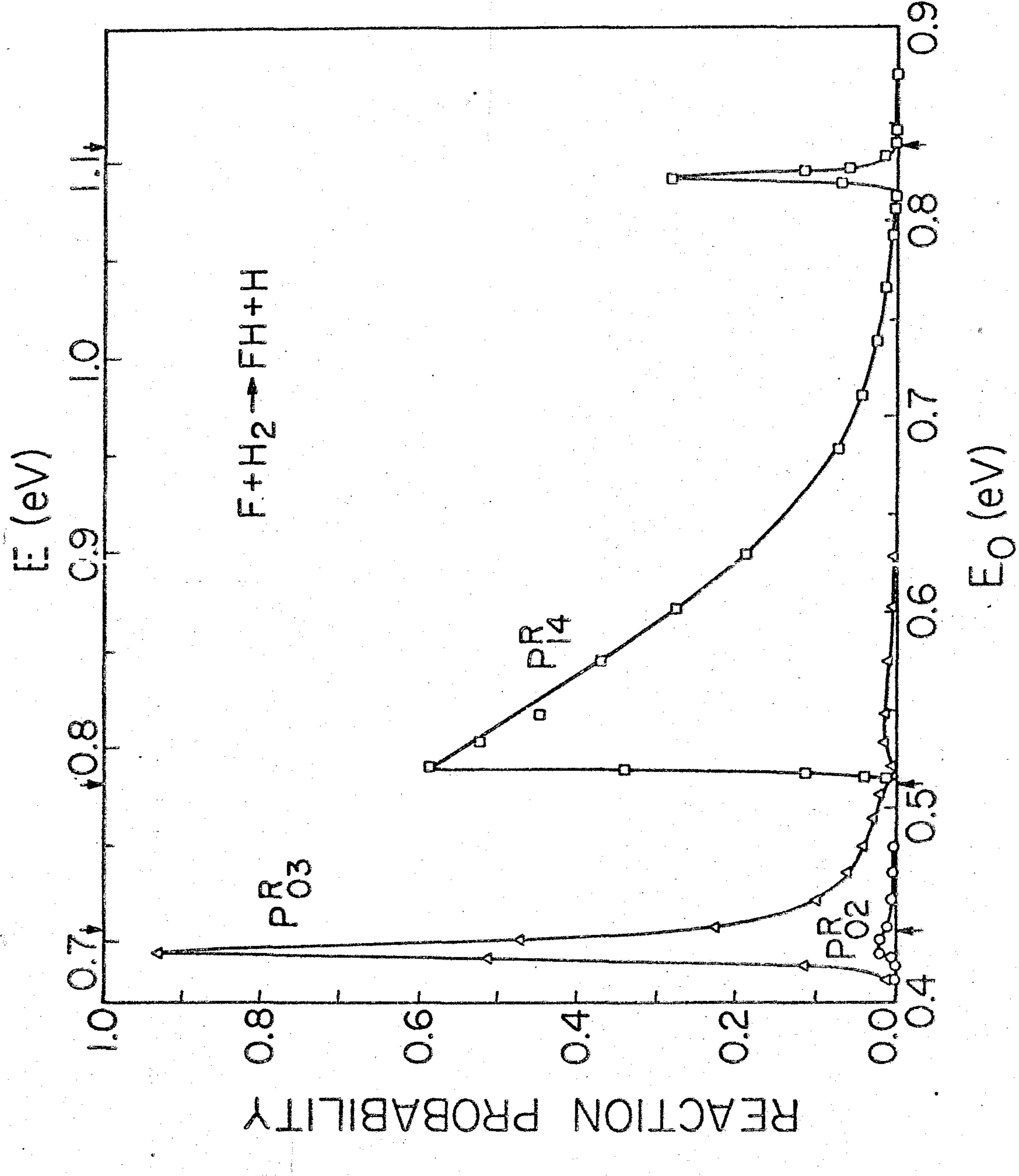
REACTION PROBABILITY
1.0
0.8
0.6
0.4
0.2
0.0
0.4
0.5
0.6
0.7
0.8
0.9
E_0 (eV)
0.7
0.8
0.9
1.0
1.1
E (eV)
$F+H_2 \rightarrow FH+H$
P^R_{03}
P^R_{02}
P^R_{14}

Figure 13

2. EXACT QUANTUM, QUASI-CLASSICAL, AND SEMI-CLASSICAL REACTION PROBABILITIES FOR THE COLLINEAR $F + D_2 \rightarrow FD + D$ REACTION[*]

---

[*] This paper appeared in the Journal of Chemical Physics **63**, 685 (1975).

EXACT QUANTUM, QUASI-CLASSICAL AND SEMI-CLASSICAL REACTION PROBABILITIES FOR THE COLLINEAR $F + D_2 \rightarrow FD + D$ REACTION[*]

George C. Schatz[†], Joel M. Bowman[†][§] and Aron Kuppermann

Arthur Amos Noyes Laboratory of Chemical Physics[**]
California Institute of Technology
Pasadena, California 91125

(Received)

Exact quantum, quasi-classical and semi-classical reaction probabilities and rate constants for the collinear reaction $F + D_2 \rightarrow FD + D$ are presented. In all calculations, a high degree of population inversion is predicted with P_{03}^R and P_{04}^R being the dominant reaction probabilities. In analogy with the $F + H_2$ reaction (ref. 1, preceding paper), the exact quantum $0 \rightarrow 3$ and $0 \rightarrow 4$ probabilities show markedly different energy dependence with P_{03}^R having a much smaller effective threshhold energy ($E_T = 0.014$ eV) than P_{04}^R (0.055 eV). The corresponding quasi-classical forward probabilities P_{03}^R and P_{04}^R are in poor agreement with the exact quantum ones, while their quasi-classical reverse and semi-classical counterparts provide much better approximations to the exact results. Similar

---

[*] Work supported in part by the United States Air Force Office of Scientific Research.

[†] Work performed in partial fulfillment of the requirements for the Ph. D. degree in Chemistry at the California Institute of Technology.

[§] Present address: Department of Chemistry, Illinois Institute of Technology, Chicago, Ill. 60616.

[**] Contribution No. 4989.

comparisons are also made in the analysis of the corresponding EQ, QCF, QCR and USC rate constants. An information theoretic analysis of the EQ and QCF reaction probabilities indicates non-linear surprisal behavior as well as a significant isotope dependence. Additional quantum results at higher energies are presented and discussed in terms of threshold behavior and resonances. Exact quantum reaction probabilities for the related F + HD → FH + D and F + DH → FD + H reactions are given and an attempt to explain the observed isotope effects is made.

1. Introduction

In the preceding paper[1] (hereafter referred to as I) we compared the exact quantum (EQ), quasi-classical forward (QCF), quasi-classical reverse (QCR) and uniform semi-classical (USC) reaction probabilities for the collinear $F + H_2 \rightarrow FH + H$ reaction. The results of all four methods agreed in their prediction of a high degree of population inversion in the products of this exothermic reaction. However, the QCF probabilities were found to differ substantially from the corresponding EQ results in threshold behavior and energy dependence. This could have important consequences regarding the validity of the standard three-dimensional quasi-classical method which has been used on $F + H_2$ (D_2) and which is the three-dimensional version of the QCF method. We found much better agreement between the exact quantum probabilities and both the quasi-classical reverse and the uniform semi-classical results thus indicating that either of the last two methods might be preferred to the quasi-classical forward one in three-dimensional calculations.

In this paper we present the analogous EQ, QCF, QCR and USC results for the collinear $F + D_2$ reaction over roughly the same range of translational energies as was used in I. We shall also make an analysis of the surprisal function for the EQ and QCF results for $F + D_2$ (and $F + H_2$) to determine if an information theoretic description of the product state distributions can be useful. In addition, exact quantum probabilities for the reactions $F + HD\,(DH) \rightarrow FH\,(FD) + H\,(D)$ are given. We also study the importance of tunnelling and resonances in $F + D_2$, $F + HD$ and $F + DH$. These calculations were done in order to assess the effect of isotopic substitution on the magnitude of the quantum effects and on the validity of the approximate methods.

The potential energy surface used in these calculations is identical to that described in I.[2] In addition, most of the numerical techniques are the same as was used in I and will not be described again here except to note changes made.

In Section 2 we discuss the EQ, QCF, QCR and USC reaction probabilities for F + D_2 and the corresponding collinear rate constants are presented in Section 3. Section 4 contains a study of the behavior of the reaction probabilities at energies sufficiently high to excite the first two vibrational states of reagent D_2. In addition, we discuss resonances in this reaction, giving specific comparisons between the results of the exact quantum, and approximate methods in the vicinity of these resonances. Section 5 contains a description of the EQ reaction probabilities for F + HD (DH) and in Section 6 we present a summary of conclusions.

2. Quantum, Quasi-Classical and Semi-Classical Reaction Probabilities for Collinear $F + D_2 \rightarrow FD + D$

2.1 Exact quantum reaction probabilities

Since the vibrational spacing in D_2 is roughly 9 kcal/mole and that in FD is about 8 kcal/mole, and the reaction is exothermic by 32 kcal/mole approximately, at least five vibrational levels of DF are accessible when D_2 has an initial quantum number $\nu = 0$. By coincidence, the $\nu = 3$ and 4 vibrational levels of DF have nearly the same total energies as the $\nu = 2$ and 3 vibrational levels of HF, respectively. This results in remarkable similarities between these two reactions despite the significant difference in the corresponding reduced masses

($\mu_{F,H_2}/\mu_{F,D_2} = 0.548$). As in I, we will designate by $P_{\nu\nu'}^R$ the reaction probability for a reagent initially in state ν to form product in state ν', and by P_{ν}^R the total reaction probability from initial state ν (i.e., $\sum_{\nu'} P_{\nu\nu'}^R$). In Figure 1 we present the exact quantum reaction probabilities P_{04}^R, P_{03}^R and P_0^R for $F + D_2$ at relative translational energies (E_0) in the range 0.0 to 0.25 eV. The corresponding probabilities P_{02}^R, P_{01}^R and P_{00}^R are plotted in Figure 2. It is apparent from these figures that P_{04}^R and P_{03}^R are the most significant contributors to P_0^R in this E_0 range. The P_{02}^R, P_{01}^R and P_{00}^R curves are all very similar in appearance to the P_{03}^R one, but with greatly reduced magnitudes ($P_{02}^R \sim 6.8 \times 10^{-2} P_{03}^R$, $P_{01}^R \sim 5 \times 10^{-4} P_{03}^R$, $P_{00}^R \sim 6 \times 10^{-6} P_{03}^R$). There is a very significant difference between the threshold behavior of P_{03}^R and that of P_{04}^R quite analogous to what was observed in I for the reaction probabilities P_{02}^R and P_{03}^R of $F + H_2$. As in I, it is convenient to define an effective threshold energy E_T for the $\nu \rightarrow \nu'$ reaction as the difference between the (lowest) energy for which the corresponding $P_{\nu\nu'}^R$ is equal, say, to 1% of the maximum value attained by this quantity and the energy at which the $\nu \rightarrow \nu'$ process becomes energetically possible. Table I contains the values of E_T for several important reaction probabilities for the reactions of F with H_2, D_2, HD and DH as well as the corresponding vibrationally adiabatic zero curvature barrier heights E_{VAZC} (described in I). From it we see that for $F + D_2$ the value of E_T for P_{03}^R(EQ), 0.014 eV, is appreciably lower than the E_{VAZC} value of 0.032 eV. This can be interpreted as an indication of the extent of vibrationally adiabatic one-dimensional tunnelling (see paper I) in this system. The value of E_T for P_{03}^R (QCF) of 0.030 eV is very close to E_{VAZC}. This suggests that the chemical motion for this system is nearly vibrationally adiabatic in the approach coordinate in the sense that the local action number for the motion transverse to the reaction coordinate should vary relatively little between the separated reagent region and the saddle point region. The corresponding values of E_T and E_{VAZC} for P_{02}^R (EQ) of $F + H_2$ are 0.005 eV and 0.026 eV, indicating somewhat more tunnelling in this system than in $F + D_2$, as expected. The effective threshold energy of P_{04}^R $(F + D_2)(E_T = 0.055$ eV)is similar to that of P_{03}^R $(F + H_2)$ (0.045 eV). The near coincidence in energy between the $\nu = 3$ and 4 vibrational levels of FD and $\nu = 2$ and 3 of FH is probably responsible for the very similar appearance of the corresponding EQ reaction probabilities. (Compare Figure 2 of I with Figure 1 of the present paper.) There are, however, differences in the maximum values of certain analogous reaction probabilities especially $P_{03}^R(F + D_2)$ and P_{02}^R $(F + H_2)$ (which have maximum values of 0.66 and 0.44 respectively). We shall see in Section 4 that the differences between analogous reaction probabilities for the two reactions become even more important for $E_0 > 0.25$ eV.

2.2 Quasi-classical reaction probabilities

In Figure 3 are plotted the QCF and EQ reaction probabilities P_{03}^R, P_{04}^R and P_0^R for $F + D_2$. No reactive trajectories yield DF with $\nu' = 0$ or 1 but there is a small probability of reaction to $\nu' = 2$ (always

< 0.1 and vanishing for $E_0 > 0.12$ eV). The corresponding QCR reaction probabilities for the same energy range ($0.0 < E_0 < 0.12$ eV). are plotted in Figure 4. In Figure 3 we see that there is a very large difference between the threshold behavior of P_{04}^R (EQ) and P_{04}^R (QCF). In analogy with the F + H_2 P_{03}^R behavior,[1] we find that the quasi-classical reverse P_{04}^R of F + D_2 (Figure 4) has a threshold behavior which is much closer to the exact quantum one than is the QCF threshold. Unlike P_{02}^R (F + H_2), the energy dependence of P_{03}^R (F + D_2) is predicted somewhat more accurately by the QCF method than by the QCR method. The EQ and QCF total reaction probabilities P_0^R (Figure 3) are in somewhat better average agreement than are the EQ and QCF total reaction probabilities in F + H_2 (Figure 4 of I). This seems to indicate that the differences between quantum and classical dynamics are less severe for F + D_2 than for F + H_2. However, at least for collinear reactions, these differences are still quite significant.

In Figure 5 we plot as a function of E_0 the fraction f_V of the total energy which appears as vibrational energy of the DF product for the EQ and QCF calculations. It can be seen that f_V(QCF) is nearly independent of E_0 and has an average value of 0.79. The corresponding EQ curve has a more pronounced E_0 dependence but about the same average value over the E_0 range considered. We find that the average value of f_V is almost the same for both F + H_2 and F + D_2. This independence of isotopic substitution agrees with the corresponding experimental result[2] and with the predictions of three-dimensional trajectory calculations[4] although our value of f_v (0.79) which ignores rotational degrees of freedom is somewhat higher than the experimental result (0.66)[3]. This general average agreement between the EQ and QCF f_v versus E_0 curves indicates that the dynamic processes governing the average energy disposal between vibrational and translational degrees of freedom of the products can be well approximated by the classical trajectory method. However, one should keep in mind that this is not so for the distribution of this vibrational energy among the available vibrational states, i.e., that large differences between product state population ratios obtained from the EQ and QCF methods do exist, as indicated in Figure 6.

2.3 Semi-classical reaction probabilities

Figure 7 shows the uniform semi-classical reaction probabilities P^R_{03} and P^R_{04} along with the corresponding EQ results. The USC results are similar to the ones obtained independently by Whitlock and Muckerman in an analogous calculation.[2b] It was noted in paper I (Section 3.3) that "raggedness" (i.e., very rapid variation of m_f with q_0) in the final action number $m_f(q_0; \nu, E)$ as a function of initial vibrational phase q_0 caused difficulties in calculating USC transition probabilities at the threshold of the $F + H_2(0) \rightarrow FH(3) + (H)$ reaction. The same problem occurred for the $0 \rightarrow 4$ transition in the $F+D_2$ reaction, and was also encountered by Whitlock and Muckerman. We were able to overcome this difficulty by using the reverse final action number function, $n(q_0; m, E)$, which was found to be smooth for $m = 4$ and n around 0. The justification for using this procedure was given in I. The curves for the forward and reverse values of m_f for this $0 \rightarrow 4$ transition at an energy $E = 0.3107$ eV ($E_0 = 0.12$ eV) are given in Figure 8. When all the relevant semi-classical quantities are well-behaved ("non-ragged") functions of q_0, the USC transition probabilities obey microscopic reversibility[5] and it is not necessary to calculate both the forward and reverse results. However, as the example above demonstrates, when "raggedness" exists, it is advisable to consider the forward and the reverse results. In our example, the reverse results are the preferred ones since there is no raggedness in the region corresponding to $D + DF(4) \rightarrow D_2(0) + F$. These were the ones used in calculating P_{04}^R (and P_{03}^R for the $F + H_2$ reaction) in its threshold region. The USC P_{04}^R transition probabilities at $E_0 = 0.08$ eV and 0.085 eV were calculated in the statistical approximation.[6] At these energies the reverse reaction showed that the $4 \rightarrow 0$ transition was dynamically forbidden. However, since statistical (i.e., ragged) behavior was evident in the forward reaction we did calculate a non-zero value for P_{04}^R at the two energies just mentioned.

The USC probabilities in Figure 7 are in much better agreement with the corresponding EQ results than are the quasi-classical ones. As was the case with the QCF P_{03}^R threshold, there is a small difference between the P_{03}^R (USC) and P_{03}^R (EQ) threshold energies, but the USC result may be improved by using complex trajectories.[7] The oscillations in P_{03}^R (USC) in the E_0 range 0.10 eV - 0.25 eV do not have any analog in the quantum results. These oscillations are due to phase interferences arising from a relatively rapid variation with energy of the differences in phases associated with the two contributing trajectories. One might expect that the raggedness in the plot of final action versus initial phase (see Figure 8a) could be an indication of resonant behavior in this energy range, but the quantum results of Figure 1 do not substantiate this. In Section 4 we discuss the possible relationship between resonances in the EQ results and "raggedness" in the USC ones.

One significant aspect of the comparison between the USC and EQ results in Figure 7 is that the maximum values of the EQ and USC reaction probabilities P_{03}^R and P_{04}^R are nearly identical. This contrasts with the results of both the QCF and QCR calculations which generally tend to underestimate the maximum values of the probabilities (Figures 3 and 4). The significant improvement in the quality of the results obtained in going from the quasi-classical to the semiclassical approximation suggests that an equivalent improvement may occur for the three-dimensional $F + D_2$ reaction and that the semiclassical results may be quite reliable for this case. However, we must stress that the utilization of uniform rather than primitive semiclassical techniques is essential to the success of this method for the collinear reaction and thus it seems likely that an analogous uniform procedure will be required in the three-dimensional problem.[8]

2.4 Comparison of EQ, QCF, QCR and USC reaction probabilities

In Figure 9 we compare the reaction probabilities P_{03}^R and P_{04}^R of $F + D_2$ as calculated by all four methods EQ, QCF, QCR and USC. Figure 10 presents the analogous comparison for the total reaction probability P_0^R. It is apparent from both figures that the USC method gives the best agreement with the EQ reaction probabilities for this reaction.

2.5 Information theoretic analysis of EQ and QCF reaction probabilities

It is also of interest to perform an information-theoretic analysis of the EQ and QCF results. In this section, we shall consider both the $F + D_2$ reaction probabilities discussed above and the $F + H_2$ probabilities described in I.

In analogy with the equations used in three-dimensional studies,[9] we have used a one-dimensional form of the surprisal for a vibrational distribution given by:

$$I(f_{\nu'}) = -\ln[P(f_{\nu'})/P^0(f_{\nu'})]$$

$P(f_{\nu'})$ is the normalized reaction probability to product vibrational state ν' expressed as a function of the fraction of the total energy which becomes vibrational energy in the product DF or HF (exclusive of product zero point energy). $P^0(f_{\nu'})$ is the statistical reaction probability to state ν' and is given by:

$$P^0(f_{\nu'}) = \frac{(1 - f_{\nu'})^{-\frac{1}{2}}}{\sum\limits_{\nu'=0}^{\nu'^*} (1 - f_{\nu'})^{-\frac{1}{2}}}$$

where the sum is over all accessible product vibrational states. Note that this expression for $P^0(f_{\nu'})$ predicts inverted statistical vibrational population distributions. This rather surprising result for such a distribution is a straightforward consequence of the use of a one-dimensional density of states function (which varies as $(E_{\nu'})^{-\frac{1}{2}}$ where $E_{\nu'}$ is the translational energy relative to vibrational state ν') rather than the corresponding three-dimensional density (which varies as $E_{\nu'}^{\frac{1}{2}}$).

Figure 11 depicts the EQ and QCF surprisal functions $I(f_{\nu'})$ versus $f_{\nu'}$ for $F + D_2$ and $F + H_2$ at three different relative translational energies. We see that none of the EQ or QCF plots has the straight line dependence on $f_{\nu'}$ required if the distribution is to be characterized by a single information theoretic temperature parameter. The most severe deviations of the EQ results from linearity occur at the lowest energies and are a direct consequence of the unusual threshold behavior of P_{04}^{R} in $F + D_2$ and P_{03}^{R} in $F + H_2$. This threshold effect is not present in the QCF results and yet the surprisal functions associated with these probabilities show strong deviations from linearity. The curves in Fig. 11 indicate that at least in this case, the information theoretic analysis has limited usefulness as a predictive tool for estimating unknown reaction probabilities from known ones. For example, if we assumed a linear surprisal function and used the results of the two largest EQ probabilities to predict the third largest by linear extrapolation, we would be in error by at least one order of magnitude in most of the examples depicted in Fig. 11.

Figure 11 also indicates that in many situations, the surprisal function is not independent of isotopic substitution. This is especially true of the EQ results with $\nu' = 0,1$ where the differences between the surprisal functions for $F + D_2$ and $F + H_2$ are quite large. However, at higher energies (Fig. 11a especially) and for higher vibrational quantum numbers ($\nu' = 2$-4), the EQ points for both $F + D_2$ and $F + H_2$ fall on essentially the same curve. In addition, the QCF results for $F + D_2$ and $F + H_2$ in both Figs. 11a and 11b seem to form a single curve and for this reason, only one dashed line was drawn through the points.

This indicates that at certain energies and for certain ranges of $f_{v'}$, the surprisal function is independent of isotopic substitution, but this property is not generally valid.

The behavior of the surprisal functions (non-linearity and dependence on isotopic substitution) observed in these collinear results contrasts strongly with the shape of the corresponding surprisal functions obtained from three-dimensional trajectory calculations and experiments on the same reactions.[9] In the three-dimensional case, linear surprisal functions which are nearly independent of isotopic substitution were obtained in an analysis of the detailed rate-constants (rather than reaction probabilities) from both quasiclassical trajectory calculations and from infrared chemiluminescence experiments (which are, of course, quantum mechanical). We have analyzed the surprisal functions for our collinear EQ rate constants for both $F + H_2$ and $F + D_2$ (Section 3) and find no marked change from the results depicted in Fig. 11, the non-linearity and dependence on isotopic substitution being essentially as pronounced as for the reaction probabilities.

Recently, the relationship between the one- and three-dimensional classical surprisal functions was computationally investigated,[10a] and it was proposed[10b] that the surprisal function should be approximately dimensionally invariant. Our comparison of the one- and three-dimensional surprisal functions for $F + H_2$ and $F + D_2$ indicates that this dimensional invariance does not hold for these reactions. Although the validity of our conclusion depends in part on the accuracy of the potential energy surface used in our calculations, we would not expect it to be qualitatively changed if a more accurate potential energy surface were used. In addition, we note that three-dimensional quasiclassical results for $F + H_2$ and $F + D_2$ on similar approximate surfaces[4] agree with experiment in their prediction of a linear surprisal function.[9] The computational comparison of one- and three-dimensional surprisal functions of Ref. 10a involved several model potential energy surfaces but none of these similated the attractive nature of the $F + H_2$ interaction. We conclude that the invariance of the surprisal function with respect to the dimensionality of the collision may depend significantly on the characteristics of the potential energy surface being considered. Therefore, caution must be exercised in attempting to obtain 3-D reaction cross sections from collinear reaction probabilities.[10b]

3. EQ, QCF, QCR and USC Rate Constants for $F + D_2$

The rate constants k_{03}^R and k_{04}^R obtained from the EQ, QCF, QCR and USC reaction probabilities P_{03}^R and P_{04}^R for $F + D_2$ are plotted in Figure 12. The expression for these rate constants is the same as the one given in I.[1] The corresponding Arrhenius parameters obtained from fits to the rate constants in the 200 to 400 K and 900 to 1200 K temperature ranges are listed in Table II. The difference between k_{04}^R (QCF) and k_{04}^R (EQ) (which results from the different threshold properties of the P_{04}^R's in Figure 9) is quite noticeable and leads to a 0.8 kcal difference between the corresponding high temperature activation energies in Table II. In analogy with our $F + H_2$ study,[1] the QCR and USC rate constants k_{04}^R and corresponding activation energies E_{04}^a agree with the EQ ones better than do the QCF quantities. The similar comparison for the rate constants k_{03}^R is much less satisfactory. The low temperature differences between the various k_{03}^R's are determined to a large extent by the different threshold energies of the corresponding reaction probabilities P_{03}^R. The transition probability P_{03}^R (QCR) has zero threshold energy and thus the largest rate constant at low temperatures, while the EQ, USC and QCF P_{03}^R's have successively higher threshold energies and therefore successively lower rate constants. (See Figure 9b.) This illustrates that the low energy (< 0.03 eV) behavior of the reaction probabilities (or cross sections) can be exceedingly important in determining the low temperature (< 300 K) behavior of the corresponding rate constants for these reactions.

The ratios k_{04}^R/k_{03}^R are plotted as a function of temperature in Figure 13. We see that the QCF ratio is nearly temperature independent while the EQ, QCR and USC ratios increase monotonically with increasing temperature, approaching the QCF ratio at high temperatures. These k_{04}^R/k_{03}^R ratios are quite similar in appearance to the k_{03}^R/k_{02}^R ratios for the $F + H_2$ reaction given in Figure 12 of I, but the $F + D_2$ ratios actually increase somewhat more slowly with temperature than do the $F + H_2$ ones.

The QCF ratio k_{04}^R/k_{03}^R is 0.63 at 300 K in approximate agreement with the experimental value[11] of 0.66. The results of three-dimensional classical trajectory calculations indicate that this ratio is not strongly temperature dependent.[12] If this is also true experimentally then, in analogy with $F + H_2$, we would have evidence that the collinear model overestimates the effects of threshold differences on reaction rates to different product vibrational states. We might note, however, that Lee and coworkers[12,13] have measured the ratio of cross sections σ_{04}/σ_{03} at three different energies and they find that it increases rapidly with increasing energy from 0.75 at $E_0 = 0.034$ eV to 3.5 at $E_0 = 0.11$ eV. If we consider the analogous collinear ratio P_{04}^R/P_{03}^R (Figure 6) we find that it also increases rapidly with increasing energy (much more rapidly than Lee's cross section ratio) from near zero at zero translational energy to roughly a value of 4.3 for $E_0 \sim 0.12$ eV. The ratios of cross sections from three-dimensional QCF trajectory calculations over a family of several potential energy surfaces do not reproduce this energy dependence (Ref. 12, Table VI). This may indicate that the differences between quantum and quasi-classical results are still significant in three dimensions and, indeed, are observable in experiments which are at least partially state selected such as cross section measurements.

4. Higher Energy Reaction Probabilities for $F + D_2$

Figure 14 shows the higher energy exact quantum reaction probabilities P_{03}^R, P_{04}^R, P_{05}^R, P_{14}^R and P_{15}^R for $F + D_2$ in the translational energy range $E_0 = 0.25$ to 0.70 eV. Those transition probabilities not plotted are all small (usually < 0.02). P_{04}^R (QCR) is also plotted in Figure 14 in the energy range 0.25 to 0.42 eV for reasons to be discussed in detail below. This figure is analogous in many ways to Figure 13 of I, although the close correlation between the reaction probabilities of $F + H_2$ and the related $F + D_2$ ones (see end of Section 2.1) becomes less important as the energy is increased. Nevertheless, many of our remarks concerning the $F + H_2$ reaction probabilities described in I are also applicable here. We note that the transition probabilities P_{15}^R in Figure 14 and P_{04}^R in Figure 1 have similar translational energy dependences except near threshold. This confirms our statement in I that reaction probabilities for reagents initially in $\nu = 1$ are virtually insensitive to the presence of a barrier in the $F + H_2$ (D_2) reagent channel. In addition, P_{15}^R is significantly larger than the other $P_{1\nu'}^R$ with $\nu' < 5$ over the energy range considered. This implies that the additional vibrational energy in the reagents is being predominantly channelled into additional vibrational energy in the products.[14]

The transition probability P_{05}^R exhibits a rather unusual energy dependence. As shown in Figure 14, it remains quite small (< 0.01), even though energetically allowed, until the total energy becomes high enough to excite $\nu = 1$ of D_2 at which point it rises suddenly to a peak value of 0.34 before finally levelling off at about 0.13. It is not obvious how simple resonance or threshold theories can explain this unusual behavior since the effective threshold is apparently related to the opening of a vibrational state not involved in the transition asymptotically. One possible explanation for the influence of the $\nu = 1$ state of D_2 on this transition probability can be formulated by observing that the inelastic $0 \rightarrow 1$ transition probability for $F + D_2$ is quite appreciable[15] (0.10 to 0.25) and, as noted above, P_{15}^R is quite large. This suggests that the $0 \rightarrow 5$ reactive transition occurs almost exclusively with $\nu = 1$ as an intermediate state. It is also significant that it is not sufficient for this state to be accessible via virtual transitions but rather it must be open asymptotically. This seems to indicate that a high degree of vibrational excitation must be maintained over a considerable region in configuration space. This would only be possible if the $\nu = 1$ vibrational state is open and hence there is no enhancement of P_{05}^R when the state is closed.

For the transitions P_{04}^R at $E_0 = 0.327$ eV and P_{15}^R at $E_0 = 0.599$ eV we see peaks in the reaction probabilities suggestive of internal excitation resonances.[16] In contrast to the resonances observed in I in $F + H_2$, the direct processes in $F + D_2$ still seem to be quite important in the vicinity of the resonances. The resultant interference between the direct and resonant contributions to the scattering amplitude leads to characteristic oscillations in the reaction probabilities in the vicinities of the resonance energies quite similar to what was observed in the $H + H_2$ reaction.[16, 17] As in the $F + H_2$ reaction, we see an approximate correspondence between the appearance of a resonance and the opening of a specific vibrational state of the product DF. ($\nu = 5$ at $E_0 = 0.29$ eV and $\nu = 6$ at $E_0 = 0.59$ eV). This implies that the virtual states of the triatomic complex may have energy levels resembling product states more than reagent states. The relation is probably complicated, however, since the correspondence between the resonance energy and the energy of the associated product vibrational level is not always in the same direction (i.e., the resonance energy is sometimes greater and sometimes smaller than the corresponding vibrational energy as can be seen in Figure 13 of I and Figure 14 in the present paper).

It is interesting to note that the QCR reaction probability P_{04}^R depicted in Figure 14 seems to "average out" the quantum oscillations in P_{04}^R (EQ) in the vicinity of the $E_0 = 0.327$ eV resonance. It is also of interest to examine the semi-classical results at this energy. Rankin and Miller have reported extensive statistical behavior in the final action number function, m_f, for the $H + Cl_2$ collision.[6] From this behavior, they inferred that a converged quantum treatment of that reaction would yield internal excitation resonances. However, as Figure 15 shows, m_f, at the resonance energy, is a reasonably smooth function of q_0 with about the same degree of "raggedness" (i.e., very rapid variation of m_f with q_0) as seen previously away from resonance in Figure 8b. An accurate EQ study of the collinear H + H_2 reaction has shown that P_{00}^R has a broad resonance at 0.90 eV total energy and a narrow one at 1.28 eV, and that both are due to interference effects between direct and compound-state mechanisms.[16] Recently, Stine and Marcus[18] searched for and found snarled (i.e., multiple collision) trajectories in the narrow region of q_0 between the reactive and nonreactive branches of the $m_f(q_0; \nu, E)$ curve. They showed that the broad resonance at 0.90 eV could be generated semi-classically if interference effects between direct and snarled trajectories are included, a result consistent with the life-time analysis of the accurate quantum calculations.[16] Were it not for the knowledge of the existence of this resonance derived from the EQ calculations, it would be easy to miss such snarled trajectories in a semi-classical calculation in which the density of the q_0 grid were not high enough.[5, 19] Inclusion of a search of these trajectories and of their effects on the reaction probabilities significantly increases the computational effort involved in the semi-classical approach. Narrow resonances, such as the one occurring at 1.28 eV in collinear H + H_2, may be even more difficult to calculate semi-classically, since its long life-time[16] suggests that it may correspond to extremely snarled trajectories, requiring inclusion of multiple collisions of high order[18] and use of an extremely high density q_0 grid. In the present paper, we have only included the effect of direct (i.e., non-snarled) trajectories in the semi-classical calculations. It would be interesting to add the effect of snarled ones, in order to verify whether they could reproduce the resonant behavior of P_{04}^R at $E_0 = 0.327$ eV.

We conclude that "raggedness" in the $m_f(q_0; \nu, E)$ curves could perhaps be a necessary condition for the existence of quantum mechanical internal excitation resonances, but it is certainly not a sufficient one, as shown by the presence of raggedness in Figure 8b, calculated at a non-resonant energy.

5. Exact Quantum Reaction Probabilities for the Reactions F + HD → FH + D and F + DH → FD + H

We have also calculated the exact quantum reaction probabilities for F + HD → FH + D and F + DH → FD + H hereafter designated F + HD and F + DH respectively. In three dimensions, these two reactions represent different product arrangement channels of the same collision system. In collinear collisions, however, they must be considered entirely separately. This implies that coupling between these two product arrangement channels is ignored in our collinear calculations.

The largest reaction probabilities for the two reactions are plotted in Figure 16[20] as a function of the reagent translational energy E_0 (relative to $\nu = 0$ of HD) in the range 0 to 0.25 eV. For F + HD, the only reaction probability greater than 0.025 in the energy range studied is P_{02}^R while P_{04}^R, P_{03}^R and P_{02}^R are the major contributors to the total reaction probability in F + DH (P_{02}^R is always less than

0.10). From Figure 16 it is apparent that the reaction probabilities P_{04}^{R} and P_{03}^{R} of F + DH are very similar in shape to the corresponding probabilities P_{04}^{R} and P_{03}^{R} of F + D_2 (Figure 10), although the sharp differences between the threshold energies of P_{04}^{R} and P_{03}^{R} (F + D_2) are reduced considerably for P_{04}^{R} and P_{03}^{R} (F + DH). In contrast, the results for F + HD do not show a strong resemblance to those for F + H_2 (Figure 2 of I). Instead, we see that P_{02}^{R} (Figure 16) consists of one very sharp (width ~ 0.0005 eV) spike near 0.012 eV and then remains quite small (< 0.02) for the remainder of the energy range studied. P_{03}^{R}, which is energetically forbidden until $E_0 = 0.039$ eV is quite small throughout the energy range considered here. The rather dramatic differences between the results for F + HD and F + DH can probably be explained as resulting from the difference in the mass of the atom being exchanged in the collinear triatomic collision system. The small mass of the H atom in F + HD in comparison with that of the D atom in F + DH results in much more important pseudo-centrifugal barriers in "turning the corner" in the former reaction than in the latter. That this should be the case is apparent from a comparison of the skew angles (defined in I) for these two systems. For F + HD, this angle is 37.3° while for F + DH it is 56.7°, thus indicating that the curvature along the reaction path should be much larger for F + HD than for F + DH. Only at low translational energies do the centrifugal effects become small enough to render F + HD dynamically allowed. For F + DH, on the other hand, the centrifugal effects are not important in the energy range studied and thus we observed very large reaction probabilities throughout that energy range.

From Figure 16, we can also conclude that the rate constant for formation of DF is predicted to be greater than that for formation of HF (except at very low temperatures (< 150°) where the slightly smaller effective threshold of F + HD becomes important). This disagrees with the experimental result[21] that the rate of H atom transfer is a factor of 1.45 faster than that for D atom transfer at 298 K. The disagreement can probably be explained by noting that the distance of the H atom from the center of mass of HD is about twice that of the D atom from the same center of mass. This means that H sweeps through a larger volume of space than D when HD rotates and thus is more "visible" to the attacking F atom. Since the barrier height is quite low (except near the "perpendicular" orientation[12]), one would expect that H should be preferentially abstracted. For collinear reactions, this three-dimensional effect is ignored and we find, instead, that dynamical effects such as pseudo-centrifugal barriers are important in the reaction. These centrifugal effects favor reaction with the D atom and thus explain why the collinear results differ from the experimental ones. A similar argument has been used to explain the J dependence of three-dimensional quasi-classical cross sections for the same reactions[4a]. One might add that for a reaction with a high barrier, which simultaneously favors reaction through collinear geometries, the three dimensional effect should be less important and the collinear results should be more representative of the experimental results. This has indeed been observed for the Cl + HD (DH) reactions.[22]

6. Discussion

We shall now summarize the differences between the results of the exact quantum, quasi-classical and semi-classical methods for studying the F + H_2 (paper I) and F + D_2 reactions. The most important of these differences may be categorized into three divisions: vibrationally adiabatic tunnelling, resonances and threshold dynamical effects. These effects may, however, be coupled to one another to a lesser or greater extent.

Vibrationally adiabatic tunnelling seems to be most significant at very low energies especially for F + H_2 and for those transitions for which at threshold there are no strongly restrictive dynamical effects (of the type occurring in P^R_{03} for F + H_2). Such tunnelling appears to be responsible for important differences between EQ and QCF rate constants at low temperatures (Figures 11a in I and also 12a in this paper). The semi-classical complex trajectory method (which was not studied here) may be able to describe tunnelling quantitatively.[5,7] Internal excitation resonances seem to be very important at higher translational energies and will therefore not be significant in thermal experiments. They may be important in beam and hot atom experiments if these resonance effects carry over without strong attenuation into three dimensions. The current semi-classical theories do not seem to furnish a computationally practical description of the interference effects associated with these resonances.[20] Threshold dynamical effects are very significant for collinear F + H_2 and F + D_2 and this leads to important differences between exact quantum and quasi-classical reaction probabilities and rate constants for thermal distributions of reagents. These threshold effects are partially classical in nature since we found that the QCR method was capable of describing roughly the proper threshold behavior within a completely classical framework. An important result of this paper was the demonstration that the uniform semiclassical method provides a greatly improved description of threshold behavior of the quantum results in comparison with the QCF method. How important these threshold effects will be in three dimensions is not entirely clear from an analysis of existing experimental and theoretical studies, but it appears that the effects are at least partially attenuated by the averaging that inevitably occurs in experimental measurements. They may, however, still be important for experiments which are sufficiently state selected.

Acknowledgements

We thank J. T. Muckerman, with whom we have exchanged results on the USC calculations, for useful discussions.

We also thank Ambassador College for the use of their computational facilities in most of the work reported here.

Table I. Effective threshold energies (E_T) for the most significant reaction probabilities in the $F + H_2$, $F + D_2$, F + DH and F + HD reactions.[a]

	$F + H_2$	F + HD
$E_T(P^R_{02}(EQ))$	0.005	0.010
$E_T(P^R_{02}(QCF))$	0.025	N.C.[b]
$E_T(P^R_{03}(EQ))$	0.045	0.071
$E_T(P^R_{03}(QCF))$	0.012	N.C.[b]
E_{VAZC}	0.026	0.028

	$F + D_2$	F + DH
$E_T(P^R_{03}(EQ))$	0.014	0.011
$E_T(P^R_{03}(QCF))$	0.030	N.C.[b]
$E_T(P^R_{04}(EQ))$	0.055	0.022
$E_T(P^R_{04}(QCF))$	0.030	N.C.[b]
E_{VAZC}	0.032	0.028

[a] All energies are in eV.

[b] No QCF calculations were done for this transition.

Table II. Arrhenius rate constant parameters for $F + D_2 \rightarrow FD + D$.[a]

	Temp. Range	EQ	QCF	QCR	USC
E_a^{03}	200 - 400 K	0.676	0.935	0.266	0.852
E_a^{04}	200 - 400	2.167	0.990	2.576	2.471
A_{03}	200 - 400	2.551×10^4	2.443×10^4	1.884×10^4	2.340×10^4
A_{04}	200 - 400	2.775×10^4	1.686×10^4	2.502×10^4	3.269×10^4
E_a^{03}	900 - 1200	0.361	0.912	0.416	0.611
E_a^{04}	900 - 1200	2.108	1.343	2.742	2.344
A_{03}	900 - 1200	2.104×10^4	2.674×10^4	2.402×10^4	2.082×10^4
A_{04}	900 - 1200	3.240×10^4	2.604×10^4	3.261×10^4	3.365×10^4

[a] E_a^{oi} is in kcal/mole and A_{oi} is in cm/(molec·sec).

References

1. G. C. Schatz, J. M. Bowman, and A. Kuppermann, preceeding paper.
2. (a) J. T. Muckerman (private communication); (b) P. A. Whitlock and J. T. Muckerman, J. Chem. Phys. **61**, 4618 (1974).
3. J. C. Polanyi and K. B. Woodhall, J. Chem. Phys. **58**, 2298 (1973).
4. (a) J. T. Muckerman, J. Chem. Phys. **54**, 1155 (1971); (b) ibid. **56**, 2997 (1972).
5. J. M. Bowman and A. Kuppermann, J. Chem. Phys. **59**, 6524 (1973).
6. C. C. Rankin and W. H. Miller, J. Chem. Phys. **55**, 3150 (1971).
7. W. H. Miller and T. F. George, J. Chem. Phys. **56**, 5668 (1972); J. D. Doll, T. F. George, and W. H. Miller, J. Chem. Phys. **58**, 1343 (1973); J. Stine and R. A. Marcus, Chem. Phys. Lett. **15**, 536 (1972).
8. W. H. Miller, J. Chem. Phys. **54**, 5386 (1971); R. A. Marcus, J. Chem. Phys. **57**, 4903 (1972); J. D. Doll and W. H. Miller, J. Chem. Phys. **57**, 5019 (1972); J. N. L. Connor, Mol. Phys. **25**, 181 (1973).
9. (a) A. Ben-Shaul, R. D. Levine and R. B. Bernstein, Chem. Phys. Lett. **15**, 160 (1972); (b) A. Ben-Shaul and R. D. Levine, J. Chem. Phys. **57**, 5427 (1972).
10. (a) C. Rebick, R. D. Levine and R. B. Bernstein, J. Chem. Phys. **60**, 4977 (1974), (b) R. B. Bernstein and R. D. Levine, preprint.
11. M. J. Berry, J. Chem. Phys. **59**, 6229 (1973).
12. N. C. Blais and D. G. Truhlar, J. Chem. Phys. **58**, 1090 (1973).

13. T. P. Schaefer, P. E. Siska, J. M. Parson, F. P. Tully, Y. C. Wong and Y. T. Lee, J. Chem. Phys. 53, 3385 (1970). See also reference 10.
14. A. Ding, L. Kirsch, D. Perry, J. Polanyi, and J. Schreiber, Disc. Far. Soc. 55, 252 (1973).
15. G. C. Schatz and A. Kuppermann, unpublished calculations.
16. G. C. Schatz and A. Kuppermann, J. Chem. Phys. 59, 964 (1973).
17. R. D. Levine and S.-F. Wu, Chem. Phys. Lett. 11, 557 (1971).
18. J. R. Stine and R. A. Marcus, Chem. Phys. Lett. 29, 575 (1974). This work appeared in print after the present paper was submitted for publication. All references to it were incorporated subsequently, at the time some revisions suggested by the referee were made.
19. J. D. Duff and D. G. Truhlar, Chem. Phys., 4, 1 (1974).
20. Note that for these calculations, a slightly different value of β(HF) was used (2.2087 Å^{-1}) than in I (2.2187 Å^{-1}).
21. A Persky, J. Chem. Phys. 59, 5578 (1973).
22. M. Baer, U. Halavee and A. Persky, J. Chem. Phys. 61, 4362 (1974).

Figure Captions

Figure 1: Exact quantum reaction probabilities for $F + D_2$ as a function of relative translational energy E_0 and total energy E (relative to minimum in D_2 diatomic potential curve). (a) Total reaction probability P_0^R. (b) Reaction probabilities P_{03}^R and P_{04}^R.

Figure 2: Exact quantum reaction probabilities P_{02}^R, P_{01}^R and P_{00}^R . for $F + D_2$ (similar to Figure 1).

Figure 3: Quasi-classical forward (dashed curve) and exact quantum (solid curve) reaction probabilities for $F + D_2$: (a) P_0^R, (b) P_{03}^R and P_{04}^R.

Figure 4: Quasi-classical reverse (dashed curve) and exact quantum (solid curve) reaction probabilities for $F + D_2$: (a) P_0^R, (b) P_{03}^R and P_{04}^R.

Figure 5: Fraction (f_V) of the total reagent energy (exclusive of product zero point energy) which ends up as vibrational energy in the product DF plotted as a function of the reagent translational energy E_0 and total energy E. Solid line indicates EQ results and dashed line QCF ones. Other notation analogous to Figure 1.

Figure 6: Ratio of reaction probabilities P_{04}^R/P_{03}^R versus translational energy E_0 and total energy E. Solid line indicates EQ results and dashed line QCF ones. Other notation analogous to Figure 1.

Figure 7: Uniform semi-classical (dashed curve) and exact quantum (solid curve) reaction probabilities for F + D_2: (a) P_0^R, (b) P_{03}^R and P_{04}^R.

Figure 8: (a) m_f versus q_0 for the forward F + $D_2(0) \rightarrow FD(m_f) + D$, at a total energy E of 0.3107 eV; (b) m_f versus q_0 for the reverse reaction $D + DF(4) \rightarrow D_2(m_f) + F$, at the same total energy E. The solid curves represent the majority of the reactive trajectories computed. The dots and crosses represent, respectively, reactive and non-reactive trajectories in regions of "raggedness," for which m_f varies very rapidly with q_0. Since the values of m_f for non-reactive trajectories correspond to a different range of variation than the reactive ones, the crosses were placed at an arbitrary ordinate, and are only meant to indicate the values of q_0 for which such trajectories occur.

Figure 9: EQ (solid), QCF (short dash), QCR (dash dot) and USC (long dash) reaction probabilities P_{04}^R (a) and P_{03}^R (b). (From Figures 1, 3-4, 7.)

Figure 10: EQ (solid), QCF (short dash), QCR (dash dot) and USC (long dash) total reaction probabilities P_0^R for F + D_2. (From Figures 1, 3-4, 7.)

Figure 11: Surprisal function $I(f_{v'})$ versus fraction $f_{v'}$ of the total product energy which is in product vibrational state v' (exclusive of zero point energy). Symbols plotted have the following meanings: circles - EQ results for F + D_2, triangles -EQ results for F + H_2, squares - QCF results for

$F + D_2$, and crosses - QCF results for $F + H_2$. (a) $E_0 = 0.12$ eV, (b) $E_0 = 0.03$ eV, (c) $E_0 = 0.005$ eV. The $F + D_2$ (EQ) results are connected by a solid line while a dashed-dotted line connects the $F + H_2$ (EQ) results. A dashed line approximately connects both $F + H_2$ and $F + D_2$ (QCF) results. Note that at the lowest energy considered (Fig. 10c), only $\nu' = 0$-2 of HF are energetically accessible and all QCF reaction probabilities are zero.

Figure 12: Arrhenius plot of EQ (solid), QCF (short dash), QCR (dash dot) and USC (long dash) rate constants for $F + D_2$: (a) k_{03}^{R}, (b) k_{04}^{R}.

Figure 13: Ratios of rate constants k_{04}^{R}/k_{03}^{R} for $F + D_2$; EQ (solid), QCF (short dash), QCR (dash dot), USC (long dash).

Figure 14: Exact quantum reaction probabilities at translational energies higher than those in Figure 1. (a) P_{03}^{R}, P_{04}^{R} and P_{05}^{R} (b) P_{14}^{R} and P_{15}^{R}. Also shown in (a) is the QCR P_{04}^{R} curve (dashed). Arrows near $E_0 = 0.29$ eV and 0.59 eV indicate the opening of $\nu = 5$ and 6 respectively of DF while that at 0.37 eV indicates the energy E_0 at which $\nu = 1$ of D_2 becomes accessible.

Figure 15: m_f versus q_0 for the reverse reaction $D + DF(4) \rightarrow D_2(m_f) + F$ at the resonance energy 0.5107 eV (corresponding to $E_0 = 0.32$ eV). See Figure 8 for explanation of dots and crosses.

Figure 16: Exact quantum reaction probabilities P_{02}^{R} for F + HD, and P_{03}^{R} and P_{04}^{R} for F + DH as a function of relative translational energy E_0 and total energy E (relative to minimum in HD diatomic potential curve). Arrow near 0.04 eV indicates the energy at which $\nu = 3$ of HF becomes accessible.

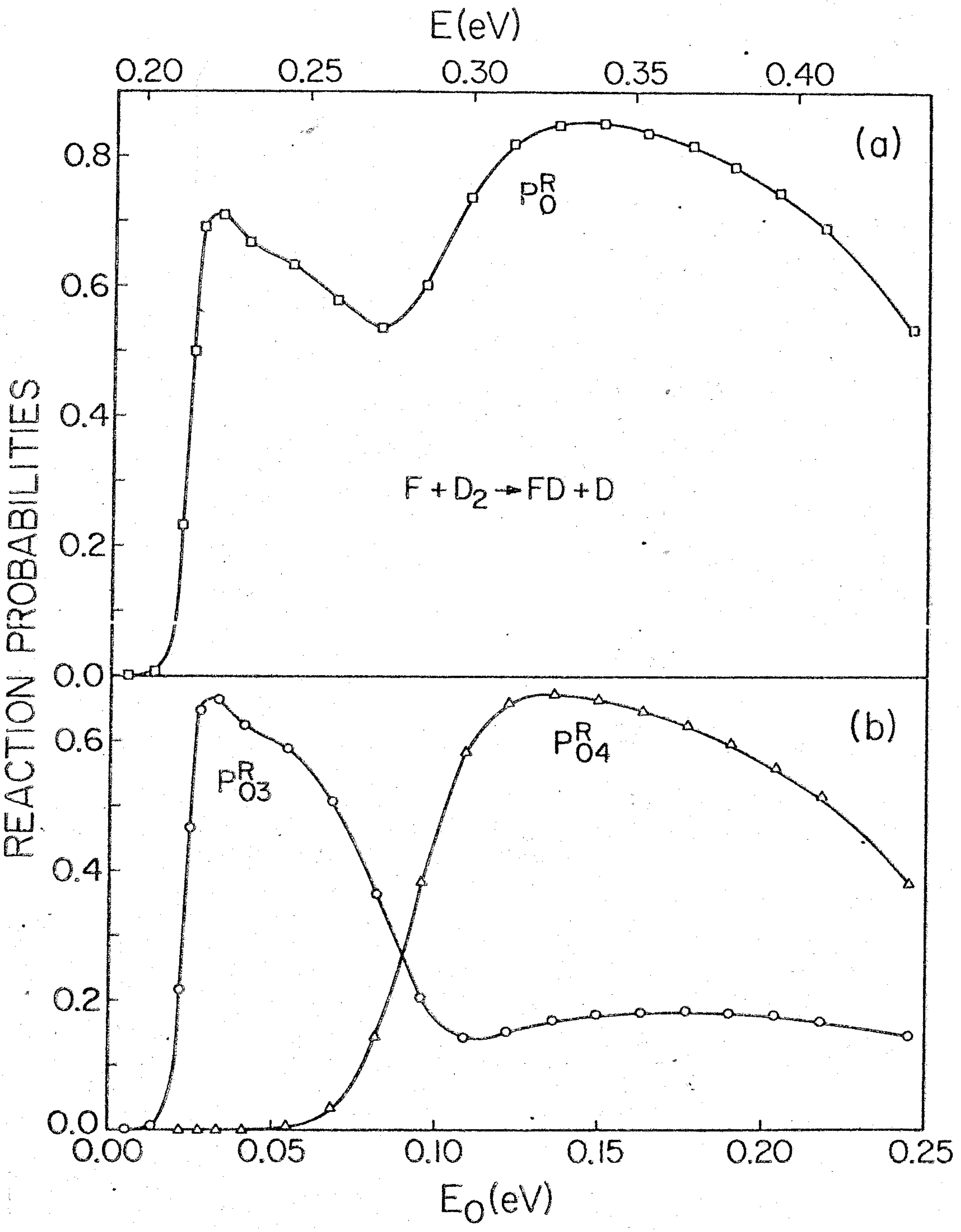
E(eV)
0.20
0.25
0.30
0.35
0.40
(a)
P_0^R
0.8
0.6
0.4
0.2
0.0
REACTION PROBABILITIES
F + D$_2$ → FD + D
(b)
P_{03}^R
P_{04}^R
0.6
0.4
0.2
0.0
0.00
0.05
0.10
0.15
0.20
0.25
E$_0$(eV)

Figure 1

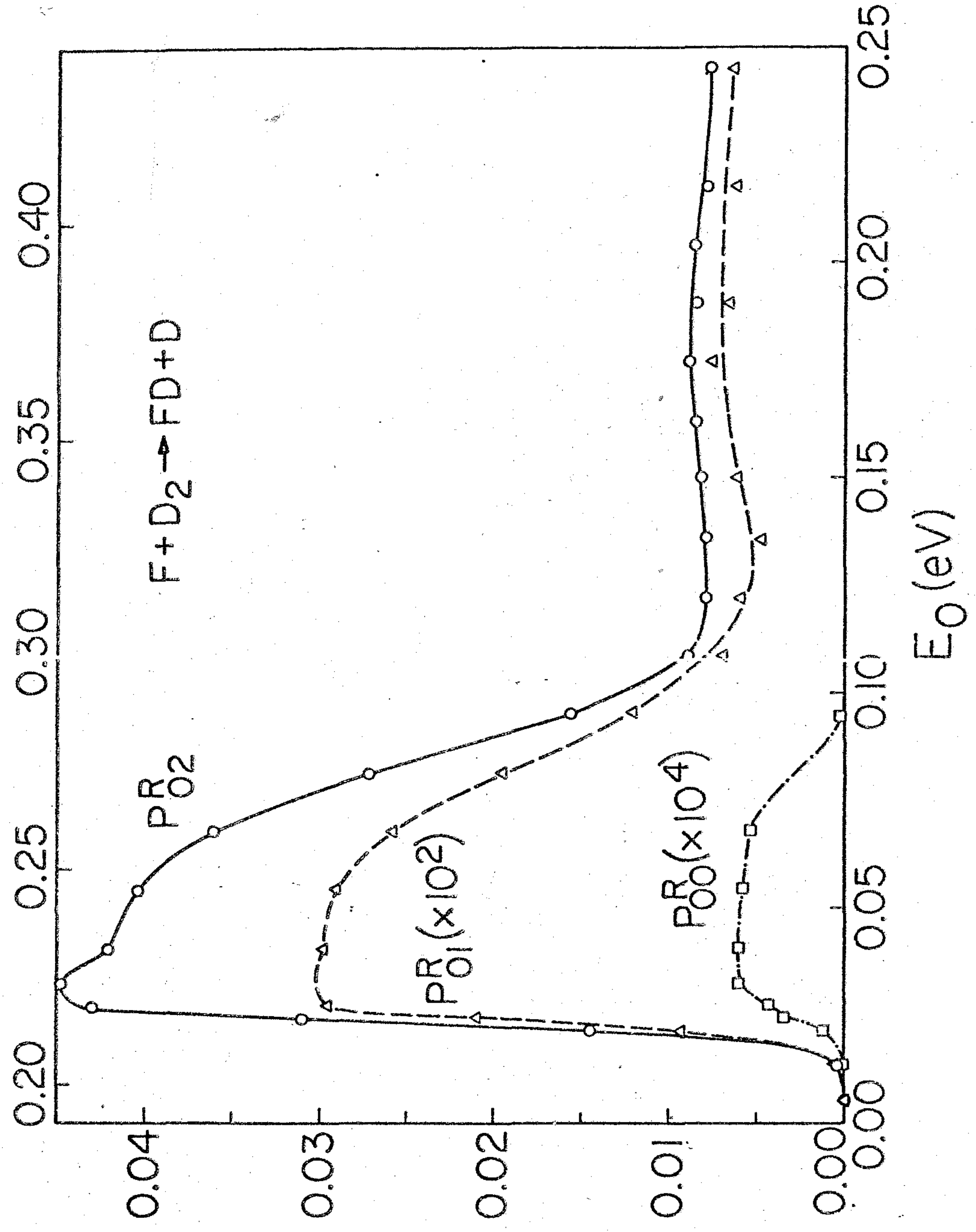
Ξ (eV)
0.20
0.25
0.30
0.35
0.40
$F + D_2 \rightarrow FD + D$
P^R_{02}
$P^R_{01} (\times 10^2)$
$P^R_{00} (\times 10^4)$
REACTION PROBABILITY
0.00
0.01
0.02
0.03
0.04
0.00
0.05
0.10
0.15
0.20
0.25
E_0 (eV)

Figure 2

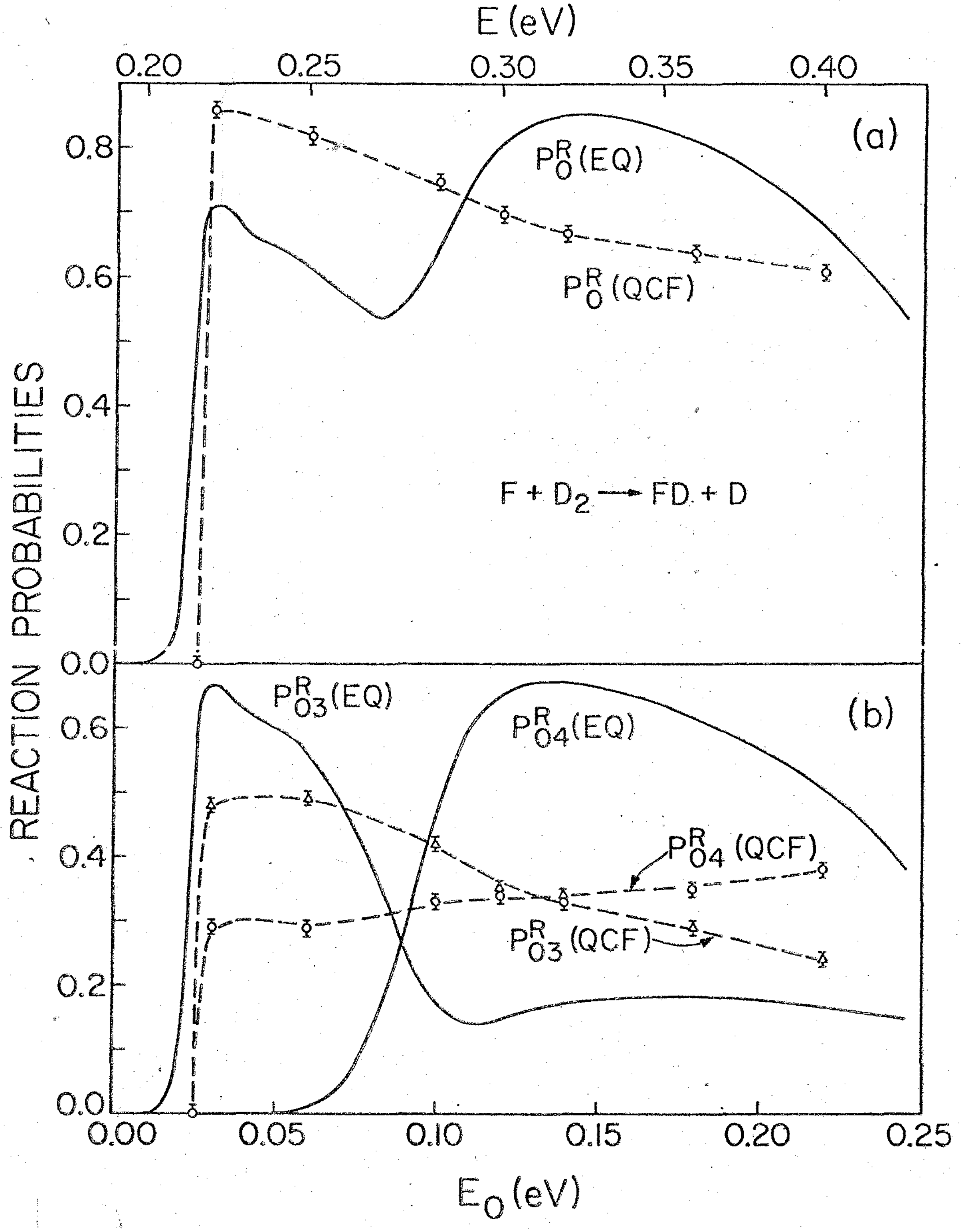
E (eV)
0.20
0.25
0.30
0.35
0.40
(a)
P_0^R(EQ)
P_0^R(QCF)
$F + D_2 \rightarrow FD + D$
0.8
0.6
0.4
0.2
0.0
REACTION PROBABILITIES
(b)
P_{03}^R(EQ)
P_{04}^R(EQ)
P_{04}^R (QCF)
P_{03}^R (QCF)
0.6
0.4
0.2
0.0
0.00
0.05
0.10
0.15
0.20
0.25
E_0 (eV)

Figure 3

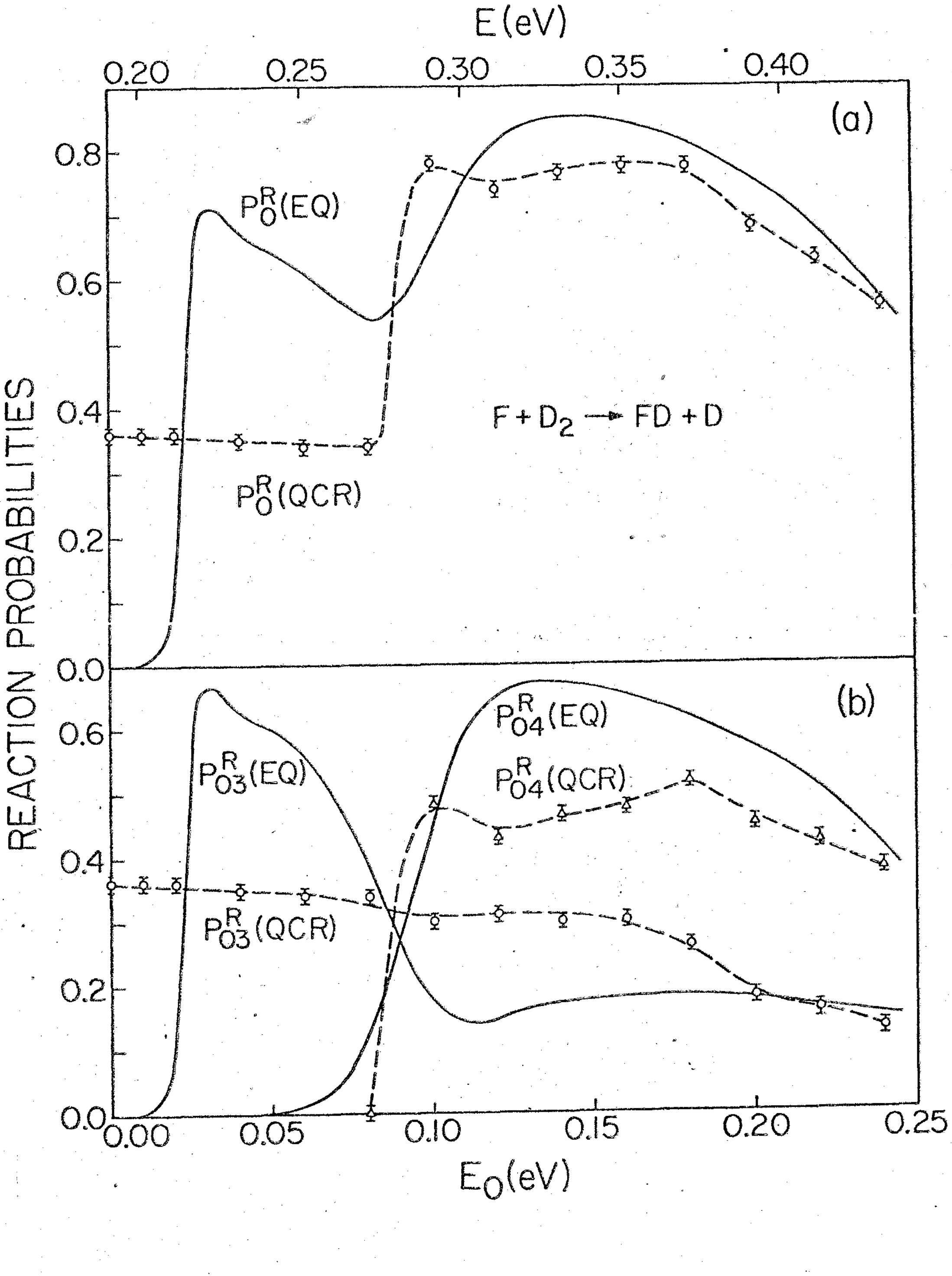
E(eV)
0.20
0.25
0.30
0.35
0.40
(a)
0.8
0.6
0.4
0.2
0.0
P_0^R(EQ)
P_0^R(QCR)
F + D_2 → FD + D
REACTION PROBABILITIES
(b)
0.6
0.4
0.2
0.0
P_{03}^R(EQ)
P_{03}^R(QCR)
P_{04}^R(EQ)
P_{04}^R(QCR)
0.00
0.05
0.10
0.15
0.20
0.25
E_0(eV)

Figure 4

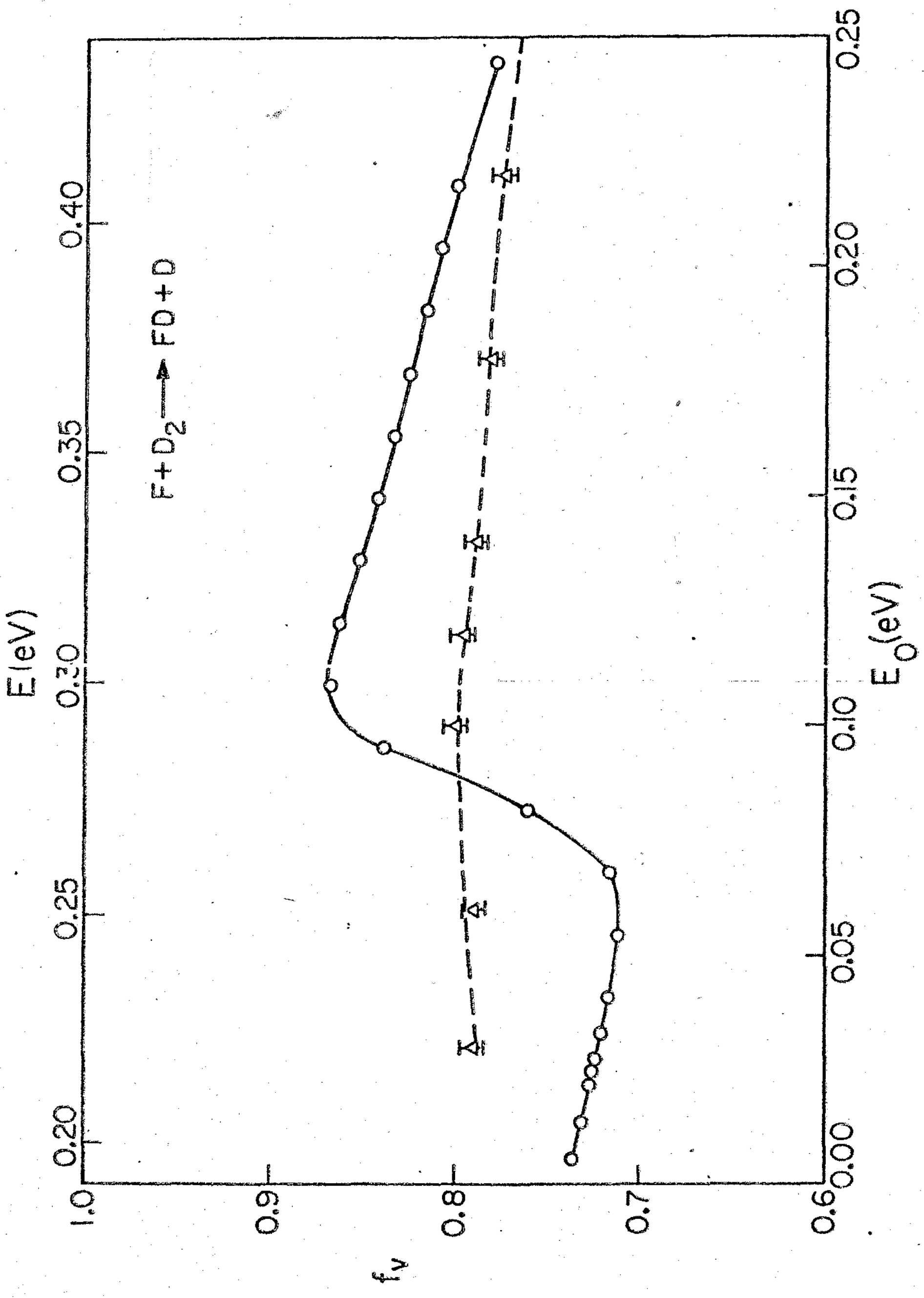
E(eV)
0.20
0.25
0.30
0.35
0.40
F + D$_2$ → FD + D
f$_v$
1.0
0.9
0.8
0.7
0.6
E$_0$(eV)
0.00
0.05
0.10
0.15
0.20
0.25

Figure 5

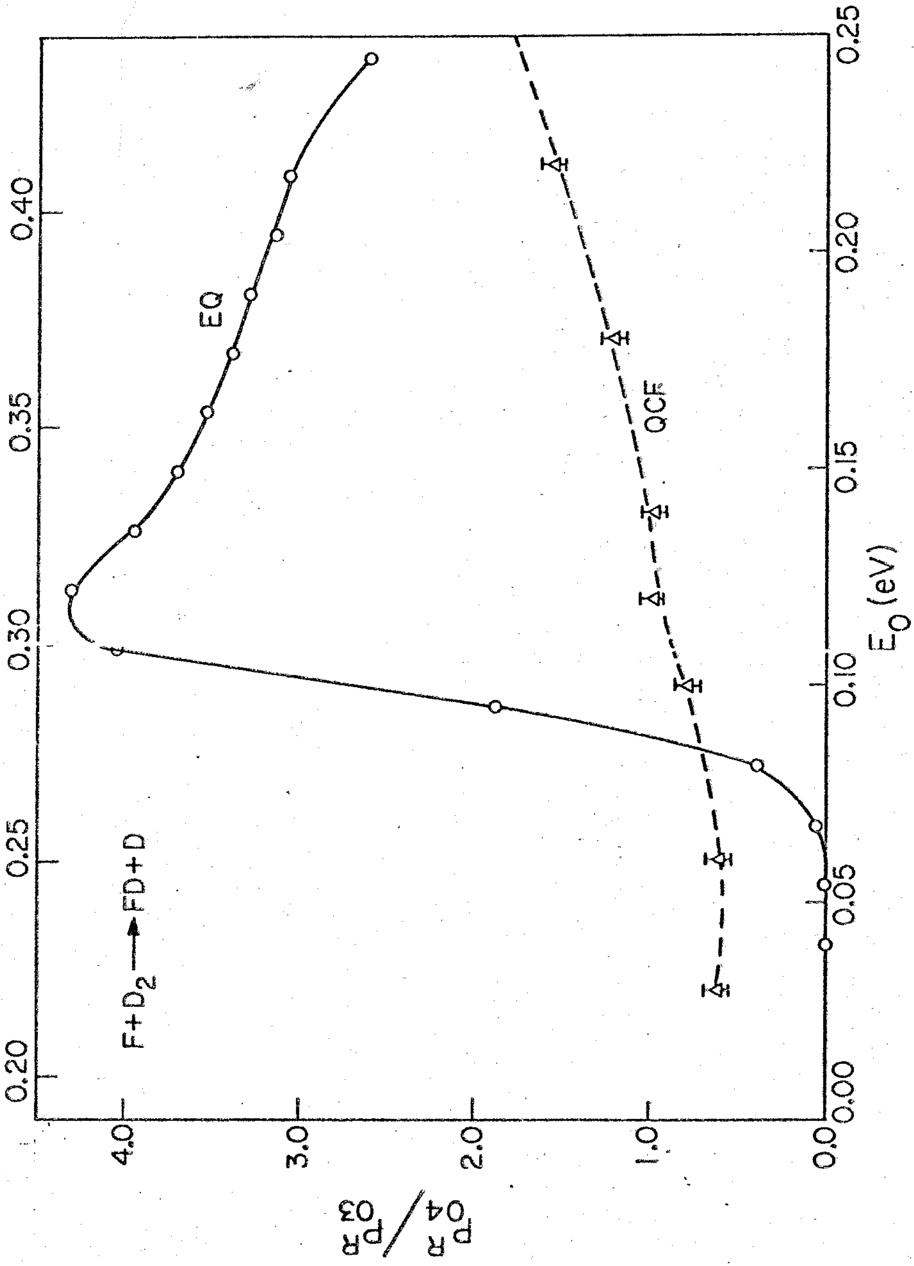
F + D_2 → FD + D
EQ
QCF
E (eV)
0.20
0.25
0.30
0.35
0.40
E_0 (eV)
0.00
0.05
0.10
0.15
0.20
0.25
P^R_{04}/P^R_{03}
0.0
1.0
2.0
3.0
4.0

Figure 6

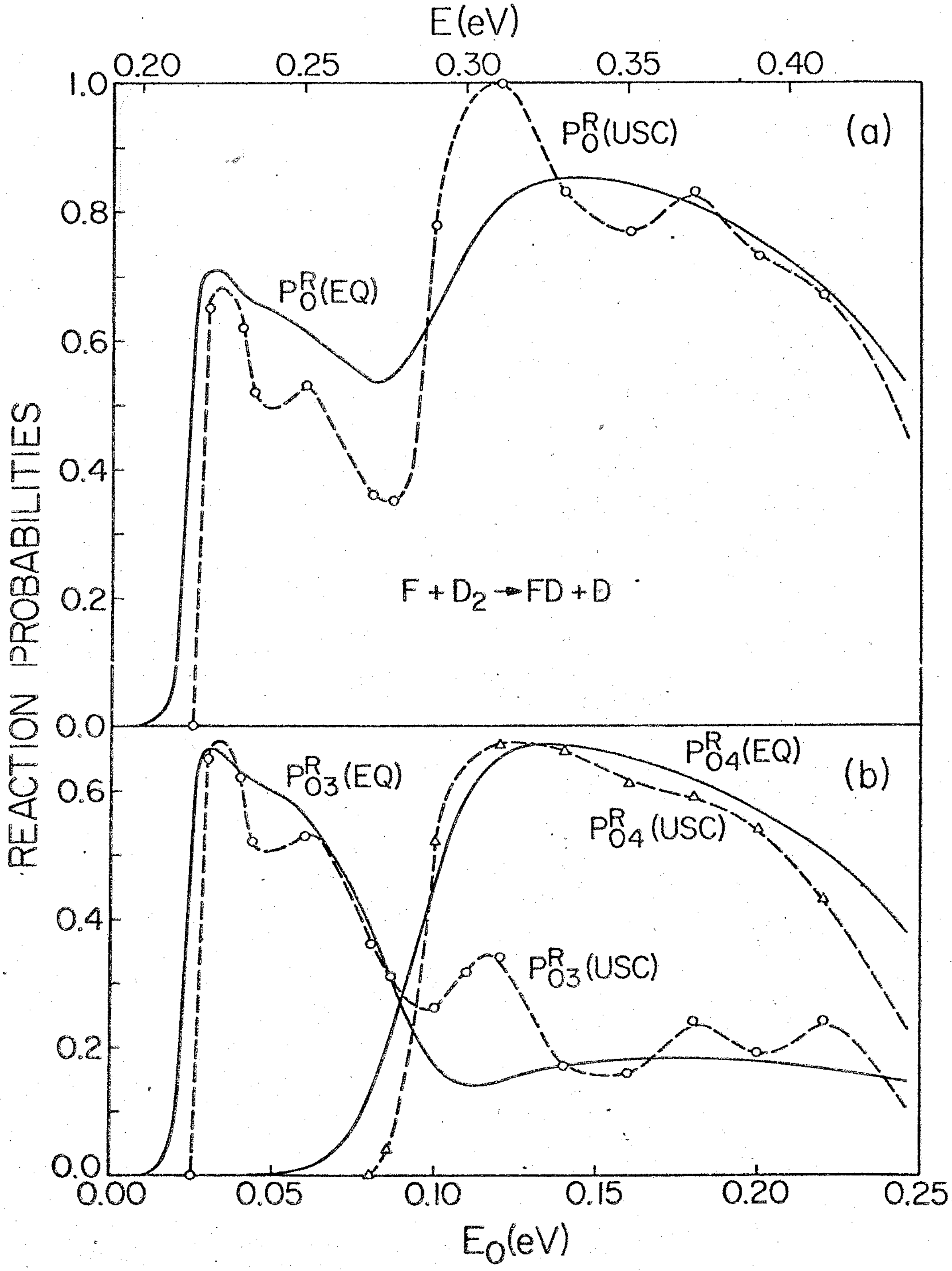
E(eV)
0.20
0.25
0.30
0.35
0.40
1.0
0.8
0.6
0.4
0.2
0.0
0.6
0.4
0.2
0.0
REACTION PROBABILITIES
P_0^R(USC)
(a)
P_0^R(EQ)
F + D$_2$ → FD + D
P_{03}^R(EQ)
P_{04}^R(EQ)
(b)
P_{04}^R(USC)
P_{03}^R(USC)
0.00
0.05
0.10
0.15
0.20
0.25
E$_0$(eV)

Figure 7

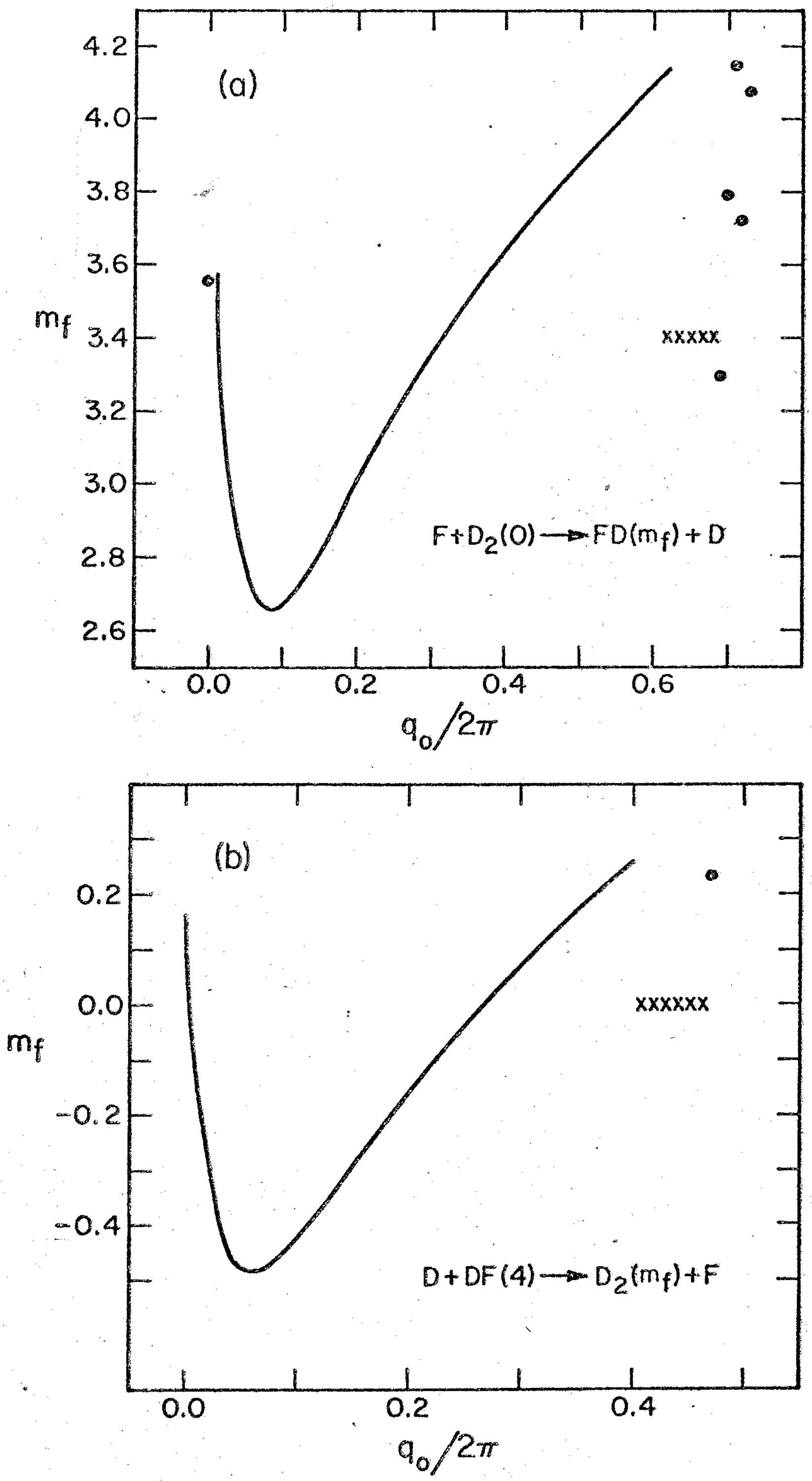
(a)
4.2
4.0
3.8
3.6
3.4
3.2
3.0
2.8
2.6
m_f
xxxxx
$F+D_2(0) \rightarrow FD(m_f)+D$
0.0
0.2
0.4
0.6
$q_o/2\pi$
(b)
0.2
0.0
-0.2
-0.4
m_f
xxxxxx
$D+DF(4) \rightarrow D_2(m_f)+F$
0.0
0.2
0.4
$q_o/2\pi$

Figure 8

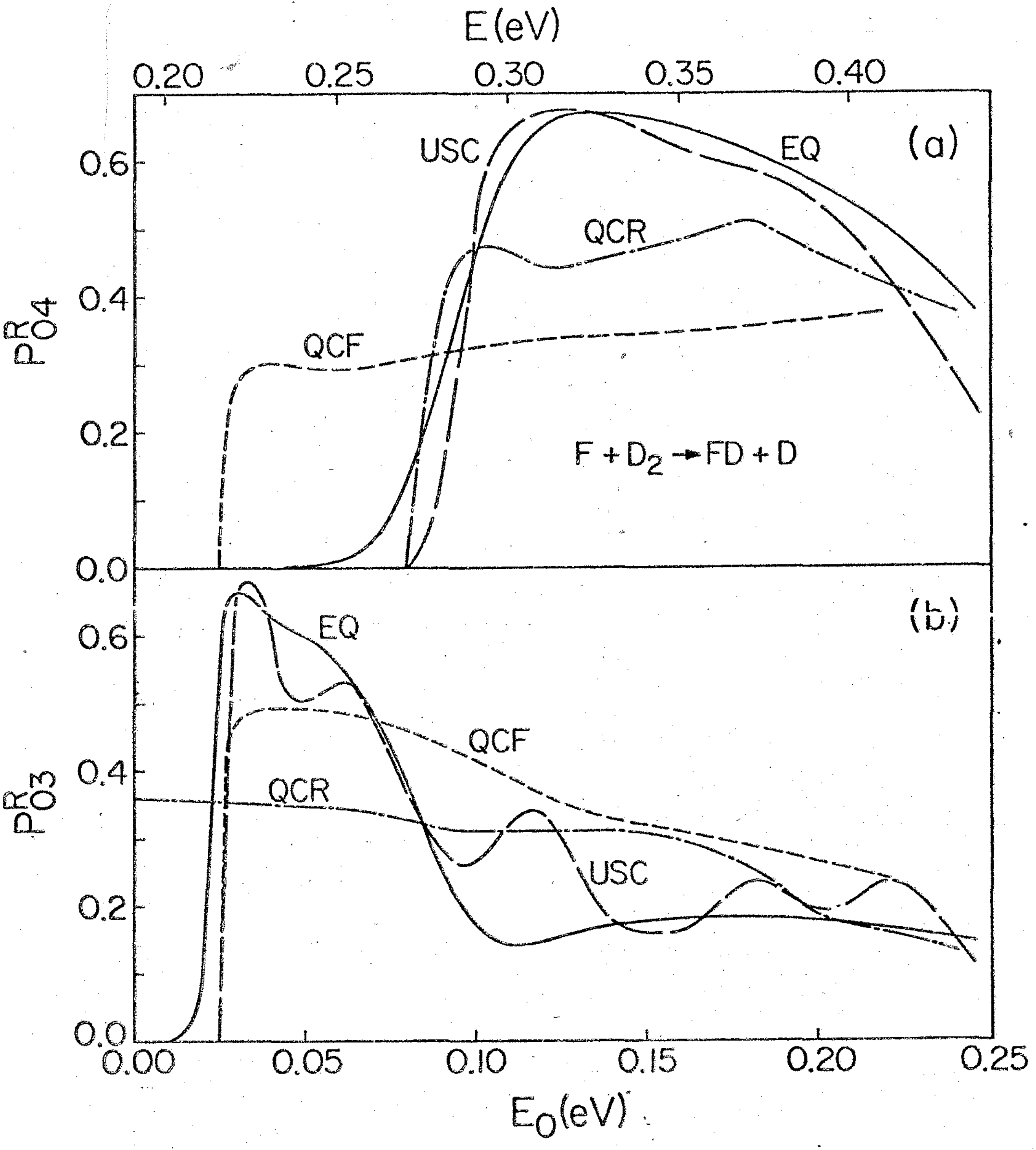
E(eV)
0.20
0.25
0.30
0.35
0.40
(a)
USC
EQ
QCR
QCF
P^R_{04}
0.6
0.4
0.2
0.0
F + D$_2$ → FD + D
(b)
EQ
QCF
QCR
USC
P^R_{03}
0.6
0.4
0.2
0.0
0.00
0.05
0.10
0.15
0.20
0.25
E$_0$(eV)

Figure 9

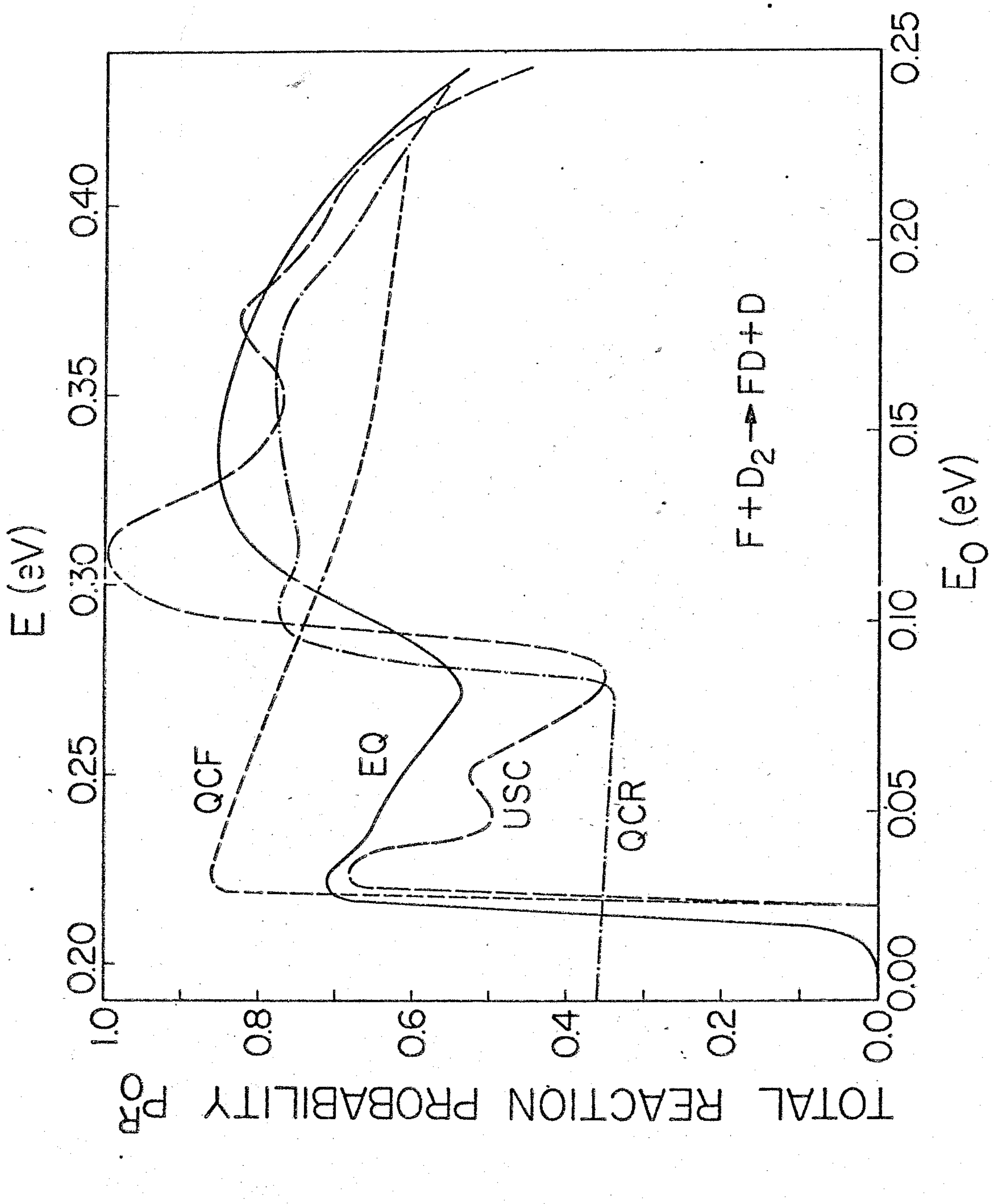
E (eV)
0.20
0.25
0.30
0.35
0.40
TOTAL REACTION PROBABILITY P_R^O
1.0
0.8
0.6
0.4
0.2
0.0
0.00
0.05
0.10
0.15
0.20
0.25
E_O (eV)
QCF
EQ
USC
QCR
$F + D_2 \rightarrow FD + D$

Figure 10

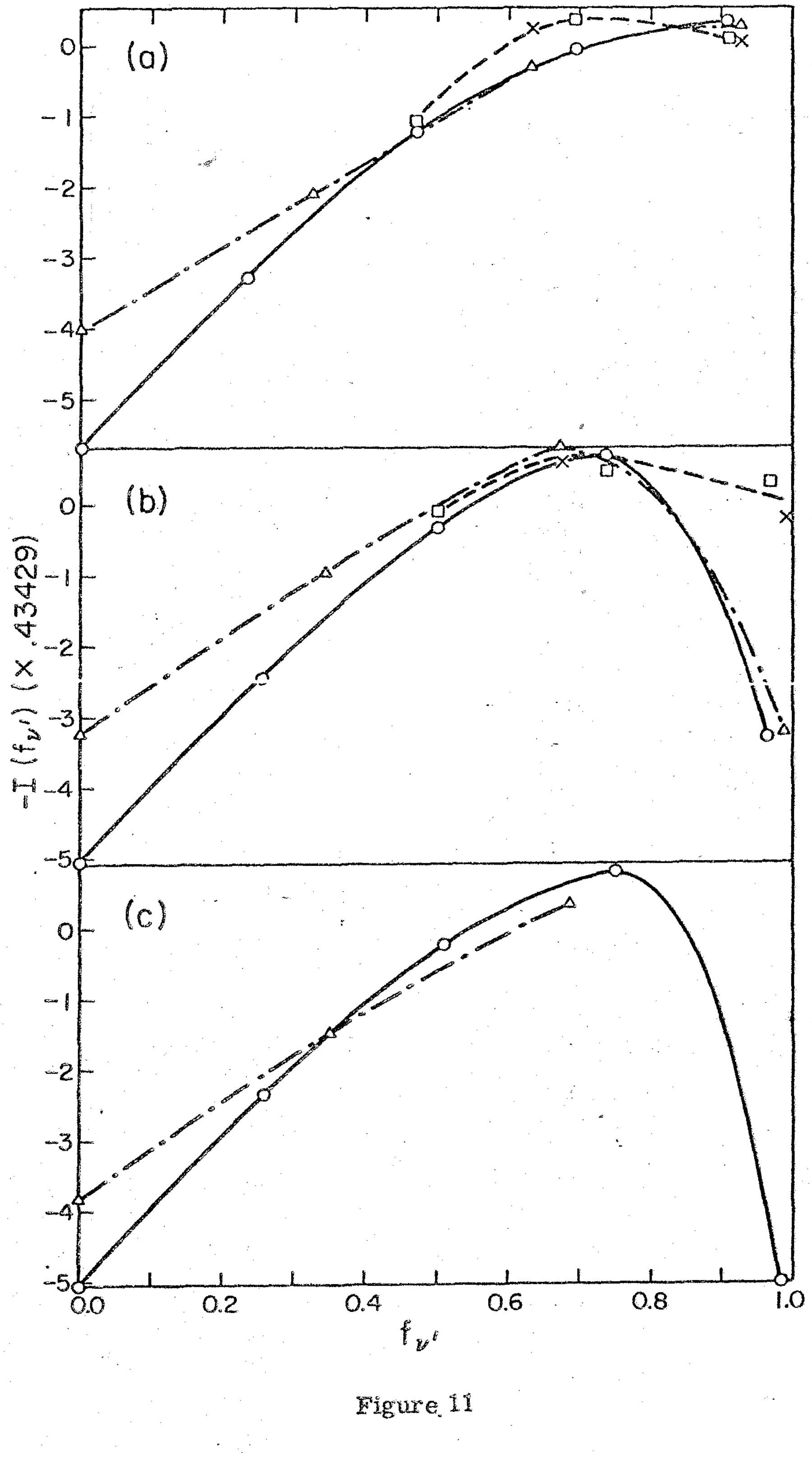

Figure 11

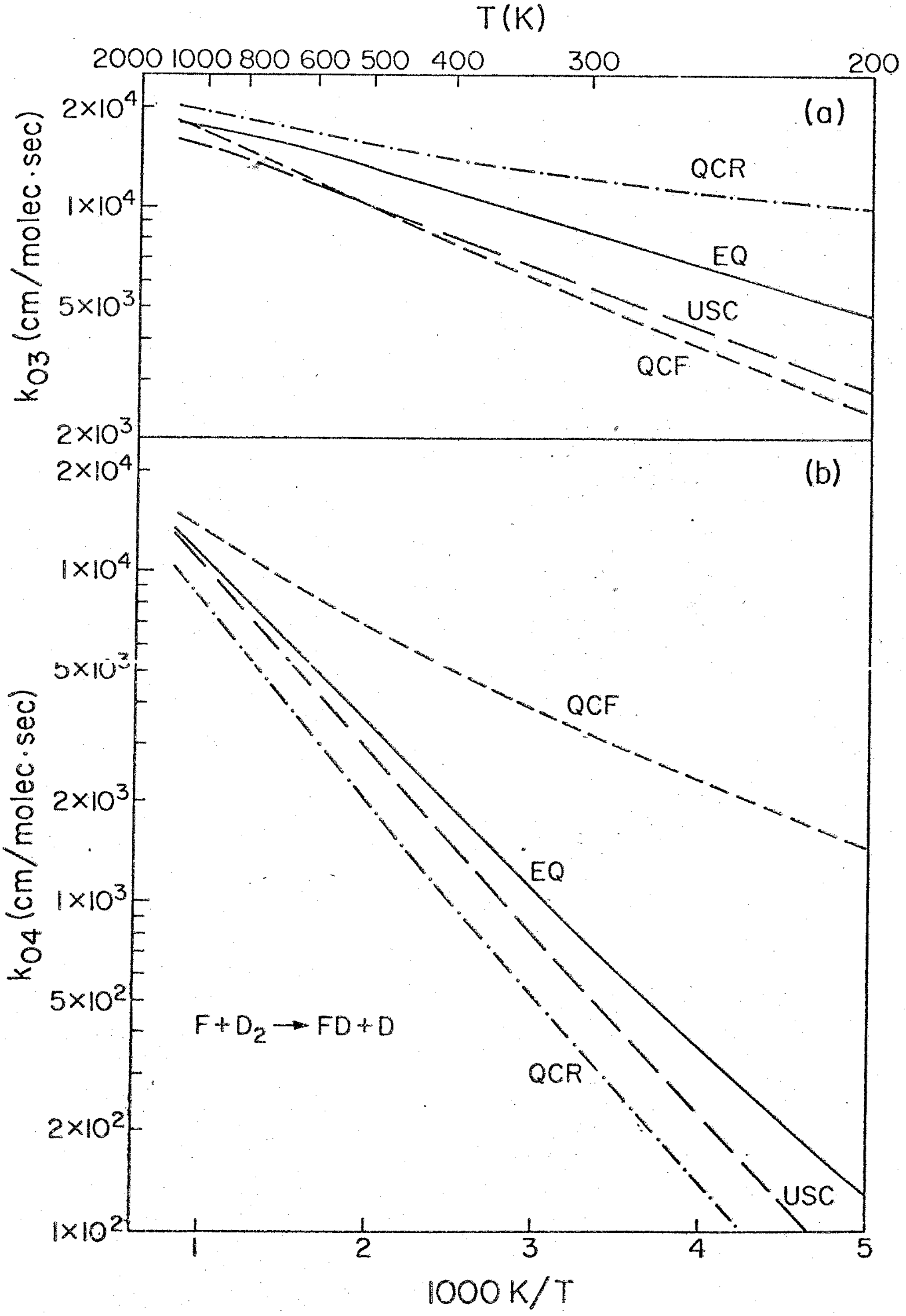
T(K)
2000
1000
800
600
500
400
300
200
(a)
2×10^4
1×10^4
5×10^3
2×10^3
k03 (cm/molec·sec)
QCR
EQ
USC
QCF
(b)
2×10^4
1×10^4
5×10^3
2×10^3
1×10^3
5×10^2
2×10^2
1×10^2
k04 (cm/molec·sec)
QCF
EQ
QCR
USC
F + D2 → FD + D
1
2
3
4
5
1000 K/T

Figure 12

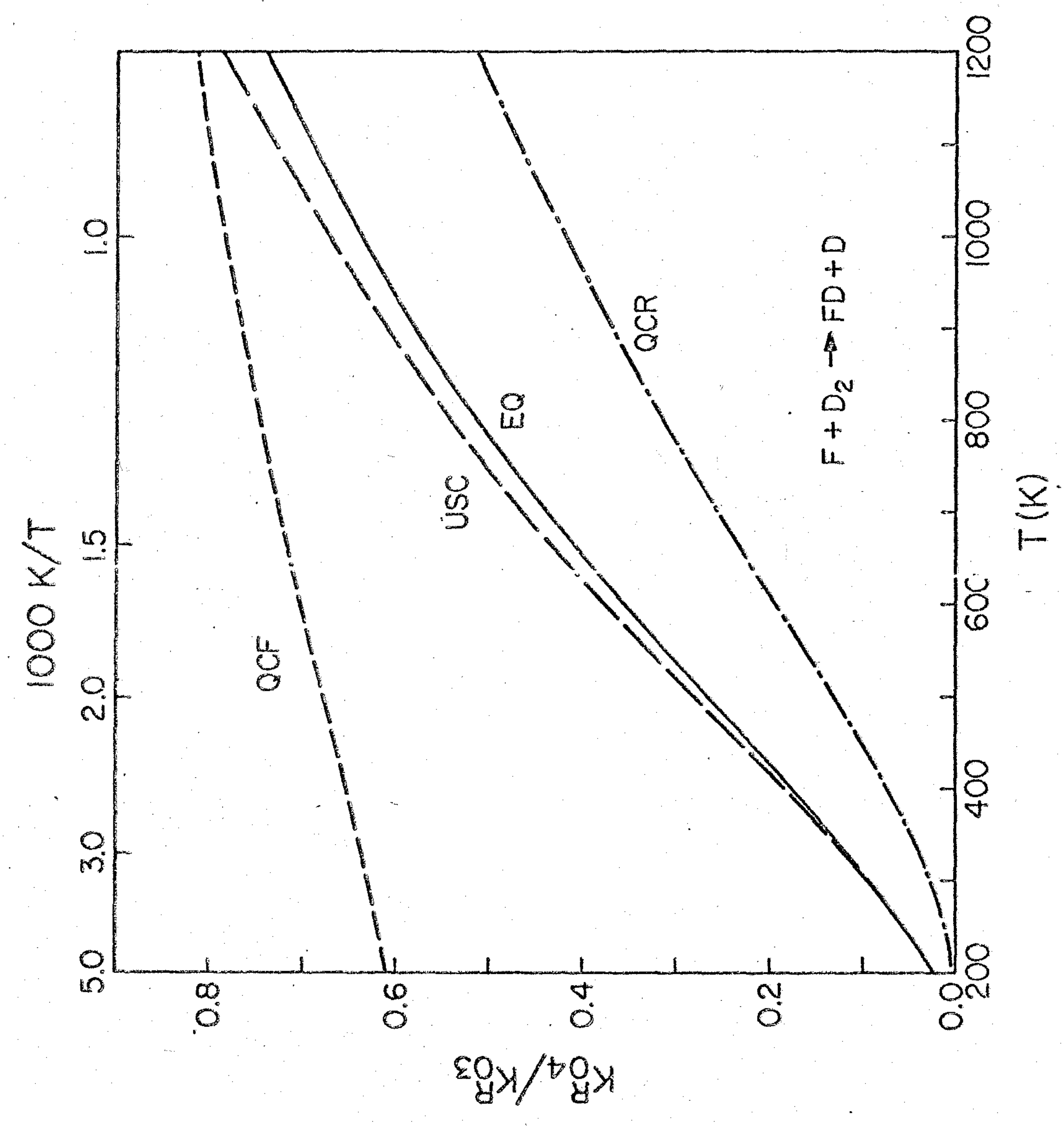
1000 K/T
5.0
3.0
2.0
1.5
1.0
0.0
0.2
0.4
0.6
0.8
KR04/KR03
200
400
600
800
1000
1200
T (K)
QCF
USC
EQ
QCR
$F + D_2 \rightarrow FD + D$

Figure 13

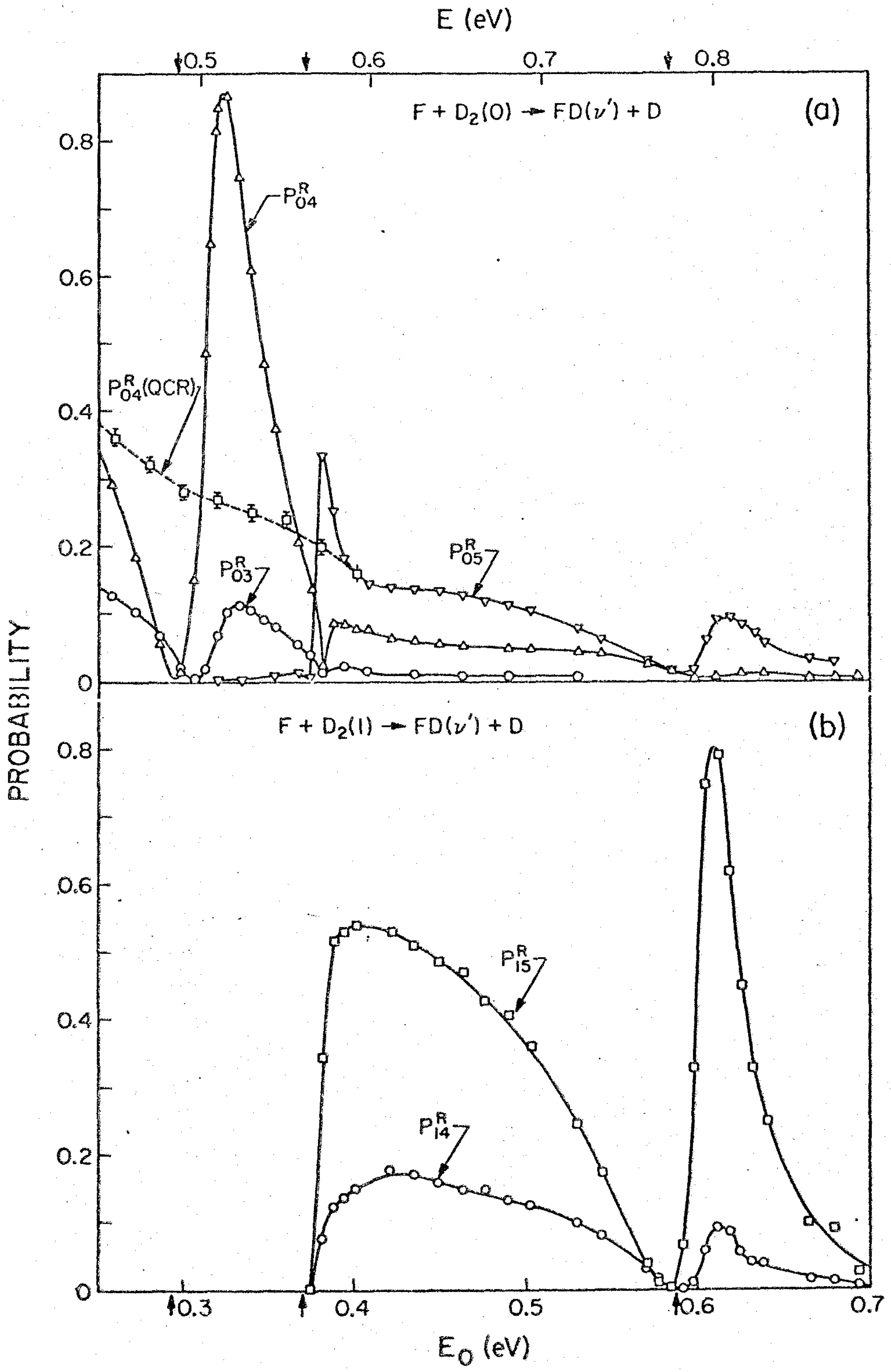
E (eV)
0.5
0.6
0.7
0.8
F + D₂(0) → FD(ν′) + D
(a)
P$^R_{04}$
P$^R_{04}$(QCR)
P$^R_{03}$
P$^R_{05}$
PROBABILITY
0
0.2
0.4
0.6
0.8
F + D₂(1) → FD(ν′) + D
(b)
P$^R_{15}$
P$^R_{14}$
0.3
0.4
0.5
0.6
0.7
E₀ (eV)

Figure 14

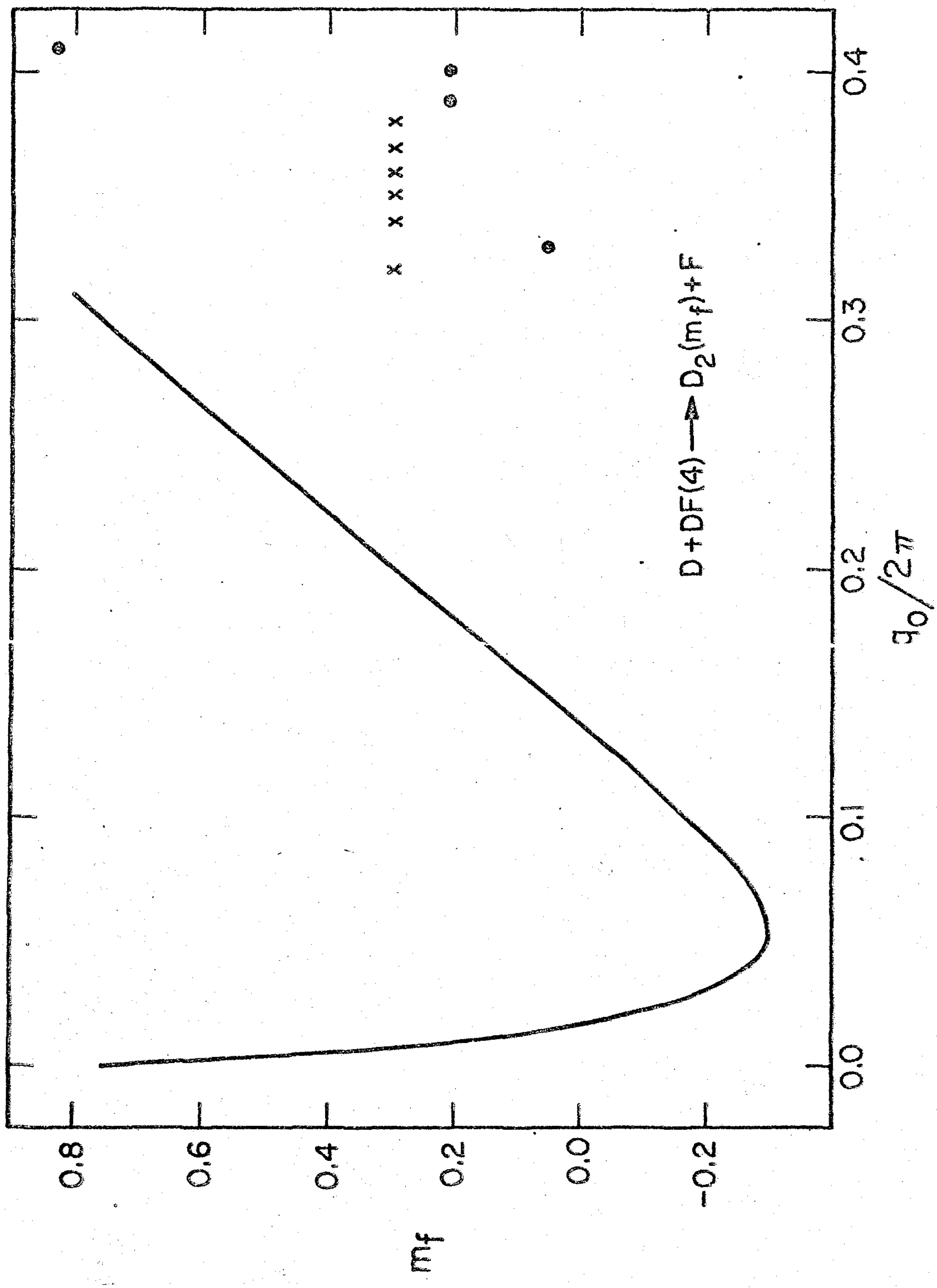
0.8
0.6
0.4
0.2
0.0
-0.2
m_f
0.0
0.1
0.2
0.3
0.4
$q_0/2\pi$
$D + DF(4) \longrightarrow D_2(m_f) + F$

Figure 15

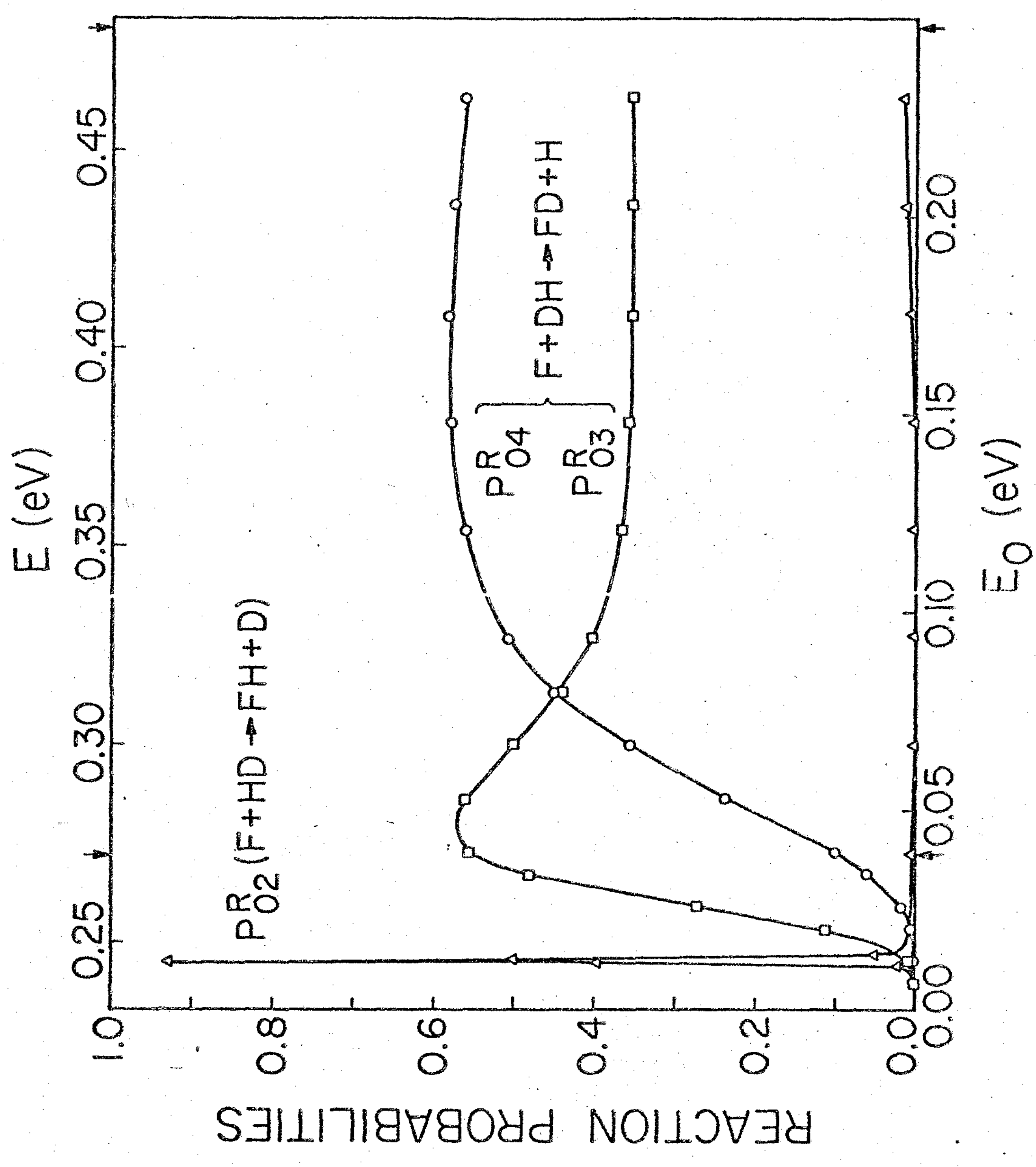
E (eV)
0.25
0.30
0.35
0.40
0.45
E_0 (eV)
0.00
0.05
0.10
0.15
0.20
REACTION PROBABILITIES
0.0
0.2
0.4
0.6
0.8
1.0
P^R_{02} (F+HD → FH+D)
P^R_{04}
P^R_{03}
F+DH → FD+H

Figure 16

3. AN EXACT QUANTUM STUDY OF VIBRATIONAL DEACTIVATION BY REACTIVE AND NONREACTIVE COLLISIONS IN COLLINEAR H + FH, D + FD, H + FD AND D + FH.

An exact quantum study of vibrational deactivation by reactive and nonreactive collisions in collinear H + FH, D + FD, H + FD and D + FH*

George C. Schatz† and Aron Kuppermann

Arthur Amos Noyes Laboratory of Chemical Physics,‡
California Institute of Technology, Pasadena, California 91125

(Received)

Accurate quantum mechanical transition probabilities and rate constants for vibrational deactivation via reactive and nonreactive collisions in collinear H + FH(v), D + FD(v), H + FD(v) and D + FH(v) are presented. In all cases, the reactive inelastic rate constants are larger than the nonreactive ones for the same initial and final vibrational states, but the ratios of these reactive and nonreactive rate constants depend strongly on the vibrational quantum number v and on isotopic composition of the reagents. Nonreactive and reactive transition probabilities for multiquantum jump transitions are generally comparable to those for single quantum transitions. This vibrationally nonadiabatic behavior is a direct consequence of the severe distortion of the diatomic that occurs in a collision on a reactive potential surface, and makes H or D more efficient deactivators of HF or DF than are nonreactive collision partners. Most conclusions are in qualitative and even quantitative agreement with those of Wilkins' three dimensional quasi-classical trajectory study on the same systems.

1. INTRODUCTION

The success of the HF chemical laser depends to a large extent on the relative rates of (a) the F + H_2 pumping reaction which produces vibrationally excited HF, and (b) deactivation of HF(v) by collisions with H_2, F, H, buffer gas and HF itself. Although the deactivation of HF by H_2,[1] F[2] and HF[3] has been both experimentally and theoretically well characterized with generally good agreement between experiment and theory, the situation is far less satisfactory for H + FH and its isotopic counterparts D + FD, H + FD and D + FH. The three experimental determinations of the H + FH (v = 1) deactivation rate[2a,4,5] give rate constants at 300 K of $< (7 \pm 4) \times 10^{11}$ [4], $\leq 9 \times 10^{9}$ [2a] and $(1.4 \pm 0.4) \times 10^{11}$ [5] cm^3/mole sec, thus disagreeing with one another by amounts well outside their respective error limits. Agreement with the results of a theoretical (classical trajectory) calculation of this rate constant[6] is no better with a predicted value of 2.2×10^{12} cm^3/mole sec at 300 K. Similar experimental and theoretical comparisons of the rate constants for the deactivation of D + FD(v = 1), D + FH (v = 1) and H + FD (v = 1) are also poor.[5]

There are two important approximations in the quasi-classical method, either of which could be important in the above mentioned disagreement between theoretical and experimental deactivation rates. First, the electronic potential surface could be in error, either because of nonadiabatic effects or because of an inaccurate determination of that surface. Second, the use of classical rather than quantum mechanics could be a poor approximation. In the trajectory studies of both Wilkins[6] and Thompson[7] on H + FH and its isotopic counterparts, the potential surfaces used were of the LEPS type and were optimized for only $F + H_2$ configurations. The use of these same surfaces for H + FH configurations is certainly questionable[8] although this same procedure has been quite successful for F + HF.[2b, 9, 10] Recently, Bender et al.[11] has shown that the barrier to reaction in H + FH can be very seriously in error if this procedure is used (1.4 kcal/mole for Wilkins LEPS surface[6] versus 49.0 kcal/mole for Bender's ab initio CI result[11]). The Bender result seems to be too high to explain the experimental rate constants adequately,[5] but it certainly indicates that the LEPS surfaces are probably not too accurate. The approximation of classical dynamics has been analyzed in detail for the $F + H_2$[12] and $F + D_2$[13] reactions and its most important consequences for reactive collisions were found to be (a) an inadequate description of resonances, (b) neglect of tunnelling and (c) dynamical threshold effects. In considering vibrational deactivation processes, we must also examine the validity of the quasi-classical prediction[6] that multiquantum jump transitions are extremely important in deactivating collisions (both nonreactive and reactive) for H + FH. If true, it could be important, for it would mean that H atoms can be very efficient deactivators of HF. In addition, much of the theoretical analysis is predicated on the assumption of the dominance of single quantum jump transitions.[7]

In this paper, we examine the dynamics of reactive and nonreactive H + FH and its isotopic counterparts using accurate quantum mechanical methods. In all calculations, we restrict our considerations to collinear collisions, an approximation which renders the quantum mechanical problem tractable while still retaining many of the important dynamical features.[14,15] The specific systems we will investigate are:

$$\begin{aligned} H + FH\ (v = 0 - 3) &\rightarrow HF\ (v' = 0 - 2) + H \\ &\rightarrow H + FH\ (v' = 0 - 2) \end{aligned} \tag{R.1}$$

$$\begin{aligned} D + FD\ (v = 0 - 1) &\rightarrow DF\ (v' = 0) + D \\ &\rightarrow D + FD\ (v' = 0) \end{aligned} \tag{R.2}$$

$$\begin{aligned} D + FH\ (v = 0, 1) &\rightarrow DF\ (v' = 0) + H \\ &\rightarrow D + FH\ (v' = 0) \end{aligned} \tag{R.3}$$

$$\begin{aligned} H + FD\ (v = 0, 1) &\rightarrow HF\ (v' = 0) + H \\ &\rightarrow H + FD\ (v' = 0) \end{aligned} \tag{R.4}$$

Reactions R.3 and R.4 are actually considered in the same calculation, since transitions between all possible open states of both reagents and products are determined simultaneously. In all the above reactions, the linear collision complex has the F atom between the hydrogens or deuteriums. The actual three dimensional collision includes other configurations, such as H + HF where the F atom is on one end of the 3-atom system. We will show that nonreactive collisions such as

$$H + HF\ (v = 1) \rightarrow H + HF\ (v' = 0) \tag{R.5}$$

are unimportant in comparison to R.1 above, and that R.1 is more representative of the actual 3D situation.

The purpose of these collinear calculations was to examine the nature of deactivation processes on a chemically reactive surface. We will examine the significance of the multiquantum jump transitions mentioned above, and we will analyze the relative importance of reactive and nonreactive mechanisms of collisional deactivation (Section 3). The validity of the potential surface (described in Section 2) will not be examined, although the influence of that surface on the collision dynamics will. A summary of the conclusions of this paper is presented in Section 4.

2. THE CALCULATION

A close coupling propagation technique[16] was used to solve the Schrödinger equation for the collinear reactive and nonreactive collisions. This method has been previously applied to $H + H_2$,[17] $F + H_2$[12,18] and $F + D_2$[13] and is more thoroughly described in Ref. 12. Between 10 and 12 channels were included in the vibrational basis sets with 1 to 4 open and the rest closed. Convergence of the transition probabilities with respect to the addition of closed channels was tested, and this, together with tests of flux conservation and microscopic reversibility indicate that the results presented are accurate to 1% or better. The potential surface used was Muckerman's Surface 5,[19,20] the LEPS parameters of which are given in Ref. 12.[21] Fig. 1 depicts equipotential contours of this surface. The barrier height is 1.23 kcal/mole (0.054 eV) which is quite similar to that of Wilkins (1.4 kcal/mole[6]). No wells or hollows are apparent in the surface. The vibrational energy levels (including zero point energy) of HF are 5.8, 17.1, 27.8 and 38.1 kcal/mole for $v = 0, 1, 2$ and 3, respectively. For DF, they are 4.2, 12.5, 20.5 and 28.1 kcal/mole for these same levels.

The primary results of the calculation are the transition probabilities (which are analogous to the 3D cross sections) and the one dimensional thermal rate constants. These results cannot be directly compared with those of 3D calculations or with experiment without additional assumptions such as the assignment of an impact parameter dependence to the reaction probability.[15] Alternatively, ratios of rate constants can be compared. This is a dangerous procedure if no allowance for rotational states is made (as is done in Ref. 22, for example) but often gives qualitatively useful comparisons as will be apparent in Section 3.2.

3. RESULTS

3.1 Transition Probabilities

We denote the transition probability from vibrational state v of the reagent to state v' of the product by the symbol $P_{vv'}$. If the collision is reactive, we use the superscript R (i.e. $P^R_{vv'}$) and if nonreactive, the superscript V ($P^V_{vv'}$). To identify the different reactions R.1 - R.4 above, we specify the reagents in parenthesis after the transition probability. Thus, P^R_{10} (H + FD) means the reaction probability for H + FD (v = 1) → HF (v' = 0) + D while P^V_{10} (H + FD) implies the nonreactive probability for H + FD (v = 1) → H + FD (v' = 0).

We first consider the ground vibrational state reaction probabilities P^R_{00} (H + FH), P^R_{00} (D + FD) and P^R_{00} (D + FH). These are plotted in Fig. 2 as a function of the reagent relative translational energy E_0. (More generally, we let E_v be the translational energy relative to vibrational state v of the reagent diatomic molecule.) P^R_{00} (H + FD) can be obtained from P^R_{00} (D + FH) by shifting the latter curve in Fig. 2 upwards in energy by 0.069 eV (which is the difference between the HF and DF zero point energies). The P_{00}^{R} curves are quite similar in shape to the analogous reaction probability P_{00}^{R} $(H + H_2)$ which has been analyzed previously in detail.[23,24] At low energies ($E_0 < 0.05$ eV) the reaction probabilities are small. This is the expected behavior when barrier tunnelling (in an adiabatic sense) is occurring. The P_{00}^{R} curves then show a sudden rise to nearly unit probability. The energies at which P_{00}^{R} equals 0.01 are $E_0 = 0.04$ eV for H + FH, 0.050 eV for D + FD, 0.030 eV for D + FH and 0.099 eV for H + FD. These effective threshold energies may be explained by examining the vibrationally adiabatic barriers as was done for $F + H_2$ and $F + D_2$ in Refs. 12 and 13, and for the isotopically related series $H + H_2$, $D + H_2$, $H + D_2$ and $D + D_2$ in Ref. 25. At higher energies, the P_{00}^{R} curves show sudden dips due to internal excitation resonances.[17] These resonances are at 0.412 eV for H + FH, 0.302 eV for D + FD and D + FH and 0.371 eV for H + FD. We shall present a more complete analysis of the H + FH resonance in a separate paper.[26] The effect of the resonances on thermal rate constants is small so we shall not be concerned with them here.

The vibrationally inelastic transition probabilities P_{10}^{R} and P_{10}^{V} for H + FH are presented in Fig. 3. E_1 in that figure is the translational energy relative to $v = 1$ of HF. We see that both P_{10}^{R} and P_{10}^{V} have very small effective threshold energies (< 0.01 eV). Above threshold, the reactive probability is significantly larger than the nonreactive one over much of the energy range scanned. Only in the vicinity of resonances (at $E_1 \sim 0.3$ eV, 0.9 eV and 1.2 eV) do the two curves cross. In regions where the two curves are smooth (where the direct processes dominate) P_{10}^{R} is usually 5 to 10 times larger than P_{10}^{V}. This indicates that reactive collisions are more important than nonreactive ones in producing vibrational deactivation in H + FH (v = 1) collisions. The same conclusion is usually also true for H + FH (v = 2, 3), as is shown in Figs. 4 - 8. In Fig. 4 we plot P_{20}^{R} and P_{20}^{V} while P_{21}^{R} and P_{21}^{V} are depicted in Fig. 5. In both figures, there is essentially zero effective threshold energy for the deactivation processes. Above threshold, we find that P_{20}^{R} is 2 to 20 times larger than P_{20}^{V}. P_{21}^{R} is also significantly larger than P_{21}^{V}, but only for the important range of energies below $E_2 = 0.15$ eV. If the probabilities in Figs. 4 and 5 are compared, we find that the 2 → 0 and 2 → 1 transition probabilities are generally comparable in magnitude. This contrasts with the dominance of the $v' = v - 1$ probability which is often obtained (or assumed) in purely nonreactive systems.[27] As might be expected, the relative strength of the individual $P_{vv'}^{V}$ or $P_{vv'}^{R}$ for fixed v and varying v' is usually dependent on the strength and nature of the interaction potential. For many nonreactive systems, the interaction potential is weak so that all inelastic transition probabilities are small with the $v' = v - 1$ being the largest (similar to transitions in a perturbed harmonic oscillator). For a reactive surface such as exists for H + FH (Fig. 1), severe distortion of the reagent diatomic can occur during the collision so that all inelastic transition probabilities become comparable (and large as well). In Figs. 6 - 9 we plot the inelastic transition probabilities from v = 3 of HF. Again we see the dominance of the reactive over the nonreactive probabilities (for the same v → v' process). In addition, the probabilities for multiquantum jump transitions are comparable to (or larger than) those for single jump transitions. Both the preceding conclusions are in agreement with the analogous 3D results of Wilkins.[6]

In Ref. 12, the collinear H + HF probabilities analogous to those for H + FH in Figs. 2 - 8 were calculated. Over the range of E_1 from 0.0 to 0.4 eV (important for thermal rate constants) we find that P_{10}^{V} (H + HF) $\leq 10^{-2}$ P_{10}^{V} (H + FH) so that the deactivation probabilities are strongly dependent on the orientation of H with respect to HF during a collision. Similar conclusions are valid for the inelastic probabilities from v = 2 and 3 of HF as well. Also of interest is the fact that for H + HF collisions, P_{21}^{V} is usually over 1,000 times larger than P_{20}^{V}, and $P_{32}^{V} \simeq 100\ P_{31}^{V} \simeq 10^{4}\ P_{30}^{V}$. This indicates the dominance of the v' = v - 1 transition probabilities for H + HF, in contrast to the behavior of the same probabilities for H + FH. Such behavior is most easily understood by examining the potential energy surfaces involved. The H + HF surface (see Ref. 12) has a largely repulsive nonreactive appearance. (The reactive channel is closed for E_0 (HF) $\leq$ 1.4 eV.) This implies that the HF is not significantly stretched or compressed in linear H + HF collisions whereas it clearly will be significantly stretched in H + FH (Fig. 1), thus explaining the different behavior of the two sets of transition probabilities. Finally we should remark that the behavior to be expected in three dimensional collisions depends on the orientation dependence of the interaction potential. For most orientations of H with respect to HF, we find potentials similar to the H + FH one in Fig. 1.[28] Only a small range of orientations gives a potential similar to the H + HF linear potential thus indicating that the H + FH system should be representative of the majority of collisions. That this conclusion is correct is evident from the qualitative agreement between our 1D and Wilkins' 3D results mentioned at the end of the previous paragraph.

We now consider the $v = 1$ to $v' = 0$ inelastic probabilities for D + FD, D + FH and H + FD. These are shown in Figs. 9 and 10. In Fig. 10 we have plotted the D + FH and H + FD results on an absolute energy scale so as to show the important relationships of the probabilities to one another. Both Figs. 9 and 10 indicate that the reactive probabilities dominate over the nonreactive ones for analogous transitions. However, at low collision energies, P_{10}^{V} (H + FD) is only slightly smaller than P_{10}^{R} (H + FD) so the corresponding rate constants should be quite similar in magnitude. This will be examined in the next section.

3.2 Rate Constants

The one dimensional thermal rate constants $k_{vv'}$ are obtained from the appropriate Boltzman average of reagent velocity times transition probability. As shown in Ref. 12, we can write this relationship as

$$k_{vv'}(T) = (2\pi\mu kT)^{-\frac{1}{2}} \int_0^\infty P_{vv'}(E_v)\, e^{-E_v/kT}\, dE_v \qquad (3.1)$$

where μ is the relative motion reduced mass and k has units of cm/(molec × sec). Note that while a Boltzman velocity distribution has been assumed, a Boltzman distribution of vibrational states has not, for we are interested in reagents initially in a single vibrational state v.

Using the above expression, rate constants for all of the transitions considered in Figs. 2 - 10 have been calculated. The resulting Arrhenius type plots are given in Figs. 11 - 16 and we shall now examine these plots individually.

Fig. 11 depicts the vibrationally elastic rate constants k_{00}^{R} for H + FH, D + FD, H + FD and D + FH. The curves are all reasonably linear with activation energies of 1.8, 1.8, 3.1 and 1.5 kcal/mole at 300 K for H + FH, D + FD, H + FD and D + FH, respectively; and 2.5, 2.2, 3.6 and 2.0 kcal/mole at 1,100 K for these same reactions. These activation energies are all somewhat higher than the effective threshold energies (Section 3.1). This probably occurs because the latter energies are so low that the peaks in $P_{00}^{R} \times \exp(-E_v/kT)$ (and hence the dominant contributions to the integral in Eq. 3.1) occur for E_v well above the effective thresholds.

Figs. 12 and 13 depict the H + FH rate constants k_{10}^{R}, k_{10}^{V}, k_{20}^{R}, k_{20}^{V}, k_{21}^{R}, k_{21}^{V}, k_{30}^{R}, k_{30}^{V}, k_{31}^{R}, k_{31}^{V}, k_{32}^{R} and k_{32}^{V}. Many of the curves in these two figures are nonlinear. This results from the fact that the corresponding transition probabilities have essentially zero threshold energies and often oscillatory behavior above threshold. As the temperature changes, the largest contributions to the integral in Eq. 3.1 come from gradually changing energies and this results in the changing of the slopes in the Arrhenius plots. To examine the degree of dominance of reactive over nonreactive deactivation mechanisms, let us consider the ratio $R_{vv'} = k_{vv'}^{R}/k_{vv'}^{V}$ at 300 K. We find that $R_{10} = 8.3$, $R_{20} = 10.4$, $R_{21} = 7.1$, $R_{30} = 5.3$, $R_{31} = 2.83$ and $R_{32} = 1.89$. This implies that the reactive and nonreactive rate constants approach each other as v approaches v'. The total inelastic rate constants k_v^R and k_v^V, obtained by summing $k_{vv'}^R$ and $k_{vv'}^V$ over all $v' \neq v$ are plotted in Fig. 14. Here, the ratio $R_v = k_v^R/k_v^V$ has the value 8.3 for v = 1, 8.5 for v = 2 and 3.5 for v = 3 so there is no systematic variation of R_v with increasing v. The total deactivation rate constant $k_v = k_v^R + k_v^V$ is plotted in Fig. 15. The k_v's all have similar temperature dependence with differences in magnitude primarily determined by differences in the total inelastic transition probabilities (obtained by summing the probabilities in Figs. 3, 4 - 5 and 6 - 8). The ratio k_2/k_1 has the value 2.1 at 300 K while $k_3/k_2 = 0.94$ at the same temperature. In his classical trajectory study,[6] Wilkins found $k_2/k_1 \simeq 3.9$, and $k_3/k_2 \simeq 1.8$ so his numbers (using a different potential surface) are somewhat higher than ours.

In Fig. 16 we plot the rate constants k_{10}^R and k_{10}^V for H + FH, D + FD, H + FD and D + FH. If we calculate the ratio $R_{10} = k_{10}^R/k_{10}^V$, at 300 K we get 8.3 for H + FH and D + FD, 1.4 for H + FD and 12.0 for D + FH. The low value for H + FD is clearly a consequence of the great similarity of P_{10}^R (H + FD) and P_{10}^V (H + FD) in Fig. 10. The corresponding ratio R_{10} calculated from Wilkins' results (see Ref. 5) are 3.2 for H + FH, 9.0 for D + FD, 1.3 for H + FD and 9.0 for D + HF. These numbers are in reasonable agreement with ours indicating that the isotopic dependence of the deactivation processes is correctly described classically.

4. SUMMARY

We now summarize the important results of this paper. First, for all transition probabilities and rate constants, the reactive mechanism dominates over the nonreactive one in producing vibrational excitation. This result is apparently of general validity over a wide range of impact parameters since the same conclusions (even the same ratios of rate constants) were obtained by Wilkins in his 3D classical calculations. Second, multiquantum jump transition probabilities are comparable in magnitude to single quantum jump transition probabilities. This is clearly a consequence of the use of a reactive potential energy surface since the analogous H + HF results (for a surface which is nonreactive at the energies considered) indicate that single quantum jump transition probabilities are orders of magnitude larger than all others.

We should add that none of our results for H + FH or D + FD explicitly include for the effects of indistinguishability of particles. Such considerations are really meaningless for collinear collisions since the particles are actually spatially distinguishable[29] whereas in 2D and 3D they are not. For D + FH and H + FD, the reactive and nonreactive collisions may be experimentally distinguished and the measurement of k_{10}^{R} and k_{10}^{V} (or their ratio) for these reactions would provide a sensitive test of the nature of the potential surface.

Finally we should again state that the potential surface used in this study is of questionable validity. Nevertheless, even if it is seriously in error for H + FH, there are a large number of similar chemically reactive systems which could be important in vibrational deactivation to which the surface used might be applicable. The present results should be a useful guide to understanding them.

[*] Research supported in part by the United States Air Force Office of Scientific Research.

[†] Work performed in partial fulfillment of the requirements for the Ph.D. in Chemistry at the California Institute of Technology.

[‡] Contribution No.

[1] J. F. Hancock and W. H. Green, J. Chem. Phys. **56**, 2474 (1972); *ibid.*, **57**, 4515 (1972).

[2] (a) G. P. Quigley and G. J. Wolga, Chem. Phys. Lett. **27**, 276 (1974); (b) R. L. Wilkins, J. Chem. Phys. **59**, 698 (1973).

[3] J. F. Bott, J. Chem. Phys. **61**, 3414 (1974).

[4] M. A. Kwok and R. L. Wilkins, J. Chem. Phys. **60**, 2189 (1974).

[5] R. F. Heidner and J. F. Bott, Report SAMSO-TR-75-80, The Aerospace Corporation, El Segundo, CA, March 1975.

[6] R. L. Wilkins, J. Chem. Phys. **58**, 3038 (1973).

[7] D. L. Thompson, J. Chem. Phys. **56**, 3570 (1972).

[8] C. A. Parr and D. G. Truhlar, J. Phys. Chem. **75**, 1844 (1971).

[9] D. L. Thompson, J. Chem. Phys. **57**, 4164 (1972).

[10] S. V. O'Neill, H. F. Schaefer and C. F. Bender, Proc. Nat'l. Acad. Sci. USA **71**, 104 (1974).

[11] C. F. Bender, B. J. Garrison and H. F. Schaefer, J. Chem. Phys. **62**, 1188 (1975).

[12] G. C. Schatz, J. M. Bowman, and A. Kuppermann, J. Chem. Phys., **63**, 674 (1975).

[13] G. C. Schatz, J. M. Bowman and A. Kuppermann, J. Chem. Phys., **63**, 685 (1975).

[14] G. C. Schatz and A. Kuppermann, Phys. Rev. Lett., submitted.

[15] G. C. Schatz and A. Kuppermann, J. Chem. Phys., in preparation.

[16] (a) A. Kuppermann, *Potential Energy Surfaces in Chemistry,* Ed. W. A. Lester (University of California at Santa Cruz, August, 1970), p. 121-129; (b) Abstracts of papers, VII International Conference on the Physics of Electronic and Atomic Collisions, Amsterdam, 1971.

[17] G. C. Schatz and A. Kuppermann, J. Chem. Phys. **59**, 964 (1973).

[18] G. C. Schatz, J. M. Bowman, and A. Kuppermann, J. Chem. Phys. **58**, 4023 (1973).

[19] (a) J. T. Muckerman, J. Chem. Phys. **54**, 1155 (1971); (b) *ibid.*, **56**, 2997 (1972).

[20] J. T. Muckerman, private communication.

[21] The value of B_e(HF) used in these calculations was 2.2087 $Å^{-1}$ (not 2.2187 $Å^{-1}$ as was used in Ref. 12).

[22] C. Rebick, R. D. Levine and R. B. Bernstein, J. Chem. Phys. **60**, 4977 (1974); R. B. Bernstein and R. D. Levine, preprint.

[23] D. G. Truhlar and A. Kuppermann, J. Chem. Phys. **56**, 2232 (1972).

[24] D. J. Diestler, J. Chem. Phys. **54**, 4547 (1971).

[25] D. G. Truhlar, A. Kuppermann and J. T. Adams, J. Chem. Phys. **59**, 395 (1973).

[26] G. C. Schatz, Ph.D. thesis, California Institute of Technology, (unpublished), 1975.

[27] For a review of nonreactive vibrational deactivation processes, see D. Rapp and T. Kassal, Chem. Rev. **69**, 61 (1969).

[28] G. C. Schatz and A. Kuppermann, unpublished results.

[29] This is true because the two hydrogens in H + FH cannot exchange with one another as long as the atoms are constrained to be collinear.

FIG. 1. Equipotential contours for the collinear H + FH surface as a function of the two HF diatomic internuclear distances r_{HF} and r'_{HF}.

FIG. 2. Reaction probability P_{00}^{R} for H + FH (solid curve and circles), D + FD (dashed curve and squares) and D + FH (dash-dotted curve and triangles) as a function of the reagent relative translational energy E_0 appropriate for each collision system.

FIG. 3. Transition probabilities P_{10}^{R} (circles) and P_{10}^{V} (squares) for H + FH as a function of the reagent relative translational energy E_1. Arrows in abscissa indicate the energies at which $v = 2$ and $v = 3$ of HF open ($E_1 = 0.466$ eV and $E_1 = 0.909$ eV, respectively).

FIG. 4. Transition probabilities P_{20}^{R} (circles) and P_{20}^{V} (squares) for H + FH as a function of the reagent relative translational energy E_2. Arrow at $E_2 = 0.444$ eV indicates the energy at which $v = 3$ of HF opens.

FIG. 5. Transition probabilities P_{21}^{R} (circles) and P_{21}^{V} (squares) for H + FH analogous to Fig. 4.

FIG. 6. Transition probabilities P_{30}^{R} (circles) and P_{30}^{V} (squares) for H + FH as a function of the reagent relative translational energy E_3.

FIG. 7. Transition probabilities P_{31}^{R} (circles) and P_{31}^{V} (squares) for H + FH analogous to Fig. 6.

FIG. 8. Transition probabilities P_{32}^{R} (circles) and P_{31}^{V} (squares) for H + FH analogous to Fig. 6.

FIG. 9. Transition probabilities P_{10}^{R} (circles) and P_{10}^{V} (squares) for D + FD as a function of E_1. Arrow at $E_1 = 0.345$ eV indicates the energy at which v = 2 of DF opens.

FIG. 10. Transition probabilities P_{10}^{R} (H + FD) (circles), P_{10}^{V} (H + FD) (triangles), P_{10}^{R} (D + FH) (squares) and P_{10}^{V} (D + FH) (triangles and dashed curve) as a function of E_1 (H + FD) (lower scale) and E_1 (D + FH) (upper scale). The v = 1 state of HF opens at E_1 (H + FD) = 0.199 eV so the H + FD and D + FH scales have been displaced by that amount.

FIG. 11. Arrhenius plot of the rate constants k_{00}^{R} for H + FH (solid), D + FD (long dashed), D + FH (short dashes) and H + FD (dash-dotted).

FIG. 12. Arrhenius plot of the rate constants k_{10}^{R}, k_{10}^{V} (solid curves), k_{20}^{R}, k_{20}^{V} (dashed) and k_{21}^{R}, k_{21}^{V} (dash-dotted).

FIG. 13. Arrhenius plot of the rate constants k_{30}^{R}, k_{30}^{V} (solid curves), k_{31}^{R}, k_{31}^{V} (dashed), and k_{32}^{R}, k_{32}^{V} (dash-dotted).

FIG. 14. Arrhenius plot of the total inelastic rate constants k_{1}^{R}, k_{1}^{V} (solid curves), k_{2}^{R}, k_{2}^{V} (dashed) and k_{3}^{R}, k_{3}^{V} (dash-dotted).

FIG. 15. Arrhenius plot of the total inelastic rate constants k_1 (solid curve), k_2 (dash-dotted), and k_3 (dashed).

FIG. 16. Arrhenius plot of the rate constants k_{10}^{R} and k_{10}^{V} for H + FH (solid curves), D + FD (long dashes), D + FH (short dashes) and H + FD (dash-dotted).

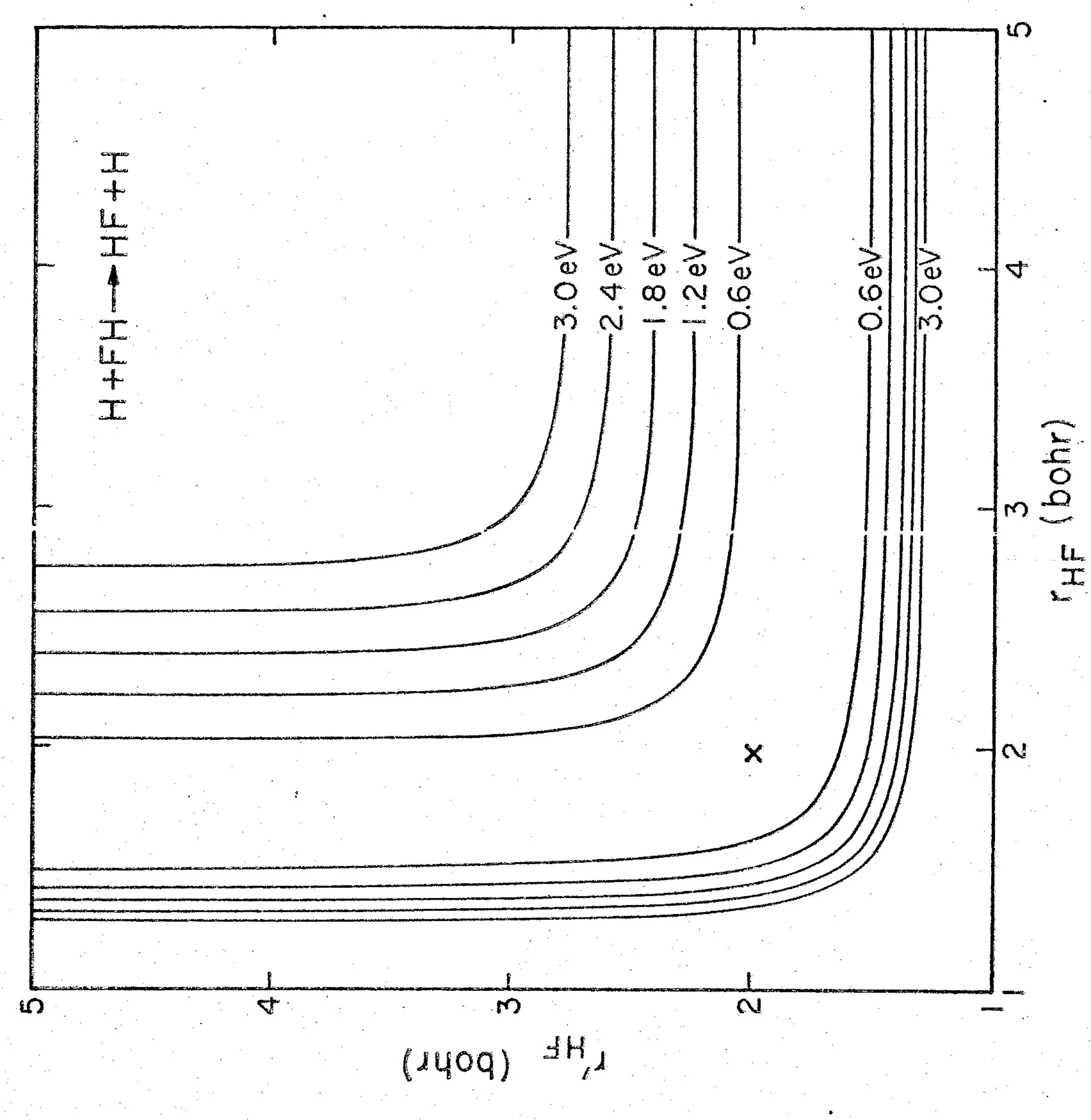
H+FH → HF+H
3.0eV
2.4eV
1.8eV
1.2eV
0.6eV
0.6eV
3.0eV
x
r_{HF} (bohr)
r'_{HF} (bohr)
1
2
3
4
5
1
2
3
4
5

Figure 1

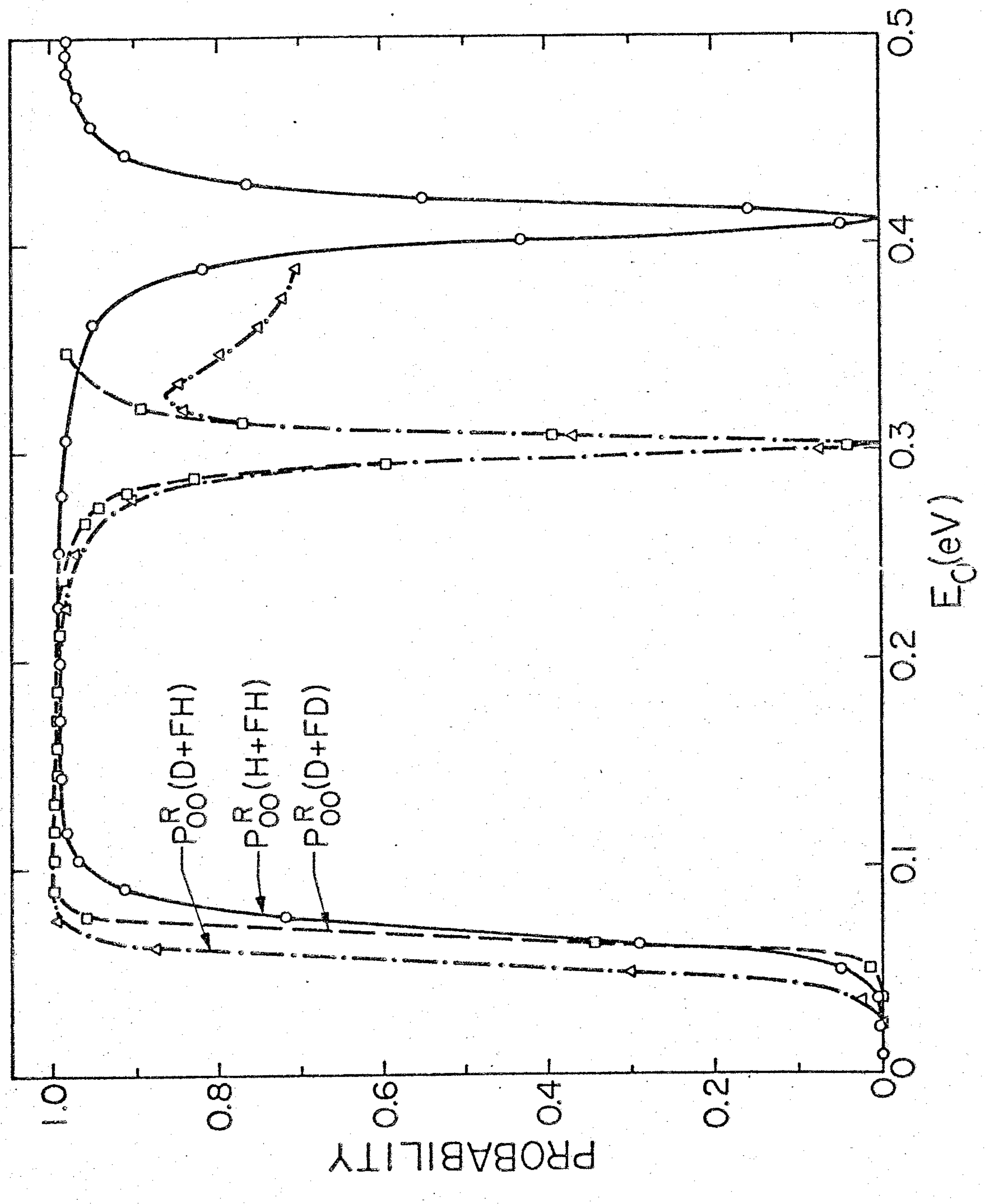
PROBABILITY
1.0
0.8
0.6
0.4
0.2
0.0
0
0.1
0.2
0.3
0.4
0.5
E_c(eV)
P^R_{00}(D+FH)
P^R_{00}(H+FH)
P^R_{00}(D+FD)

Figure 2

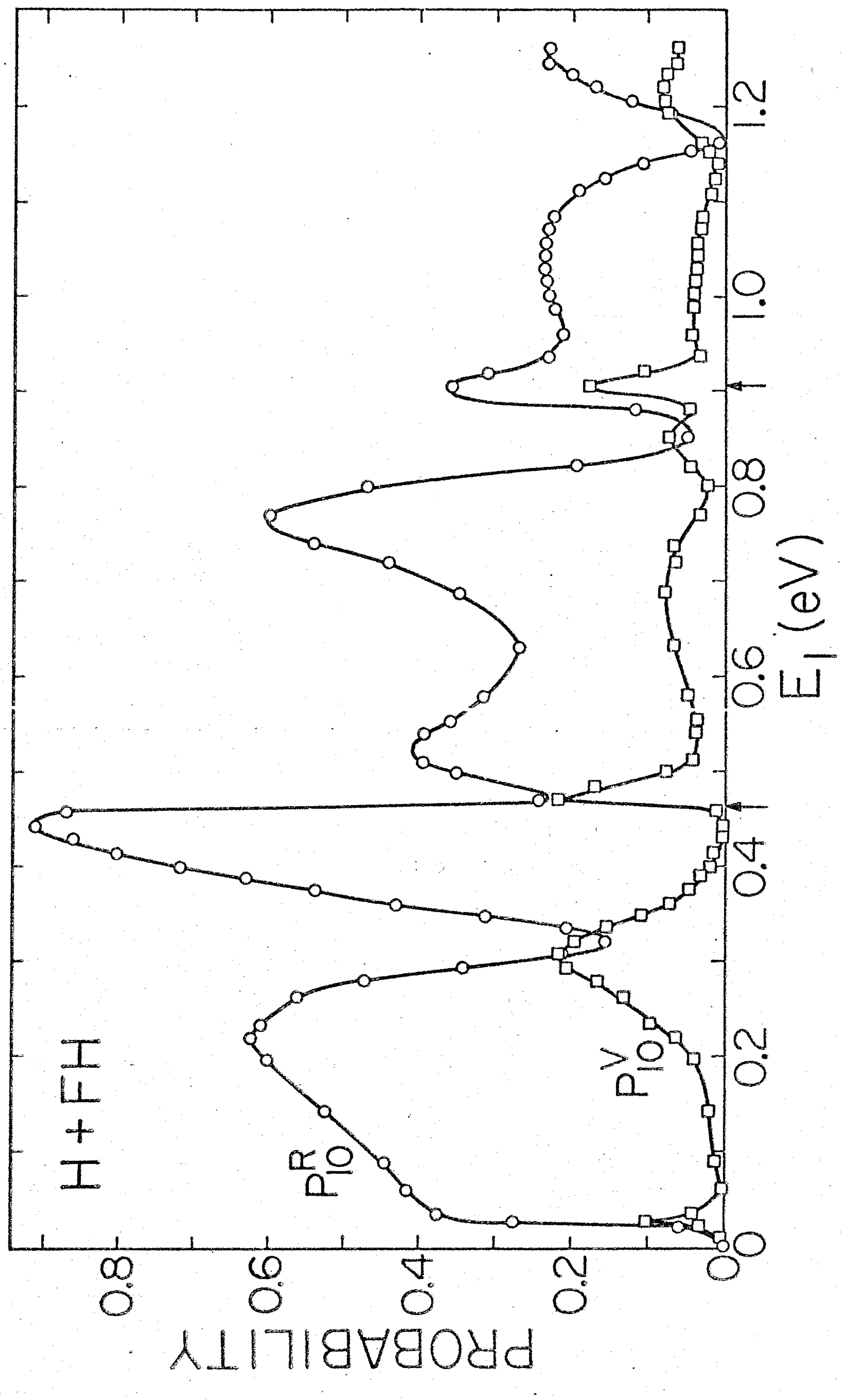

Figure 3

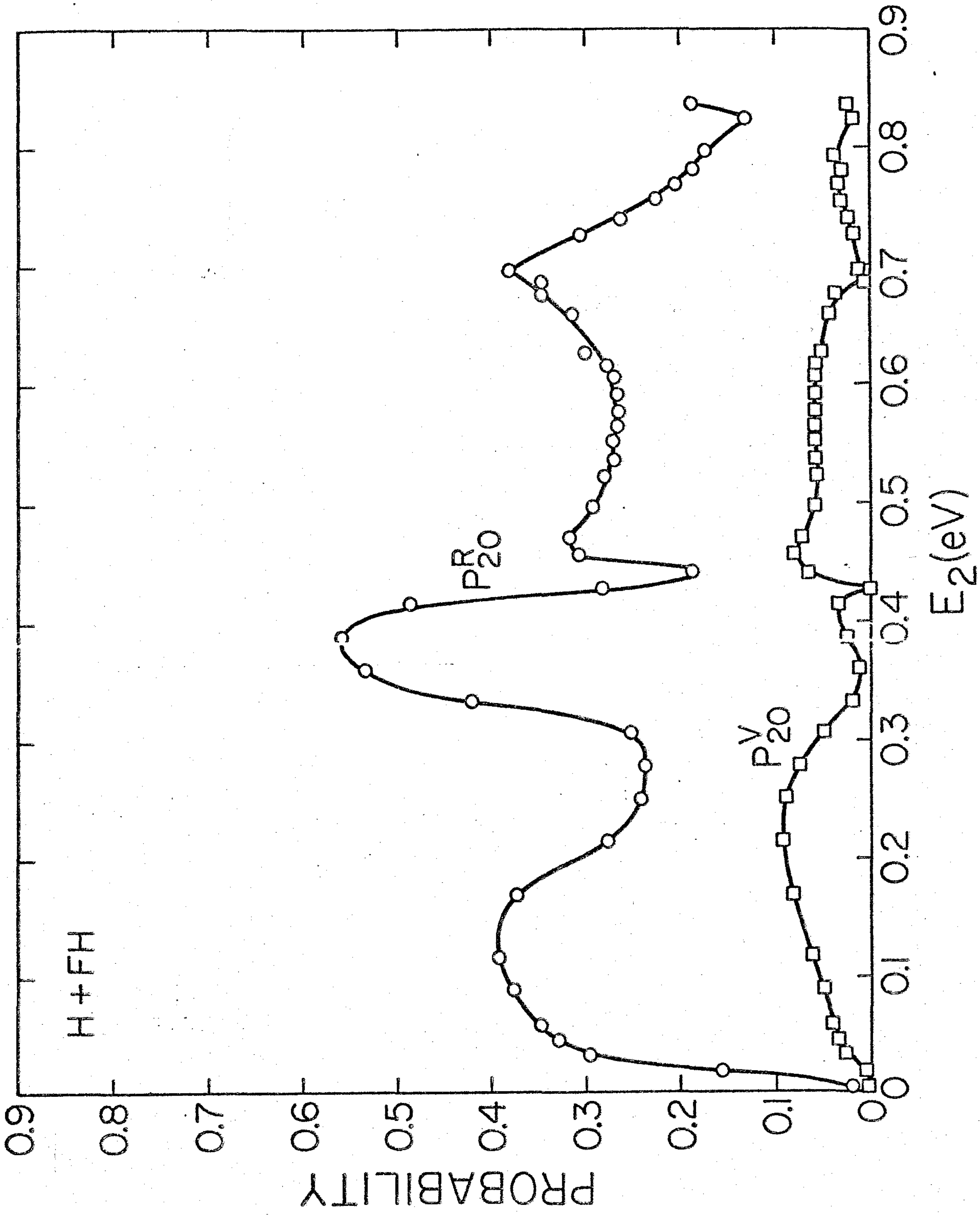
H + FH
P^R_{20}
P^V_{20}
PROBABILITY
0
0.1
0.2
0.3
0.4
0.5
0.6
0.7
0.8
0.9
E_2(eV)
0
0.1
0.2
0.3
0.4
0.5
0.6
0.7
0.8
0.9

Figure 4

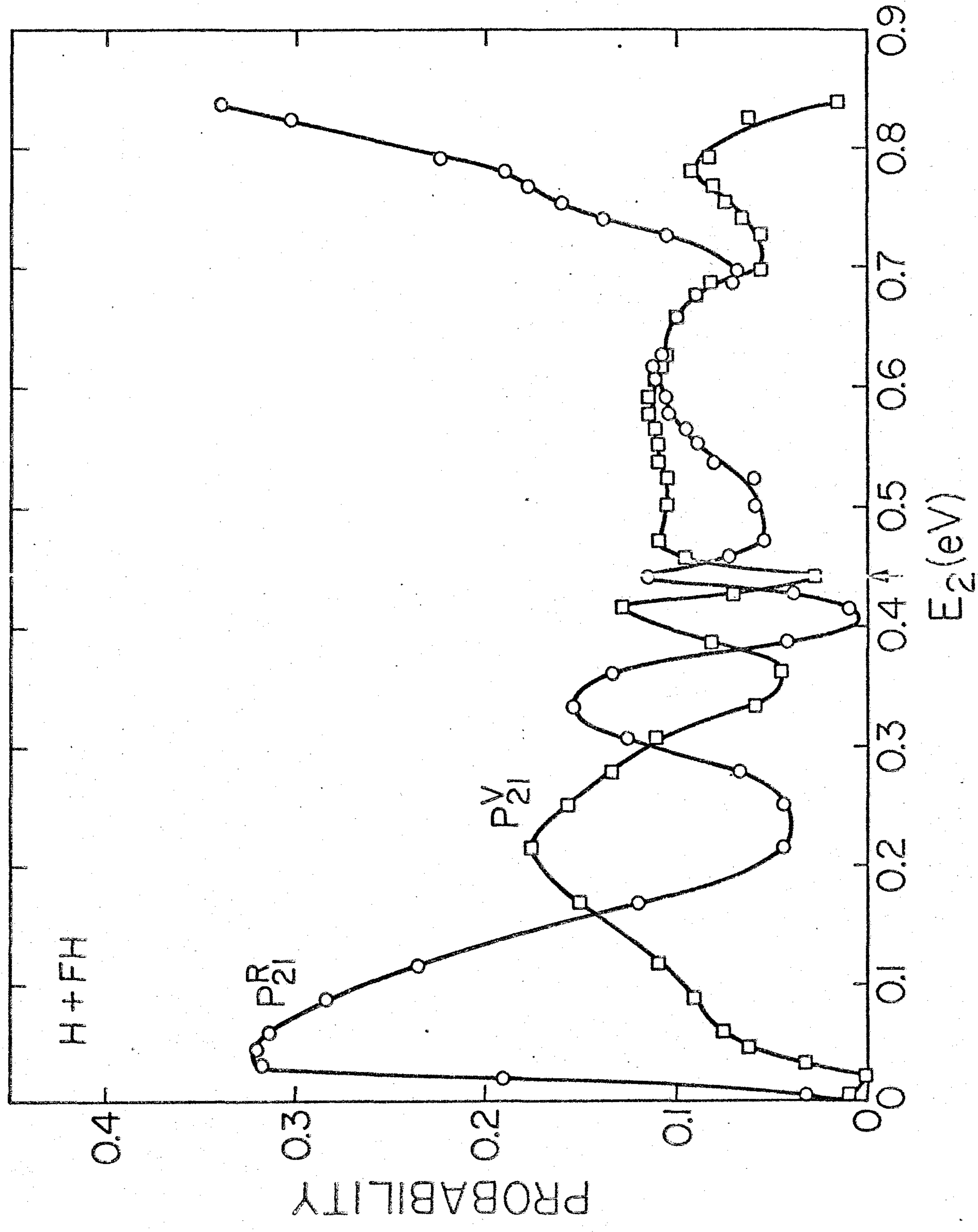
H + FH
P^R_{21}
P^V_{21}
PROBABILITY
0
0.1
0.2
0.3
0.4
E_2(eV)
0
0.1
0.2
0.3
0.4
0.5
0.6
0.7
0.8
0.9

Figure 5

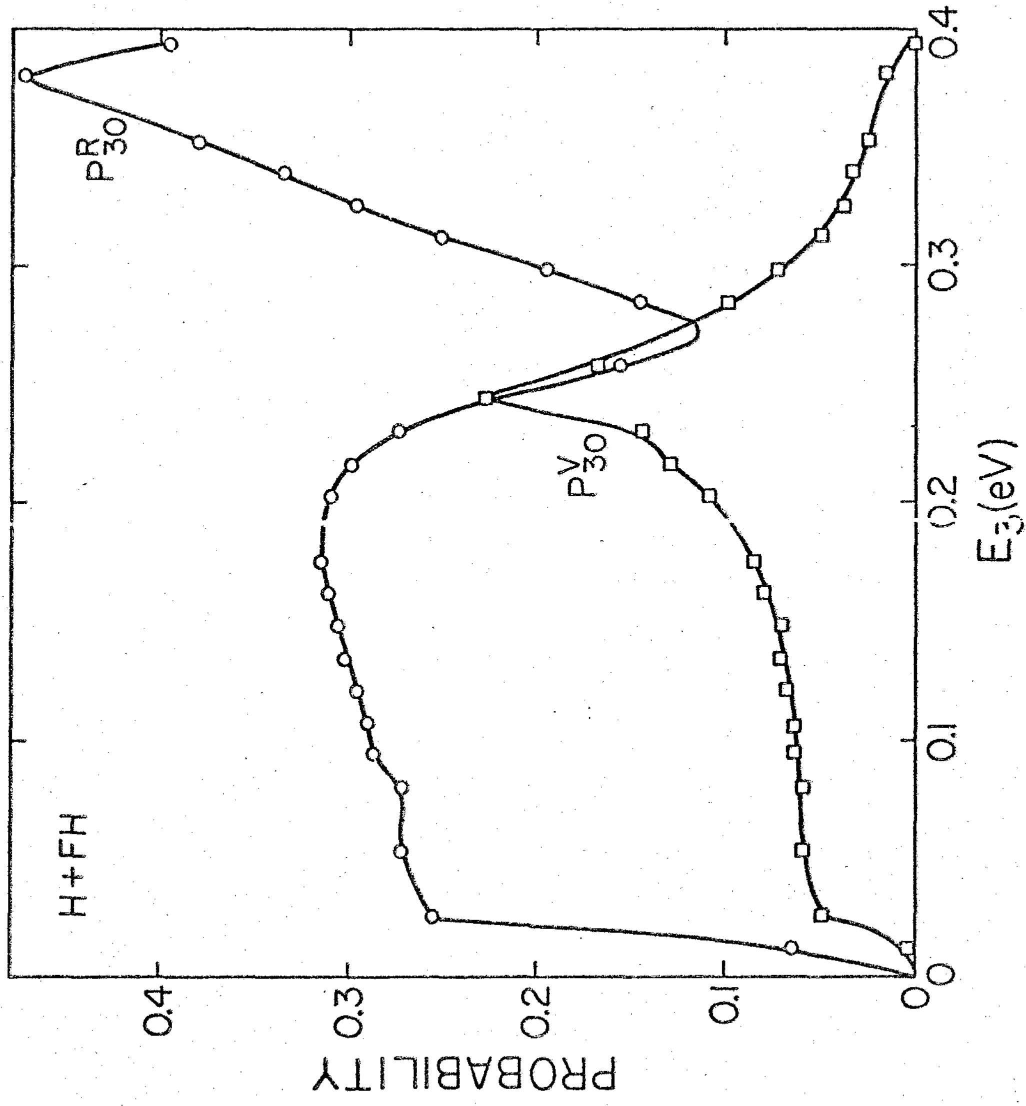

Figure 6

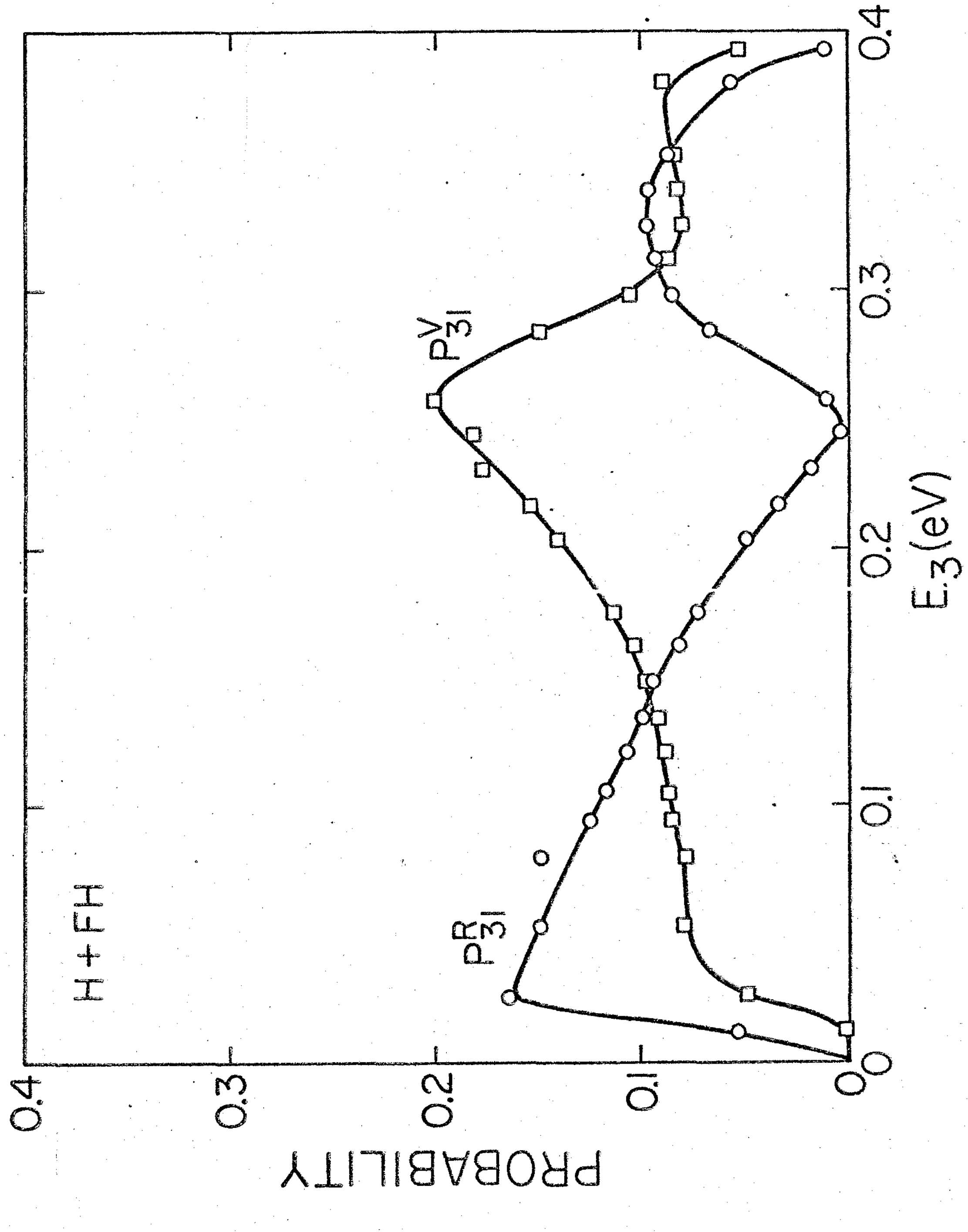

Figure 7

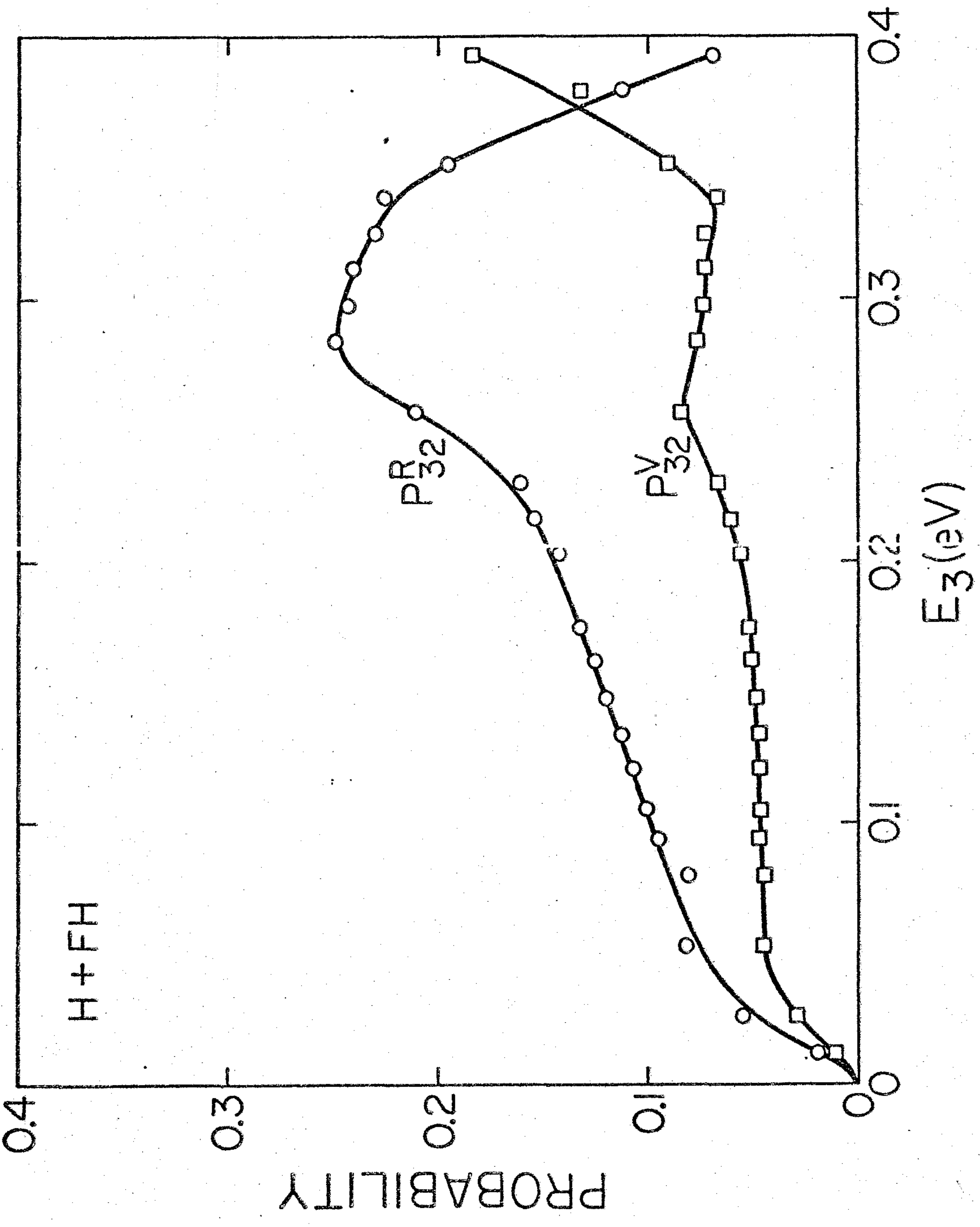

Figure 8

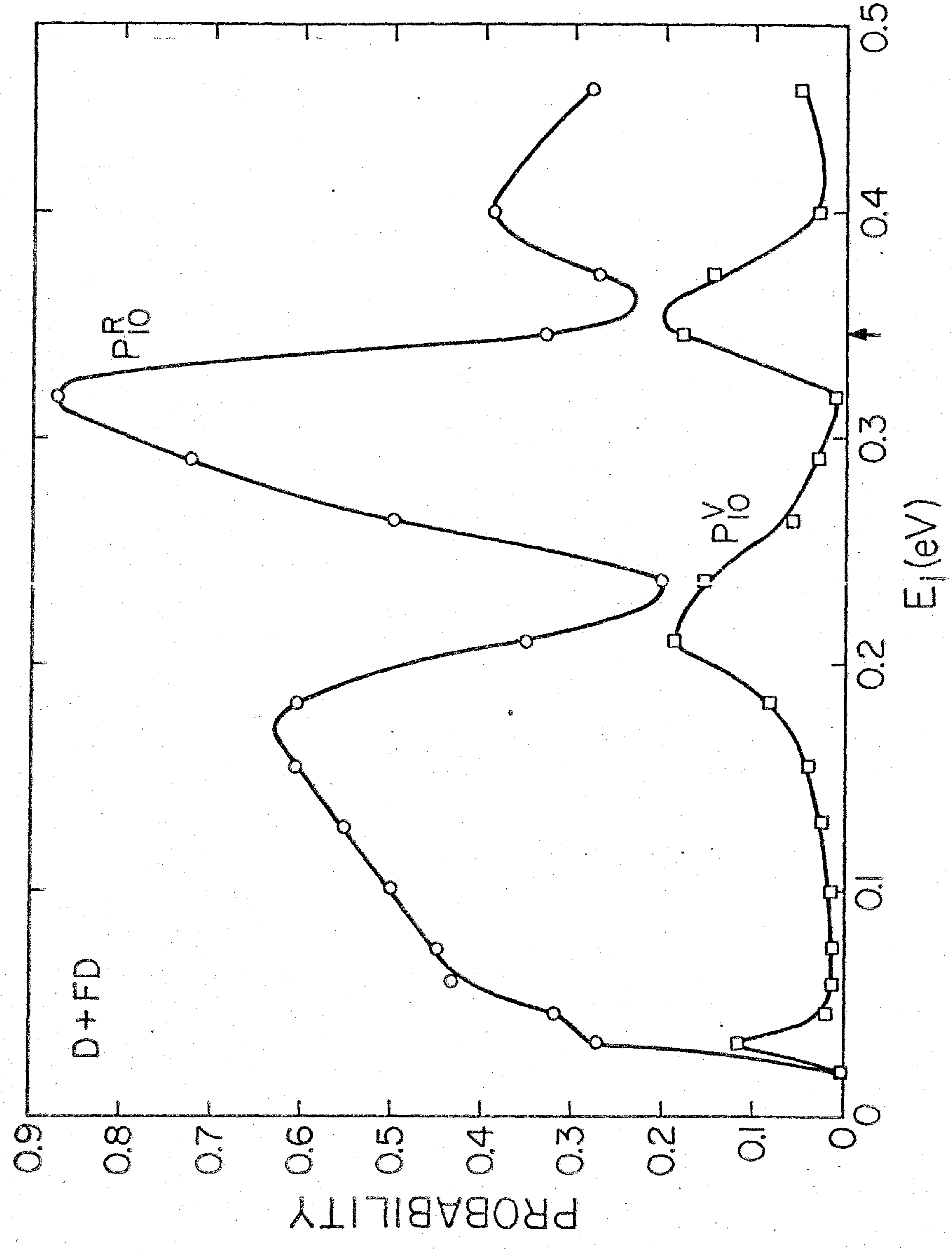
D + FD
P^R_{10}
P^V_{10}
PROBABILITY
0
0.1
0.2
0.3
0.4
0.5
0.6
0.7
0.8
0.9
E_i (eV)
0
0.1
0.2
0.3
0.4
0.5

Figure 9

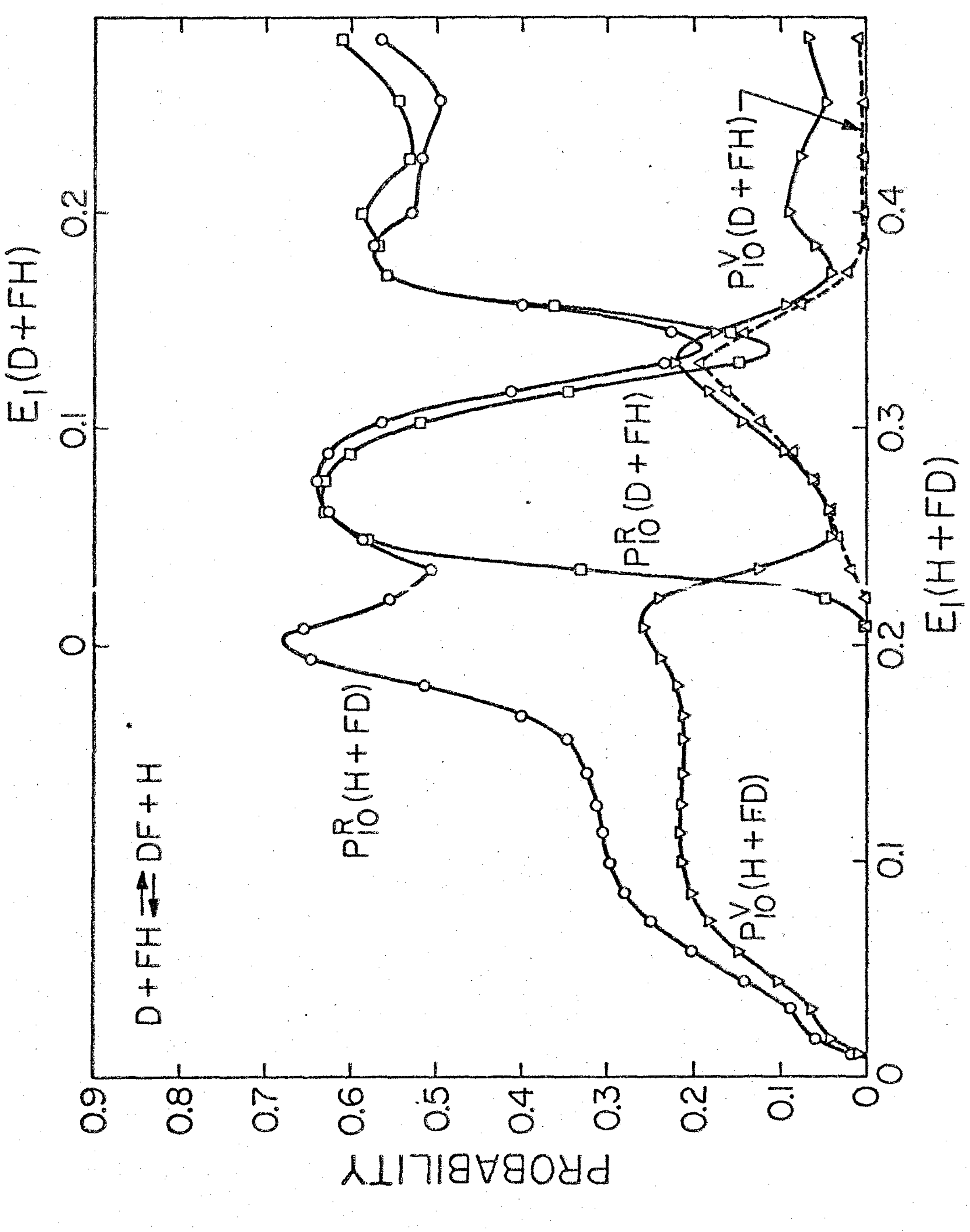
D + FH ⇌ DF + H
PROBABILITY
0
0.1
0.2
0.3
0.4
0.5
0.6
0.7
0.8
0.9
E_1(D + FH)
0
0.1
0.2
E_1(H + FD)
0
0.1
0.2
0.3
0.4
P^R_{10}(H + FD)
P^V_{10}(H + FD)
P^R_{10}(D + FH)
P^V_{10}(D + FH)

Figure 10

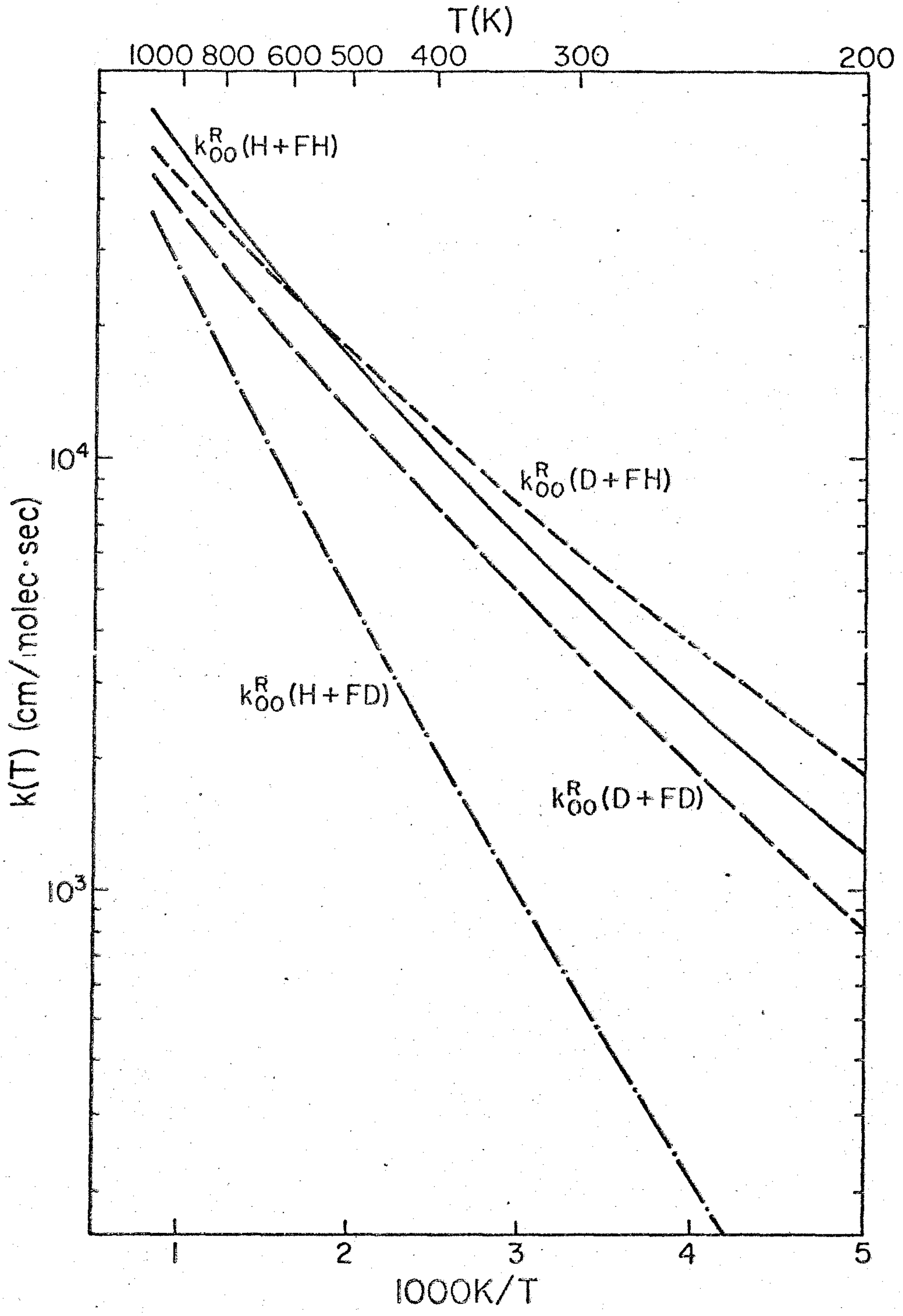
T(K)
1000
800
600
500
400
300
200
k^R_{00}(H+FH)
k^R_{00}(D+FH)
k^R_{00}(H+FD)
k^R_{00}(D+FD)
10^4
10^3
k(T) (cm/molec·sec)
1
2
3
4
5
1000K/T

Figure 11

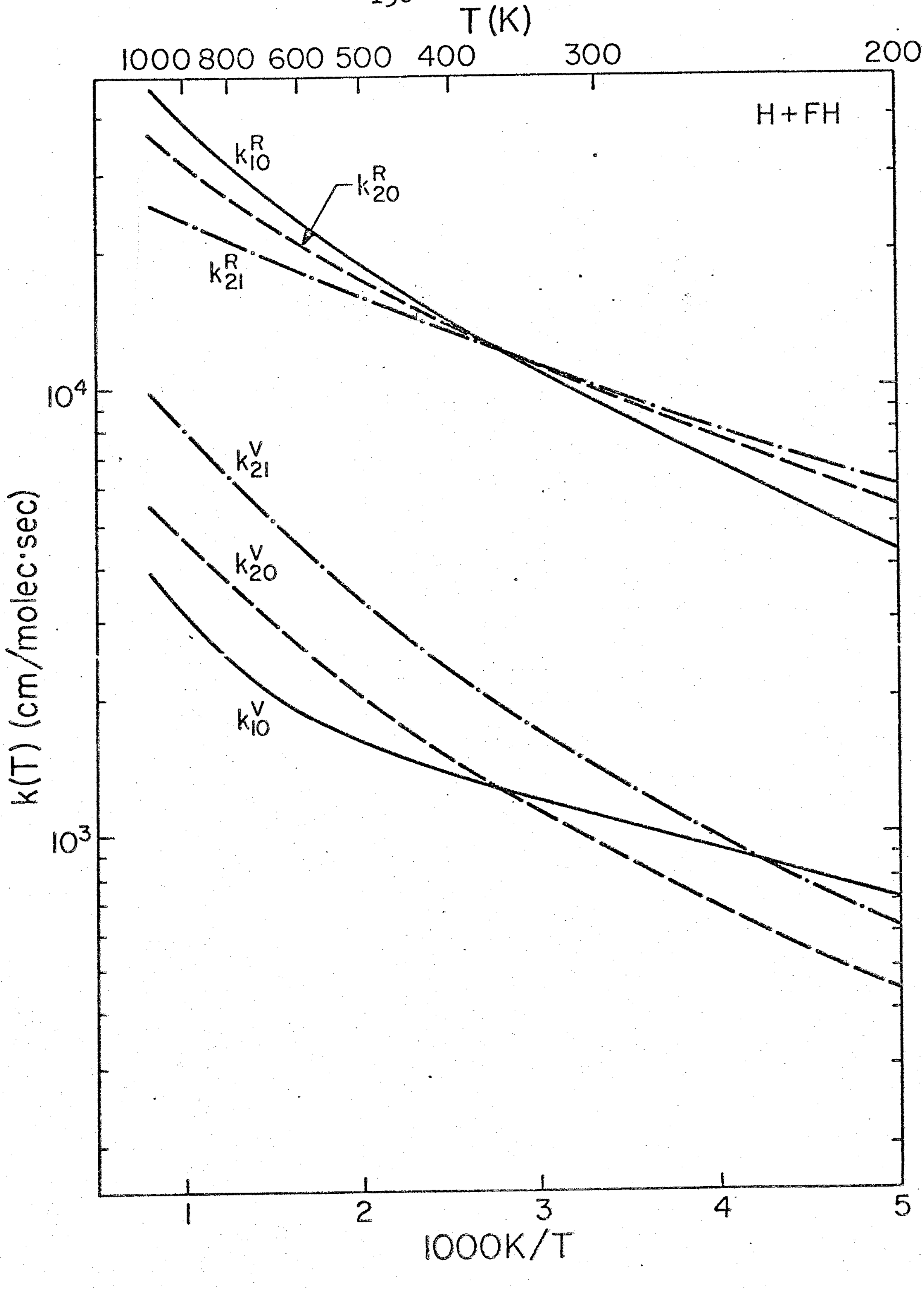
T(K)
1000
800
600
500
400
300
200
H + FH
k_{10}^R
k_{20}^R
k_{21}^R
10^4
k_{21}^V
k_{20}^V
k_{10}^V
10^3
k(T) (cm/molec·sec)
1
2
3
4
5
1000K/T

Figure 12

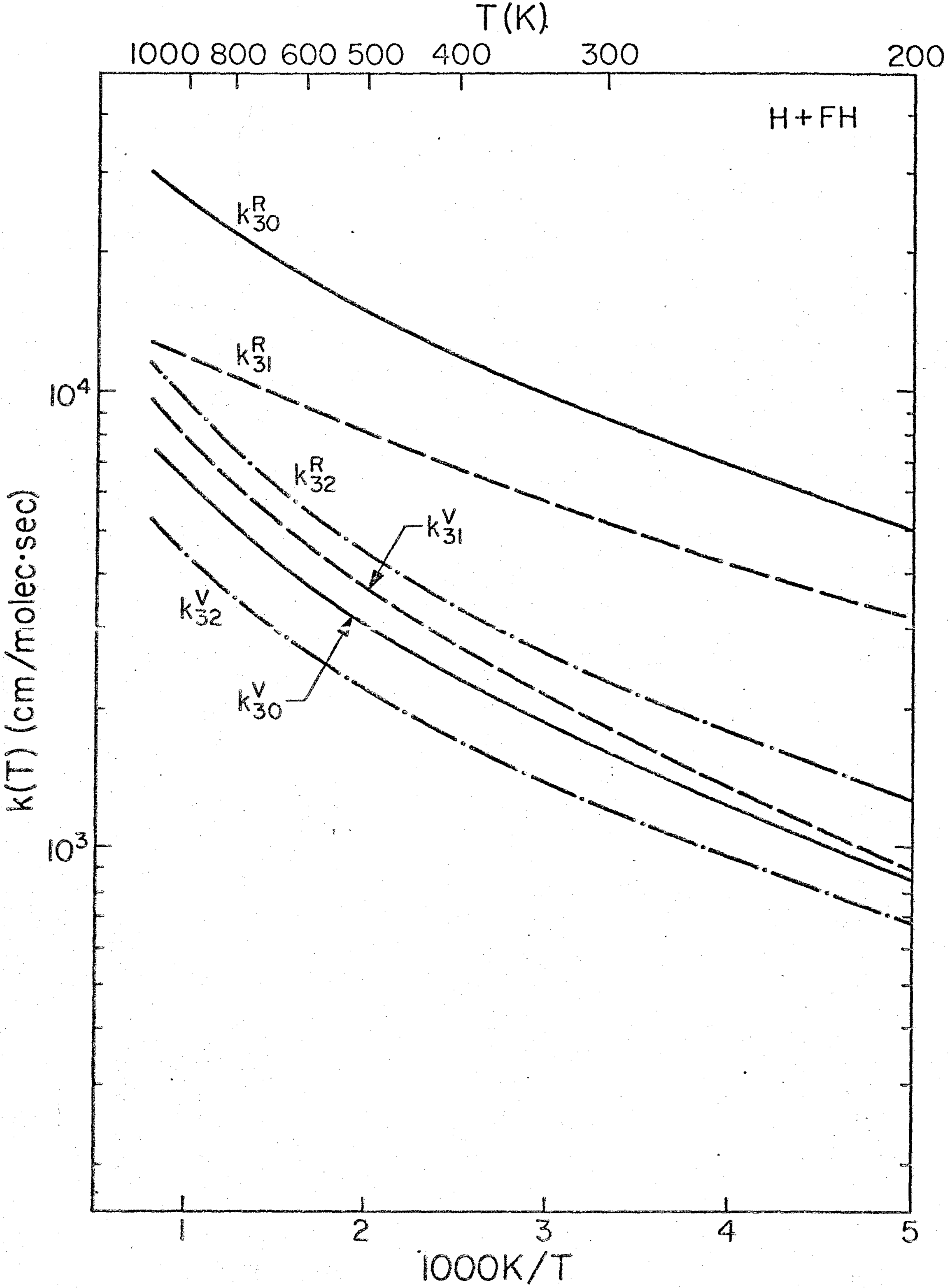
T(K)
1000
800
600
500
400
300
200
H+FH
k^R_{30}
k^R_{31}
k^R_{32}
k^V_{31}
k^V_{32}
k^V_{30}
10^4
10^3
k(T) (cm/molec·sec)
1
2
3
4
5
1000K/T

Figure 13

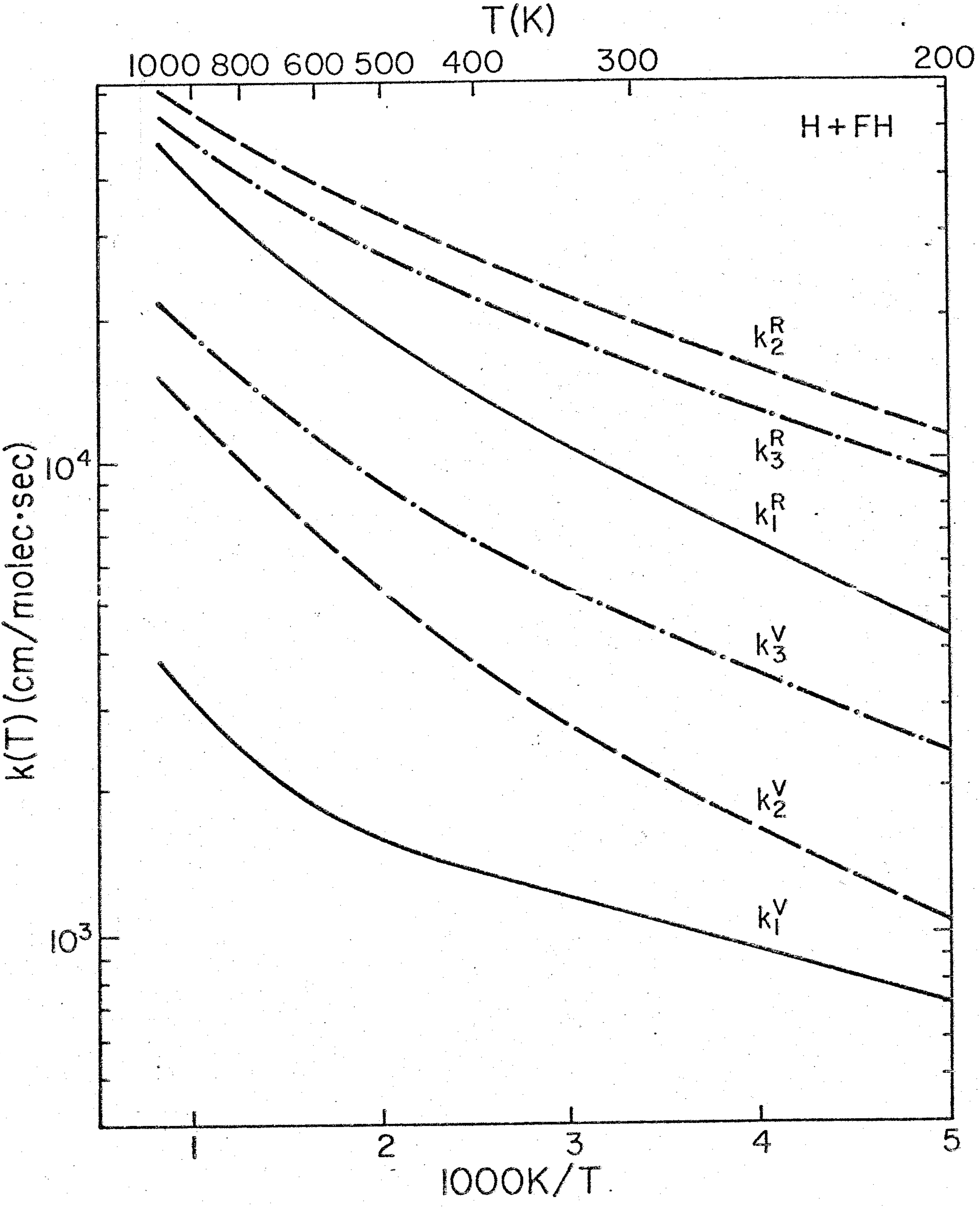
T(K)
1000
800
600
500
400
300
200
H + FH
k_2^R
k_3^R
k_1^R
k_3^V
k_2^V
k_1^V
10^4
10^3
k(T) (cm/molec·sec)
1
2
3
4
5
1000K/T

Figure 14

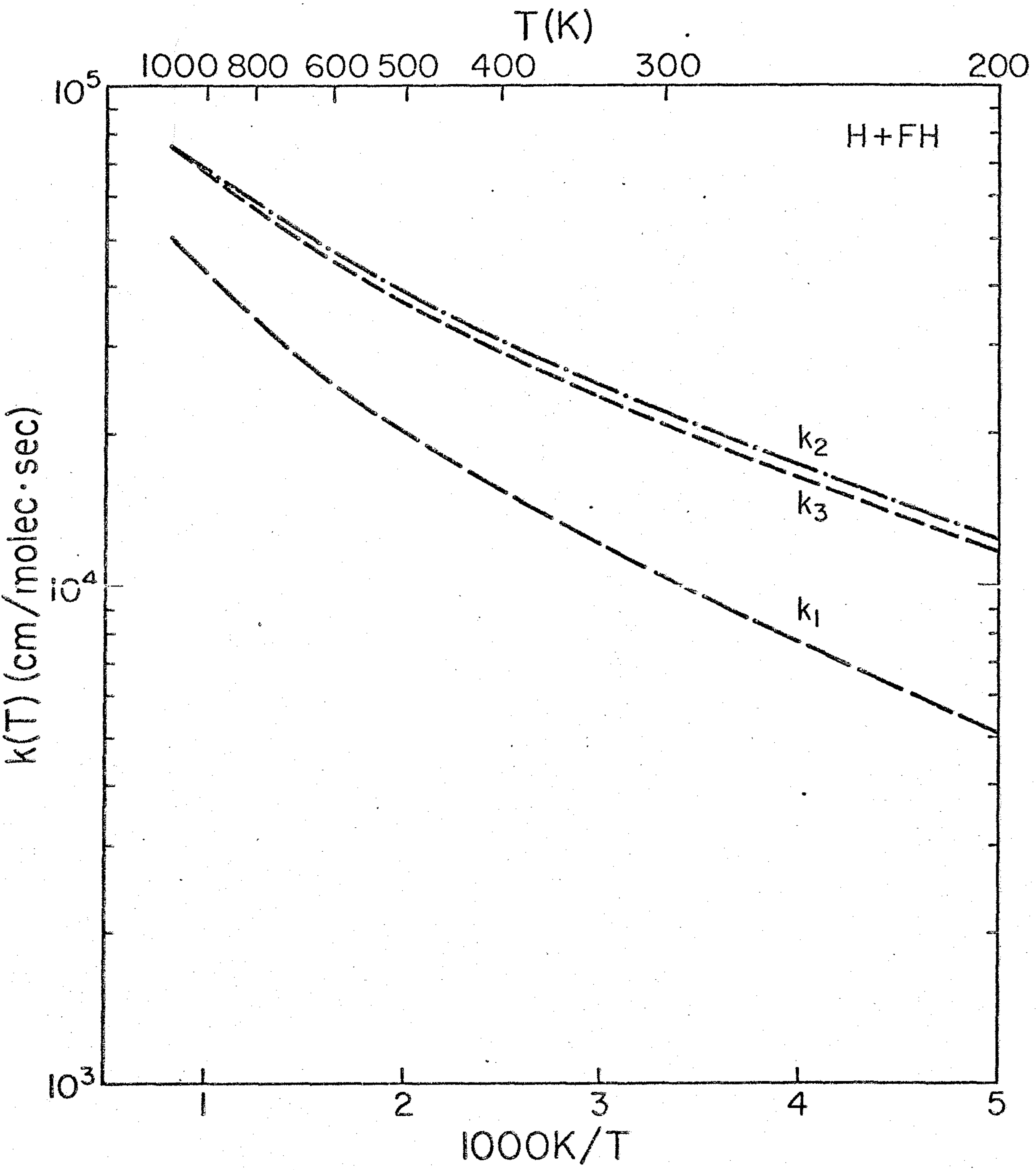
T(K)
1000
800
600
500
400
300
200
H+FH
k(T) (cm/molec·sec)
10^5
10^4
10^3
k_2
k_3
k_1
1
2
3
4
5
1000K/T

Figure 15

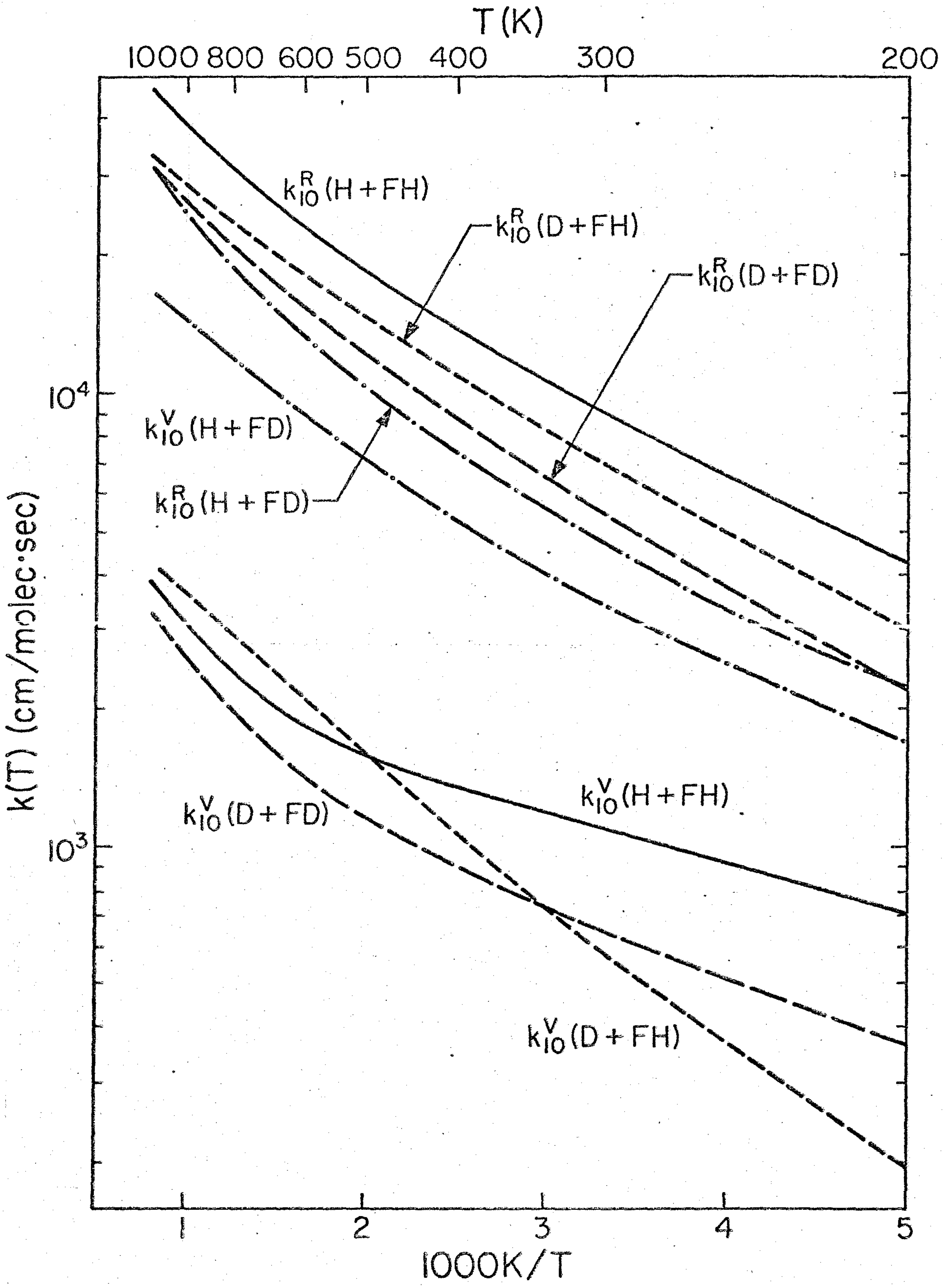
T (K)
1000
800
600
500
400
300
200
k_{10}^{R}(H + FH)
k_{10}^{R}(D + FH)
k_{10}^{R}(D + FD)
10^4
k_{10}^{V}(H + FD)
k_{10}^{R}(H + FD)
k(T) (cm/molec·sec)
k_{10}^{V}(H + FH)
k_{10}^{V}(D + FD)
10^3
k_{10}^{V}(D + FH)
1
2
3
4
5
1000K/T

Figure 16

4. QUANTUM MECHANICAL REACTIVE SCATTERING: THEORY FOR PLANAR ATOM PLUS DIATOM SYSTEMS

Quantum mechanical reactive scattering: Theory for planar atom plus diatom systems*

by A. KUPPERMANN, G. C. SCHATZ† and M. BAER‡

Arthur A. Noyes Laboratory of Chemical Physics§
California Institute of Technology, Pasadena, California 91125

(Received)

A method is presented for accurately solving the Schrödinger equation for the reactive collision of an atom with a diatomic molecule on a space fixed plane. The procedure consists primarily of two sequential steps. First, the Schrödinger equation in each of the three arrangement channel regions is transformed into a set of coupled differential equations and numerically integrated in each of these regions to generate primitive solutions. The rotational part of the vibration rotation basis functions involved is not changed from its asymptotic form during this propagation, but the vibrational eigenfunctions as well as the integration variable are changed periodically so as to follow the vibrational motions in a nearly adiabatic manner. In the second step, the primitive solutions generated in each of the three arrangement channels are smoothly matched to each other on a set of appropriately chosen matching surfaces. The resulting

solutions are then linearly combined to satisfy the proper asymptotic boundary conditions, and the scattering matrix, scattering amplitudes and cross sections are determined. Application of this procedure to the special case of the $H + H_2$ reaction is discussed in detail including simplifications arising from the additional symmetries involved, and the inclusion of effects resulting from indistinguishability of identical particles.

1. INTRODUCTION

In recent years, much interest has developed in the ab initio calculation of bimolecular reaction cross sections on realistic potential energy surfaces by accurate quantum mechanical techniques. The motivation for such calculations has been to interpret the results of crossed molecular beam experiments, to understand the effect of the relative translational energy of the reactants and of their internal state on such cross sections and on the disposal of energy among the reaction products, to elucidate the role of direct and compound state dynamical mechanisms, to test the range and degree of validity of approximate reaction models (such as the adiabatic and statistical ones), to develop new physical models of known reliability, to examine the correctness of the dynamical assumptions of transition state theory, to establish the conditions of applicability of the quasi-classical trajectory calculations and of semi-classical improvements thereof and last, but not least, to make detailed qualitative and quantitative predictions from first principles about reactions difficult to investigate experimentally.

Due in part to the lack of appropriate numerical techniques and to limitations of the memory size and computational speed and cost of present-day large computers, most of these quantum calculations so far have been performed for collinear atom-diatom reactions [1-13]. In recent years, several attempts have been made to do calculations for non-linear triatomic systems. Saxon and Light [14] and Altenberger-Siczek and Light [15] have investigated the coplanar $H + H_2$

exchange reaction by a close-coupling technique which excluded closed vibrational channels. Wolken and Karplus [16] have made a study of this same reaction in three dimensions, also ignoring closed vibrational channels. Wyatt and coworkers [17] have developed techniques which include closed vibrations in calculations on one and two reaction path atom plus diatom reactions, and Elkowitz and Wyatt [17a] have applied these methods to the three-dimensional $H + H_2$ reaction. Baer and Kouri [18] have done fully converged calculations in three dimensions on a model (one reaction path) triatomic system in which one of the atoms was assumed infinitely heavy and in which the simple potential used allowed a partially analytic treatment.

In an earlier communication [19] we presented preliminary results of the first fully converged quantum mechanical calculation for a coplanar reaction on a realistic electronically adiabatic potential energy surface, that for $H + H_2$. These results indicated that the quantitative differences between calculations in which closed vibrations are included and those for which they are not can be quite serious. In this paper, we will present a detailed description of the method used to perform such calculations. We will formulate the method for a general atom plus diatomic molecule collision on a single reactive potential energy surface using $H + H_2$ as a specific example. A detailed description of the results of our extensive calculations on coplanar $H + H_2$ will be given elsewhere [20].

The method is based on an earlier close-coupling propagation technique [5] which has been extensively applied to the collinear $H + H_2$

and F + H_2 reactions [10]. The spirit of the collinear method is to choose different variables and different pseudo vibrational basis functions for expansion of the solutions of the Schrödinger equation in different local regions of the (collinear) configuration space so as to minimize the number of terms needed for accurate convergence of the expansions. This concept is retained for the vibrational motion in our application of the method to coplanar collisions. However, the variables and basis functions describing rotational motion are not changed (and hence retain their asymptotic meanings) during the integration into the interaction region from each of the three separated arrangement channel regions of internal configuration space. As a result, an additional step is required at the completion of the integration in which the primitive solutions in each of the three arrangement channel regions are smoothly matched to each other on a set of three appropriately chosen surfaces which separate these three regions [21]. The restriction that the three atoms should be confined to a space-fixed plane was introduced for computational convenience to test out the effectiveness of the method without excessive expenditure of compution time. Extension to reactions in three-dimensional space is reasonably straightforward and has recently been implemented by Kuppermann and Schatz [22] for 3-D H + H_2 in the first fully converged quantum mechanical treatment of a chemical reaction on a realistic potential energy surface.

In Section 2 of this paper we formulate the Schrödinger equation for the problem and describe the partial wave expansion used to obtain the partial differential equations in internal configuration coordinates which must be solved. The method used to integrate these equations in the different regions of configuration space is described in Section 3, and in Section 4 we describe how we smoothly match the solutions obtained from these integrations. The asymptotic analysis is developed in Section 5 including the methods of calculating the reactance and scattering matrices, the scattering amplitudes and the cross sections. Finally, in Section 6 we describe the simplifications and changes involved in an application of the method to the $H + H_2$ exchange reaction due to the identicity of the three atoms, including a discussion of the technique of anti-symmetrizing the scattering wave function (post antisymmetrization).

2. FORMULATION OF THE PROBLEM

2.1. General considerations

We are interested in calculating cross sections for the exchange reaction A + BC in which the three atoms A, B and C are confined to remain on a space fixed plane. We assume that the Born-Oppenheimer separation approximation between the electron and nuclear motions is valid and that the resulting ground electronic state potential energy surface V is known. We further assume that all higher potential energy functions are sufficiently greater than the total energy E of the system everywhere in configuration space for us to be able to neglect their influence. This "single potential energy surface" model is applicable to a high degree of accuracy to many triatomic reactions. We also assume that E is sufficiently low for the existence and effect of break-up collisions of the type A + BC → A + B + C to be negligible. Finally we assume that the interactions between the nuclear spin and nuclear orbital angular momenta are negligible.

Let $\underset{\sim}{r}_A$, $\underset{\sim}{r}_B$ and $\underset{\sim}{r}_C$ be the position vectors of nuclei A, B and C, respectively, with respect to their center of mass. We wish to obtain a solution to the time independent Schrödinger equation for the motion of the nuclei which satisfies the following three conditions:

(a) In configuration space $\underset{\sim}{r}_A$, $\underset{\sim}{r}_B$, $\underset{\sim}{r}_C$ it is everywhere single valued and continuous and has gradients which are everywhere continuous (except at points where two of the three atoms coincide).

(b) It is antisymmetric (symmetric) with respect to exchange of the space and spin coordinates of any two identical nuclei of half odd-integral (integral) nuclear spin.

(c) It satisfies the asymptotic conditions describing the collision phenomenon under consideration, i.e., the collision of A and BC with a given relative kinetic energy and a given initial internal quantum state of BC, to produce receding product A + BC, AB + C, or AC + B in all possible internal states of the diatom compatible with the total energy of the system.

If we can find a sufficient number of independent solutions satisfying condition (a), it is possible to obtain linear combinations of them which, in addition, satisfy conditions (b) (by post-antisymmetrization methods [23]) and (c) (by reactance or scattering matrix analysis techniques [24]).

2.2. The Schrödinger equation

Let $\underset{\sim}{\bar{R}}_{\alpha}$ be the position vector of A with respect to the center of mass of BC and $\underset{\sim}{\bar{r}}_{\alpha}$ the position vector of C with respect to B, as indicated in Fig. 1. As $\bar{R}_{\alpha} \rightarrow \infty$ with $\bar{r}_{\alpha}$ finite, we denote the corresponding configuration as arrangement channel $\alpha \equiv (A, BC)$. Let $(\bar{r}_{\alpha}, \theta_{\alpha})$ and $(\bar{R}_{\alpha}, \chi_{\alpha})$ be respectively the planar polar coordinates of $\underset{\sim}{\bar{r}}_{\alpha}$ and $\underset{\sim}{\bar{R}}_{\alpha}$ with respect to a fixed system of reference attached to the plane (all angles being measured from the x axis of Fig. 1). The reduced mass associated to the motion of B with respect to C is denoted $\mu_{\beta\gamma}$ and that associated to atom A with respect to molecule BC is $\mu_{\alpha,\beta\gamma}$. We define analogous vectors $\underset{\sim}{\bar{r}}_{\beta}$, $\underset{\sim}{\bar{R}}_{\beta}$ and $\underset{\sim}{\bar{r}}_{\gamma}$, $\underset{\sim}{\bar{R}}_{\gamma}$ (Fig. 1) and associated coordinates and reduced masses so that as $\bar{R}_{\beta} \rightarrow \infty$ or $\bar{R}_{\gamma} \rightarrow \infty$ with $\bar{r}_{\beta}$ or $\bar{r}_{\gamma}$ finite, we obtain the arrangement channels $\beta \equiv (B, CA)$ and $\gamma \equiv (C, AB)$, respectively. Note that the directions of vectors in Fig. 1 are defined in a cyclic manner in the indices $\alpha\beta\gamma$. Finally, let $\lambda\nu\kappa$ represent any one of the three possible cyclic permutations $\alpha\beta\gamma$, $\beta\gamma\alpha$ and $\gamma\alpha\beta$.

In the system of coordinates characterized by index λ $(= \alpha, \beta \text{ or } \gamma)$, the Schrödinger equation describing the internal motion of the three particle system is

$$\left\{-\frac{\hbar^2}{2\mu_{\nu\kappa}}\left(\frac{1}{\bar{r}_\lambda}\frac{\partial}{\partial\bar{r}_\lambda}\bar{r}_\lambda\frac{\partial}{\partial\bar{r}_\lambda}+\frac{1}{\bar{r}_\lambda^2}\frac{\partial^2}{\partial\theta_\lambda}\right)\right.$$

$$-\frac{\hbar^2}{2\mu_{\lambda,\nu\kappa}}\left(\frac{1}{\bar{R}_\lambda}\frac{\partial}{\partial\bar{R}_\lambda}\bar{R}_\lambda\frac{\partial}{\partial\bar{R}_\lambda}+\frac{1}{\bar{R}_\lambda^2}\frac{\partial^2}{\partial\chi_\lambda^2}\right)$$

$$\left.+\,V^\lambda(\bar{r}_\lambda,\bar{R}_\lambda,\gamma_\lambda)-E\right\}\Psi^\lambda(\bar{r}_\lambda,\bar{R}_\lambda,\theta_\lambda,\chi_\lambda)=0 \qquad (2.1)$$

where V^λ is the potential energy function of the system expressed in λ coordinates and E its total energy. γ_λ is by definition the angle in the range $-\pi/2 \leq \gamma_\lambda \leq 3\pi/2$ equal to $\theta_\lambda - \chi_\lambda$ modulo 2π, and is related to the angle between $\underset{\sim}{\bar{R}}_\lambda$ and $\underset{\sim}{\bar{r}}_\lambda$ [25]. In the absence of external fields, the potential function depends only on the internal variables R_λ, r_λ, γ_λ and satisfies the relation $V^\lambda(\bar{R}_\lambda, \bar{r}_\lambda, \gamma_\lambda) = V^\lambda(\bar{R}_\lambda, \bar{r}_\lambda, 2\pi - \gamma_\lambda)$.

Let us now introduce a set of coordinates used previously by Delves [26] and by Jepsen and Hirschfelder [27]. They have the advantage of leading to an equation containing an effective mass independent of the arrangement channel λ, which simplifies many of the equations presented below. These coordinates are:

$$\underset{\sim}{r}_\lambda = a_\lambda^{-1}\,\underset{\sim}{\bar{r}}_\lambda \qquad (2.2a)$$

$$\underset{\sim}{R}_\lambda = a_\lambda\,\underset{\sim}{\bar{R}}_\lambda \qquad (2.2b)$$

where a_λ is a dimensionless scaling constant defined by

$$a_\lambda = (\mu_{\lambda,\nu\kappa}/\mu_{\nu\kappa})^{\frac{1}{4}} \tag{2.3}$$

Substitution into Eq. 2.1 leads to:

$$\left\{-\frac{\hbar^2}{2\mu}\left[\frac{1}{r_\lambda}\frac{\partial}{\partial r_\lambda}r_\lambda\frac{\partial}{\partial r_\lambda}+\frac{1}{r_\lambda^2}\frac{\partial^2}{\partial\theta_\lambda^2}+\frac{1}{R_\lambda}\frac{\partial}{\partial R_\lambda}R_\lambda\frac{\partial}{\partial R_\lambda}+\frac{1}{R_\lambda^2}\frac{\partial^2}{\partial\chi_\lambda^2}\right]\right.$$

$$\left.+\, V^\lambda(r_\lambda,R_\lambda,\gamma_\lambda) - E\right\}\Psi^\gamma(r_\lambda,R_\lambda,\theta_\lambda,\chi_\lambda) = 0 \tag{2.4}$$

where the circular polar angles of $\underset{\sim}{R}_\lambda$, $\underset{\sim}{r}_\lambda$ are the same as those of $\bar{\underset{\sim}{R}}_\lambda$, $\bar{\underset{\sim}{r}}_\lambda$, and μ is the effective mass alluded to above and defined by

$$\mu = (\mu_{\nu\kappa}\,\mu_{\lambda,\nu\kappa})^{\frac{1}{2}} = (m_\alpha m_\beta m_\gamma/M)^{\frac{1}{2}} \tag{2.5}$$

where

$$M = m_\alpha + m_\beta + m_\gamma$$

is the total mass of the system and m_α, m_β, and m_γ are the masses of atoms A, B and C respectively. We now change from the angular variables θ_λ, χ_λ to γ_λ, χ_λ, obtaining the following expression from Eq. 2.5:

$$\left\{-\frac{\hbar^2}{2\mu}\left[\frac{1}{r_\lambda}\frac{\partial}{\partial r_\lambda}r_\lambda\frac{\partial}{\partial r_\lambda}+\frac{1}{r_\lambda^2}\frac{\partial^2}{\partial\gamma_\lambda^2}+\frac{1}{R_\lambda}\frac{\partial}{\partial R_\lambda}R_\lambda\frac{\partial}{\partial R_\lambda}\right.\right.$$

$$\left.+\frac{1}{R_\lambda^2}\left(\frac{\partial^2}{\partial\chi_\lambda^2}-2\frac{\partial^2}{\partial\chi_\lambda\partial\gamma_\lambda}+\frac{\partial^2}{\partial\gamma_\lambda^2}\right)\right]+V^\lambda(r_\lambda,R_\lambda,\gamma_\gamma)$$

$$\left.-\,E\right\}\Psi^\lambda(r_\lambda,R_\lambda,\gamma_\lambda,\chi_\lambda) = 0\,. \tag{2.6}$$

This is called the body-fixed Schrödinger equation because γ_λ is the angle of $\underset{\wedge}{r}_\lambda$ with respect to $\underset{\wedge}{R}_\lambda$, and $\underset{\wedge}{r}_\lambda$ is attached to the triatom instead of to the laboratory fixed x axis. Similarly, $R_\lambda, \chi_\lambda, r_\lambda, \gamma_\lambda$ are called the body-fixed λ coordinates. The independence of V^λ on χ in the above equation introduces very convenient simplifications as is shown in the next section.

2.3. Partial Wave Expansion

The total angular momentum $\underset{\wedge}{J}$ of the triatomic system (with respect to its center of mass) is a constant of the motion which commutes with the Hamiltonian H. The solution of the Schrödinger equation we are seeking, satisfying conditions (a), (b), and (c) above, is not an eigenfunction of $\underset{\wedge}{J}$ [28]. It is however convenient to perform the coplanar analog of partial wave analysis by expanding Ψ^λ in terms of the simultaneous eigenfunctions Ψ_J^λ of H and $\underset{\wedge}{J}$.

In the system of coordinates $r_\lambda, R_\lambda, \theta_\lambda, \chi_\lambda$ the operator $\underset{\wedge}{J}$ is given by

$$\underset{\wedge}{J} = \left[\frac{\hbar}{i}\left(\frac{\partial}{\partial \chi_\lambda}\right)_{\theta_\lambda} + \frac{\hbar}{i}\left(\frac{\partial}{\partial \theta_\lambda}\right)_{\chi_\lambda}\right] \underset{\wedge}{\hat{z}} \qquad (2.7)$$

$$\lambda = \alpha, \beta, \gamma$$

where $\underset{\wedge}{\hat{z}}$ is the unit vector perpendicular to the fixed plane of motion of the three particles. We recognize from Eq. 2.7 that $\underset{\wedge}{J}$ is the <u>algebraic</u> sum of the rotational angular momentum $\underset{\wedge}{j}_\lambda = \frac{\hbar}{i}\left(\frac{\partial}{\partial \theta_\lambda}\right)_{\chi_\lambda} \hat{z}$ and the orbital angular momentum $\underset{\wedge}{\ell}_\lambda = \frac{\hbar}{i}\left(\frac{\partial}{\partial \chi_\lambda}\right)_{\theta_\lambda} \hat{z}$.

Transforming $\underset{\wedge}{J}$ to the angular variables $\chi_\lambda, \gamma_\lambda$, we get

$$\underset{\sim}{J} = \frac{\hbar}{i}\left(\frac{\partial}{\partial \chi_\lambda}\right)_{\gamma_\lambda} \hat{z} \qquad \lambda = \alpha, \beta, \gamma \tag{2.8}$$

which may be physically interpreted as indicating that if γ_λ is maintained constant, a variation of the angular coordinate χ_λ of $\underset{\sim}{R}_\lambda$ produces a rotation of the entire triatomic system.

The orthonormal eigenfunctions of $\underset{\sim}{J}$ are given by [29]

$$\varphi_J(\chi_\lambda) = (2\pi)^{-\frac{1}{2}} \exp i J \chi_\lambda \qquad J = 0, \pm 1, \pm 2, \ldots \tag{2.9}$$

The simultaneous eigenfunctions of H with energy E and of $\underset{\sim}{J}$ with total angular momentum $J\hbar$ are of the form

$$\Psi_J^\lambda(r_\lambda, R_\lambda, \gamma_\lambda, \chi_\lambda) = \varphi_J(\chi_\lambda)\, \psi_J^\lambda(r_\lambda, R_\lambda, \gamma_\lambda) \tag{2.10}$$

where

$$\Big\{ -\frac{\hbar}{2\mu}\Big[\frac{1}{r_\lambda}\frac{\partial}{\partial r_\lambda} r_\lambda \frac{\partial}{\partial r_\lambda} + \frac{1}{r_\lambda^2}\frac{\partial^2}{\partial \gamma_\lambda^2} + \frac{1}{R_\lambda}\frac{\partial}{\partial R_\lambda} R_\lambda \frac{\partial}{\partial R_\lambda}$$
$$+ \frac{1}{R_\lambda^2}\Big(-J^2 - 2iJ\frac{\partial}{\partial \gamma_\lambda} + \frac{\partial^2}{\partial \gamma_\lambda^2}\Big)\Big] + V^\lambda(r_\lambda, R_\lambda, \gamma_\lambda)$$
$$- E\Big\}\, \psi_J^\lambda(r_\lambda, R_\lambda, \gamma_\lambda) = 0 . \tag{2.11}$$

Any solution Ψ^λ of the Schrödinger equation, which is not necessarily an eigenfunction of $\underset{\sim}{J}$ can be written as

$$\Psi^\lambda(r_\lambda, R_\lambda, \gamma_\lambda, \chi_\lambda) = \sum_{J=-\infty}^{\infty} a_J^\lambda\, \Psi_J^\lambda(r_\lambda, R_\lambda, \gamma_\lambda, \chi_\lambda) . \tag{2.12}$$

The constant coefficients a_J^λ appropriate for the problem being considered will be determined by the asymptotic conditions specified in requirement (c) of Section 2.1 and will be discussed in Section 5.2.

We now simplify Eq. 2.11 by defining a new function F_J^λ by

$$F_J^\lambda (r_\lambda, R_\lambda, \gamma_\lambda) = (r_\lambda R_\lambda)^{-\frac{1}{2}} \psi_J (r_\lambda, R_\lambda, \gamma_\lambda). \qquad (2.13)$$

Substituting this into Eq. 2.11, we obtain

$$\left\{ -\frac{\hbar^2}{2\mu} \left[\frac{\partial^2}{\partial r_\lambda^2} + \frac{\partial^2}{\partial R_\lambda^2} + \frac{1}{r_\lambda^2} \frac{\partial^2}{\partial \gamma_\lambda^2} + \frac{1}{R_\lambda^2} \left(-J^2 - 2iJ \frac{\partial}{\partial \gamma_\lambda} + \frac{\partial^2}{\partial \gamma_\lambda^2} \right) \right] \right.$$

$$\left. + V^\lambda - E \right\} F_J^\lambda (r_\lambda, R_\lambda, \gamma_\lambda) = 0 . \qquad (2.14)$$

This equation is solved numerically by the method described in Sections 3 and 4.

3. INTEGRATION OF THE SCHRÖDINGER EQUATION

3.1. The partitioning of configuration space into arrangement channel regions

We now wish to expand $F_J^\lambda (r_\lambda, R_\lambda, \gamma_\lambda)$ in terms of sets of two variable internal state basis functions in order to reduce the partial differential Eq. 2.12 to a system of coupled ordinary differential equations. Our choice for the internal state basis functions and the corresponding variables will be different in different regions of the three-dimensional internal configuration space $r_\lambda, R_\lambda, \gamma_\lambda$ and will be largely determined by the local shape of the potential energy function $V^\lambda (r_\lambda, R_\lambda, \gamma_\lambda)$. This is done in order to represent solutions to the full Schrödinger equation in an efficient manner in all regions of configuration space so as to reduce computation time as much as possible. A useful conceptualization of the nature of the problem can be gained by noting the appearance of the potential energy function $V^\lambda (r_\lambda, R_\lambda, \gamma_\lambda)$. This function is most conveniently displayed with the aid of a mapping procedure previously developed for this purpose [30]. In this mapping we consider a space $OX_\lambda Y_\lambda Z_\lambda$ in which a point $\underline{P}$ has spherical polar coordinates $\zeta, \omega_\lambda, \gamma_\lambda$ where the radial variable ζ is defined by

$$\zeta = (r_\lambda^2 + R_\lambda^2)^{\frac{1}{2}} \tag{3.1a}$$

and is independent of λ as shown in Eq. A.6 of Appendix A, and the polar angle ω_λ is defined by

$$\omega_\lambda = 2 \tan^{-1} (r_\lambda / R_\lambda); \; 0 \le \omega_\lambda \le \pi \quad . \tag{3.1b}$$

The azimuthal angle γ_λ has been defined after Eq. 2.1. Using the example of the $H + H_2$ reaction, the resulting contour plot of the Porter Karplus [31] potential for six different values of γ_λ is depicted in Fig. 2. This representation has the advantage of treating all three arrangement channels equivalently in that a change from coordinates λ to coordinates ν produces a clockwise rotation without distortion of Fig. 2 around the OY_λ axis by an angle of 120° [27]. We see from the Figure that the accessible areas of configuration space are in the form of three tube-like regions whose mutual intersection defines the three particle interaction region. For less symmetric potentials

Fig. 2 would be less symmetric, but the considerations below have general validity.

Our approach for solving the Schrödinger equation consists of dividing the configuration space depicted in Fig. 2 into three subspaces called <u>arrangement channel regions</u> and labelled by the indices λ, ν, κ. Each of these three arrangement channel regions includes one of the three tubes corresponding to a separated atom plus diatom, along with that part of the interaction region which retains the "general appearance" of that particular tube. For the $H + H_2$ system, a very natural separation of the three arrangement channel regions is obtained by the use of the three half planes $\pi_{\nu\lambda}$, $\pi_{\kappa\nu}$ and $\pi_{\lambda\kappa}$ whose common edge is the Y_λ axis and which intersect the $OX_\lambda Z_\lambda$ plane in the symmetrical positions depicted in Fig. 2a. A general definition of these three half-planes which is also applicable to reactions other than $H + H_2$ is

$$\pi_{\nu\lambda}: \quad r_\lambda = r_\nu \qquad -\frac{\pi}{2} \leqslant \gamma_\lambda \leqslant \frac{\pi}{2} \tag{3.2a}$$

$$\pi_{\kappa\nu}: \quad r_\nu = r_\kappa \qquad -\frac{\pi}{2} \leqslant \gamma_\nu \leqslant \frac{\pi}{2} \tag{3.2b}$$

$$\pi_{\lambda\kappa}: \quad r_\kappa = r_\lambda \qquad -\frac{\pi}{2} \leqslant \gamma_\kappa \leqslant \frac{\pi}{2} \tag{3.2c}$$

A proof that these equations do indeed define half-planes whose edge is the Y_λ axis, as graphically indicated in Fig. 2a, is given in Appendix A along with the equations describing the λ to ν coordinate transformation. For some reactions, the half-planes defined above may be inadequate as they may not separate the three arrangement channel regions into physically intuitive ones as determined by the shape of the potential functions. In these cases, alternative surfaces may then be chosen and treated by a straightforward extension of the theory presented in this paper. For the reactions $H + H_2$, $D + H_2$, $H + D_2$, etc., the half-planes of Eqs. 3.1 are quite satisfactory, so we shall proceed to formulate our theory using the arrangement channel regions into which they divide internal configuration space.

With these arrangement channel regions thus defined, we organize the work involved in solving Eq. 2.14 into two sequential steps. First, within each of the three arrangement channel regions, we integrate the Schrödinger equation using rotational coordinates and basis functions appropriate to the asymptotic part of that arrangement channel but changing vibrational coordinates and basis functions in a way which transforms "smoothly" from one arrangement channel to another. Then, we match the resulting three sets of solutions to one another on the three half-planes $\pi_{\nu\lambda}$, $\pi_{\kappa\nu}$, $\pi_{\lambda\kappa}$ described above (and hereafter called the <u>matching surfaces</u>). Since the vibrational coordinates are designed to transform smoothly from one arrangement channel to the others, it is primarily the rotational parts of the wave functions which must be considered in the matching procedure. Our rotational expansion is similar to that of Saxon and Light [14] but not to that of Wyatt and coworkers [17] who allow both their vibrational and rotational coordinates to transform smoothly in going from one arrangement channel to the next.

In the remainder of this section, we will detail the method used for integrating the Schrödinger equation in each of the arrangement channel regions. The crucial smooth matching procedure is outlined in Section 4.

3.2 The rotationally coupled Schrödinger equations

We now consider the solution of Eq. 2.14 in each of the three arrangement channel regions $\lambda = \alpha, \beta, \gamma$.

The body-fixed rotational angular momentum operator $\underset{\sim}{j}_\lambda$ associated with $\underset{\sim}{r}_\lambda$ is defined as

$$\underset{\sim}{j}_\lambda = \frac{\hbar}{i} \left(\frac{\partial}{\partial \gamma_\lambda}\right)_{\chi_\lambda, R_\lambda, r_\lambda} \hat{\underset{\sim}{z}} \tag{3.3}$$

and its eigenfunctions are

$$\varphi_{j_\lambda}(\gamma_\lambda) = (2\pi)^{-\frac{1}{2}} \exp(i j_\lambda \gamma_\lambda) \qquad j_\lambda = 0, \pm 1, \pm 2 \ldots \tag{3.4}$$

The expansion of F_J^λ, defined by Eq. 2.13, in terms of these eigenfunctions is

$$F_J^\lambda(r_\lambda, R_\lambda, \gamma_\lambda) = \sum_{j'_\lambda} \varphi_{j'_\lambda}(\gamma_\lambda)\, G^\lambda_{Jj'_\lambda}(r_\lambda, R_\lambda) \; . \tag{3.5}$$

Substituting this into Eq. 2.14 and taking the scalar product of both sides by φ_{j_λ}, we obtain the following set of coupled partial differential equations in the two scaled distances r_λ, R_λ:

$$-\frac{\hbar^2}{2\mu}\left[\frac{\partial^2}{\partial r_\lambda^2}+\frac{\partial^2}{\partial R_\lambda^2}-\frac{j_\lambda^2-\frac{1}{4}}{r_\lambda^2}-\frac{(J-j_\lambda)^2-\frac{1}{4}}{R_\lambda^2}\right]G^\lambda_{Jj_\lambda}(r_\lambda,R_\lambda)$$

$$+\sum_{j'_\lambda=-\infty}^{\infty}V^\lambda_{j_\lambda j'_\lambda}(r_\lambda,R_\lambda)\,G^\lambda_{Jj'_\lambda}(r_\lambda,R_\lambda)=E\,G^\lambda_{Jj'_\lambda}(r_\lambda,R_\lambda) \qquad (3.6)$$

$$J,j_\lambda=0,\pm1,\pm2,\ldots$$

where

$$V^\lambda_{j_\lambda j'_\lambda}(r_\lambda,R_\lambda)=\langle j_\lambda|V^\lambda|j'_\lambda\rangle$$

$$=\int_{-\pi/2}^{3\pi/2}\varphi^{\lambda*}_{j_\lambda}(\gamma_\lambda)\,V^\lambda(r_\lambda,R_\lambda,\gamma_\lambda)\,\varphi^\lambda_{j'_\lambda}(\gamma_\lambda)\,d\gamma_\lambda \qquad (3.7)$$

Since $V^\lambda(r_\lambda,R_\lambda,\gamma_\lambda)=V^\lambda(r_\lambda,R_\lambda,2\pi-\gamma_\lambda)$, we can expand the potential in terms of a cosine Fourier series

$$V^\lambda(r_\lambda,R_\lambda,\gamma_\lambda)=\sum_{k=0}^{\infty}V^\lambda_k(r_\lambda,R_\lambda)\cos(k\gamma_\lambda) \qquad (3.8a)$$

where

$$V^\lambda_k(r_\lambda,R_\lambda)=\frac{2}{(1+\delta_{k0})\pi}\int_0^\pi\cos(k\gamma_\lambda)\,V^\lambda(r_\lambda,R_\lambda,\gamma_\lambda)\,d\gamma_\lambda \qquad (3.8b)$$

Substituting Eq. 3.8 into 3.7 and integrating, we find that

$$V^\lambda_{j_\lambda j'_\lambda}(r_\lambda,R_\lambda)=\frac{1}{2-\delta_{|j_\lambda-j'_\lambda|,0}}V^\lambda_{|j_\lambda-j'_\lambda|}(r_\lambda,R_\lambda)$$

$$=\frac{1}{\pi}\int_0^\pi\cos[\,|j_\lambda-j'_\lambda|\gamma_\lambda\,]\,V^\lambda(r_\lambda,R_\lambda,\gamma_\lambda)\,d\gamma_\lambda \qquad (3.9)$$

Equation 3.9 shows that $V^{\lambda}_{j_\lambda j'_\lambda}$ depends on j_λ and j'_λ only through $|j_\lambda - j'_\lambda|$. We can write Eq. 3.6 in a condensed matrix notation by regarding $\underset{\sim}{G}^{\lambda}_{J}(r_\lambda, R_\lambda)$ as a column vector whose elements are the $G^{\lambda}_{Jj_\lambda}(r_\lambda, R_\lambda)$. We get

$$T^{\lambda}\, \underset{\sim}{G}^{\lambda}_{J} + \underset{\approx}{V}^{\lambda e}_{J}\, \underset{\sim}{G}^{\lambda}_{J} = E\, \underset{\sim}{G}^{\lambda}_{J} \tag{3.10}$$

where T^{λ} is the kinetic energy operator

$$T^{\lambda} = -\frac{\hbar^2}{2\mu}\left(\frac{\partial^2}{\partial R^2_\lambda} + \frac{\partial^2}{\partial r^2_\lambda}\right) \tag{3.11}$$

and the $\underset{\approx}{V}^{\lambda e}_{J}(r_\lambda, R_\lambda)$ is an effective potential energy matrix defined by

$$\underset{\approx}{V}^{\lambda e}_{J}(r_\lambda, R_\lambda) = \underset{\approx}{V}^{\lambda}(r_\lambda, R_\lambda) + \underset{\approx}{V}^{\lambda c}_{J}(r_\lambda, R_\lambda) \tag{3.12}$$

$\underset{\approx}{V}^{\lambda}$ is the J-independent interaction potential matrix whose elements are the $V^{\lambda}_{j_\lambda j'_\lambda}$ defined by Eq. 3.9 while $\underset{\approx}{V}^{\lambda c}_{J}$ is the diagonal centrifugal potential matrix defined by

$$\left[\underset{\approx}{V}^{\lambda c}_{J}(r_\lambda, R_\lambda)\right]_{j_\lambda j'_\lambda} = \frac{\hbar^2}{2\mu}\left[\frac{j^2_\lambda - \frac{1}{4}}{r^2_\lambda} + \frac{(J - j_\lambda)^2 - \frac{1}{4}}{R^2_\lambda}\right]\delta_{j_\lambda j'_\lambda} \tag{3.13}$$

From Eqs. 3.6 and 3.9 we conclude that the $G^{\lambda}_{Jj_\lambda}$ for different j_λ are coupled through the $V^{\lambda}_{k}(r_\lambda, R_\lambda)$ functions with $k > 0$, V^{λ}_{0} representing a non-coupling potential.

3.3. The division of r_λ, R_λ space into regions and the choice of variables in each region

We now consider the expansion of the function $G^\lambda_{Jj_\lambda}(r_\lambda, R_\lambda)$ in terms of a set of single-variable functions which describe a vibration-like motion. To pick this vibration variable and the corresponding vibrational basis set it is convenient to examine the behavior of $V_0^\lambda(r_\lambda, R_\lambda)$ since, as one can conclude from the remark at the end of Section 3.2, this function together with the centrifugal potential $(\hbar^2/2\mu)(j^2_\lambda - 1/4)/r^2_\lambda$, determines the r_λ-dependence of $G^\lambda_{Jj_\lambda}$ in the absence of j_λ (i.e., rotational) coupling. For the $H + H_2$ reaction, equipotentials of $V_0^\lambda(r_\lambda, R_\lambda)$ are represented in Fig. 3, together with the corresponding line L of steepest ascents and descents. Cuts of V_0^λ normal to L look like diatomic internuclear potential energy functions, displaying a minimum on L, a dissociation plateau in the direction away from the coordinate axes and a steep repulsive point in the opposite direction. These characteristics are analogous to those presented by collinear triatomic potential energy functions, and suggest that we divide the r_λ, R_λ space in regions in a manner analogous to that employed for collinear reactions [5,10], using different coordinates and/or vibration basis functions in each region. The corresponding vibration coordinates will be a distance along the lines which are more or less transverse to L. In each region, in addition to such vibration coordinates, there will be a "propagation" coordinate in terms of which Eq. 3.6 will be expressed as a system of coupled ordinary differential equations. For $H + H_2$ we indicate a convenient choice for these regions in Fig. 3. They are denoted as: I - the asymptotic region, II - the weak interaction region, III - the strong interaction region, and IV - the matching region. The boundary points P_0', P_0 and P_1 in Fig. 3 are chosen as follows. The abscissa r_{λ_0} of P_0' and P_0 is chosen so that these points lie in the classically forbidden plateau area where the wave function may be assumed to vanish. The ordinate R_{λ_0}' of P_0' is picked large enough so that the potential $V_0^\lambda(r_\lambda, R_\lambda)$ is independent of R_λ for $R_\lambda \geqslant R_{\lambda_0}'$. R_{λ_0} is determined by the requirement that P_0 lie on the line whose equation is obtained from A.11 of Appendix A by setting $\gamma_\lambda = 0$, <u>i.e.</u>,

$$R_{\lambda_0} = r_{\lambda_0} \tan(\alpha_{\nu\lambda}/2) \tag{3.14}$$

$P_1(r_{\lambda_1}, R_{\lambda_1})$ also lies high in the plateau region, on the line determined from Eq. A.11 by setting $\gamma_\lambda = \pi/2$, <u>i.e.</u>,

$$R_{\lambda_1} = r_{\lambda_1} \tag{3.15}$$

The reasons for the necessity of imposing Eqs. 3.14 and 3.15 on the positions of P_0 and P_1 will be explained subsequently.

The coordinate systems used in each of these four regions are as follows. In the asymptotic region (I) and in the weak interaction region (II), we use the Cartesian coordinates r_λ, R_λ as vibration and propagation coordinates respectively. In the strong interaction region (III) we switch to the polar coordinates $\rho_\lambda, \varphi_\lambda$ (as depicted in Fig. 4) with $P_0(r_{\lambda_0}, R_{\lambda_0})$ as origin and related to r_λ, R_λ by

$$r_\lambda = r_{\lambda_0} - \rho_\lambda \cos \varphi_\lambda \tag{3.16a}$$

$$R_\lambda = R_{\lambda_0} - \rho_\lambda \sin \varphi_\lambda \tag{3.16b}$$

ρ_λ is the vibration and φ_λ the propagation coordinate for this region. In the matching region (IV), we use another set of polar coordinates (ζ, η_λ) which have their origin at Q (Fig. 4) and which are related to r_λ, R_λ by

$$r_\lambda = \zeta \sin \eta_\lambda \tag{3.17a}$$

$$R_\lambda = \zeta \cos \eta_\lambda \tag{3.17b}$$

ζ (≥ 0) and η_λ (in range 0 to $\pi/2$) are respectively the vibration and propagation variables for region IV. We note that the ζ defined here is identical to that given by Eq. 3.1a while the angles ω_λ and η_λ are related, as can be seen from Eqs. 3.17 and 3.16, by

$$\omega_\lambda = 2\eta_\lambda \tag{3.18}$$

Once we know the $G^\lambda_{Jj_\lambda}$ functions for a fixed η_λ and variable ζ, Eq. 3.5 furnishes the wavefunction F^λ_J on a cone of constant ω_λ $(=2\eta_\lambda)$ in the $OX_\lambda Y_\lambda Z_\lambda$ coordinate system, as depicted in Fig. 5a.

We actually want to determine this wave function on the matching surfaces $\pi_{\nu\lambda}$ and $\pi_{\lambda\kappa}$ rather than on the ω_λ = constant cones since it is on these surfaces that we will smoothly match the solutions obtained from the integration of the Schrödinger equation in the three arrangement channels $\lambda = \alpha, \beta, \gamma$. However, for a given ω_λ (within a certain range) we do have the wave functions on the lines of intersection of the constant ω_λ cone with the half-planes $\pi_{\nu\lambda}$ and $\pi_{\lambda\kappa}$ (See Fig. 5a). The relation between ω_λ and γ_λ at the lines of intersection with $\pi_{\nu\lambda}$ is given by Eq. A.14 of Appendix A. As ω_λ is scanned from $\omega_{\lambda_0} = 2\eta_{\lambda_0}$ to $\omega_{\lambda_1} = 2\eta_{\lambda_1}$ (Figs. 3 and 5), these intersection lines scan the entire $\pi_{\nu\lambda}$ matching half-plane and thus we can obtain the desired wave function F_J^λ on it from a knowledge of the $G_{Jj_\lambda}^\lambda(\zeta, \eta_\lambda)$ for η_λ in the range η_{λ_0} to η_{λ_1}. The angles ω_{λ_0} and ω_{λ_1} correspond to the intersection of $\pi_{\nu\lambda}$ with the $\gamma_\lambda = 0$ and $\gamma_\lambda = \pi/2$ half-plane respectively (in $OX_\lambda Y_\lambda Z_\lambda$ internal configuration space). From Eq. A.14 we find that $\omega_{\lambda_0} = \pi - \alpha_{\nu\lambda}$ and $\omega_{\lambda_1} = \pi/2$. These values determine the values of η_{λ_0} and η_{λ_1} of Fig. 3 through Eq. 3.18 and consequently the positions of P_0 and P_1 [32]. Indeed, by using Eqs. 3.17 and 3.18 together with the values of ω_{λ_0} and ω_{λ_1} given above, we obtain the Eqs. 3.14 and 3.15 that were previously used in locating P_0 and P_1. One additional complication in this procedure arises when $m_\nu \neq m_\kappa$ (for the integration in arrangement channel λ). In that case, the angles $\alpha_{\nu\lambda}$ and $\alpha_{\lambda\kappa}$ are different (see Eq. A.3) so that the value of ω_{λ_0} for $\pi_{\nu\lambda}$ (i.e., $\omega_{\lambda_0} = \pi - \alpha_{\nu\lambda}$) is different from ω'_{λ_0} for $\pi_{\lambda\kappa}$ ($\omega'_{\lambda_0} = \pi - \alpha_{\lambda\kappa}$). In order to obtain the wavefunction on both of the matching surfaces $\pi_{\nu\lambda}$ and $\pi_{\lambda\kappa}$ we modify our definition of ω_{λ_0} to

$$\omega_{\lambda_0} = \min(\pi - \alpha_{\nu\lambda}, \pi - \alpha_{\lambda\kappa}) \qquad (3.19)$$

ω_{λ_1}, on the other hand, is mass-independent and always equal to $\pi/2$ for the choice of matching surfaces given by Eq. 3.2.

Having defined the four regions of each r_λ, R_λ space ($\lambda = \alpha, \beta, \gamma$)

and their associated vibration-propagation coordinate systems, we are ready to introduce a vibrational expansion into the Schrödinger equations Eq. 3.6 (or their matrix counterpart Eq. 3.9), thus obtaining the actual ordinary coupled differential equations to be integrated. We shall do this for each region separately starting with the asymptotic region.

3.4. The coupled Schrödinger equations in the propagation variable

3.4.1. The asymptotic region

As mentioned above, the vibration and propagation variables for this region are r_λ and R_λ, respectively. The function $V^\lambda(r_\lambda, R_\lambda, \gamma_\lambda)$ becomes the isolated diatomic potential $v^\lambda(r_\lambda)$ for $R_\lambda \geqslant R'_{\lambda_0}$ and the potential matrix $\underset{\approx}{V}^\lambda$ appearing in the right hand side of Eq. 3.12 becomes diagonal:

$$\underset{\approx}{V}^\lambda (r_\lambda, R_\lambda \geqslant R_{\lambda_0}) = v^\lambda (r_\lambda) \, \underset{\approx}{I} \tag{3.20}$$

where $\underset{\approx}{I}$ is the identity matrix. This leads to a total decoupling of Eqs. 3.6 and 3.10. For a given J and j_λ, we obtain:

$$\left\{ - \frac{\hbar^2}{2\mu} \left[\frac{\partial^2}{\partial r_\lambda^2} + \frac{\partial^2}{\partial R_\lambda^2} - \frac{(j_\lambda^2 - \frac{1}{4})}{r_\lambda^2} + \frac{(J - j_\lambda)^2 - \frac{1}{4}}{R_\lambda^2} \right] + v^\lambda \right\} G_{Jj_\lambda}^{\lambda(a)} = E \, G_{Jj_\lambda}^{\lambda(a)} \tag{3.21}$$

where the superscript (a) refers to the asymptotic region. This equation may be solved by separation of variables. The solution can be expanded as

$$G^{\lambda(a)}_{Jj_\lambda}(r_\lambda, R_\lambda) = \sum_{v_\lambda} g^{\lambda(a)}_{Jv_\lambda j_\lambda}(R_\lambda)\,\phi^{\lambda(a)}_{v_\lambda j_\lambda}(r_\lambda) \tag{3.22}$$

where $\phi^{\lambda(a)}_{v_\lambda j_\lambda}$ is a vibrational eigenfunction with vibrational energy $E^{\lambda(a)}_{v_\lambda j_\lambda}$ satisfying the equation

$$\left\{-\frac{\hbar^2}{2\mu}\frac{d^2}{dr_\lambda^2} + \left[v^\lambda(r_\lambda) + \frac{(j_\lambda^2 - \frac{1}{4})}{r_\lambda^2}\right]\right\}\phi^{\lambda(a)}_{v_\lambda j_\lambda} = E^{\lambda(a)}_{v_\lambda j_\lambda}\,\phi^{\lambda(a)}_{v_\lambda j_\lambda} \tag{3.23}$$

with boundary conditions $\phi^{\lambda(a)}_{v_\lambda j_\lambda}(0) = \phi^{\lambda(a)}_{v_\lambda j_\lambda}(r_{\lambda_0}) = 0$. $g^{\lambda(a)}_{Jv_\lambda j_\lambda}(R_\lambda)$ describes the translational motion associated with the propagation variable, R_λ and satisfies the equation

$$\left\{-\frac{\hbar^2}{2\mu}\frac{d^2}{dR_\lambda^2} + \left[\frac{(J - j_\lambda)^2 - \frac{1}{4}}{R_\lambda^2} - \left(E - E^{\lambda(a)}_{v_\lambda j_\lambda}\right)\right]\right\} g^{\lambda(a)}_{v_\lambda j_\lambda} = 0\,. \tag{3.24}$$

This equation is closely related to the Bessel equation and its general solution can be written as

$$g^{\lambda(a)}_{Jv_\lambda j_\lambda}(R_\lambda) = (k^{\lambda(a)}_{v_\lambda j_\lambda} R_\lambda)^{\frac{1}{2}} \begin{cases} A^\lambda_{Jv_\lambda j_\lambda}\, J_{J-j_\lambda}(k^{\lambda(a)}_{v_\lambda j_\lambda} R_\lambda) + B^\lambda_{Jv_\lambda j_\lambda}\, Y_{J-j_\lambda}(k^{\lambda(a)}_{v_\lambda j_\lambda} R_\lambda) \\ \qquad \text{for } E^{\lambda(a)}_{v_\lambda j_\lambda} < E \\ \qquad \text{(open channels)} \\ A^\lambda_{Jv_\lambda j_\lambda}\, I_{J-j_\lambda}(|k^{\lambda(a)}_{v_\lambda j_\lambda}| R_\lambda) + B^\lambda_{Jv_\lambda j_\lambda}\, K_{J-j_\lambda}(|k^{\lambda(a)}_{v_\lambda j_\lambda}| R_\lambda) \\ \qquad \text{for } E^{\lambda(a)}_{v_\lambda j_\lambda} > E \\ \qquad \text{(closed channels)} \end{cases} \tag{3.25}$$

where

$$k^{\lambda(a)}_{v_\lambda j_\lambda} = \frac{1}{\hbar}\left[2\mu\left(E - E^{\lambda(a)}_{v_\lambda j_\lambda}\right)\right]^{\frac{1}{2}} . \tag{3.26}$$

is the wavenumber for the vibration rotation state with quantum numbers $v_\lambda j_\lambda$. The functions J_ℓ and Y_ℓ are respectively the regular and irregular ordinary Bessel functions [33] of order ℓ and have the asymptotic behavior

$$x^{\frac{1}{2}} J_\ell(x) \underset{x\to\infty}{\sim} (2/\pi)^{\frac{1}{2}} \cos(x - \ell\pi/2 - \pi/4) \tag{3.27a}$$

$$x^{\frac{1}{2}} Y_\ell(x) \underset{x\to\infty}{\sim} (2/\pi)^{\frac{1}{2}} \sin(x - \ell\pi/2 - \pi/4) \tag{3.27b}$$

whereas I_ℓ and K_ℓ are the modified Bessel functions [33] and have the asymptotic behavior

$$x^{\frac{1}{2}} I_\ell(x) \underset{x\to\infty}{\sim} (2\pi)^{-\frac{1}{2}} \exp(x) \tag{3.28a}$$

$$x^{\frac{1}{2}} K_\ell(x) \underset{x\to\infty}{\sim} (\pi/2)^{\frac{1}{2}} \exp(-x) \ . \tag{3.28b}$$

In Section 5 we will consider scattering asymptotic conditions which will determine the constants $A^\lambda_{Jv_\lambda j_\lambda}$ and $B^\lambda_{Jv_\lambda j_\lambda}$.

Let us rewrite Eqs. 3.24 and 3.25 in matrix notation, which will appreciably simplify the equations in the rest of the paper. Let $\underset{\sim}{g}^{\lambda(a)}_J(R_\lambda)$ be the column vector whose elements, labeled by the $v_\lambda j_\lambda$ index pair, are given by Eq. 3.25. When replaced into Eqs. 3.22, 3.5 and 2.13, it furnishes a single $\psi^\lambda_J(R_\lambda, r_\lambda, \gamma_\lambda)$, corresponding to a single $\underset{\sim}{A}_J^{\lambda}, \underset{\sim}{B}_J^{\lambda}$ column vector pair, the elements of which are the $A^{\lambda}_{Jv_\lambda j_\lambda}$ and $B^{\lambda}_{Jv_\lambda j_\lambda}$ of Eq. 3.25. In order to satisfy condition (c) of Section 2.1, we will need all of the possible linearly independent solutions to the Schrödinger equation. The number of such solutions is twice the number of $v_\lambda j_\lambda$ channels included in the expansions of Eqs. 3.22 and 3.5. We can assemble the corresponding $\underset{\sim}{g}_J^{\lambda(a)}$ vectors to form two square matrices which we shall label $\underset{\approx}{g}_J^{\lambda(a)+}(R\ )$ and $\underset{\approx}{g}_J^{\lambda(a)-}(R_\lambda)$. In each of these two matrices, the rows will be labelled by (v_λ, j_λ) pairs and the columns by (v'_λ, j'_λ) pairs. In the course of our integration, we will obtain the solutions labelled (+) by a propagation from region I to IV and those labelled (-) by a propagation in the opposite direction. If we similarly form the matrices $\underset{\approx}{A}_J^{\pm}$ and $\underset{\approx}{B}_J^{\pm}$ from the corresponding $\underset{\sim}{A}_J^{\pm}$ and $\underset{\sim}{B}_J^{\pm}$ vectors, we can rewrite Eqs. 3.24 and 3.25 as:

$$-\frac{\hbar^2}{2\mu}\frac{d^2 \underset{\approx}{g}_J^{\lambda(a)\pm}}{dR_\lambda^2} + \underset{\approx}{V}_J^{c\lambda}\,\underset{\approx}{g}_J^{\lambda(a)\pm} = \underset{\approx}{\mathcal{E}}^{\lambda(a)}\,\underset{\approx}{g}_J^{\lambda(a)\pm} \tag{3.29}$$

and

$$\underset{\approx}{g}_J^{\lambda(a)\pm}(R_\lambda) = \underset{\approx}{J}_J^{\lambda}(R_\lambda)\,\underset{\approx}{A}_J^{\lambda\pm} + \underset{\approx}{Y}_J^{\lambda}(R_\lambda)\,\underset{\approx}{B}_J^{\lambda\pm} \tag{3.30}$$

where,

$$[\underset{\approx}{V}_J^{c\lambda}(R_\lambda)]^{v'_\lambda j'_\lambda}_{v_\lambda j_\lambda} = \hbar^2\,\frac{[(J-j_\lambda)^2-\frac{1}{4}]}{2\mu R_\lambda^2}\,\delta^{v'_\lambda j'_\lambda}_{v_\lambda j_\lambda} \tag{3.31}$$

$$[\underset{\approx}{\mathcal{E}}^{\lambda(a)}]^{v'_\lambda j'_\lambda}_{v_\lambda j_\lambda} = [E - E^{\lambda(a)}_{v_\lambda j_\lambda}]\,\delta^{v'_\lambda j'_\lambda}_{v_\lambda j_\lambda} \tag{3.32}$$

$$[\underset{\approx}{J}_J^\lambda]_{v_\lambda j_\lambda}^{v'_\lambda j'_\lambda} = R_\lambda^{\frac{1}{2}}\,\delta_{v_\lambda j_\lambda}^{v'_\lambda j'_\lambda} \times \begin{cases} J_{J-j_\lambda}(k_{v_\lambda j_\lambda}^{\lambda(a)} R_\lambda) \\ \qquad \text{for } E_{v_\lambda j_\lambda}^{\lambda(a)} < E \\ \\ I_{J-j_\lambda}(|k_{v_\lambda j_\lambda}^{\lambda(a)}| R_\lambda) \\ \qquad \text{for } E_{v_\lambda j_\lambda}^{\lambda(a)} > E \end{cases} \tag{3.33}$$

$$[\underset{\approx}{Y}_J^\lambda]_{v_\lambda j_\lambda}^{v'_\lambda j'_\lambda} = R_\lambda^{\frac{1}{2}}\,\delta_{v_\lambda j_\lambda}^{v'_\lambda j'_\lambda} \times \begin{cases} Y_{J-j_\lambda}(k_{v_\lambda j_\lambda}^{\lambda(a)} R_\lambda) \\ \qquad \text{for } E_{v_\lambda j_\lambda}^{\lambda(a)} < E \\ \\ K_{J-j_\lambda}(|k_{v_\lambda j_\lambda}^{\lambda(a)}| R_\lambda) \\ \qquad \text{for } E_{v_\lambda j_\lambda} > E \end{cases} \tag{3.34}$$

In Eqs. 3.31 through 3.34 the subscripts in a matrix element represents its row label, and the superscript its column label. Note that the centrifugal potential matrix $\underset{\approx}{V}_J^{c\lambda}$ in Eq. 3.31 is not the same as the $\underset{\approx}{V}_J^{\lambda c}$ in Eq. 3.13. Equations analogous to Eq. 3.29 will be developed for each of the other three subregions. Equation 3.30 and similar equations will be used in the reactance matrix analysis (Section 5).

3.4.2. The weak interaction region

In this region, we retain the vibration-propagation variables r_λ, R_λ. However, since $V^\lambda(r_\lambda, R_\lambda, \gamma_\lambda)$ and $\underset{\approx}{V}^\lambda(r_\lambda, R_\lambda)$ do vary with R_λ, the asymptotic vibrational eigenfunctions $\phi^{\lambda(a)}_{v_\lambda j_\lambda}$ are not necessarily the best basis for expanding the $G^\lambda_{Jj_\lambda}(r_\lambda, R_\lambda)$. To optimize a choice of basis functions, we divide region II into n^λ_{II} subregions II_i $(i=1,2,\cdots n^\lambda_{II})$ by constant R_λ lines having $R_\lambda = (R'_{\lambda_0}, R'_{\lambda_1}, \ldots, R'_{\lambda n^\lambda_{II}} = R_{\lambda_0})$. The range of R_λ for the i^th^ sub-region is $R'_{\lambda_{i-1}} \le R_\lambda \le R'_{\lambda_i}$. Let $R^0_{\lambda_i}$ be a selected value of R_λ in this range, such as its midpoint. We choose as a basis set for expansion in this subregion the functions $\phi^{\lambda(w)}_{v_\lambda j_\lambda}(r_\lambda; R^0_{\lambda_i})$ which satisfy the eigenvalue equation

$$\left\{-\frac{\hbar^2}{2\mu}\frac{d^2}{dr_\lambda^2} + \left[V^\lambda_{\rm ref}(r_\lambda; R^0_{\lambda_i}) + \frac{(j_\lambda^2 - \frac{1}{4})\hbar^2}{2\mu r_\lambda^2}\right]\right\}\phi^{\lambda(w)}_{v_\lambda j_\lambda}$$

$$= E^{\lambda(w)}_{v_\lambda j_\lambda}(R^0_{\lambda_i})\,\phi^{\lambda(w)}_{v_\lambda j_\lambda} \tag{3.35}$$

with boundary conditions $\phi^{\lambda(w)}_{v_\lambda j_\lambda}(0; R^0_{\lambda_i}) = \phi^{\lambda(w)}_{v_\lambda j_\lambda}(r_{\lambda_0}; R^0_{\lambda_i}) = 0$. The superscript (w) refers to the weak interaction region. $V^\lambda_{\rm ref}(r_\lambda; R^0_{\lambda_i})$ is a reference potential for vibrational motion which is, in principle, arbitrary but which, in practice, must be chosen so that the vibrational basis functions $\phi^{\lambda(w)}_{v_\lambda j_\lambda}$ serve as an efficient representation of the r_λ dependence of the functions $G^\lambda_{Jj_\lambda}(r_\lambda, R_\lambda)$. Examples of possible reference potentials are (a) the first coefficient in the Fourier expansion (Eq. 3.8) $V_0^\lambda(r_\lambda, R_\lambda)$, and (b) the exact potential $V^\lambda(R_\lambda, r_\lambda, \bar{\gamma}_\lambda)$ for a fixed $\bar{\gamma}_\lambda$. One important test of vibrational convergence in our method is the invariance of the final results to the choice of V_{ref}^λ. Eq. 3.35 is the radial Schrödinger equation of a pseudo molecule whose interatomic potential is $V_{\text{ref}}^\lambda(r_\lambda; R_{\lambda_i}^0)$, characteristic of subregion II_i, rather than $v^\lambda(r_\lambda)$ which characterizes the asymptotic region. (Its centrifugal potential is however not the normal $j_\lambda(j_\lambda + 1)\hbar^2/2\mu r_\lambda^2$ one). The $\phi_{v_\lambda j_\lambda}^{\lambda(w)}$ and $E_{v_\lambda j_\lambda}^{\lambda(w)}$ are obtained by numerically solving Eq. 3.35, subject to the boundary conditions just mentioned.

We now expand $G_{Jj_\lambda}^\lambda(r_\lambda, R_\lambda)$ in terms of the above vibrational basis functions:

$$G_{Jj_\lambda}^\lambda(r_\lambda, R_\lambda) = \sum_{v_\lambda} g_{Jv_\lambda j_\lambda}^{\lambda(w)}(R_\lambda; R_{\lambda_i}^0)\, \phi_{v_\lambda j_\lambda}^{\lambda(w)}(r_\lambda; R_{\lambda_i}^0) \tag{3.36}$$

Substituting this into Eq. 3.6, multiplying by $\phi_{v'_\lambda j_\lambda}(r_\lambda; R_{\lambda_i}^0)$ and integrating over r_λ, then interchanging v_λ and v'_λ and expressing the resulting coupled equations in the matrix form of the previous section we get

$$-\frac{\hbar^2}{2\mu}\frac{d^2}{dR_\lambda^2}\, \underset{\approx}{g}_J^{\lambda(w)\pm}(R_\lambda; R_{\lambda_i}^0) + \underset{\approx}{V}_J^{e\lambda(w)}(R_\lambda; R_{\lambda_i}^0)\, \underset{\approx}{g}_J^{\lambda(w)\pm}$$

$$= \underset{\approx}{\mathcal{E}}^{\lambda(w)}(R_{\lambda_i}^0)\, \underset{\approx}{g}_J^{\lambda(w)\pm} \tag{3.37}$$

where the effective potential matrix $\underset{\approx}{V}_J^{e\lambda(w)}$ is defined by

$$\underset{\approx}{V}_J^{e\lambda(w)}(R_\lambda;R^0_{\lambda_i}) = \underset{\approx}{V}^{\lambda(w)}(R_\lambda;R^0_{\lambda_i}) + \underset{\approx}{V}_J^{c\lambda}(R_\lambda) - \underset{\approx}{V}_{ref}^{\lambda(w)}(R^0_{\lambda_i}) \tag{3.38}$$

The diagonal matrices $\underset{\approx}{V}_J^{c\lambda}$ and $\underset{\approx}{\mathcal{E}}^{\lambda(w)}$ are defined by Eqs. 3.31 and 3.32, respectively, with the superscript (a) replaced by (w) in Eq. 3.32. The potential matrix $\underset{\approx}{V}^{\lambda(w)}(R_\lambda;R^0_{\lambda_i})$ is given by

$$[\underset{\approx}{V}^{\lambda(w)}(R_{\lambda_i};R^0_{\lambda_i})]_{v_\lambda j_\lambda}^{v'_\lambda j'_\lambda} = \langle \phi^{\lambda(w)}_{v_\lambda j_\lambda}(r_\lambda;R^0_{\lambda_i}) | V^\lambda_{j_\lambda j'_\lambda}(r_\lambda,R_\lambda) | \phi^{\lambda(w)}_{v'_\lambda j'_\lambda}(r_\lambda;R^0_{\lambda_i})\rangle$$

$$= \langle \varphi^\lambda_{j_\lambda}(\gamma_\lambda)\, \phi^\lambda_{v_\lambda j_\lambda}(r_\lambda;R^0_{\lambda_i}) | V^\lambda(r_\lambda,R_\lambda,\gamma_\lambda) | \phi^{\lambda(w)}_{v'_\lambda j'_\lambda}(r_\lambda;R^0_{\lambda_i})\, \varphi^\lambda_{j'_\lambda}(\gamma_\lambda)\rangle$$

$$= \langle v_\lambda j_\lambda | V^\lambda | v'_\lambda j'_\lambda \rangle \tag{3.39}$$

and the reference potential matrix $\underset{\approx}{V}_{ref}^{\lambda(w)}(R^0_{\lambda_i})$ is given by

$$[V_{ref}^{\lambda(w)}(R^0_{\lambda_i})]_{v_\lambda j_\lambda}^{v'_\lambda j'_\lambda} = \langle \phi^{\lambda(w)}_{v_\lambda j_\lambda}(r_\lambda;R^0_{\lambda_i}) | V^\lambda_{ref}(r_\lambda;R^0_{\lambda_i}) | \phi^{\lambda(w)}_{v_\lambda j_\lambda}(r_\lambda;R^0_{\lambda_i})\rangle\, \delta_{j_\lambda j'_\lambda} \tag{3.40}$$

As long as the anisotropy of the potential remains small and the reference potential provides an efficient vibrational basis set for expanding the functions $G^\lambda_{Jj_\lambda}(r_\lambda;R_\lambda)$ within each subregion, the potential matrix $\underset{\approx}{V}_J^{e\lambda(w)}$ should be nearly diagonal and Eqs. 3.37 are only weakly coupled. The number and size of the subregions into which region II is divided depends on the steepness of the variation of the potential matrix $\underset{\approx}{V}^{\lambda(w)}$ with R_λ. This number is generally small (i.e., less than 3).

As we propagate the solutions of Eq. 3.37 through region II towards regions I or III, the wavefunctions $\psi_J^\lambda(r_\lambda, R_\lambda, \gamma_\lambda)$ must remain continuous and smooth during the change of basis functions that occurs at the boundaries of neighboring subregions. This requirement leads to the following relations between the functions $g^{\lambda(w)}_{Jv_\lambda j_\lambda}(R_\lambda; R^0_{\lambda_i})$ and $g^{\lambda(w)}_{Jv_\lambda j_\lambda}(R_\lambda; R^0_{\lambda_{i+1}})$ and their derivatives at the boundary of subregions i and $i+1$:

$$\underset{\approx}{g}_J^{\lambda(w)\pm}(R'_{\lambda_i};R^0_{\lambda_{i+1}}) = \underset{\approx}{S}_i^{\lambda(w)}\,\underset{\approx}{g}_J^{\lambda(w)\pm}(R'_{\lambda_i};R^0_{\lambda_i}) \tag{3.41a}$$

$$\frac{d\underset{\approx}{g}_J^{\lambda(w)\pm}}{dR_\lambda}(R'_{\lambda_i};R^0_{\lambda_{i+1}}) = \underset{\approx}{S}_i^{\lambda(w)}\,\frac{d\underset{\approx}{g}_J^{\lambda(w)\pm}}{dR_\lambda}(R'_{\lambda_i};R^0_{\lambda_i}) \quad . \tag{3.41b}$$

where the overlap matrix $\underset{\approx}{S}_i^{\lambda(w)}$ is given by

$$[\underset{\approx}{S}_i^{\lambda(w)}]^{v'_\lambda j'_\lambda}_{v_\lambda j_\lambda} = \delta_{j_\lambda j'_\lambda}\,\langle\phi^{\lambda(w)}_{v_\lambda j_\lambda}(r_\lambda;R^0_{\lambda_{i+1}})\,|\,\phi^{\lambda(w)}_{v'_\lambda j'_\lambda}(r_\lambda;R^0_{\lambda_i})\rangle \; . \tag{3.42}$$

An important criterion for the choice of the size of the subregions is that the $\underset{\approx}{S}_i^{\lambda(w)}$ should be nearly orthogonal matrices. Lack of orthogonality implies lack of completeness of the basis sets $\phi^{\lambda(w)}_{v_\lambda j_\lambda}$, and results in the loss of information about the wavefunction as a result of the transformation of Eqs. 3.41. The relations at the boundary separating regions I and II is achieved by setting i = 0 in Eqs. 3.41 and interpreting $R^0_{\lambda_0}$ to mean R'_{λ_0} and $\phi^{\lambda(w)}_{v_\lambda j_\lambda}(r_\lambda; R^0_{\lambda_0})$ to mean $\phi^{\lambda(a)}_{v_\lambda j_\lambda}(r_\lambda)$.

3.4.3. The strong interaction region

In this region we use the polar coordinates $\rho_\lambda, \varphi_\lambda$ regarding φ_λ as the propagation variable. If we transform Eq. 3.10 to these polar coordinates with the aid of Eq. 3.16, we obtain the vector equation

$$T^{\lambda(s)} \underset{\sim}{G}{}^{\lambda(s)}_J(\rho_\lambda, \varphi_\lambda) + \underset{\approx}{V}{}^{\lambda e(s)}_J \underset{\sim}{G}{}^{\lambda(s)}_J = E\, \underset{\sim}{G}{}^{\lambda(s)}_J \tag{3.43}$$

where the superscript s refers to "strong interaction region." $T^{\lambda(s)}$ is given by

$$T^{\lambda(s)} = -\frac{\hbar^2}{2\mu}\left(\frac{\partial^2}{\partial \rho_\lambda^2} + \frac{1}{\rho_\lambda}\frac{\partial}{\partial \rho_\lambda} + \frac{1}{\rho_\lambda^2}\frac{\partial^2}{\partial \varphi_\lambda^2}\right) \tag{3.44}$$

and the matrix $\underset{\approx}{V}{}^{\lambda e(s)}_J(\rho_\lambda, \varphi_\lambda)$ is simply $\underset{\approx}{V}{}^{\lambda e}_J(r_\lambda, R_\lambda)$ expressed in the coordinates $\rho_\lambda, \varphi_\lambda$.

For a typical reference potential V^λ_{ref} such as the $V^\lambda_0(r_\lambda, R_\lambda)$ defined by Eq. 3.8b and plotted in Fig. 3 for H + H_2, the shape of the potential as a function of ρ_λ for a fixed φ_λ $(0 \le \varphi_\lambda \le \varphi_{\lambda_0})$ is very much like that for a diatomic molecule. The deep potential well character of these cuts at constant φ_λ permits one to use their bound state eigenfunctions to efficiently represent the ρ_λ dependence of the wavefunction in this region. Accordingly, we divide region III into n^λ_{III} subregions III_i $(i = 1, 2, \cdots n^\lambda_{III})$ by lines of constant φ_λ $(\varphi_\lambda = 0, \varphi'_{\lambda_1}, \varphi'_{\lambda_2}, \cdots \varphi'_{\lambda_{n^\lambda_{III}}} = \varphi_{\lambda_0})$. For each such subregion, we choose a cut at a specific value $\varphi^0_{\lambda_i}$ of φ_λ (where $\varphi_{\lambda_{i-1}} \leq \varphi^0_{\lambda_i} \leq \varphi_{\lambda_i}$) to define our vibrational basis functions $\phi^{\lambda(s)}_{v_\lambda}(\rho_\lambda; \varphi^0_{\lambda_i})$ and energy eigenvalues $E^{\lambda(s)}_{v_\lambda}(\varphi^0_{\lambda_i})$ as the solutions of the Schrödinger equation:

$$\left\{-\frac{\hbar^2}{2\mu}\frac{d^2}{d\rho^2_\lambda} + V^\lambda_{ref}(\rho_\lambda, \varphi^0_{\lambda_i})\right\} \phi^{\lambda(s)}_{v_\lambda}(\rho_\lambda; \varphi^0_{\lambda_i}) = E^{\lambda(s)}_{v_\lambda}(\varphi^0_{\lambda_i})\, \phi^{\lambda(s)}_{v_\lambda} \tag{3.45}$$

satisfying the boundary conditions $\phi^{\lambda(s)}_{v_\lambda}(\rho_\lambda = 0) = \phi^{\lambda(s)}_{v_\lambda}(\rho_\lambda = \rho'_{\lambda_i}) = 0$ where ρ'_{λ_i} is the value of ρ_λ at the intersection of the line $\varphi_\lambda = \varphi^0_{\lambda_i}$ with the R_λ axis (Fig. 3). The potential $V^\lambda_{ref}(\rho_\lambda, \varphi_\lambda)$ is one of the reference potentials $V^\lambda_{ref}(r_\lambda, R_\lambda)$ defined in Section 3.4.2 expressed in $\rho_\lambda, \varphi_\lambda$ coordinates. Note that we have not included any j_λ dependent centrifugal terms in the Hamiltonian of Eq. 3.45 (all of these terms being included in the "propagation part" of the Hamiltonian), and hence our eigenvalues and eigenfunctions depend only on the vibrational quantum number v_λ. This is done for computational convenience and does not seriously hinder the rate of convergence of our close coupling expansion.

We now expand the solutions $\underset{\sim}{G}^{\lambda(s)}_J$ of Eq. 3.43 in terms of the vibrational functions $\phi^{\lambda(s)}_{v_\lambda}$

$$G^{\lambda(s)}_{Jj_\lambda}(\rho_\lambda,\varphi_\lambda) = \rho_\lambda^{-\frac{1}{2}} \sum_{v_\lambda} g^{\lambda(s)}_{Jv_\lambda j_\lambda}(\varphi_\lambda;\varphi^0_{\lambda_i})\, \phi^{\lambda(s)}_{v_\lambda}(\rho_\lambda;\varphi^0_{\lambda_i}) \tag{3.46}$$

The counterpart of Eq. 3.37 becomes

$$\left\{-\frac{\hbar^2}{2\mu}\frac{d^2}{d\varphi_\lambda^2} + \underset{\approx}{V}^{e\lambda(s)}_J(\varphi_\lambda;\varphi^0_{\lambda_i})\right\} \underset{\approx}{g}^{\lambda(s)\pm}_J = \underset{\approx}{\mathcal{E}}^{\lambda(s)}(\varphi^0_{\lambda_i})\, \underset{\approx}{g}^{\lambda(s)\pm}_J \tag{3.47}$$

where the effective "potential" matrix (which has physical dimensions of an energy times the square of a distance) is partitioned as

$$\begin{aligned} \underset{\approx}{V}^{e\lambda(s)}_J(\varphi_\lambda;\varphi^0_{\lambda_i}) &= \underset{\approx}{\rho}^2_\lambda \left\{\underset{\approx}{V}^{c\lambda(s)}_J(\varphi_\lambda;\varphi^0_{\lambda_i}) \right. \\ &\quad \left. + \underset{\approx}{V}^{\lambda(s)}(\varphi_\lambda;\varphi^0_{\lambda_i}) - \underset{\approx}{V}^{\lambda(s)}_{\text{ref}}(\varphi^0_{\lambda_i})\right\} \end{aligned} \tag{3.48}$$

with the matrix $\underset{\approx}{\rho}^2_\lambda$ given by

$$\left[\underset{\approx}{\rho}^2_\lambda(\varphi^0_{\lambda_i})\right]^{v'_\lambda j'_\lambda}_{v_\lambda j_\lambda} = \langle v_\lambda | \rho^2_\lambda | v'_\lambda \rangle\, \delta_{j_\lambda j'_\lambda} \tag{3.49}$$

The potential matrix $\underset{\approx}{V}^{\lambda(s)}$ and reference potential matrix $\underset{\approx}{V}^{\lambda(s)}_{\text{ref}}$ are quite similar to those in Eqs. 3.39 and 3.40 and are given by

$$\left[\underset{\approx}{V}^{\lambda(s)}\right]^{v'_\lambda j'_\lambda}_{v_\lambda j_\lambda} = \langle v_\lambda | V^\lambda_{j_\lambda j'_\lambda} | v'_\lambda \rangle \tag{3.50}$$

and

$$\left[\underset{\approx}{V}^{\lambda(s)}_{\text{ref}}\right]^{v'_\lambda j'_\lambda}_{v_\lambda j_\lambda} = \langle v_\lambda | V^\lambda_{\text{ref}} | v'_\lambda \rangle\, \delta_{j_\lambda j'_\lambda} \tag{3.51}$$

respectively, but the centrifugal potential matrix is now defined as

$$[\underset{\approx}{V}_J^{c\lambda(s)}(\varphi_\lambda;\varphi_{\lambda_i})]^{v'_\lambda j'_\lambda}_{v_\lambda j_\lambda} = \langle v_\lambda | \frac{\hbar^2}{2\mu} \{ \frac{j_\lambda^2 - \frac{1}{4}}{(r_{\lambda_0} - \rho_\lambda \cos\varphi_\lambda)^2}$$

$$+ \frac{(J - j_\lambda)^2 - \frac{1}{4}}{(R_{\lambda_0} - \rho_\lambda \sin\varphi_\lambda)^2} - \frac{1}{4\rho_\lambda^2} \} | v'_\lambda \rangle \delta_{j_\lambda j'_\lambda} \qquad (3.52)$$

where the first term in the curled bracket in Eq. 3.52 arises from the rotation of the diatom, the second from rotation of the atom-diatom system and the third is a pseudo-centrifugal potential arising from the use of the $\rho_\lambda, \varphi_\lambda$ coordinates and associated with the non-physical swinging motion around the point P_0 of Fig. 3 as φ_λ is changed. The matrix $\underset{\approx}{\mathcal{E}}^{\lambda(s)}$ is equal to the product of $\underset{\approx}{\rho}_\lambda^2$ and a diagonal matrix $\underset{\approx}{\bar{\mathcal{E}}}^{\lambda(s)}$ which is analogous to $\underset{\approx}{\mathcal{E}}^{\lambda}$ of Eq. 3.32 with the superscript (s) replacing (a). The matrices $\underset{\approx}{V}^{c\lambda(s)}$ and $\underset{\approx}{V}_{\rm ref}^{e\lambda(s)}$ are diagonal in j_λ, j'_λ but not in v_λ, v'_λ. In addition to the usual potential coupling resulting from the off-diagonal terms of $\underset{\approx}{V}^{\lambda(s)}$ we also have coupling arising from the nondiagonal $\underset{\approx}{\rho}_\lambda^2$ matrix which appears in Eq. 3.48 as a result of the swinging motion around P_0. The neglect of this latter coupling could introduce serious errors since $\underset{\approx}{\rho}_\lambda^2$ has large off-diagonal elements. Such an approximation has nevertheless often been used [14,15], since it is one of the consequences of the one vibrational basis function approximation. Note also that the effective potential matrix $\underset{\approx}{V}_J^{e\lambda(s)}$ is not symmetric, but is the product of two symmetric matrices as can be seen from Eq. 3.48. In Section 3.5 we discuss the Gordon method [35] used to integrate Eq. 3.47, and the modifications of it which are required when dealing with matrices of this type.

The smooth matching across the boundary separating any two neighboring subregions III_i is achieved through expressions analogous to Eqs. 3.41 in which the overlap matrix $\underset{\approx}{S}_i^\lambda$ is given by

$$[\underset{\approx}{S}_i^\lambda(\varphi^0_{\lambda_i})]^{v'_\lambda j'_\lambda}_{v_\lambda j_\lambda} = \delta_{j_\lambda j'_\lambda} \langle \phi^{\lambda(s)}_{v_\lambda}(\rho_\lambda;\varphi^0_{\lambda_{i+1}}) | \phi^{\lambda(s)}_{v'_\lambda}(\rho_\lambda;\varphi^0_{\lambda_i})\rangle \qquad (3.53)$$

and has elements which are independent of j_λ, j'_λ. Since the general characteristics of the ρ_λ dependence of the reference potential $V^\lambda_{\text{ref}}(\rho_\lambda, \varphi_\lambda)$ usually change quite rapidly as φ_λ is changed, the number of subregions in region III required to keep $\underset{\approx}{S}_i^\lambda$ nearly orthogonal for a truncated vibrational basis set is generally large (on the order of 20 to 30).

The smooth matching of the wavefunction ψ_J^λ across the boundary between regions II and III is achieved by the relations

$$\underset{\approx}{g}_J^{\lambda(s)\pm}(\varphi_\lambda = 0;\varphi^0_{\lambda_i}) = \underset{\approx}{\rho}_\lambda^{\frac{1}{2}}\, \underset{\approx}{g}_J^{\lambda(w)\pm}(R_{\lambda_0};R^0_{\lambda_{n^\lambda_{II}}}) \qquad (3.54a)$$

and

$$\frac{d\underset{\approx}{g}_J^{\lambda(s)\pm}}{d\varphi_\lambda}(\varphi_\lambda = 0;\varphi^0_{\lambda_i}) = -\underset{\approx}{\rho}_\lambda^{\frac{3}{2}}\, \frac{d\underset{\approx}{g}_J^{\lambda(w)\pm}}{dR_\lambda}(R_{\lambda_0};R^0_{\lambda_{n^\lambda_{II}}}) \qquad (3.54b)$$

where

$$(\underset{\approx}{\rho}^{b}_{\lambda})^{v'_\lambda j'_\lambda}_{v_\lambda j_\lambda} = \langle \phi^{\lambda(s)}_{v_\lambda} (\rho_\lambda ; \varphi^{0}_\lambda) | \rho^{b}_\lambda | \phi^{\lambda(w)}_{v'_\lambda j'_\lambda} (r_{\lambda_0} - \rho_\lambda ; R^{0}_{\lambda_{n^\lambda_{II}}}) \rangle \delta_{j_\lambda j'_\lambda} \qquad (3.55)$$

$$b = \tfrac{1}{2}, \tfrac{3}{2}$$

3.4.4. The matching region

As described in Section 3.3, the coordinates used in this region are the polar variables ζ, η_λ depicted in Fig. 4 with η_λ being the propagation variable. The Schrödinger equation in region IV is very similar to that in region III (see Eqs. 3.43 to 3.52) with $\rho_\lambda, \varphi_\lambda$ replaced by ζ, η_λ. From Eqs. 3.17 in Eq. 3.10 we obtain the counterpart to Eq. 3.43:

$$T^{\lambda(m)} \underset{\sim}{G}^{\lambda(m)}_{j} (\zeta, \eta_\lambda) + \underset{\approx}{V}^{\lambda e(m)}_{J} (\zeta, \eta_\lambda) \underset{\sim}{G}^{\lambda(m)}_{J} = E \underset{\sim}{G}^{\lambda(m)}_{J} \qquad (3.56)$$

where

$$T^{\lambda(m)} = - \frac{\hbar^2}{2\mu} \left(\frac{\partial^2}{\partial \zeta^2} + \frac{1}{\zeta} \frac{\partial}{\partial \zeta} + \frac{1}{\zeta^2} \frac{\partial^2}{\partial \eta_\lambda^2} \right) \qquad (3.57)$$

The superscript (m) denotes "matching region" and $\underset{\approx}{V}^{\lambda e(m)}_{J} (\zeta, \eta_\lambda)$ is obtained from $\underset{\approx}{V}^{\lambda e}_{J} (r_\lambda, R_\lambda)$ by using Eq. 3.17. The division of region IV into subregions is analogous to that for regions II and III, and the vibrational basis functions $\phi^{\lambda(m)}_{v_\lambda} (\zeta ; \eta^{0}_{\lambda_i})$ with eigenvalue $E^{\lambda(m)}_{v_\lambda} (\eta^{0}_{\lambda i})$ satisfy the equation

$$\left\{ - \frac{\hbar^2}{2\mu} \frac{d^2}{d\zeta^2} + V^{\lambda}_{ref} (\zeta, \eta^{0}_{\lambda_i}) \right\} \phi^{\lambda(m)}_{v_\lambda} = E^{\lambda(m)}_{v_\lambda} (\eta^{0}_{\lambda i} \; \phi^{\lambda(m)}_{v_\lambda}) \qquad (3.58)$$

with boundary conditions $\phi^{\lambda(m)}_{v_\lambda} (0) = \phi^{\lambda(m)}_{v_\lambda} (\zeta = \zeta_0) = 0$. The potential

$V^{\lambda}_{ref}(\zeta,\eta_\lambda)$ is one of the reference potentials V^{λ}_{ref} defined in Sections 3.42 and 3.43 but expressed in ζ, η_λ coordinates. Writing

$$G^{\lambda(m)}_{Jj_\lambda} = \zeta^{-\frac{1}{2}} \sum_{v_\lambda} g^{\lambda(m)}_{Jv_\lambda j_\lambda}(\eta_\lambda ; \eta^{o}_{\lambda_i})\, \phi^{\lambda(m)}_{v_\lambda}(\zeta ; \eta^{o}_{\lambda_i}) \tag{3.59}$$

the counterpart of Eq. 3.47 becomes

$$\{- \frac{\hbar^2}{2\mu} \frac{d^2}{d\eta^2_\lambda} + \underset{\approx}{V}^{e\lambda(m)}_{J}(\eta_\lambda)\}\, \underset{\approx}{g}^{\lambda(m)}_{J}(\eta_\lambda ; \eta^{o}_{\lambda_i}) = \underset{\approx}{\mathcal{E}}^{\lambda(m)}(\eta^{o}_{\lambda_i})\, \underset{\approx}{g}^{\lambda(m)}_{J} \tag{3.60}$$

where the effective "potential" matrix (again having physical dimensions of energy times square of distance) is

$$\underset{\approx}{V}^{e\lambda(m)}_{J} = \underset{\approx}{\zeta}^{2} \{\underset{\approx}{V}^{c\lambda(m)}_{J}(\eta_\lambda ; \eta^{o}_{\lambda_i}) + \underset{\approx}{V}^{\lambda(m)}(\eta_\lambda ; \eta^{o}_{\lambda_i}) - \underset{\approx}{V}^{\lambda(m)}_{ref}(\eta^{o}_{\lambda_i})\} \tag{3.61}$$

with

$$[\underset{\approx}{\zeta}^{2}]^{v'_\lambda j'_\lambda}_{v_\lambda j_\lambda} = \langle v_\lambda | \zeta^2 | v'_\lambda \rangle\, \delta_{j_\lambda j'_\lambda} \tag{3.62}$$

$\underset{\approx}{V}^{\lambda(m)}$ and $\underset{\approx}{V}^{\lambda(m)}_{ref}$ are given by Eqs. 3.50 and 3.51, respectively, with (m) replacing (s), while the centrifugal potential matrix is given by

$$[\underset{\approx}{V}^{c\lambda(m)}_{J}(\eta_\lambda ; \eta^{o}_{\lambda_i})]^{v'_\lambda j'_\lambda}_{v_\lambda j_\lambda} = \langle v_\lambda | \frac{\hbar^2}{2\mu} \{ \frac{j^2_\lambda - \frac{1}{4}}{\zeta^2 \sin^2 \eta_\lambda}$$

$$+ \frac{(J - j_\lambda)^2 - \frac{1}{4}}{\zeta^2 \cos^2 \eta_\lambda} - \frac{1}{4\zeta^2} | v'_\lambda \rangle\, \delta_{j_\lambda j'_\lambda} . \tag{3.63}$$

The energy matrix is equal to $\underset{\approx}{\zeta}^2 \underset{\approx}{\bar{\mathcal{E}}}^{\lambda(m)}$ where $\bar{\mathcal{E}}^{\lambda(m)}$ is defined by Eq. 3.32 (without the bar) with (m) substituted for (a).

Smooth transformation between subregions in region IV involves Eqs. 3.41 with the overlap matrix $\underset{\approx}{S}{}_i^\lambda$ given by

$$[\underset{\approx}{S}{}_i^\lambda(\eta^0_{\lambda_i})]^{v'_\lambda j'_\lambda}_{v_\lambda j_\lambda} = \delta_{j_\lambda j'_\lambda} \langle \phi^{\lambda(m)}_{v_\lambda}(\zeta, \eta^0_{\lambda_{i+1}}) | \phi^{\lambda(m)}_{v'_\lambda}(\zeta, \eta^0_{\lambda_i}) \rangle \qquad (3.64)$$

and the transformation between regions III and IV is achieved with equations

$$g^{\lambda(m)\pm}_{J}(\eta_{\lambda_0}; \eta^0_{\lambda_1}) = \underset{\approx}{\zeta}^{\frac{1}{2}} \underset{\approx}{g}{}^{\lambda(s)\pm}_{J}(\varphi_{\lambda_0}; \varphi^0_{\lambda_{n_{\mathrm{III}}^\lambda}}) \qquad (3.65a)$$

and

$$\frac{d\underset{\approx}{g}{}^{\lambda(m)\pm}_{J}}{d\eta_\lambda}(\eta_{\lambda_0}; \eta^0_{\lambda_1}) = \underset{\approx}{\zeta}^{\frac{3}{2}} \frac{dg^{\lambda(s)\pm}_{J}}{d\varphi_\lambda}(\varphi_{\lambda_0}; \varphi^0_{\lambda_{n_{\mathrm{III}}^\lambda}}) \qquad (3.65b)$$

where

$$(\underset{\approx}{\zeta}^{b})^{v'_\lambda j'_\lambda}_{v_\lambda j_\lambda} = \delta_{j_\lambda j'_\lambda} \langle \phi^{\lambda(m)}_{v_\lambda}(\zeta; \eta^0_{\lambda_1}) | \left(\frac{\zeta}{\rho_{\lambda_0} - \zeta}\right)^{b} | \phi^{\lambda(s)}_{v'_\lambda}(\rho_{\lambda_0} - \zeta; \varphi^0_{\lambda_{n_{\mathrm{III}}^\lambda}}) \rangle$$

$$b = \tfrac{1}{2}, \tfrac{3}{2} \qquad (3.66)$$

3.5. Integration of the Schrödinger equation

We generate solutions $\underset{\approx}{g}{}^{\lambda+}_{J}$ and their derivatives with respect to the propagation variable by choosing at $R_\lambda = R'_{\lambda_0}$ arbitrary initial values for these two matrices and integrating numerically Eqs. 3.37, 3.47 and 3.60 from the beginning of region II to the end of region IV. Similarly, we generate the $\underset{\approx}{g}_J^{\lambda -}$ solutions and their derivatives by choosing arbitrary initial values for these two matrices at $\eta_\lambda = \eta_{\lambda_1}$ and integrating numerically these equations from the end of region IV to the beginning of region II.

Any appropriate numerical procedure may be employed to integrate the coupled equations. The one we used, which is well suited to equations of the type of Eqs. 3.37, 3.47 and 3.60, is the one developed by Gordon [30]. In region II, it can be applied without modification [36], but in regions III and IV, the non-symmetric nature of the effective interaction potential matrices (Eqs. 3.48 and 3.61) requires a short modification of the method. As formulated by Gordon [35], in propagating a system of coupled equations, a transformation to a representation in which the effective potential matrix (say $\underset{\approx}{U}$) becomes diagonal is required. This necessitates finding the eigenvalues of $\underset{\approx}{U}$. In the special case where $\underset{\approx}{U}$ is symmetric, these eigenvalues are real and the eigenvector matrix is orthogonal. This simplifies the calculation and allows for an efficient program. The effective potential matrices of Regions III and IV as given by Eqs. 3.48 and 3.61 are real but non-symmetric and thus could have complex eigenvalues and eigenvectors. These potential matrices are, however, equal to the product of two symmetric matrices, one of which ($\underset{\approx}{\rho}_\lambda^2$ for Region III and $\underset{\approx}{\zeta}^2$ for region IV) is the matrix representation of a positive definite operator (ρ_λ^2 or ζ^2) and hence has positive definite eigenvalues. By using these special properties to define the "square root" of $\underset{\approx}{\rho}_{\lambda}^{2}$ and $\underset{\approx}{\zeta}^{2}$, it is shown in Appendix B that both the eigenvalues and eigenvectors of the effective potential matrix are always real but the eigenvector matrix is not generally orthogonal. This allows us to use real variables throughout the integration with the only major program changes from the usual Gordon method being in the routines needed to find the eigenvalues and eigenvectors of the effective potential matrix, and in the manipulation of the eigenvector matrices.

3.6. Restrictions and limitations

We should at this point summarize the possible limitations and restrictions on the method other than those inherent in the numerical procedures involved or those arising from computer limitations.

First, the choice of matching surfaces in Eqs. 3.2 is largely determined by the shape of the potential energy surface in Fig. 2 and for many reactions, an efficient choice will require somewhat different matching planes. A change in the exact mathematical form of the matching surfaces can significantly affect the details of the integration in region IV and in the matching procedure although the basic concepts will be preserved. In choosing the matching surfaces for a given reaction, primary consideration should be given to obtaining an efficient representation of the wavefunction in the vicinity of the matching surfaces. This requires us to avoid too large a potential anisotropy in the matching region, for in that case, our close coupling solution will require many closed rotational channels for convergence. At the same time, too small a potential anisotropy (resulting in considerable flux "leakage" through $\gamma_\lambda = \pi/2$ configurations in the matching region can result in poor convergence of the matching procedure (as will be discussed in Section 4). One therefore needs to be clever in choosing these surfaces and it is possible that for certain reactions, no choice satisfies all of the above criteria and simultaneously leads to a mathematically tractable matching procedure.

One case where the choice of surfaces specified by Eqs. 3.2 leads to a set of coupled equations in the matching region (Eqs. 3.60), which is not easily solved without including a large number of closed rotational channels, is when $\alpha_{\nu\lambda}$ (or $\alpha_{\lambda\kappa}$) $\geq 3\pi/4$. The reason for this is that when this inequality is satisfied, integration in the matching region will extend into those regions of configuration space for which r_ν (or r_κ) $= 0$; and hence will sample the very high potential energy in those configurations [for which $\gamma_\lambda = 0$ (or π)] while possibly sampling low potential energy for other configurations (near $\gamma_\lambda = \pi/2$). That this is the case can be verified by noting that during the integration in the matching region, η_λ must scan the range from $(\pi - \alpha_{\nu\lambda})/2$ to $\pi/4$ (from Eqs. 3.14, 3.15 and 3.17) and that Eq. A.5 yields $r_\nu = 0$ when $\gamma_\lambda = 0$ and $\alpha_{\nu\lambda} \geq 3\pi/4$ at some η_λ within this range. From Eqs. A.3 we note that $\alpha_{\nu\lambda} \geq 3\pi/4$ implies $m_\kappa (m_\lambda + m_\nu + m_\kappa) < m_\lambda m_\nu$ so that this restriction applies primarily to reactions with one atom of the triatomic system considerably lighter than the other two. We should also point out that this problem can be eliminated by the use of a different coordinate system in the matching region or by the use of "rotationally adiabatic" rotational basis functions [rather than $\varphi_{j_\lambda}(\gamma_\lambda)$].

When one of the three arrangement channels is closed, the method must be somewhat modified [21], but this is not a complication. Other practical limitations to the method occur for reactions where break-up collisions are allowed or for which virtual excitations to closed dissociative channels influence the other reactive and non-reactive processes significantly. The present method is not capable of treating any dissociation process, but this is not a serious limitation for many reactions at energies of chemical interest. A more general method which utilizes generalized hyperspherical functions is currently being developed in these laboratories for the purpose of treating both break-up and rearrangement collisions.

4. THE MATCHING

4.1.1. Projection of the wavefunction onto the matching surface basis functions

At the completion of the integration in arrangement channel region λ, we have generated solutions which satisfy the Schrödinger equation in that region, but which do not, in general, match smoothly with the corresponding wavefunctions obtained from the integrations in the other arrangement channel regions ν and κ. In this section we describe the procedure for accomplishing this smooth matching. This procedure may conveniently be broken up into two parts. First, we consider the projection of the full wavefunction and its normal derivative to the matching surface onto a set of orthonormal basis functions which span the two-dimensional matching surfaces. Second, we take linear combinations of the wavefunctions in each arrangement channel region and match them to linear combinations of the corresponding wavefunctions in the other arrangement channel regions. The resulting matrix equations can be solved to yield a set of smoothly matched solutions which can subsequently (see Section 5.1) be used to form the scattering solutions.

Let us consider the projection procedure for the matching surface $\pi_{\nu\lambda}$ (Fig. 2a). The analogous equations for $\pi_{\kappa\nu}$ and $\pi_{\lambda\kappa}$ are obtained from those derived below by cyclic permutation of the indices $\lambda\nu\kappa$. We first consider the wavefunction on $\pi_{\nu\lambda}$ obtained from the integration in arrangement channel λ. Using Eqs. 3.59, 3.5, 2.13 and 2.10, we get the following expression for the wavefunction in region IV (subregion i):

$$\Psi_J^{\lambda v'_\lambda j'_\lambda \pm}(\chi_\lambda, \zeta, \eta_\lambda, \gamma_\lambda) = \frac{\sqrt{2}\,\varphi_J(\chi_\lambda)}{\zeta^{\frac{3}{2}}(\sin 2\eta_\lambda)^{\frac{1}{2}}} \Big\{ \sum_{v_\lambda j_\lambda} \varphi_{j_\lambda}(\gamma_\lambda)\, \phi_{v_\lambda}^{\lambda}(\zeta; \eta_{\lambda_i}^{0}) \times g_{J v_\lambda j_\lambda}^{\lambda v'_\lambda j'_\lambda \pm}(\eta_\lambda; \eta_{\lambda_i}^{0}) \Big\} \qquad (4.1)$$

Throughout Section 4 we will consider superscript (m) of Section 3.4.4 to be present implicitly and will omit writing it explicitly. We have, however, added the indices $v'_\lambda j'_\lambda$ to denote different linearly independent solutions obtained by using different initial conditions in the numerical solution of the Schrödinger equation. As explained in

Section 3.4.1, if we truncate the close coupling expansion after N vibration-rotation basis functions, there will be N sets of indices $v'_\lambda j'_\lambda$ in Eq. 4.1.

The expression in brackets in Eq. 4.1 is expanded in terms of a different set of vibrational functions $\phi^\lambda_{v_\lambda}(\zeta;\eta^o_{\lambda_i})$ for each subregion i of region IV. We now transform to a representation in terms of a single set of vibration rotation basis functions $\varphi_{j_\lambda}(\gamma_\lambda)\,\phi^\lambda_{v_\lambda}(\zeta)$ for all of region IV. The actual functions $\phi^\lambda_{v_\lambda}(\zeta)$ to be used are arbitrary but for reactions such as H + H_2 which favor reaction through collinear geometries, the most efficient set for this purpose (as will be explained in more detail below) are the functions $\phi^\lambda_{v_\lambda}(\zeta;\eta_{\lambda_0})$ defined along the cut $\eta_\lambda = \eta_{\lambda_0}$, and which will be denoted by $\phi^\lambda_{v_\lambda}(\zeta)$ simply. The transformation equations associated with the change in the vibrational basis set are given by equations similar to Eqs. 3.41 and 3.53 where a different overlap matrix will be generated for each subregion i. We will denote the new "g" function thus obtained by $g^{\lambda v'_\lambda j'_\lambda \pm}_{Jv_\lambda j_\lambda}(\eta_\lambda)$ (we will omit the parametric η_{λ_0}). With this change of vibrational basis, we can write a single expression for $\Psi_J^{\lambda v'_\lambda j'_\lambda \pm}$ valid throughout all of Region IV:

$$\Psi_J^{\lambda v'_\lambda j'_\lambda \pm}(X_\lambda,\zeta,\eta_\lambda,\gamma_\lambda) = \frac{\sqrt{2}\,\varphi_J(X_\lambda)}{\zeta^{\frac{3}{2}}(\sin 2\eta_\lambda)^{\frac{1}{2}}}\, X_J^{\lambda v'_\lambda j'_\lambda \pm}(\eta_\lambda,\zeta,\gamma_\lambda) \qquad (4.2)$$

where

$$X_J^{\lambda v'_\lambda j'_\lambda \pm} = \sum_{v_\lambda j_\lambda} \varphi_{j_\lambda}(\gamma_\lambda)\,\phi^\lambda_{v_\lambda}(\zeta)\,g^{\lambda v'_\lambda j'_\lambda \pm}_{Jv_\lambda j_\lambda}(\eta_\lambda) \qquad (4.3)$$

On the matching surface $\pi_{\nu\lambda}$, η_λ and γ_λ are related to each other by the equation (from Eqs. A.14 and 3.18):

$$\cot 2\eta_\lambda = -\cot\alpha_{\nu\lambda}\cos\gamma_\lambda \qquad -\frac{\pi}{2} \leq \gamma_\lambda \leq \frac{\pi}{2} \tag{4.4}$$

Hence if we substitute $\eta_\lambda(\gamma_\lambda)$ as obtained from Eq. 4.4 into Eqs. 4.2 and 4.3 we obtain the desired wave function on $\pi_{\nu\lambda}$.

In order to insure a smooth matching of the wave functions, we need also to match the derivative of the wave function of Eqs. 4.2 and 4.3 at the matching surfaces. Although many types of derivatives are possible, the normal derivative $\partial/\partial n_{\nu\lambda}$ to the matching half plane possesses many useful mathematical properties (some of which are seen below), and for this reason we will consider it in the following discussion. Expressions for $\partial/\partial n_{\nu\lambda}$ in terms of γ_λ, ζ and η_λ are derived in Appendix A (Eq. A.18). Since this derivative is defined in terms of the internal variables $\eta_\lambda, \zeta, \gamma_\lambda$ we are free to choose one external variable (such as χ_λ or χ_ν) to hold constant during the differentiation process. We must, however, use this same choice in deriving all equations concerning the derivative matching on $\pi_{\nu\lambda}$. Choosing χ_λ as this external variable and introducing Eq. A.18 into Eqs. 4.2 and 4.3, and then using Eq. 4.4 to express everything on the matching surface, we obtain:

$$\frac{\partial \Psi_J^{\lambda v'_\lambda j'_\lambda \pm}}{\partial n_{\nu\lambda}} = \frac{\sqrt{2}\,\varphi_J(\chi_\lambda)\sin\alpha_{\nu\lambda}}{\zeta^{\frac{5}{2}}(\sin 2\eta_\lambda)^{\frac{3}{2}}}\, X'^{\,\lambda v'_\lambda j'_\lambda \pm}_J(\zeta, \gamma_\lambda) \tag{4.5}$$

where

$$X'^{\lambda v'_\lambda j'_\lambda}_{J}(\zeta,\gamma_\lambda) = \sum_{v_\lambda j_\lambda} \phi^{\lambda}_{v_\lambda}(\zeta)\,\varphi_{j_\lambda}(\gamma_\lambda)\left\{\frac{1}{2}\,\frac{dg^{\lambda v'_\lambda j'_\lambda \pm}_{J v_\lambda j_\lambda}}{d\eta_\lambda}\right.$$

$$\left. + \cot\alpha_{\nu\lambda}\left(\tfrac{1}{2}\cos\gamma_\lambda + i j_\lambda \sin\gamma_\lambda\right) g^{\lambda v'_\lambda j'_\lambda \pm}_{J v_\lambda j_\lambda}\left[\eta_\lambda(\gamma_\lambda)\right]\right\} \tag{4.6}$$

Note that the symbol X' does not mean that it is a derivative of X (Eq. 4.3). The derivative $dg/d\eta_\lambda$ must be evaluated by allowing η_λ to be independent of γ_λ before the expression $\eta_\lambda = \eta_\lambda(\gamma_\lambda)$ is used.

We now wish to expand the functions $X^{\lambda v'_\lambda j'_\lambda}_{J}$ and $X'^{\lambda v'_\lambda j'_\lambda}_{J}$ on the matching surface $\pi_{\nu\lambda}$ in terms of a set of basis functions $T^{\nu\lambda}_{v_\lambda j_\lambda}$ which span that surface, ζ and γ_λ being the independent variables. We choose the $T^{\nu\lambda}_{v_\lambda j_\lambda}$ to be

$$T^{\nu\lambda}_{v_\lambda j_\lambda}(\zeta,\gamma_\lambda) = \phi^{\lambda}_{v_\lambda}(\zeta)\; D^{\nu\lambda}_{j_\lambda}(\gamma_\lambda) \tag{4.7}$$

where the $\phi^{\lambda}_{v_\lambda}$'s were defined above (in the paragraph preceding Eq. 4.2), and the $D^{\nu\lambda}_{j_\lambda}(\gamma_\lambda)$ are a set of rotational functions which we shall require to be orthonormal and complete on the domain $-\frac{\pi}{2} \leq \gamma_\lambda \leq \frac{\pi}{2}$. For convenience, we will also impose the condition that $D^{\nu\lambda}_{j_\lambda}(\gamma_\lambda)$ be real and that

$$D^{\nu\lambda}_{j_\lambda}(\gamma_\lambda) = D^{\nu\lambda}_{j_\lambda}(-\gamma_\lambda)\,(-1)^{j_\lambda} \tag{4.8}$$

This is not a significantly restrictive assumption, and will lead to matching equations involving only real quantities.

The crucial characteristic in our choice of basis functions in Eq. 4.7 is the use of a set of rotational basis functions which is complete for the domain of γ_λ from $-\pi/2$ to $\pi/2$. This contrasts with the $-\pi/2$ to $3\pi/2$ interval over which the asymptotic rotational functions $\varphi_{j_\lambda}(\gamma_\lambda)$ are complete. What we have actually done is to divide the domain of γ_λ into two equal subdomains: (a) $(-\pi/2, \pi/2)$ on which we choose the $\pi_{\nu\lambda}$ rotational functions $D^{\nu\lambda}_{j_\lambda}(\gamma_\lambda)$, and (b) $(\pi/2, 3\pi/2)$ where we use the analogous functions $D^{\lambda\kappa}_{j_\lambda}(\gamma_\lambda)$ which span $\pi_{\lambda\kappa}$. The union $D^{\lambda}_{j_\lambda}(\gamma_\lambda)$ of the two sets of functions $\{D^{\nu\lambda}_{j_\lambda}, D^{\lambda\kappa}_{j_\lambda}\}$ forms a set of rotational functions which spans $(-\pi/2, 3\pi/2)$ and this allows us to establish a one-to-one correspondence between the rotational functions $D^{\lambda}_{j_\lambda}$ which span the matching surfaces, and the asymptotic functions $\varphi^{\lambda}_{j_\lambda}(\lambda_\gamma)$. More specifically, if we have N vibration rotation basis functions asymptotically in arrangement channel λ, the sum of the number of $T^{\nu\lambda}$ and $T^{\lambda\kappa}$ functions must be N. For a symmetric reaction (i.e., one in which channels ν and κ are equivalent), we must use N/2 functions in each of these two sets. In this case, the rotational quantum numbers j_λ spanned by the $T^{\nu\lambda}_{v_\lambda j_\lambda}$ (for each vibrational quantum number v_λ) include only one half of those spanned by the asymptotic functions φ_{j_λ}. The number of the latter should in such cases be even, which is not a severe constraint.

We now discuss possible choices for the functions $D^{\nu\lambda}_{j_\lambda}$. Two sets of functions which are both orthonormal and complete over the range $-\pi/2 \le \gamma_\lambda \le \pi/2$ are $(\pi)^{-\frac{1}{2}} \exp 2ij_\lambda \gamma_\lambda$ and $(\pi)^{-\frac{1}{2}} \exp(2j_\lambda+1)i\gamma_\lambda$ for $j_\lambda = 0, \pm 1, \pm 2, \cdots$. These do not satisfy the condition of Eq. 4.8, but certain linear combinations of them do such as (a) $(\pi)^{-\frac{1}{2}}$, $(2/\pi)^{\frac{1}{2}} \cos 2\gamma_\lambda$, $(2/\pi)^{\frac{1}{2}} \sin 2\gamma_\lambda$, $(2/\pi)^{\frac{1}{2}} \cos 4\gamma_\lambda$, $(2/\pi)^{\frac{1}{2}} \sin 4\gamma_\lambda, \cdots$ and (b) $(2/\pi)^{\frac{1}{2}} \sin\gamma_\lambda$, $(2/\pi)^{\frac{1}{2}} \cos\gamma_\lambda$, $(2/\pi)^{\frac{1}{2}} \sin 3\gamma_\lambda$, $(2/\pi)^{\frac{1}{2}} \cos 3\gamma_\lambda \cdots$. We can also choose mixtures of (a) and (b) above such as (c) $(2/\pi)^{\frac{1}{2}} \cos\gamma_\lambda$, $(2/\pi)^{\frac{1}{2}} \sin 2\gamma_\lambda$, $(2/\pi)^{\frac{1}{2}} \cos 3\gamma_\lambda, \cdots$. This last set of functions has the property that all its members vanish at $\gamma_\lambda = \pm\pi/2$. This makes these functions very efficient for expanding the wavefunctions for certain reactions, as described below. An alternative to analytical functions would be a numerically determined set such as the rotational eigenfunctions for some approximate potential on the matching surface. To see what these functions might look like for $H + H_2$, in Fig. 6 we plot contours of the exact potential $V(r_\lambda, R_\lambda, \gamma_\lambda)$ on the two-dimensional matching half plane $\pi_{\nu\lambda}$. The lines converging at the origin are intersections of $\pi_{\nu\lambda}$ with γ_λ = constant planes and correspond therefore to constant values of η_λ also. The figure indicates that only the region of the matching surface for which γ_λ is in the range -60° to 60° (and η_λ in the range $\eta_{\lambda_0} = 30°$ to $36.9°$) has a a low enough potential energy to contribute significantly to the reaction at energies less than 1eV. This implies that we should choose a basis set $T^{\nu\lambda}$ which describes the wavefunction best near $\gamma_\lambda = 0$, i.e., near $\eta_\lambda = \eta_{\lambda_0}$. For this reason, we previously chose the vibrational eigenfunctions $\phi^\lambda_{v_\lambda}(\zeta)$ to be solutions to Eq. 3.5 for $\eta_\lambda = \eta_{\lambda_0}$. (See paragraph preceding Eq. 4.2.) Although there is no single

γ_λ-dependent rotational potential which describes the rotational motion on the matching surface correctly for all ζ, it should be clear from Fig. 6 that rotational functions which are numerically determined from the potential on the matching surface for a fixed ζ (such as the ζ for which this potential, at $\gamma_\lambda = 0$, has a minimum) will be localized near $\gamma_\lambda = 0$ and must be very nearly zero near $\gamma_\lambda = \pm\pi/2$. For this reason, the analytical set (c) should be efficient for expanding the wavefunction on $\pi_{\nu\lambda}$. Finally, we should mention that an important test of the correctness of the method is to demonstrate the invariance of the final converged results to our choice of $D_{j_\lambda}^{\lambda}$.

We now expand the functions $X_J^{\lambda v'_\lambda j'_\lambda \pm}$ and $X_J'^{\lambda v'_\lambda j'_\lambda \pm}$ (defined by Eqs. 4.3 and 4.6), in terms of the matching surface functions $T_{v_\lambda j_\lambda}^{\nu\lambda}$ as follows:

$$X_J^{\lambda v'_\lambda j'_\lambda \pm} = \sum_{v_\lambda j_\lambda} \bar{h}_{J v_\lambda j_\lambda}^{\lambda v'_\lambda j'_\lambda \pm} \; T_{v_\lambda j_\lambda}^{\nu\lambda} (\zeta, \gamma_\lambda) \tag{4.9}$$

$$X_J'^{\lambda v'_\lambda j'_\lambda \pm} = \sum_{v_\lambda j_\lambda} \bar{h}'^{\lambda v'_\lambda j'_\lambda \pm}_{J v_\lambda j_\lambda} \; T_{v_\lambda j_\lambda}^{\nu\lambda} (\zeta, \gamma_\lambda) \tag{4.10}$$

Whereas the indices $v'_\lambda j'_\lambda$ assume N values, $v_\lambda j_\lambda$ assume fewer values than that. In view of our previous discussion, N/2 is a convenient choice for this number for the highly symmetric H_3 system.

The coefficients $\bar{h}^{\lambda v'_\lambda j'_\lambda \pm}_{J v_\lambda j_\lambda}$ and $\bar{h}'^{\lambda v'_\lambda j'_\lambda \pm}_{J v_\lambda j_\lambda}$ may be found by equating Eq. 4.3 on $\pi_{\nu\lambda}$ with Eq. 4.9, and Eq. 4.6 with Eq. 4.10, multiplying the resulting expressions by $T^{*\nu\lambda}_{v_\lambda j_\lambda}$ and integrating them over ζ and γ_λ using the orthonormality of the $T^{\nu\lambda}_{v_\lambda j_\lambda}$ functions on the matching surface and Eq. 4.8. We get

$$\bar{h}^{\lambda v'_\lambda j'_\lambda \pm}_{J v_\lambda j_\lambda} = \sqrt{\frac{2}{\pi}} \sum_{j''_\lambda} \int_0^{\pi/2} d\gamma_\lambda \, D^{\nu\lambda}_{j_\lambda}(\gamma_\lambda) \, g^{\lambda v'_\lambda j'_\lambda \pm}_{J v_\lambda j''_\lambda}[\eta_\lambda(\gamma_\lambda)] \left\{ \begin{matrix} \cos j''_\lambda \gamma_\lambda \\ i \sin j''_\lambda \gamma_\lambda \end{matrix} \right\} \tag{4.11}$$

$$\begin{aligned} \bar{h}'^{\lambda v'_\lambda j'_\lambda \pm}_{J v_\lambda j_\lambda} = \frac{1}{\sqrt{2\pi}} \sum_{j''_\lambda} \int_0^{\pi/2} d\gamma_\lambda \, D^{\nu\lambda}_{j_\lambda}(\gamma_\lambda) & \left[\frac{d g^{\lambda v'_\lambda j'_\lambda \pm}_{J v_\lambda j''_\lambda}}{d\eta_\lambda} (\eta_\lambda(\gamma_\lambda)) \right. \\ \times \left\{ \begin{matrix} \cos j''_\lambda \gamma_\lambda \\ i \sin j''_\lambda \gamma_\lambda \end{matrix} \right\} + \cot \alpha_{\nu\lambda} & \left((j''_\lambda + \tfrac{1}{2}) \left\{ \begin{matrix} \cos (j''_\lambda + 1) \gamma_\lambda \\ i \sin (j''_\lambda + 1) \gamma_\lambda \end{matrix} \right\} \right. \\ - (j''_\lambda - \tfrac{1}{2}) \left\{ \begin{matrix} \cos (j''_\lambda - 1) \gamma_\lambda \\ i \sin (j''_\lambda - 1) \gamma_\lambda \end{matrix} \right\} \Bigg) & \left. g^{\lambda v'_\lambda j'_\lambda \pm}_{J v_\lambda j''_\lambda} (\eta_\lambda(\gamma_\lambda)) \right] \end{aligned} \tag{4.12}$$

where the upper term in the curled brackets is to be used for even j_λ, and the lower for odd j_λ.

We now must consider the expansion of the wave function obtained from the integration in channel ν, in the same matching surface basis functions $T^{\nu\lambda}_{v_\lambda j_\lambda}$ of Eq. 4.7. To do this we first express the wave-function and its normal derivative in a form analogous to Eqs. 4.2, 4.3, 4.4, 4.5 and 4.6. For the wavefunction we get

$$\Psi_J^{\nu v'_\nu j'_\nu \pm} = \frac{\sqrt{2}\, \varphi_J(X_\nu)}{\zeta^{\frac{3}{2}} (\sin 2\eta_\nu)^{\frac{1}{2}}} \; X_J^{\nu v'_\nu j'_\nu \pm}(\eta_\nu, \zeta, \gamma_\nu) \tag{4.13}$$

where

$$X_J^{\nu v'_\nu j'_\nu \pm} = \sum_{v_\nu j_\nu} \varphi_{j_\nu}(\gamma_\nu)\, \phi^\nu_{v_\nu}(\zeta)\, g_{J v_\nu j_\nu}^{\nu v'_\nu j'_\nu \pm}(\eta_\nu) \tag{4.14}$$

The vibrational basis function $\phi^\nu_{v_\nu}(\zeta)$ is defined in a manner similar to $\phi^\lambda_{v_\lambda}(\zeta)$ and, in fact, may be identical to it (for $v_\nu = v_\lambda$) if the reference potentials are defined appropriately. In terms of the ν arrangement channel coordinates, the relation between η_ν and γ_ν on the matching surface $\pi_{\nu\lambda}$ is given by:

$$\cot 2\eta_\nu = \cot \alpha_{\nu\lambda} \cos\gamma_\nu \tag{4.15}$$

$$\frac{\pi}{2} \leqslant \gamma_\nu \leqslant \frac{3\pi}{2}$$

This is easily derived from Eq. 4.4, using the relations A.12 and A.15 of the Appendix and Eq. 3.18.

In calculating the normal derivative of the wavefunction of Eq. 4.13 on the matching surface $\pi_{\nu\lambda}$, we must remember that X_λ must be held constant during the differentiation. It is therefore desirable to express X_ν in Eq. 4.13 in terms of X_λ

$$\chi_\nu = \chi_\lambda + \Delta\chi_{\nu\lambda} \tag{4.16}$$

where $\Delta\chi_{\nu\lambda}$ is a function of the internal variables $R_\lambda, r_\lambda, \gamma_\lambda$ only as seen in Eqs. A.9 of the Appendix. If we express those two equations in terms of the variables η_λ, ζ and γ_λ, then find the normal derivative of $\Delta\chi_{\nu\lambda}$ using Eq. A. 18 and finally use Eq. 4.4 to express all quantities on the matching surface $\pi_{\nu\lambda}$, we obtain the very useful equation valid only on this surface:

$$\frac{\partial\Delta\chi_{\nu\lambda}}{\partial n_{\nu\lambda}}(\zeta,\eta_\lambda,\gamma_\lambda) = 0 \tag{4.17}$$

As a consequence of this simplification, we can express the normal derivative of the wavefunction in arrangement channel ν on $\pi_{\nu\lambda}$ by:

$$\frac{\partial\Psi_J^{\nu v'_\nu j'_\nu \pm}}{\partial n_{\nu\lambda}} = \frac{\sqrt{2}\,\varphi_J(\chi_\lambda)\,e^{iJ\Delta\chi_{\nu\lambda}}}{\zeta^{\frac{5}{2}}(\sin 2\eta_\nu)^{\frac{3}{2}}}\,\chi'^{\,\nu v'_\nu j'_\nu \pm}_J(\zeta,\gamma_\nu) \tag{4.18}$$

where

$$\chi'^{\,\nu v'_\nu j'_\nu}_J(\zeta,\gamma_\nu) = \sum_{j_\nu v_\nu} \varphi_{j_\nu}(\gamma_\nu)\,\phi^\nu_{v_\nu}(\zeta)\left\{\frac{1}{2}\left(\frac{dg^{\nu v'_\nu j'_\nu \pm}_{Jv'_\nu j'_\nu}}{d\eta_\nu}\right)_{\eta_\nu=\eta_\nu(\gamma_\nu)}\right.$$

$$\left. - \cot\alpha_{\nu\lambda}\left(\tfrac{1}{2}\cos\gamma_\nu + ij_\nu\sin\gamma_\nu\right) g^{\nu v'_\nu j'_\nu \pm}_{Jv_\nu j_\nu}\left(\eta_\nu(\gamma_\nu)\right)\right\} \tag{4.19}$$

We now expand the functions $\chi_J^{\nu v_\nu j_\nu \pm}$ and $\chi_J'^{\,\nu v_\nu j_\nu \pm}$ in terms of the matching surface functions $T^{\nu\lambda}_{v_\nu j_\nu}(\zeta,\gamma_\lambda)$. Note that we use the λ arrangement channel variables to express the ν arrangement channel wave function, using the transformation equations A.12, A.14 and 3.18 to relate the λ and ν sets of coordinate systems. The resulting expansions are

$$\chi_J^{\nu v_\nu' j_\nu' \pm}(\zeta,\gamma_\lambda) = \sum_{v_\nu j_\nu} \bar{f}_{J v_\nu j_\nu}^{\nu v_\nu' j_\nu' \pm} \; T^{\nu\lambda}_{v_\nu j_\nu}(\zeta,\gamma_\lambda) \tag{4.20}$$

$$\chi_J'^{\,\nu v_\nu' j_\nu' \pm}(\zeta,\gamma_\lambda) = \sum_{v_\nu j_\nu} \bar{f}_{J v_\nu j_\nu}'^{\,\nu v_\nu' j_\nu' \pm} \; T^{\nu\lambda}_{v_\nu j_\nu}(\zeta,\gamma_\lambda) \tag{4.21}$$

where the expansion coefficients are given by:

$$\bar{f}_{J v_\nu j_\nu}^{\nu v_\nu' j_\nu' \pm} = \sqrt{\frac{2}{\pi}} \int_0^{\pi/2} d\gamma_\lambda \sum_{v_\nu'' j_\nu''} (-1)^{j_\nu''} S^{\nu\lambda}_{v_\nu v_\nu''} D^{\nu\lambda}_{j_\nu}(\gamma_\lambda)$$

$$\times\, g^{\nu v_\nu' j_\nu' \pm}_{J v_\nu'' j_\nu''}\Big(\eta_\nu\big(\gamma_\nu(\gamma_\lambda)\big)\Big) \left\{ \begin{array}{c} \cos j_\nu'' \gamma_\lambda \\ -i \sin j_\nu'' \gamma_\lambda \end{array} \right\} \tag{4.22}$$

$$\vec{f}^{\,\nu v'_\nu j'_\nu \pm}_{J v_\nu j_\nu} = -\frac{1}{\sqrt{2\pi}} \int_0^{\pi/2} d\gamma_\lambda \sum_{v''_\nu j''_\nu} (-1)^{j''_\nu} S^{\nu\lambda}_{v_\nu v''_\nu} D^{\nu\lambda}_{j_\nu} (\gamma_\lambda)$$

$$\times \Bigg[\left(\frac{d g^{\nu v'_\nu j'_\nu \pm}_{J v''_\nu j''_\nu}}{d\eta_\nu} \right)_{\eta_\nu = \eta_\nu(\gamma_\nu(\gamma_\lambda))} \left\{ \begin{matrix} \cos j''_\nu \gamma_\lambda \\ -i \sin j''_\nu \gamma_\lambda \end{matrix} \right\} + \cot\alpha_{\nu\lambda} \Bigg((j''_\nu - \tfrac{1}{2})$$

$$\left\{ \begin{matrix} \cos (j''_\nu + 1) \gamma_\lambda \\ -i \sin (j''_\nu + 1) \gamma_\lambda \end{matrix} \right\} - (j''_\nu - \tfrac{1}{2}) \left\{ \begin{matrix} \cos (j''_\nu - 1) \gamma_\lambda \\ -i \sin (j''_\nu - 1) \gamma_\lambda \end{matrix} \right\} \Bigg) g^{\nu v_\nu j_\nu \pm}_{J v_\nu j_\nu} \left(\eta_\nu \left(\gamma_\nu \left(\gamma_\lambda \right) \right) \right) \Bigg] \tag{4.23}$$

where

$$S^{\nu\lambda}_{v_\nu v_{\nu'}} = \int_0^\infty \phi^\lambda_{v_\nu} (\zeta)\, \phi^\nu_{v_{\nu'}} (\zeta)\, d\zeta \tag{4.24}$$

As before, the upper term in the curled brackets is used for even j_ν and the lower for odd j_ν.

4.2. The matching equations

With the wavefunctions from the integrations in both channels ν and λ expressed in terms of the basis set $T^{\nu\lambda}_{v_\lambda j_\lambda}(\zeta, \gamma_\lambda)$ on $\pi_{\nu\lambda}$, we can now take the appropriate linear combinations of these solutions to yield solutions to the full Schrödinger equation which are continuous and smooth throughout all of configuration space. Let us denote the fully matched solutions thus obtained by $\Phi^{(i)vj}_J$. There are N set of indices vj and the superscript (i) can have the values 1, 2 or 3. The full set of indices (i)vj thus scans 3N values and we will therefore obtain 3N linearly independent solutions to the Schrödinger equation [37].

We now write $\Phi_J^{(i)vj}$ in terms of the solutions $\Psi_J^{\lambda v_\lambda j_\lambda}$ and also in terms of the $\Psi_J^{\nu v_\nu j_\nu}$:

$$\Phi_J^{(i)vj} = \sum_{v'_\lambda j'_\lambda} \left\{ \Psi_J^{\lambda v'_\lambda j'_\lambda +} C^{(i)vj+}_{J\lambda v'_\lambda j'_\lambda} + \Psi_J^{\lambda v'_\lambda j'_\lambda -} C^{(i)vj-}_{J\lambda v'_\lambda j'_\lambda} \right\}$$

$$= \sum_{v'_\nu j'_\nu} \left\{ \Psi_J^{\nu v'_\nu j'_\nu +} C^{(i)vj+}_{J\nu v'_\nu j'_\nu} + \Psi_J^{\nu v'_\nu j'_\nu -} C^{(i)vj-}_{J\nu v'_\nu j'_\nu} \right\} \qquad (4.25)$$

and

$$\frac{\partial \Phi_J^{(i)vj}}{\partial n_{\nu\lambda}} = \sum_{v'_\lambda j'_\lambda} \left\{ \frac{\partial \Psi_J^{\lambda v'_\lambda j'_\lambda +}}{\partial n_{\nu\lambda}} C^{(i)vj+}_{J\lambda v'_\lambda j'_\lambda} + \frac{\partial \Psi_J^{\lambda v'_\lambda j'_\lambda -}}{\partial n_{\nu\lambda}} C^{(i)vj-}_{J\nu v'_\nu j'_\nu} \right\}$$

$$= \sum_{v'_\nu j'_\nu} \left\{ \frac{\partial \Psi_J^{\nu v'_\nu j'_\nu +}}{\partial n_{\nu\lambda}} C^{(i)vj+}_{J\nu v'_\nu j'_\nu} + \frac{\partial \Psi_J^{\nu v'_\nu j'_\nu -}}{\partial n_{\nu\lambda}} C^{(i)vj-}_{J\nu v'_\nu j'_\nu} \right\} \qquad (4.26)$$

The coefficients $C^{(i)vj\pm}_{J\lambda v'_\lambda j'_\lambda}$ and $C^{(i)vj\pm}_{J\nu v'_\nu j'_\nu}$ are to be determined by applying these two sets of equations on $\pi_{\nu\lambda}$ (and similar equations on $\pi_{\kappa\nu}$ and $\pi_{\lambda\kappa}$), and by imposing the scattering solution boundary conditions as explained in Section 5.1. Equations 4.25 and 4.26, when evaluated on $\pi_{\nu\lambda}$, comprise the smooth matching conditions.

By substituting Eqs. 4.2, 4.13 and 4.16 into Eqs. 4.25, we obtain the following expression

$$\sum_{v'_\lambda j'_\lambda} \left\{ \chi_J^{\lambda v'_\lambda j'_\lambda +} \; C^{(i)vj+}_{J\lambda v'_\lambda j'_\lambda} + \chi_J^{\lambda v'_\lambda j'_\lambda -} \; C^{(i)vj-}_{J\lambda v'_\lambda j'_\lambda} \right\}$$

$$= e^{iJ\Delta\chi_{\nu\lambda}} \sum_{v'_\nu j'_\nu} \left\{ \chi_J^{\nu v'_\nu j'_\nu +} \; C^{(i)vj+}_{J\nu v'_\nu j'_\nu} + \chi_J^{\nu v'_\nu j'_\nu -} \; C^{(i)vj-}_{J\nu v'_\nu j'_\nu} \right\} \qquad (4.27)$$

The analogous expression for the normal derivatives is obtained from Eq. 4.27 by replacing "χ" by "χ'" in that equation. If we now substitute the expansions given by Eqs. 4.9, 4.10, 4.20 and 4.21 into Eq. 4.27 and its equivalent for the normal derivatives then multiply through by $T^{\nu\lambda}_{v_\lambda j_\lambda}(\zeta, \gamma_\lambda)$, use the relations between the λ and ν coordinates given by Eqs. A.12, A.14 and 3.18 and integrate over ζ and γ_λ, we obtain the following system of linear algebraic equations:

$$\sum_{v'_\lambda j'_\lambda} \left\{ \bar{h}^{\lambda v'_\lambda j'_\lambda +}_{J v_\lambda j_\lambda} \; C^{(i)vj+}_{J\lambda v'_\lambda j'_\lambda} + \bar{h}^{\lambda v'_\lambda j'_\lambda -}_{J v_\lambda j_\lambda} \; C^{(i)vj}_{J\lambda v'_\lambda j'_\lambda} \right\}$$

$$= \sum_{v_\nu j_\nu} \left(\bar{\underset{\approx}{s}}^{J}_{\nu\lambda}\right)^{v_\nu j_\nu}_{v_\lambda j_\lambda} \sum_{v'_\nu j'_\nu} \left\{ \bar{f}^{\nu v'_\nu j'_\nu +}_{J v_\nu j_\nu} \; C^{(i)vj+}_{J\nu v'_\nu j'_\nu} + \bar{f}^{\nu v'_\nu j'_\nu -}_{J v_\nu j_\nu} \; C^{(i)vj-}_{J\nu v'_\nu j'_\nu} \right\} \qquad (4.28)$$

with the analogous equation for derivatives obtained by using $\bar{h}'$ and $\bar{f}'$ instead of $\bar{h}$ and $\bar{f}$ above. The matrix $\bar{\underset{\approx}{s}}^{J}_{\nu\lambda}$ is defined by

$$(\bar{s}^{J}_{\nu\lambda})^{v_\nu j_\nu}_{v_\lambda j_\lambda} = \delta_{v_\lambda v_\nu} \times \left\{ \begin{array}{l} 2 \int_0^{\pi/2} D_{j_\lambda} D_{j_\nu} \cos J \Delta \chi_{\nu\lambda} \, d\gamma_\lambda \\ \qquad\qquad \text{for } j_\lambda + j_\nu = \text{even} \\ 2i \int_0^{\pi/2} D_{j_\lambda} D_{j_\nu} \sin J \Delta \chi_{\nu\lambda} \, d\gamma_\lambda \\ \qquad\qquad \text{for } j_\lambda + j_\nu = \text{odd} \end{array} \right\} . \tag{4.29}$$

or, by the expression (which is only equivalent to it for a complete set of functions $T^{\nu\lambda}$)

$$\underset{\approx}{\bar{s}}{}^{J}_{\nu\lambda} = \exp (i J \underset{\approx}{\Delta}^{\nu\lambda}) \tag{4.30}$$

where

$$(\underset{\approx}{\Delta}^{\nu\lambda})^{v_\nu j_\nu}_{v_\lambda j_\lambda} = \langle T^{\nu\lambda}_{v_\lambda j_\lambda} | \Delta \chi_{\nu\lambda} | T^{\nu\lambda}_{v_\nu j_\nu} \rangle \tag{4.31}$$

As should be evident from Eqs. 4.30 and 4.31, the matrix $\underset{\approx}{\bar{s}}{}^{J}_{\nu\lambda}$ is unitary, since $\Delta\chi_{\nu\lambda}$ is real and therefore $\underset{\approx}{\Delta}^{\nu\lambda}$ is hermitian.

By examining the definitions given in Eqs. 4.11, 4.12, 4.22, 4.23 and 4.29 for the various symbols used in Eq. 4.28 and its equivalent for the derivatives, we find that the latter set of equations involve either purely real terms or purely imaginary terms. Let us omit the factor i appearing in Eqs. 4.11, 4.12, 4.22 and 4.23, and replace it in Eq. 4.29 by $(-1)^{j_\nu}$. We denote all of the real coefficients thus obtained by removing the bars which previously appeared above their symbols. Eq. 4.28 and its normal derivative counterpart continue to be valid for the unbarred quantities, which permits all of the calculations associated with the matching to be performed using real number arithmetic, a considerable computational simplification. Regarding the real coefficients appearing in these equations as elements of matrices, we can rewrite them as

$$\underset{\approx}{h}_J^{\lambda+}\,\underset{\approx}{C}_{J\lambda}^{(i)+} + \underset{\approx}{h}_J^{\lambda-}\,\underset{\approx}{C}_{J\lambda}^{(i)-} = \underset{\approx}{s}_{\nu\lambda}^{J}\left\{\underset{\approx}{f}_J^{\nu+}\,\underset{\approx}{C}_{J\nu}^{(i)+} + \underset{\approx}{f}_J^{\nu-}\,\underset{\approx}{C}_{J\nu}^{(i)-}\right\} \qquad (4.32)$$

and

$$\underset{\approx}{h}{}_J^{\prime\,\lambda+}\,\underset{\approx}{C}_{J\lambda}^{(i)+} + \underset{\approx}{h}{}_J^{\prime\,\lambda-}\,\underset{\approx}{C}_{J\lambda}^{(i)-} = \underset{\approx}{s}_{\nu\lambda}^{J}\left\{\underset{\approx}{f}{}_J^{\prime\,\nu+}\,\underset{\approx}{C}_{J\nu}^{(i)+} + \underset{\approx}{f}{}_J^{\prime\,\nu-}\,\underset{\approx}{C}_{J\nu}^{(i)-}\right\} \qquad (4.33)$$

where $\underset{\approx}{s}_{\nu\lambda}^{J}$ is orthogonal if the $T^{\nu\lambda}$ form a complete set. As shown in the previous section, the number of basis functions $T_{v_\lambda j_\lambda}^{\nu\lambda}$ used to expand the wavefunction on $\pi_{\nu\lambda}$ is N/2 where N is the total number of vibration-rotation functions used in the close coupling expansion. This implies that there should only be N/2 rows in the matrices $\underset{\approx}{h}_J^{\lambda\pm}$. There are, however, N columns because the different columns denote the N linearly independent solutions propagated in either the forward (+) or backwards (-) integrations. Summarizing, the dimensions of the various matrices in Eqs. 4.32 or 4.33 are symbolically represented as follows:

$$\begin{aligned}&(N/2\times N)\,(N\times N) + (N/2\times N)\,(N\times N)\\&\qquad = (N/2\times N/2)\left\{(N/2\times N)\,(N\times N) + (N/2\times N)\,(N\times N)\right\}\end{aligned} \qquad (4.34)$$

We can combine Eqs. 4.32 and 4.33 into a single expression which contains only square N × N matrices by defining the augmented N × N matrices $\hat{\underset{\approx}{h}}{}^{\lambda\pm}_{J}$, $\hat{\underset{\approx}{f}}{}^{\nu\pm}_{J}$ and $\hat{\underset{\approx}{s}}{}^{J}_{\nu\lambda}$ as

$$\hat{\underset{\approx}{h}}{}^{\lambda\pm}_{J} = \begin{pmatrix} \underset{\approx}{h}{}^{\lambda\pm}_{J} \\ \underset{\approx}{h}{}'^{\lambda\pm}_{J} \end{pmatrix} \tag{4.35}$$

$$\hat{\underset{\approx}{f}}{}^{\nu\pm}_{J} = \begin{pmatrix} \underset{\approx}{f}{}^{\nu\pm}_{J} \\ \underset{\approx}{f}{}'^{\nu\pm}_{J} \end{pmatrix} \tag{4.36}$$

$$\hat{\underset{\approx}{s}}{}^{J}_{\nu\lambda} = \begin{pmatrix} \underset{\approx}{s}{}^{J}_{\nu\lambda} & \underset{\approx}{O} \\ \underset{\approx}{O} & \underset{\approx}{s}{}^{J}_{\nu\lambda} \end{pmatrix} \tag{4.37}$$

where $\underset{\approx}{O}$ denotes an (N/2 × N/2) matrix of zeros. The resulting matching equation on $\pi_{\nu\lambda}$ becomes

$$\hat{\underset{\approx}{h}}{}^{\lambda+}_{J}\, \underset{\approx}{C}{}^{(i)+}_{J\lambda} + \hat{\underset{\approx}{h}}{}^{\lambda-}_{J}\, \underset{\approx}{C}{}^{(i)-}_{J\lambda} = \hat{\underset{\approx}{s}}{}^{J}_{\nu\lambda} \left\{ \hat{\underset{\approx}{f}}{}^{\nu+}_{J}\, \underset{\approx}{C}{}^{(i)+}_{J\nu} + \hat{\underset{\approx}{f}}{}^{\nu-}_{J}\, \underset{\approx}{C}{}^{(i)-}_{J\nu} \right\} \tag{4.38}$$

In order to solve for the unknown matrix of coefficients $\underset{\approx}{C}{}^{(i)\pm}_{J\lambda}$, $\underset{\approx}{C}{}^{(i)\pm}_{J\nu}$ (and $\underset{\approx}{C}{}^{(i)\pm}_{J\kappa}$), we must couple Eq. 4.38 with the corresponding equations obtained from the matching on $\pi_{\kappa\nu}$ and $\pi_{\lambda\kappa}$. Using the same notation as in Eq. 4.38, the matching equations on these two additional surfaces are

$$\underset{\approx}{\hat{h}}{}^{\nu+}_{J}\,\underset{\approx}{C}{}^{(i)+}_{J\nu} + \underset{\approx}{\hat{h}}{}^{\nu-}_{J}\,\underset{\approx}{C}{}^{(i)-}_{J\nu} = \underset{\approx}{\hat{s}}{}^{J}_{\kappa\nu}\left\{ \underset{\approx}{\hat{f}}{}^{\kappa+}_{J} C^{(i)+}_{J\kappa} + \underset{\approx}{\hat{f}}{}^{\kappa-}_{J}\,\underset{\approx}{C}{}^{(i)-}_{J\kappa} \right\} \tag{4.39}$$

and

$$\underset{\approx}{\hat{h}}{}^{\kappa+}_{J}\,\underset{\approx}{C}{}^{(i)+}_{J\kappa} + \underset{\approx}{\hat{h}}{}^{\kappa-}_{J}\,\underset{\approx}{C}{}^{(i)-}_{J\kappa} = \underset{\approx}{\hat{s}}{}^{J}_{\lambda\kappa}\left\{ \underset{\approx}{\hat{f}}{}^{\lambda+}_{J}\,\underset{\approx}{C}{}^{(i)+}_{J\lambda} + \underset{\approx}{\hat{f}}{}^{\lambda-}_{J}\,\underset{\approx}{C}{}^{(i)-}_{J\lambda} \right\} \tag{4.40}$$

We can now combine Eqs. 4.38, 4.39 and 4.40 into the following single matrix equation which involves matrices of dimension $3N \times 3N$

$$\underset{\approx}{N}{}^{+}_{J}\,\underset{\approx}{C}{}^{+}_{J} + \underset{\approx}{N}{}^{-}_{J}\,\underset{\approx}{C}{}^{-}_{J} = \underset{\approx}{O} \tag{4.41}$$

where

$$\underset{\approx}{N}{}^{\pm}_{J} = \begin{pmatrix} \underset{\approx}{\hat{h}}{}^{\lambda\pm}_{J} & -\underset{\approx}{\hat{s}}{}^{J}_{\nu\lambda}\,\underset{\approx}{\hat{f}}{}^{\nu\pm}_{J} & \underset{\approx}{O} \\ \underset{\approx}{O} & \underset{\approx}{\hat{h}}{}^{\nu\pm}_{J} & -\underset{\approx}{\hat{s}}{}^{J}_{\kappa\nu}\,\underset{\approx}{\hat{f}}{}^{\kappa\pm}_{J} \\ -\underset{\approx}{\hat{s}}{}^{J}_{\lambda\kappa}\,\underset{\approx}{\hat{f}}{}^{\lambda\pm}_{J} & \underset{\approx}{O} & \underset{\approx}{\hat{h}}{}^{\kappa\pm}_{J} \end{pmatrix} \tag{4.42}$$

$$\underset{\approx}{C}{}^{\pm}_{J} = \begin{pmatrix} \underset{\approx}{C}{}^{(1)\pm}_{J\lambda} & \underset{\approx}{C}{}^{(2)\pm}_{J\lambda} & \underset{\approx}{C}{}^{(3)\pm}_{J\lambda} \\ \underset{\approx}{C}{}^{(1)\pm}_{J\nu} & \underset{\approx}{C}{}^{(2)\pm}_{J\nu} & \underset{\approx}{C}{}^{(3)\pm}_{J\nu} \\ \underset{\approx}{C}{}^{(1)\pm}_{J\kappa} & \underset{\approx}{C}{}^{(2)\pm}_{J\kappa} & \underset{\approx}{C}{}^{(3)\pm}_{J\kappa} \end{pmatrix} \tag{4.43}$$

and the $\underset{\approx}{O}$ stands for a matrix of zeros of the appropriate dimensionality. Let us rearrange Eq. 4.41 to the form

$$\underset{\approx}{C}_J^{+} (\underset{\approx}{C}_J^{-})^{-1} = -(\underset{\approx}{N}_J^{+})^{-1} \underset{\approx}{N}_J^{-} \tag{4.44}$$

Equation 4.44 is the essential result of the smooth matching procedure. It expresses the unknown coefficients $\underset{\approx}{C}_J^{\pm}$ in terms of the known $\underset{\approx}{N}_J^{\pm}$ and thus determines which linear combination of the solutions obtained from the integrations in each arrangement channel region will produce smoothly matched wavefunctions. Of course, Equation 4.44 supplies only one $3N \times 3N$ matrix equation for the two $3N \times 3N$ unknown matrices $\underset{\approx}{C}_J^{\pm}$. This tells us that our matched solutions are not completely unique which is not unexpected since we have not yet specified the asymptotic conditions which our matched wavefunctions must satisfy. We will do so in the next section, and when these additional conditions are combined with Eq. 4.43, we will obtain unique expressions for the coefficient matrices $\underset{\approx}{C}_J^{\pm}$.

5. ASYMPTOTIC ANALYSIS

5.1. The reactance and scattering matrices

We will now describe how to obtain the reactance $(\underset{\approx}{R}_J)$ and scattering $(\underset{\approx}{S}_J)$ matrices from the asymptotic values of the primitive (but smoothly matched) solutions $\Phi_J^{(i)j\nu}$ described in the previous section. These functions are defined in the entire configuration space. Their asymptotic behavior in each of the three arrangement channels $\lambda = \alpha, \beta, \gamma$ can be obtained from Eqs. 3.22, 3.5, 2.13 and 4.25, and is

$$\Phi_J^{(i)vj} \underset{R_\lambda \to \infty}{\sim} \varphi_J(\chi_\lambda) \sum_{v_\lambda j_\lambda} \frac{\varphi_{j_\lambda}(\gamma_\lambda)\, \phi^\lambda_{v_\lambda j_\lambda}(r_\lambda)}{\sqrt{r_\lambda R_\lambda}}$$

$$\sum_{v''_\lambda j''_\lambda} \left\{ g^{\lambda v''_\lambda j''_\lambda +}_{J v_\lambda j_\lambda}\, C^{(i)vj+}_{J\lambda v''_\lambda j''_\lambda} + g^{\lambda v''_\lambda j''_\lambda -}_{J v_\lambda j_\lambda}\, C^{(i)vj-}_{J\lambda v''_\lambda j''_\lambda} \right\} \tag{5.1}$$

$$\lambda = \alpha, \beta, \gamma$$

where we have dropped the superscript (a) as it will be implicit throughout Section 5. The product functions $r_\lambda^{-\frac{1}{2}} \varphi_{j_\lambda}(\gamma_\lambda)\, \phi^\lambda_{v_\lambda j_\lambda}(\gamma_\lambda)$ are the asymptotic vibration-rotation wavefunctions of the diatomic molecule corresponding to the λ arrangement channel. We note that $\phi^\lambda_{v_\lambda j_\lambda}(r_\lambda)$ vanishes in the asymptotic regions of arrangement channels ν and κ because $r_\lambda \to \infty$ in these regions. As a result, Eq. 5.1 can be rewritten as

$$\Phi_J^{(i)vj} \sim \sum_\lambda \varphi_J(\chi_\lambda) \sum_{v_\lambda j_\lambda} \frac{\varphi_{j_\lambda}(\gamma_\lambda)\, \phi^\lambda_{v_\lambda j_\lambda}(r_\lambda)}{\sqrt{r_\lambda R_\lambda}}\; e^{(i)vj}_{J\lambda v_\lambda j_\lambda}(R_\lambda) \tag{5.2}$$

where

$$e^{(i)vj}_{J\lambda v_\lambda j_\lambda} = \sum_{v''_\lambda j''_\lambda} \left\{ g^{\lambda v''_\lambda j''_\lambda +}_{J v_\lambda j_\lambda}\, C^{(i)vj+}_{J v''_\lambda j''_\lambda} + g^{\lambda v''_\lambda j''_\lambda -}_{J v_\lambda j_\lambda}\, C^{(i)vj-}_{J\lambda v''_\lambda j''_\lambda} \right\} \tag{5.3}$$

and λ summation extends over arrangement channels α, β and γ. The analogous expression for the function $R_\lambda^{-\frac{1}{2}} \frac{\partial}{\partial R_\lambda} (R_\lambda^{\frac{1}{2}} \Phi_J^{(i)vj})$ is obtained from Eqs. 5.2 and 5.3 by replacing $g_{Jv_\lambda j_\lambda}^{\lambda v''_\lambda j''_\lambda}$ by $\frac{dg_{Jv_\lambda j_\lambda}^{\lambda v''_\lambda j''_\lambda}}{dR_\lambda}$ in the latter.

We now define the reactance and scattering matrix solution for each partial wave J. In analogy with their corresponding three-dimensional multichannel definitions [34], and using the asymptotic behavior of the coplanar solutions given in Eqs. 3.25, we define the reactance and scattering solutions and the corresponding matrices as follows

$$\Psi_{R,SJ}^{\lambda' v_{\lambda'} j_{\lambda'}} \sim \sum_{\lambda} \varphi_J(\chi_\lambda) \sum_{v_\lambda j_\lambda} \frac{\varphi_{j_\lambda}(\gamma_\lambda)\, \phi^{\lambda}_{v_\lambda j_\lambda}(r_\lambda)}{\sqrt{r_\lambda R_\lambda}}\, b_{R,SJ\lambda v_\lambda j_\lambda}^{\lambda' v_{\lambda'} j_{\lambda'}}(R_\lambda) \tag{5.4}$$

where, for the $\underset{\approx}{R}_J$ matrix solution,

$$b_{RJ\lambda v_\lambda j_\lambda}^{\lambda' v_{\lambda'} j_{\lambda'}} = \left(\frac{\mu R_\lambda}{\hbar}\right)^{\frac{1}{2}} \begin{cases} J_{J-j_\lambda}(k^\lambda_{v_\lambda j_\lambda} R_\lambda)\, \delta^{\lambda v_\lambda j_\lambda}_{\lambda' v_{\lambda'} j_{\lambda'}} + Y_{J-j_\lambda}(k_{v_\lambda j_\lambda} R_\lambda)\, R^{\lambda v_\lambda j_\lambda}_{J\lambda' v_{\lambda'} j_{\lambda'}} \\ \qquad\qquad \text{(for the open channels)} \\ I_{J-j_\lambda}(|k^\lambda_{v_\lambda j_\lambda}| R_\lambda)\, \delta^{\lambda v_\lambda j_\lambda}_{\lambda' v_{\lambda'} j_{\lambda'}} + K_{J-j_\lambda}(|k_{v_\lambda j_\lambda}| R_\lambda)\, R^{\lambda v_\lambda j_\lambda}_{J\lambda' v_{\lambda'} j_{\lambda'}} \\ \qquad\qquad \text{(for the closed channels)} \end{cases} \tag{5.5}$$

and for the $\underset{\approx}{S}_J$ matrix solution

$$b_{SJ\lambda v_\lambda j_\lambda}^{\lambda' v_{\lambda'} j_{\lambda'}} = \left(\frac{\mu R_\lambda}{\hbar}\right)^{\frac{1}{2}} \begin{cases} H^{(2)}_{J-j_\lambda}(k^\lambda_{v_\lambda j_\lambda} R_\lambda)\,\delta^{\lambda v_\lambda j_\lambda}_{\lambda' v_{\lambda'} j_{\lambda'}} + H^{(1)}_{J-j_\lambda}(k^\lambda_{v_\lambda j_\lambda} R_\lambda)\, S^{\lambda v_\lambda j_\lambda}_{J\lambda' v_{\lambda'} j_{\lambda'}} \\ \qquad \text{(for the open channels)} \\ I_{J-j_\lambda}(|k^\lambda_{v_\lambda j_\lambda}| R_\lambda)\,\delta^{\lambda v_\lambda j_\lambda}_{\lambda' v_{\lambda'} j_{\lambda'}} + K_{J-j_\lambda}(|k^\lambda_{v_\lambda j_\lambda}| R_\lambda)\, S^{\lambda v_\lambda j_\lambda}_{J\lambda' v_{\lambda'} j_{\lambda'}} \\ \qquad \text{(for the closed channels)} \end{cases} \tag{5.6}$$

and the Hankel functions H_ℓ^{+} are related to the Bessel functions J_ℓ, Y_ℓ by

$$H_\ell^{(1,2)} = J_\ell \pm i Y_\ell \tag{5.7}$$

The $\underset{\approx}{R}_J$ and $\underset{\approx}{S}_J$ matrices defined in Eqs. 5.5 and 5.6 have dimensions $3N \times 3N$ and include both open and closed channel initial and final states. Only the open → open transitions have direct physical significance and we will label these by the symbols $\underset{\approx}{R}_J^0$ and $\underset{\approx}{S}_J^0$. It is these open channel matrices $\underset{\approx}{R}_J^0$ and $\underset{\approx}{S}_J^0$ which obey the usual properties that $\underset{\approx}{R}_J^0$ is real and symmetric and $\underset{\approx}{S}_J^0$ is unitary and symmetric [24], as a result of the time reversal invariance and conservation of flux properties of the Schrödinger equation. Actually, Eqs. 5.4 through 5.7 are expressed in terms of the mass scaled variables $\underset{\sim}{r}_\lambda, \underset{\sim}{R}_\lambda$ of Eqs. 2.2a and 2.2b, whereas the reactive and scattering matrices we are interested in, are defined in terms of equivalent expressions involving the unscaled $\overline{\underset{\wedge}{r}}_\lambda, \overline{\underset{\wedge}{R}}_\lambda$. However, Eq. 5.4 and its unscaled variable counterpart are proportional to one another and as a result $\underset{\approx}{R}_J$ and $\underset{\approx}{S}_J$ are invariant under the $\underset{\wedge}{r}_\lambda, \underset{\wedge}{R}_\lambda \rightarrow \overline{\underset{\wedge}{r}}_\lambda, \overline{\underset{\wedge}{R}}_\lambda$ transformation; this permits us to use directly the unbarred variable results to calculate them. Using Eqs. 5.7 in Eqs. 5.5 and 5.6, we can relate the open channel subblocks of the reactance and scattering matrices by the following expression [39]

$$\underset{\approx}{S}^0_J = (\underset{\approx}{I} - i\underset{\approx}{R}^0_J)(\underset{\approx}{I} + i\underset{\approx}{R}^0_J)^{-1} \tag{5.8}$$

where $\underset{\approx}{I}$ is the identity matrix. We will discuss the physical significance of the scattering matrix at the end of this section.

Let us indicate how $\underset{\approx}{R}_J$ can be obtained from the numerically determined solutions $\Phi^{(i)vj}_J$. We rewrite Eqs. 5.3 and 5.5 in $3N \times 3N$ matrix form as

$$\underset{\approx}{e}_J = \underset{\approx}{g}^+_J \underset{\approx}{C}^+_J + \underset{\approx}{g}^-_J \underset{\approx}{C}^-_J \tag{5.9}$$

and

$$\underset{\approx}{b}_J = \underset{\approx}{V}^{-\frac{1}{2}} [\underset{\approx}{J}_J + \underset{\approx}{Y}_J \tilde{\underset{\approx}{R}}_J] \tag{5.10}$$

where

$$(\underset{\approx}{g}^{\pm}_J)^{\lambda' v_{\lambda'} j_{\lambda'}}_{\lambda v_\lambda j_\lambda} = \delta_{\lambda\lambda'}\, g^{\lambda' v_{\lambda'} j_{\lambda'}}_{J v_\lambda j_\lambda} \tag{5.11}$$

$$(\underset{\approx}{V}^{-\frac{1}{2}})^{\lambda v_{\lambda'} j_{\lambda'}}_{\lambda v_\lambda j_\lambda} = \delta_{\lambda\lambda'}\, \delta^{v_{\lambda'} j_{\lambda'}}_{v_\lambda j_\lambda}\, (V^\lambda_{v_\lambda j_\lambda})^{-\frac{1}{2}} \tag{5.12a}$$

$$V^{\lambda}_{v_\lambda j_\lambda} = \hbar k^{\lambda}_{v_\lambda j_\lambda}/\mu \tag{5.12b}$$

$$(\underset{\approx}{J}_J)^{\lambda' v_{\lambda'} j_{\lambda'}}_{\lambda v_\lambda j_\lambda} = \delta_{\lambda\lambda'}\, \delta^{v_{\lambda'} j_{\lambda'}}_{v_\lambda j_\lambda} (|k_{v_\lambda j_\lambda}| R_\lambda)^{\frac{1}{2}} \times \begin{cases} J_{J-j_\lambda}(k^{\lambda}_{v_\lambda j_\lambda} R_\lambda) & \text{(open channels)} \\ I_{J-j_\lambda}(|k^{\lambda}_{v_\lambda j_\lambda}| R_\lambda) & \text{(closed channels)} \end{cases} \tag{5.13}$$

$$(\underset{\approx}{Y}_J)^{\lambda' v_{\lambda'} j_{\lambda'}}_{\lambda v_\lambda j_\lambda} = \delta_{\lambda\lambda'}\, \delta^{v_{\lambda'} j_{\lambda'}}_{v_\lambda j_\lambda} (|k^{\lambda}_{v_\lambda j_\lambda}| R_\lambda)^{\frac{1}{2}} \times \begin{cases} Y_{J-j_\lambda}(k^{\lambda}_{v_\lambda j_\lambda} R_\lambda) & \text{(open channels)} \\ K_{J-j_\lambda}(|k_{v_\lambda j_\lambda}| R_\lambda) & \text{(closed channels)} \end{cases} \tag{5.14}$$

and $\tilde{\underset{\approx}{R}}_J$ is the transpose of $\underset{\approx}{R}_J$. The elements of the $\underset{\approx}{e}_J$ and $\underset{\approx}{b}_J$ matrices are the $e^{(i)vj}_{J\lambda v_\lambda j_v}$ and $b^{(i)vj}_{J\lambda v_\lambda j_\lambda}$, respectively. In all these matrix elements, the subscripts other than J denote the row and the superscripts the column to which they belong. The reactance matrix solution $\Psi^{\lambda' v_{\lambda'} j_{\lambda'}}_{RJ}$ can be obtained from our numerically determined solutions $\Phi^{(i)vj}_{J}$ by taking linear combinations of the latter:

$$\Psi_{RJ}^{\lambda' v_{\lambda'} j_{\lambda'}} = \sum_{i=1}^{3} \sum_{vj} \Phi_J^{(i)vj} \, D_{J(i)vj}^{\lambda' v_{\lambda'} j_{\lambda'}} \tag{5.15}$$

As was mentioned at the end of Section 4, the matching equation (Eq. 4.44) determines $\underset{\approx}{C}_J^{+}(\underset{\approx}{C}_J^{-})^{-1}$ but not $\underset{\approx}{C}_J^{+}$ or $\underset{\approx}{C}_J^{-}$ individually. To complete their evaluation we choose $D_J = \delta_{ivj}^{\lambda' v_\lambda' j_\lambda' \lambda}$ in Eq. 5.15 and require that the $\underset{\approx}{C}_J^{\pm}$ produce not only the correctly matched solutions, but also the correct asymptotic solutions as well. We then substitute Eqs. 5.2 and 5.4 into Eq. 5.15 and equate coefficients of terms having the same arrangement channel λ and vibration rotation basis functions $r_\lambda^{-\frac{1}{2}} \varphi_{j_\lambda}(\gamma_\lambda)\, \phi_{v_\lambda j_\lambda}^{\lambda}(r_\lambda)$. Expressing the resulting equations in matrix form and using Eqs. 5.9 and 5.10, we obtain

$$(\underset{\approx}{g}_J^{+} \underset{\approx}{C}_J^{+} + \underset{\approx}{g}_J^{-} \underset{\approx}{C}_J^{-}) = \underset{\approx}{V}^{-\frac{1}{2}} (\underset{\approx}{J}_J + \underset{\approx}{Y}_J \underset{\approx}{\tilde{R}}_J) \tag{5.16}$$

The analogous equation for the derivatives $(R_\lambda)^{-\frac{1}{2}} \frac{\partial}{\partial R_\lambda} [(R_\lambda)^{\frac{1}{2}} \Psi_{RJ}]$ and $(R_\lambda)^{-\frac{1}{2}} \frac{\partial}{\partial R_\lambda} [R_\lambda^{\frac{1}{2}} \Phi_J]$ is

$$(\underset{\approx}{g}_J^{+\prime} \underset{\approx}{C}_J^{+} + \underset{\approx}{g}_J^{-\prime} \underset{\approx}{C}_J^{-}) = \underset{\approx}{V}^{-\frac{1}{2}} (\underset{\approx}{J}_J' + \underset{\approx}{Y}_J' \underset{\approx}{\tilde{R}}_J) \tag{5.17}$$

where prime denotes differentiation with respect to R_λ, with $\lambda = \alpha, \beta, \gamma$ as appropriate. These last two equations and Eq. 4.44 can then be simultaneously solved to yield the following expression for $\underset{\approx}{\tilde{R}}_J$,

$$\begin{aligned}\underset{\approx}{\tilde{R}}_J = & -\underset{\approx}{V}^{\frac{1}{2}}\,\underset{\approx}{W}_J^{-1}\,[(\underset{\approx}{J}'_J\,\underset{\approx}{g}_J^{+} - \underset{\approx}{J}_J\,\underset{\approx}{g}_J^{+\prime})\,(\underset{\approx}{N}_J^{+})^{-1}\,\underset{\approx}{N}_J^{-} \\ & - (\underset{\approx}{J}'_J\,\underset{\approx}{g}_J^{-} - \underset{\approx}{J}_J\,\underset{\approx}{g}_J^{-\prime})][(\underset{\approx}{Y}'_J\,\underset{\approx}{g}_J^{+} - \underset{\approx}{Y}_J\,\underset{\approx}{g}_J^{+\prime})\,(\underset{\approx}{N}_J^{+})^{-1}\,N_J^{-} \\ & - (\underset{\approx}{Y}'_J\,\underset{\approx}{g}_J^{-} - \underset{\approx}{Y}_J\,\underset{\approx}{g}_J^{-\prime}\,]^{-1}\,\underset{\approx}{W}_J\,\underset{\approx}{V}^{-\frac{1}{2}} \end{aligned} \tag{5.18}$$

where

$$\underset{\approx}{W} = \underset{\approx}{Y}'_J\,\underset{\approx}{J}_J - \underset{\approx}{J}'_J\,\underset{\approx}{Y}_J \tag{5.19}$$

Transposition of Eq. 5.18 gives $\underset{\approx}{R}_J$, and Eqs. 5.18 and 4.44 when substituted into Eqs. 5.16 or 5.17 will yield expressions for $\underset{\approx}{C}_J^{+}$ and $\underset{\approx}{C}_J^{-}$.

The procedure just described furnishes the full $\underset{\approx}{R}_J$ matrix. Its closed channel parts may now be discarded, and the open channel part of the scattering matrix $\underset{\approx}{S}_J^{0}$ calculated from Eq. 3.8. $\underset{\approx}{S}_J^{0}$ may then be used to calculate $P_{J\lambda v_\lambda j_\lambda}^{\lambda' v_{\lambda'} j_{\lambda'}}$, the probability [40] of transition from a given initial arrangement channel λ and internal state $v_\lambda j_\lambda$ to final arrangement channel λ' and internal state $v_{\lambda'} j_{\lambda'}$ (for a given total angular momentum quantum number J) through the relation

$$P_{J\lambda v_\lambda j_\lambda}^{\lambda' v_{\lambda'} j_{\lambda'}} = | S_{J\,\lambda v_\lambda j_\lambda}^{0\lambda' v_{\lambda'} j_{\lambda'}} |^2 \tag{5.20}$$

Note that this is a distinguishable atom transition probability. Effects of indistinguishability of particles will not be considered until Section 6.2. As mentioned in Section 2.3, the total angular momentum is simply equal to the algebraic sum of the rotational and orbital angular momenta, i. e., $J = j_\lambda + \ell_\lambda$. This allows us to reexpress $P_{J\lambda v_\lambda j_\lambda}^{\lambda' v_{\lambda'} j_{\lambda'}}$ in terms of initial and final orbital angular momenta ℓ_λ and $\ell_{\lambda'}$. This has a useful semiclassical interpretation since the initial orbital angular momentum quantum number ℓ_λ is related to the classical impact parameter b_λ through the relation

$$\ell_\lambda = \bar{k}_{v_\lambda j_\lambda}^{\lambda} \, b_\lambda \tag{5.21}$$

where $\bar{k}_{v_\lambda j_\lambda}^{\lambda}$ is the wave number in the $\bar{R}_\lambda, \bar{r}_\lambda$ coordinate system (defined in Section 2.2)

$$\begin{aligned} \bar{k}_{v_\lambda j_\lambda}^{\lambda} &= \left[\frac{2\mu_{\lambda,\nu\kappa}}{\hbar^2} \left(E - E_{v_\lambda j_\lambda}^{\lambda}\right) \right]^{\frac{1}{2}} \\ &= a_\lambda \, k_{v_\lambda j_\lambda}^{\lambda} \end{aligned} \tag{5.22}$$

5.2. Distinguishable atom scattering amplitudes and cross sections

In this section we define the "physical" scattering solution, and the distinguishable atom scattering amplitudes and cross sections. In addition, we derive a relation between the coplanar scattering amplitudes and scattering matrix analogous to that of the usual three-dimensional partial wave theory.

Let us consider a collision between atom A_λ and molecule $A_\nu A_\kappa$. Let the latter be in internal vibrational-rotational state $v_\lambda j_\lambda$ and let the relative initial velocity of the colliding partners be $\bar{V}^\lambda_{v_\lambda j_\lambda}$. In addition, we choose the direction of relative approach to be the x axis of Fig. 1. The "physical" wavefunction $\bar{\Psi}_p^{\lambda v_\lambda j_\lambda}$ which describes the outcome of such a collision is the solution of the Schrödinger equation (Eq. 2.1) which behaves asymptotically at large $\bar{R}_\lambda$, $\bar{R}_\nu$ or $\bar{R}_\kappa$ as

$$\bar{\Psi}_p^{\lambda v_\lambda j_\lambda} \sim e^{i\bar{k}^\lambda_{v_\lambda j_\lambda} \bar{R}_\lambda \cos \chi_\lambda} \varphi_{j_\lambda}(\theta_\lambda)\, \bar{r}_\lambda^{-\frac{1}{2}}\, \bar{\phi}^\lambda_{v_\lambda j_\lambda}(\bar{r}_\lambda)$$

$$+ \sum_{\lambda' v_{\lambda'} j_{\lambda'}} \bar{f}^{\lambda' v_{\lambda'} j_{\lambda'}}_{\lambda v_\lambda j_\lambda}(\chi_{\lambda'})\, \bar{R}_{\lambda'}^{-\frac{1}{2}}\, e^{i\bar{k}^{\lambda'}_{v_{\lambda'} j_{\lambda'}} \bar{R}_{\lambda'}} \varphi_{j_{\lambda'}}(\theta_{\lambda'})\, \bar{r}_{\lambda'}^{-\frac{1}{2}}\, \bar{\phi}^{\lambda'}_{v_{\lambda'} j_{\lambda'}}(\bar{r}_{\lambda'}) \tag{5.23}$$

The summation extends over open and closed channels. For closed channels, $\bar{k}^\lambda_{v_{\lambda'} j_{\lambda'}}$ is a pure imaginary and $e^{i\bar{k}^{\lambda'}_{v_{\lambda'} j_{\lambda'}} R_{\lambda'}}$ is an exponentially decreasing function of $\bar{R}_{\lambda'}$. The $\bar{f}$ corresponding to open channels are the scattering amplitudes for the $\lambda v_\lambda j_\lambda \rightarrow \lambda' v_{\lambda'} j_{\lambda'}$ scattering processes. The first exponential factor in the righthand side of Eq. 5.23 represents the incident relative motion line wave (the 2-D equivalent of the 3-D plane wave) whereas for the open channels the $\bar{R}_{\lambda'}^{-\frac{1}{2}} \exp(i\bar{k}^{\lambda'}_{v_{\lambda'} j_{\lambda'}} \bar{R}_{\lambda'})$ represent the scattered circular non-reactive $(\lambda' = \lambda)$ and reactive $(\lambda' \neq \lambda)$ waves. The $\bar{r}_{\lambda}^{-\frac{1}{2}} \varphi_{j_{\lambda'}}(\theta_\lambda) \bar{\phi}^{\lambda}_{v_{\lambda'} j_{\lambda'}}(\bar{r}_{\lambda'})$ are the planar motion vibrational-rotational wavefunctions of the isolated A_ν, A_κ molecule in state $v_{\lambda'}, j_{\lambda'}$ and differ from the corresponding unbarred function only by the proportionality factor $(1/a_{\lambda'})$ (see Eq. 2.3).

The differential cross section for the $\lambda v_\lambda j_\lambda \rightarrow \lambda' v_{\lambda'} j_{\lambda'}$ process (assuming that both these states are open at the total energy E considered) is defined as the ratio of the outgoing radial flux per unit $\chi_{\lambda'}$ angle to the incident line wave flux. In the 2-D world being considered it has dimensions of a length per unit angle. For the case in which all three atoms are distinguishable, it is related to the corresponding scattering amplitude by

$$\sigma^{\lambda' v_{\lambda'} j_{\lambda'}}_{\lambda v_\lambda j_\lambda}(\chi_{\lambda'}) = (\bar{v}^{\lambda'}_{v_{\lambda'} j_{\lambda'}} / \bar{v}^{\lambda}_{v_\lambda j_\lambda}) \left| \bar{f}^{\lambda' v_{\lambda'} j_{\lambda'}}_{\lambda v_\lambda j_\lambda} \right|^2 \qquad (5.24)$$

For either reactive or non-reactive collisions $\chi_{\lambda'}$ is the angle between the initial and final velocity vectors of the atom with respect to the diatom (i.e., between the initial and final directions of motion of the atom in the center of mass system--the G_{xy} system of Fig. 1).

The integral cross section for the same process is

$$Q_{\lambda v_{\lambda} j_{\lambda}}^{\lambda' v_{\lambda'} j_{\lambda'}} = \int_{0}^{2\pi} \sigma_{\lambda v_{\lambda} j_{\lambda}}^{\lambda' v'_{\lambda} j'_{\lambda}} (\chi_{\lambda'})\, d\chi_{\lambda'} \tag{5.25}$$

It has the dimensions of a length.

We define the unbarred $\Psi_{p}^{\lambda v_{\lambda} j_{\lambda}}$ as a solution to the Schrödinger Eq. 2.4 (involving the mass-scaled coordinates $\underset{\sim}{r}_{\lambda}, \underset{\sim}{R}_{\lambda}$) which behaves asymptotically at large R_{λ}, R_{ν} or R_{κ} as given by Eq. 5.23, but with all bars removed. It is straightforward to prove that

$$\bar{\Psi}_{p}^{\lambda v_{\lambda} j_{\lambda}} = a_{\lambda}^{-1} \Psi_{p}^{\lambda v_{\lambda} j_{\lambda}} \tag{5.26}$$

and as a result that

$$\bar{f}_{\lambda v_{\lambda} j_{\lambda}}^{\lambda' v_{\lambda'} j_{\lambda'}} (\chi_{\lambda'}) = \frac{a_{\lambda'}^{\frac{1}{2}}}{a_{\lambda}} f_{\lambda v_{\lambda} j_{\lambda}}^{\lambda' v_{\lambda'} j_{\lambda'}} (\chi_{\lambda'}) \tag{5.27}$$

If we now define the dimensionless scattering amplitude $\hat{f}$ by

$$\hat{f}_{\lambda v_{\lambda} j_{\lambda}}^{\lambda' v_{\lambda'} j_{\lambda'}} (\chi_{\lambda'}) = \left(\frac{\mu \left| V_{v_{\lambda'} j_{\lambda'}}^{\lambda'} \right|}{\hbar}\right)^{\frac{1}{2}} f_{\lambda v_{\lambda} j_{\lambda}}^{\lambda' v_{\lambda'} j_{\lambda'}} (\chi_{\lambda'}) \tag{5.28}$$

expression 5.24 becomes simply

$$\sigma_{\lambda v_\lambda j_\lambda}^{\lambda' v_{\lambda'} j_{\lambda'}}(\chi_{\lambda'}) = \frac{1}{\bar{k}^{\lambda}_{v_\lambda j_\lambda}} \left| \hat{f}_{\lambda v_\lambda j_\lambda}^{\lambda' v_{\lambda'} j_{\lambda'}}(\chi_{\lambda'}) \right|^2 \tag{5.29}$$

Therefore, once the open channel dimensionless scattering amplitudes $\hat{f}$ are known, the differential and total distinguishable atom scattering cross sections are easily calculated from Eqs. 5.29 and 5.25, respectively.

In terms of the $\hat{f}$ the unbarred version of Eq. 5.23 can be written as

$$\Psi_p^{\lambda v_\lambda j_\lambda} \sim \sum_{\lambda' v_{\lambda'} j_{\lambda'}} \left[\delta_{\lambda v_\lambda j_\lambda}^{\lambda' v_{\lambda'} j_{\lambda'}} e^{ik^{\lambda}_{v_{\lambda'} j_{\lambda'}} R_{\lambda'} \cos \chi_{\lambda'}} + \left(\frac{\hbar}{\mu \left| v^{\lambda'}_{v_{\lambda'} j_{\lambda'}} \right|} \right)^{\frac{1}{2}} \hat{f}_{\lambda v_\lambda j_\lambda}^{\lambda' v_{\lambda'} j_{\lambda'}}(\chi_{\lambda'}) \frac{1}{R_{\lambda'}^{\frac{1}{2}}} e^{ik^{\lambda'}_{v_{\lambda'} j_{\lambda'}} R_{\lambda'}} \right] \varphi_{j_{\lambda'}}(\theta_{\lambda'}) \, r_{\lambda'}^{-\frac{1}{2}} \phi^{\lambda'}_{v_{\lambda'} j_{\lambda'}}(r_{\lambda'}) \tag{5.30}$$

We now relate the scattering amplitudes to the scattering matrix. To do this, we expand the physical solution Eq. 5.30 in terms of the scattering matrix solution (Eqs. 5.4 and 5.6) using an equation analogous to 2.12

$$\Psi_p^{\lambda v_\lambda j_\lambda} = \sum_{J=-\infty}^{\infty} a_{SJ}^{\lambda v_\lambda j_\lambda} \Psi_{SJ}^{\lambda v_\lambda j_\lambda} \tag{5.31}$$

To find expressions for the coefficients $a_{SJ}^{\lambda v_\lambda j_\lambda}$ and the scattering amplitudes $\hat{f}_{\lambda v_\lambda j_\lambda}^{\lambda' v_{\lambda'} j_{\lambda'}}$, we first expand the $\chi_{\lambda'}$-dependent portions of Eq. 5.30 in terms of the eigenfunctions $\varphi_J(\chi_{\lambda'})$, then express the $R_{\lambda'}$-dependent portions of Eqs. 5.30 and 5.6 in their asymptotic forms (Eqs. 3.25 and 3.26) involving exponentials. We finally equate the coefficients of the corresponding $R_{\lambda'}$ exponentials, $\varphi_J(\chi_{\lambda'})$ and rotation-vibration basis functions in both sides of Eq. 5.31 and solve the resulting equations for $a_{SJ}^{\lambda v_\lambda j_\lambda}$ and for the coefficients of the expression of $\hat{f}_{\lambda v_\lambda j_\lambda}^{\lambda' v_{\lambda'} j_{\lambda'}}(\chi_{\lambda'})$ in the $\varphi_J(\chi_{\lambda'})$.

The expansion for the line wave is [41]

$$e^{ik_{v_{\lambda'} j_{\lambda'}}^{\lambda'} R_{\lambda'} \cos \chi_{\lambda'}} = \sum_{J=-\infty}^{\infty} i^J e^{iJ\chi_{\lambda'}} J_J(k_{v_{\lambda'} j_{\lambda'}}^{\lambda'} R_{\lambda'})$$

$$\underset{R_{\lambda'} \to \infty}{\sim} \frac{1}{k_{v_{\lambda'} j_{\lambda'}}^{\lambda'} R_{\lambda'}} \sum_{J=-\infty}^{\infty} \Bigg[e^{ik_{v_{\lambda'} j_{\lambda'}}^{\lambda'} R_{\lambda'}} e^{-i\frac{\pi}{4}}$$

$$+ (-1)^J e^{-ik_{v_{\lambda'} j_{\lambda'}}^{\lambda'} R_{\lambda'}} e^{i\frac{\pi}{4}} \Bigg] \varphi_J(\chi_{\lambda'}) \tag{5.32}$$

As a result of the relation between γ_λ, χ_λ and θ_λ given after Eq. 2.1, and of Eq. 2.9 we have

$$\varphi_{j_{\lambda'}}(\theta_{\lambda'}) = (2\pi)^{\frac{1}{2}}\,\varphi_{j_{\lambda'}}(\chi_{\lambda'})\,\varphi_{j_{\lambda'}}(\gamma_{\lambda'}) \tag{5.33}$$

Using Eqs. 5.30 through 5.33 and following the procedure outlined above we get

$$a_{SJ}^{\lambda v_\lambda j_\lambda} = \left(\frac{\hbar\pi}{2\mu}\right)^{\frac{1}{2}} \exp\left[\,i(J - j_\lambda)\,\frac{\pi}{2}\,\right] \tag{5.34}$$

and, for the dimensionless scattering amplitudes to open channels,

$$\hat{f}_{\lambda v_\lambda j_\lambda}^{\lambda' v_{\lambda'} j_{\lambda'}}(\chi_{\lambda'}) = \exp(-i\,j_{\lambda'}\,\chi_{\lambda'})\,\exp\left[\,i\,(j_{\lambda'} - j_\lambda - \tfrac{1}{2})\,\frac{\pi}{2}\,\right] \sum_{J=-\infty}^{\infty}\left[S^{o\,\lambda' v_{\lambda'} j_{\lambda'}}_{J\lambda v_\lambda j_\lambda} - \delta_{\lambda v_\lambda j_\lambda}^{\lambda' v_{\lambda'} j_{\lambda'}}\right]\varphi_J(\chi_{\lambda'}) \tag{5.35}$$

Eq. 5.35 differs from that obtained by Walker and Wyatt [40] only by the phase factor $\exp(-i j_{\lambda'}\chi_{\lambda'})$. Substitution of Eq. 5.35 into (5.29) and of the result into Eq. 5.25 leads to the following rather simple expression for the integral cross section:

$$Q_{\lambda v_\lambda j_\lambda}^{\lambda' v_{\lambda'} j_{\lambda'}} = \frac{1}{\bar{k}^{\lambda}_{v_\lambda j_\lambda}} \sum_{J=-\infty}^{\infty}\left|\,S^{o\,\lambda v_{\lambda'} j_{\lambda'}}_{J\lambda v_\lambda j_\lambda} - \delta_{\lambda v_\lambda j_\lambda}^{\lambda' v_{\lambda'} j_{\lambda'}}\right|^2 \tag{5.36}$$

Eqs. 5.35 and 5.36 may be written in terms of a sum over J from 0 to ∞ by using the relation

$$S^{0\lambda' v_{\lambda'} j_{\lambda'}}_{J\lambda v_{\lambda} j_{\lambda}} = S^{0\lambda' v_{\lambda'} -j_{\lambda'}}_{J\lambda v_{\lambda} -j_{\lambda}} \tag{5.37}$$

This expression is a consequence of the symmetry of the Hamiltonian with respect to reflection through the plane of motion. Additional symmetry relations which follow from Eq. 5.37 are

$$\hat{f}^{\lambda' v_{\lambda'} -j_{\lambda'}}_{\lambda v_{\lambda} -j_{\lambda}}(-\chi_{\lambda'}) = \hat{f}^{\lambda' v_{\lambda'} j_{\lambda'}}_{\lambda v_{\lambda} j_{\lambda}}(\chi_{\lambda'}) \tag{5.38}$$

and

$$Q^{\lambda' v_{\lambda'} -j_{\lambda'}}_{\lambda v_{\lambda} -j_{\lambda}} = Q^{\lambda' v_{\lambda'} j_{\lambda'}}_{\lambda v_{\lambda} j_{\lambda}} \tag{5.39}$$

Eqs. 5.37, through 5.39 are valid for any planar atom plus diatomic molecule collision process. For reactions of higher symmetry such as $H + H_2$, there exist additional relationships some of which will be discussed in the next section.

6. APPLICATION TO PLANAR $H + H_2$

6.1. The integration, matching and distinguishable atom asymptotic analysis

In the application of the methods described in Sections 3 and 4 to the $H + H_2$ exchange reaction, a considerable reduction in computation time can be realized by utilizing two important symmetry properties of this collision system. The first is the invariance of the collision system and associated coordinate systems with respect to a cyclic permutation of the three atoms. Mathematically this means that all equations derived in Sections 3, 4 and 5 are invariant to a cyclic permutation of the indices $\lambda\nu\kappa$, which implies (1) that we need to integrate the Schrödinger equation in only one of the three arrangement channel regions depicted in Fig. 2, (2) that we need only calculate the projection coefficients $\bar{h}$, $\bar{h}'$, $\bar{f}$ and $\bar{f}'$ defined in Eqs. 4.11, 4.12, 4.22 and 4.23 on one of the three matching surfaces (such as $\pi_{\nu\lambda}$), and (3) that the $\lambda \rightarrow \nu$, $\nu \rightarrow \kappa$ and $\kappa \rightarrow \lambda$ distinguishable atom scattering amplitudes are all identical as are $\nu \rightarrow \lambda$, $\lambda \rightarrow \kappa$, $\kappa \rightarrow \nu$, and $\lambda \rightarrow \lambda$, $\nu \rightarrow \nu$, $\kappa \rightarrow \kappa$ so we may restrict ourselves to a calculation of the $\lambda \rightarrow \lambda$, $\lambda \rightarrow \nu$ and $\lambda \rightarrow \kappa$ scattering amplitudes only. The second symmetry property is related to the invariance of the collision system (but not the associated coordinate systems) with respect to an interchange of any two of the three atoms. This results in a potential function $V^{\lambda}(r_{\lambda}, R_{\lambda}, \gamma_{\lambda})$ which is symmetric about $\gamma_{\lambda} = \pm\pi/2$

$$V^{\lambda}(r_{\lambda}, R_{\lambda}, \pi - \gamma_{\lambda}) = V^{\lambda}(r_{\lambda}, R_{\lambda}, \gamma_{\lambda}) \tag{6.1}$$

To a large extent, the consequences of this property depend on the coordinate system being used, for while Eq. 6.1 is valid in all regions of configuration space, the λ arrangement channel coordinates, $r_{\lambda}, R_{\lambda}, \gamma_{\lambda}$ are not the most convenient coordinates to use in all three arrangement channel regions. In arrangement channel region λ, Eq. 6.1 has the immediate effect of decoupling rotational states of even and odd quantum numbers j_{λ}. This means that the integration in arrangement channel region λ can be done in two separate steps, one for even j_{λ} and one for odd j_{λ}. In each of these steps the total number of basis functions required is only about half of that needed in the absence of this decoupling. Since the computation time varies as N^{a} where N is the number of states being integrated, and a is 2 for $N < 10$ and 3 for $N > 30$ [20], we see that a saving of factors of 2 to 4 in computation time may be realized by this decoupling. In a similar manner, the calculation of the matching surface coefficients of Eqs. 4.11, 4.12, 4.22 and 4.23 may be done in two separate steps, one for even $\underset{\approx}{j}_{\lambda}$ and one for odd $\underset{\approx}{j}_{\lambda}$, and the coefficient matrices $\underset{\approx}{f}_{J}^{\nu\pm}$ and $\underset{\approx}{f}'^{\nu\pm}$ may be obtained from $\underset{\approx}{h}_{J}^{\lambda\pm}$ and $\underset{\approx}{h}_{J}'^{\lambda\pm}$ by using the simple relations

$$(\underset{\approx}{f}_{J}^{\nu\pm})_{v_{\lambda} j_{\lambda}}^{v'_{\lambda} j'_{\lambda}} = (-1)^{j_{\lambda} + j'_{\lambda}} (\underset{\approx}{h}_{J}^{\lambda\pm})_{v_{\lambda} j_{\lambda}}^{v'_{\lambda} j'_{\lambda}} \tag{6.2a}$$

$$(f'^{\nu\pm}_{J})^{v'_\lambda j'_\lambda}_{v_\lambda j_\lambda} = -(-1)^{j_\lambda + j'_\lambda} (h'^{\lambda\pm}_{j})^{v'_\lambda j'_\lambda}_{v_\lambda j_\lambda} \tag{6.2b}$$

We must note, however, that the number of matching surface functions $T^{\nu\lambda}_{v_\lambda j_\lambda}$ is still N/2 where N is the total number of even plus odd j_λ states. The matching procedure ultimately couples the even and odd rotational states j_λ (through Eq. 4.44) so that decoupling beyond that point is lost. However, symmetry of the system about $\gamma_\lambda = \pm\pi/2$ (Eq. 6.1) may be used to relate the $\lambda \rightarrow \nu$ and $\lambda \rightarrow \kappa$ scattering amplitudes according to:

$$\hat{f}^{\nu v' j'}_{\lambda v j} = (-1)^{j + j'} \hat{f}^{\kappa v' j'}_{\lambda v j} \tag{6.3}$$

as is shown in Appendix C. Equation 6.3 may be used to reduce the work involved in the asymptotic analysis to the calculation of only the $\lambda \rightarrow \lambda$ and $\lambda \rightarrow \nu$ scattering amplitudes. An additional consequence of Eq. 6.1 valid only for the $\lambda \rightarrow \lambda$ scattering amplitudes (*i.e.,* the non-reactive transitions) is the familiar relation (also derived in Appendix C)

$$\hat{f}^{\lambda v' j'}_{\lambda v j} = 0 \text{ for } j - j' = \text{odd} \tag{6.4}$$

and the incorporation of this relation into the asymptotic analysis can also result in a reduction of computational effort. We should note, however, that the two symmetries given by Eqs. 6.3 and 6.4 depend on our use of a complete basis set $T^{\nu\lambda}_{v_\lambda j_\lambda}$ for expanding the wave function on the matching surface and therefore may be used as a test of the convergence of the method provided these symmetries are not built in to the calculations.

6.2. Post antisymmetrization

Up to this point, we have considered the three atoms to be distinguishable. However, to calculate physically measurable quantities such as cross sections for reactions like $H + H_2$, we must include for effects due to indistinguishability of the three atoms and the Pauli principle. Since the three hydrogen nuclei each have a spin of $\frac{1}{2}$, it is necessary to antisymmetrize our wavefunctions with respect to interchange of any two nuclei. This can be done by the well known procedure of post antisymmetrization [23]. The application of this procedure to the hydrogen exchange reaction is given in Appendix D and the results, which were previously given by Doll, George and Miller [42] are summarized below (where the direct and exchange amplitudes $\hat{f}_1^1$ and $\hat{f}_2^1$ of that Appendix are relabelled as $\hat{f}^\lambda_\lambda$ and $\hat{f}^\nu_\lambda$ respectively).

(a) para → para

$$\sigma^{p\,v'j'}_{p\,vj}(X) = \frac{1}{\bar{k}^{\lambda}_{vj}} \left| \hat{f}^{\lambda\,v'j'}_{\lambda\,vj}(X) - \hat{f}^{\nu\,v'j'}_{\lambda\,vj}(X) \right|^2 \tag{6.5a}$$

(b) para → ortho

$$\sigma^{o\,v'j'}_{p\,vj}(X) = \frac{3}{\bar{k}^{\lambda}_{vj}} \left| \hat{f}^{\nu\,v'j'}_{\lambda\,vj}(X) \right|^2 \tag{6.5b}$$

(c) ortho → para

$$\sigma_{o\,vj}^{p\,v'j'}(\chi) = \frac{1}{\bar{k}_{vj}^{\lambda}} \left| \hat{f}_{\lambda\,vj}^{\nu\,v'j'}(\chi) \right|^2 \tag{6.5c}$$

(d) ortho → ortho

$$\sigma_{o\,vj}^{o\,v'j'}(\chi) = \frac{1}{\bar{k}_{vj}^{\lambda}} \{ \left| \hat{f}_{\lambda\,vj}^{\lambda\,v'j'}(\chi) + \hat{f}_{\lambda\,vj}^{\nu\,v'j'}(\chi) \right|^2$$

$$+ 2 \left| \hat{f}_{\lambda\,vj}^{\nu\,v'j'}(\chi) \right|^2 \} \tag{6.5d}$$

Note that there is no reference to arrangement channel on the left sides of Eqs. 6.5 since this distinction has no meaning after the effect of the Pauli principle is included. The corresponding integral cross sections are:

(a) para → para

$$Q_{p\,vj}^{p\,v'j'} = \frac{1}{\bar{k}_{vj}^{\lambda}} \sum_{J=-\infty}^{\infty} \left| S_{J\lambda vj}^{o\lambda v'j'} - \delta_{vj}^{v'j'} - S_{J\lambda vj}^{o\nu v'j'} \right|^2 \tag{6.6a}$$

(b) para → ortho

$$Q_{p\,vj}^{o\,v'j'} = \frac{3}{\bar{k}_{vj}^{\lambda}} \sum_{J=-\infty}^{\infty} \left| S_{J\lambda vj}^{o\lambda v'j'} \right|^2 \tag{6.6b}$$

(c) ortho → para

$$Q_{o\,vj}^{p\,v'j'} = \frac{1}{\bar{k}_{vj}^{\lambda}} \sum_{J=-\infty}^{\infty} \left| S_{J\lambda vj}^{o\nu v'j'} \right|^2 \tag{6.6c}$$

(d) ortho → ortho

$$Q_{o\,vj}^{o\,v'j'} = \frac{1}{\bar{k}_{vj}^{\lambda}} \sum_{J=-\infty}^{\infty} \{ | S_{J\lambda vj}^{o\lambda v'j'} - \delta_{vj}^{v'j'} + S_{J\lambda vj}^{o\nu v'j'} |^2 + 2 | S_{J\lambda vj}^{o\nu v'j'} |^2 \} \tag{6.6d}$$

As expected, the para → ortho and ortho → para cross sections are simply proportional to the distinguishable atom reactive cross sections since only exchange scattering amplitudes contribute to them. These cross sections furnish direct information on the reactive process alone. The para → para and ortho → ortho cross sections will show effects due to the interference between the reactive and non-reactive (i.e., direct and exchange) scattering amplitudes. The interference effects should be most important when these two amplitudes have comparable magnitudes. We will discuss this interference phenomenon in more detail when presenting our results for planar $H + H_2$ [20].

APPENDIX A. THE $\lambda \rightarrow \nu$ TRANSFORMATION EQUATIONS AND RELATIONS ON THE MATCHING SURFACES

In this Appendix we derive the important relations between the mass-scaled coordinates $\underset{\sim}{R}_\lambda, \underset{\sim}{r}_\lambda$ $(\lambda = \alpha, \beta, \gamma)$ defined by Eqs. 2.2. They permit us to change from coordinates appropriate for one arrangement channel to those appropriate for another one. We also examine the simplifications that occur when these relationships are evaluated on the matching surfaces defined by Eq. 3.2. This will allow us to prove that these surfaces are half-planes whose edge is the Y_λ axis in the $OX_\lambda Y_\lambda Z_\lambda$ space introduced in Section 3.1. We will consider only the relationships between the arrangement channel coordinates $\underset{\sim}{R}_\lambda, \underset{\sim}{r}_\lambda$ and $\underset{\sim}{R}_\nu, \underset{\sim}{r}_\nu$ explicitly. The corresponding relations between $\underset{\sim}{R}_\nu, \underset{\sim}{r}_\nu$ and $\underset{\sim}{R}_\kappa, \underset{\sim}{r}_\kappa$, and between $\underset{\sim}{R}_\kappa, \underset{\sim}{r}_\kappa$ and $\underset{\sim}{R}_\lambda, \underset{\sim}{r}_\lambda$ may be obtained by cyclic permutation of the indices $\lambda\nu\kappa$.

The following relations between the vectors $\bar{\underset{\sim}{R}}_\lambda, \bar{\underset{\sim}{r}}_\lambda$ and $\bar{\underset{\sim}{R}}_\nu, \bar{\underset{\sim}{r}}_\nu$, valid for <u>any</u> configuration of the three atoms, follows from Fig. 1

$$\bar{\underset{\sim}{R}}_\nu = -\bar{\underset{\sim}{r}}_\lambda - \frac{m_\lambda}{m_\lambda + m_\kappa} \bar{\underset{\sim}{r}}_\nu$$

$$\bar{\underset{\sim}{r}}_\nu = \bar{\underset{\sim}{R}}_\lambda - \frac{m_\nu}{m_\nu + m_\kappa} \bar{\underset{\sim}{r}}_\lambda$$

From these and Eqs. 2.2 we get

$$\begin{pmatrix} \underset{\sim}{R}_{\nu} \\ \\ \underset{\sim}{r}_{\nu} \end{pmatrix} = \underset{\approx}{M} \begin{pmatrix} \underset{\sim}{R}_{\lambda} \\ \\ \underset{\sim}{r}_{\lambda} \end{pmatrix} . \tag{A.1}$$

where $\underset{\approx}{M}$ is the 2×2 orthogonal matrix

$$\underset{\approx}{M} = \begin{pmatrix} \cos\alpha_{\nu\lambda} & -\sin\alpha_{\nu\lambda} \\ \sin\alpha_{\nu\lambda} & \cos\alpha_{\nu\lambda} \end{pmatrix} \tag{A.2}$$

$\alpha_{\nu\lambda}$ being the angle between $\pi/2$ and π determined by

$$\cos\alpha_{\nu\lambda} = -\left[\frac{m_{\lambda}\, m_{\nu}}{(m_{\lambda} + m_{\kappa})\,(m_{\nu} + m_{\kappa})}\right]^{\frac{1}{2}} \tag{A.3a}$$

and

$$\sin\alpha_{\nu\lambda} = \left[\frac{m_{\kappa} M}{(m_{\lambda} + m_{\kappa})\,(m_{\kappa} + m_{\nu})}\right]^{\frac{1}{2}} \tag{A.3b}$$

From these expressions we can get the equations for the $\chi_{\lambda}, R_{\lambda}, r_{\lambda}, \gamma_{\lambda} \rightarrow \chi_{\nu}, R_{\nu}, r_{\nu}, \gamma_{\nu}$ transformation. Indeed, from Eqs. A.1 and A.2 and footnote 25 we get

$$R_{\nu}^2 = \underset{\sim}{R}_{\nu} \cdot \underset{\sim}{R}_{\nu} = \cos^2\alpha_{\nu\lambda}\, R_{\lambda}^2 + \sin^2\alpha_{\nu\lambda}\, r_{\lambda}^2 - \sin 2\alpha_{\nu\lambda}\, r_{\lambda} R_{\lambda} \cos\gamma_{\lambda} \tag{A.4}$$

$$r_\nu^2 = \underset{\sim}{r}_\nu \cdot \underset{\sim}{r}_\nu = \sin^2\alpha_{\nu\lambda}\, R_\lambda^2 + \cos^2\alpha_{\nu\lambda}\, r_\lambda^2 + \sin 2\alpha_{\nu\lambda}\, r_\lambda R_\lambda \cos\gamma_\lambda \tag{A.5}$$

and therefore

$$R_\nu^2 + r_\nu^2 = R_\lambda^2 + r_\lambda^2 \tag{A.6}$$

which is a manifestation of the orthogonality of $\underset{\approx}{M}$. In addition, it follows from Eqs. A.1 and A.2 that the cross products $\underset{\sim}{R}_\lambda \times \underset{\sim}{r}_\lambda$ and $\underset{\sim}{R}_\nu \times \underset{\sim}{r}_\nu$ are equal and therefore that

$$R_\nu r_\nu \sin\gamma_\nu = R_\lambda r_\lambda \sin\gamma_\lambda \tag{A.7a}$$

Since γ_ν is in the range 0 to 2π, in order to have it completely specified we should obtain its cosine. From footnote 25 and Eqs. A.4 and A.5 we get

$$\cos\gamma_\nu = \frac{\underset{\sim}{R}_\nu \cdot \underset{\sim}{r}_\nu}{R_\nu r_\nu} = \frac{1}{R_\nu r_\nu}\left[\tfrac{1}{2}\sin 2\alpha_{\nu\lambda}(R_\lambda^2 - r_\lambda^2) + \cos 2\alpha_{\nu\lambda}\cos\gamma_\lambda\right] \tag{A.7b}$$

Eqs. A.4, A.5 and A.7 completely describe the $R_\lambda, r_\lambda, \gamma_\lambda \rightarrow R_\nu, r_\nu, \gamma_\nu$ transformation. To complete the $\lambda \rightarrow \nu$ transformation we define the angle $\Delta X_{\nu\lambda}$

$$\Delta X_{\nu\lambda} = X_\nu - X_\lambda \tag{A.8}$$

and express it in terms of the λ coordinates. We can write

$$\underset{\sim}{R}_\lambda = R_\lambda (\cos \chi_\lambda \hat{\underset{\sim}{x}} + \sin \chi_\lambda \hat{\underset{\sim}{y}})$$

$$\underset{\sim}{r}_\lambda = r_\lambda [\cos (\chi_\lambda + \gamma_\lambda) \hat{\underset{\sim}{x}} + \sin (\chi_\lambda + \gamma_\lambda) \hat{\underset{\sim}{y}}] \cdot$$

where $\hat{\underset{\sim}{x}}$ and $\hat{\underset{\sim}{y}}$ are the unit vectors along the laboratory-fixed axis depicted in Fig. 1. From these expressions, their ν counterpart and Eqs. A.1 and A.2 we can easily obtain the following expressions which determine $\Delta\chi_{\nu\lambda}$ modulo 2π:

$$R_\nu \cos \Delta\chi_{\nu\lambda} = R_\lambda \cos \alpha_{\nu\lambda} - r_\lambda \sin\alpha_{\nu\lambda} \cos \gamma_\lambda \tag{A.9a}$$

$$R_\nu \sin\Delta\chi_{\nu\lambda} = -r_\lambda \sin\alpha_{\nu\lambda} \sin\gamma_\lambda \tag{A.9b}$$

We see that $\Delta\chi_{\nu\lambda}$ is independent of χ_λ and a function of R_λ, r_λ and γ_λ only. This is due to the fact that these three variables uniquely determine the internal configuration of the triatomic system and hence the angle $\Delta\chi_{\nu\lambda}$ between $\underset{\sim}{R}_\nu$ and $\underset{\sim}{R}_\lambda$ (see Fig. 1).

Equations A.4, A.5 and A.7 through A.9 completely describe the $\lambda \rightarrow \nu$ transformation. It is useful to obtain the expressions they reduce to on the $\pi_{\nu\lambda}$ surface defined by Eq. 3.2a. In view of this definition and of Eq. A.6 we have, on this surface,

$$r_\nu = r_\lambda \tag{A.10a}$$

$$R_\nu = R_\lambda \tag{A.10b}$$

From these and Eq. A.4 we get the very useful relation

$$\frac{R_\lambda}{r_\lambda} = -\cot\alpha_{\nu\lambda}\cos\gamma_\lambda + (1 + \cot^2\alpha_{\nu\lambda}\cos^2\gamma_\lambda)^{\frac{1}{2}} \tag{A.11}$$

between R_λ/r_λ and γ_λ on this surface. Other important relations among the internal variables are obtained by substituting Eqs. A.10 and A.11 into A.7. We find

$$\sin\gamma_\nu = \sin\gamma_\lambda$$

and, after some algebraic effort,

$$\cos\gamma_\nu = -\cos\gamma_\lambda$$

which imply that

$$\gamma_\nu = \pi - \gamma_\lambda \tag{A.12}$$

Since $-\frac{\pi}{2} \leqslant \gamma_\lambda \leqslant \frac{\pi}{2}$, we see that $\frac{\pi}{2} \leqslant \gamma_\lambda \leqslant \frac{3\pi}{2}$ on $\pi_{\nu\lambda}$.

From Eqs. A.10 through A.12 plus the expressions resulting from replacing those equations in A.9, the $\lambda \rightarrow \nu$ transformation equations on the $\pi_{\nu\lambda}$ matching surface are completely specified. In addition, since from Eqs. A.9 and A.10

$$\cos\Delta\chi_{\nu\lambda} = \cos\alpha_{\nu\lambda} - \sin\alpha_{\nu\lambda}\cos\gamma_\lambda\left(\frac{r_\lambda}{R_\lambda}\right) \tag{A.13a}$$

and

$$\sin\Delta\chi_{\nu\lambda} = -\left(\frac{r_\lambda}{R_\lambda}\right)\sin\alpha_{\nu\lambda}\sin\gamma_\lambda \tag{A.13b}$$

and since from Eq. A.11, r_λ/R_λ is a function of γ_λ only (on $\pi_{\nu\lambda}$), so is $\Delta\chi_{\nu\lambda}$.

We shall now show that Eq. A.11 when evaluated over the range $-\frac{\pi}{2} \leqslant \gamma_\lambda \leqslant \frac{\pi}{2}$ represents a half plane whose edge is the Y_λ axis in the $OX_\lambda Y_\lambda Z_\lambda$ space defined in Section 3.1 and illustrated in Fig. 2. From Eqs. 3.1 and A.11, we obtain the simple expression

$$\cot \omega_\lambda = -\cot \alpha_{\nu\lambda} \cos \gamma_\lambda ; \quad -\frac{\pi}{2} \leqslant \gamma_\lambda \leqslant \frac{\pi}{2} \tag{A.14}$$

for the equation of $\pi_{\nu\lambda}$ in spherical polar coordinates. In addition, from Eqs. 3.1b and A.10 we have, on $\pi_{\nu\lambda}$,

$$\omega_\lambda = \omega_\nu \tag{A.15}$$

To display the geometrical character of $\pi_{\nu\lambda}$ we switch from polar coordinates $\zeta, \omega_\lambda, \gamma_\lambda$ to cartesian ones $X_\lambda, Y_\lambda, Z_\lambda$. Equation A.14 then becomes

$$Z_\lambda = -\cot \alpha_{\nu\lambda} X_\lambda ; \quad -\frac{\pi}{2} \leqslant \gamma_\lambda \leqslant \frac{\pi}{2} \tag{A.16}$$

This is the equation of a half plane whose edge is the Y_λ axis and which makes an angle of $\pi - \alpha_{\nu\lambda}$ with respect to the Z_λ axis (measured counter-clockwise from OZ_λ to $\pi_{\nu\lambda}$ as viewed from OY_λ).

Another quantity of considerable importance in the matching procedure is the derivative operator $\partial/\partial n_{\nu\lambda}$ normal to the surface $\pi_{\nu\lambda}$ in the direction of increasing ω_λ (Section 4.1). Since this surface is a half plane, this operator is easily found by using the standard expression

$$\frac{\partial}{\partial n_{\nu\lambda}} = \underset{\sim}{\hat{n}}_{\nu\lambda} \cdot \underset{\sim}{\nabla} \qquad \text{(A.17)}$$

where $\underset{\sim}{\hat{n}}_{\nu\lambda}$ is a unit vector normal to $\pi_{\nu\lambda}$ in the direction of increasing ω_λ and $\underset{\sim}{\nabla}$ is the gradient operator in $X_\lambda Y_\lambda Z_\lambda$ coordinates. Expressing Eq. A.17 in the spherical polar coordinates ζ, ω_λ and γ_λ we find

$$\begin{aligned}
\frac{\partial}{\partial n_{\nu\lambda}} &= \frac{1}{\zeta} \frac{\sin\alpha_{\nu\lambda}}{\sin\omega_\lambda} \left[\left(\frac{\partial}{\partial\omega_\lambda}\right)_{\gamma_\lambda,\zeta} + \cot\alpha_{\nu\lambda} \sin\gamma_\lambda \left(\frac{\partial}{\partial\gamma_\lambda}\right)_{\omega_\lambda,\zeta} \right] \\
&= \frac{1}{\zeta} (\sin^2\alpha_{\nu\lambda} + \cos^2\alpha_{\nu\lambda} \cos^2\gamma_\lambda)^{\frac{1}{2}} \left[\left(\frac{\partial}{\partial\omega_\lambda}\right)_{\gamma_\lambda,\zeta} \right. \\
&\qquad \left. + \cot\alpha_{\nu\lambda} \sin\gamma_\lambda \left(\frac{\partial}{\partial\gamma_\lambda}\right)_{\omega_\lambda,\zeta} \right] \\
&= \frac{1}{\zeta} \frac{\sin\alpha_{\nu\lambda}}{\sin 2\eta_\lambda} \left\{ \frac{1}{2} \left(\frac{\partial}{\partial\eta_\lambda}\right)_{\gamma_\lambda,\zeta} + \cot\alpha_{\nu\lambda} \sin\gamma_\lambda \left(\frac{\partial}{\partial\gamma_\lambda}\right)_{\eta_\lambda,\zeta} \right\}
\end{aligned} \qquad \text{(A.18)}$$

and the indicated differentiations must be done on the full wavefunction with ζ, ω_λ (or η_λ) and γ_λ considered as independent variables before the relation between ω_λ (or η_λ) and γ_λ describing $\pi_{\nu\lambda}$ is used. The third line of Eq. A.18 results from the use of η_λ rather than ω_λ as discussed in Section 3.2. Equation A.17 can also be evaluated in terms of ν arrangement channel coordinates in which case we find

$$\frac{\partial}{\partial n_{\nu\lambda}} = -\frac{1}{\zeta}\,\frac{\sin\alpha_{\nu\lambda}}{\sin\omega_{\nu}}\,\left\{\left(\frac{\partial}{\partial\omega_{\lambda}}\right)_{\gamma_{\nu},\zeta} - \cot\alpha_{\nu\lambda}\,\sin\gamma_{\lambda}\,\left(\frac{\partial}{\partial\gamma_{\nu}}\right)_{\omega_{\nu},\zeta}\right\}$$

$$= -\frac{1}{\zeta_{\lambda}}\,(\sin^{2}\alpha_{\nu\lambda} + \cos^{2}\alpha_{\nu\lambda}\cos^{2}\gamma_{\lambda})^{\frac{1}{2}}\,\left\{\left(\frac{\partial}{\partial\omega_{\nu}}\right)_{\gamma_{\nu},\zeta}\right.$$

$$\left. - \cot\alpha_{\nu\lambda}\,\sin\gamma_{\lambda}\,\left(\frac{\partial}{\partial\gamma_{\nu}}\right)_{\omega_{\nu},\zeta}\right\}$$

$$= -\frac{1}{\zeta}\,\frac{\sin\alpha_{\nu\lambda}}{\sin 2\eta_{\lambda}}\,\left\{\frac{1}{2}\left(\frac{\partial}{\partial\eta_{\nu}}\right)_{\gamma_{\nu},\zeta} - \cot\alpha_{\nu\lambda}\,\sin\gamma_{\lambda}\,\left(\frac{\partial}{\partial\gamma_{\nu}}\right)_{\eta_{\nu},\zeta}\right\}$$

(A.19)

APPENDIX B. EIGENVALUES OF A MATRIX OF THE FORM $\underset{\approx}{U} = \underset{\approx}{\rho}^2 \underset{\approx}{V}$

In this Appendix we show that the potential matrices in the strong interaction and matching regions (Eqs. 3.48 and 3.61) always have real eigenvalues even though they are not symmetric. These matrices have the general form:

$$\underset{\approx}{U} = \underset{\approx}{\rho}^2 \underset{\approx}{V} \tag{B.1}$$

where the real matrix $\underset{\approx}{\rho}^2$ is the matrix representation of a positive definitive operator (Eq. 3.49) and therefore has positive real eigenvalues. $\underset{\approx}{V}$ is a real symmetric matrix whose eigenvalues may be positive, negative or zero.

The first step in finding the eigenvalues of $\underset{\approx}{U}$ involves a diagonalization of $\underset{\approx}{\rho}^2$

$$\underset{\approx}{\widetilde{K}}\, \underset{\approx}{\rho}^2\, \underset{\approx}{K} = \underset{\approx}{\Lambda} \tag{B.2}$$

where $\underset{\approx}{\Lambda}$ is a diagonal matrix whose elements are the various (positive) eigenvalues of ρ^2, and $\underset{\approx}{K}$ is the real orthogonal matrix of eigenvalues. We now form the real matrix $\underset{\approx}{\rho}$ by:

$$\underset{\approx}{\rho} = \underset{\approx}{\widetilde{K}}\, \underset{\approx}{\Lambda}^{\frac{1}{2}}\, \underset{\approx}{K} \tag{B.3}$$

where the diagonal matrix $\underset{\approx}{\Lambda}^{\frac{1}{2}}$ has diagonal elements which are the square roots of those of Λ. $\underset{\approx}{\rho}$ behaves as if it were the "square root" of $\underset{\approx}{\rho}^2$ in many applications, since, from Eqs. B.2 and B.3,

$$\underset{\approx}{\rho}\,\underset{\approx}{\rho} = \underset{\approx}{\rho}^{2} \tag{B.4}$$

Next, we define the real matrix $\underset{\approx}{W}$ as:

$$\underset{\approx}{W} = \underset{\approx}{\rho}^{-1}\,\underset{\approx}{U}\,\underset{\approx}{\rho} = \underset{\approx}{\rho}\,\underset{\approx}{V}\,\underset{\approx}{\rho} \tag{B.5}$$

where the second equality in Eq. B.5 follows from Eq. B.1. From Eq. B.5, it is obvious that $\underset{\approx}{W}$ is real symmetric, and it may therefore be diagonalized by a real orthogonal matrix which we denote by $\underset{\approx}{T}$:

$$\tilde{\underset{\approx}{T}}\,\underset{\approx}{W}\,\underset{\approx}{T} = \underset{\approx}{E} \tag{B.6}$$

The diagonal matrix $\underset{\approx}{E}$ contains the real eigenvalues of $\underset{\approx}{W}$.

Finally, if we define the nonorthogonal, but real matrix $\underset{\approx}{S}$ by:

$$\underset{\approx}{S} = \underset{\approx}{\rho}\,\underset{\approx}{T} \tag{B.7}$$

we obtain, from Eqs. B.5 and B.6

$$\underset{\approx}{S}^{-1}\,\underset{\approx}{U}\,\underset{\approx}{S} = \underset{\approx}{E} \tag{B.8}$$

which proves that the matrix $\underset{\approx}{S}$ diagonalizes $\underset{\approx}{U}$ with the resulting real eigenvalues contained in $\underset{\approx}{E}$.

APPENDIX C. RELATIONS BETWEEN DISTINGUISHABLE ATOM SCATTERING AMPLITUDES FOR ATOM DIATOM REACTIONS INVOLVING HOMONUCLEAR DIATOMIC MOLECULES

In this Appendix we investigate the consequences of two-atom permutational symmetry (as discussed in Section 6.1) on the distinguishable atom scattering amplitudes. We show that in collisions for which Eq. 6.1 is valid (*i.e.*, collisions of an atom with a homonuclear diatomic molecule), the resultant scattering amplitudes $f^{\nu v' j'}_{\lambda v j}$ and $f^{\kappa v' j'}_{\lambda v j}$ are related by Eq. 6.3 and that $f^{\lambda v' j'}_{\lambda v j}$ obeys Eq. 6.4. The circumflex on $\hat{f}$ of Eq. 5.28 will be omitted in this Appendix.)

We first rewrite the scattering solution Eq. 5.30 for collisions with incident linewave in channel λ:

$$\Psi_p^{\lambda v_\lambda j_\lambda} \underset{R_\lambda \to \infty}{\sim} e^{ik^{\lambda}_{v_\lambda j_\lambda} R_\lambda \cos \chi_\lambda} \varphi_{j_\lambda}(\theta_\lambda) \frac{\phi^{\lambda}_{v_\lambda j_\lambda}(r_\lambda)}{\sqrt{r_\lambda}}$$

$$+ \sum_{v'_\lambda j'_\lambda} \frac{e^{ik^{\lambda}_{v'_\lambda j'_\lambda} R_\lambda}}{\sqrt{R_\lambda}} f^{\lambda v'_\lambda j'_\lambda}_{\lambda v_\lambda j_\lambda}(\chi_\lambda)\, \varphi_{j'_\lambda}(\theta_\lambda)$$

$$\times \frac{\phi^{\lambda}_{v'_\lambda j'_\lambda}(r_\lambda)}{\sqrt{r_\lambda}} \cdot \left(\frac{\hbar}{\mu |V^{\lambda}_{v'_\lambda j'_\lambda}|} \right)^{\frac{1}{2}}$$

$$\underset{R_\nu \to \infty}{\sim} \sum_{v_\nu j_\nu} \frac{e^{ik^{\nu}_{v_\nu j_\nu} R_\nu}}{\sqrt{R_\nu}} f^{\nu v_\nu j_\nu}_{\lambda v_\lambda j_\lambda}(\chi_\nu)\, \varphi_{j_\nu}(\theta_\nu)$$

$$\times \frac{\phi^{\nu}_{v_\nu j_\nu}(r_\nu)}{\sqrt{r_\nu}} \left(\frac{\hbar}{\mu \left| V^{\nu}_{v_\nu j_\nu} \right|} \right)^{\frac{1}{2}}$$

$$\underset{R_\kappa \to \infty}{\sim} \sum_{v_\kappa j_\kappa} \frac{e^{ik^{\kappa}_{v_\kappa j_\kappa} R_\kappa}}{\sqrt{R_\kappa}} f^{\kappa v_\kappa j_\kappa}_{\lambda v_\lambda j_\lambda}(\chi_\kappa)\, \varphi_{j_\kappa}(\theta_\kappa)$$

$$\times \frac{\phi^{\kappa}_{v_\kappa j_\kappa}(r_\kappa)}{\sqrt{r_\kappa}} \left(\frac{\hbar}{\mu \left| V^{\kappa}_{v_\kappa j_\kappa} \right|} \right)^{\frac{1}{2}} \tag{C.1}$$

If the diatomic target in the incident channel is homonuclear, the physical system should be invariant to the operator $P_{\nu\kappa}$ which interchanges the two identical atoms A_ν and A_κ involved. If we perform this interchange, the coordinates which define the system in each arrangement channel become (by inspection of Fig. 1):

$$\begin{aligned}
(R_\lambda, \chi_\lambda) &\to (R_\lambda, \chi_\lambda) \\
(r_\lambda, \theta_\lambda) &\to (r_\lambda, \theta_\lambda + \pi) \\
(R_\nu, \chi_\nu) &\to (R_\kappa, \chi_\kappa) \\
(r_\nu, \theta_\nu) &\to (r_\kappa, \theta_\kappa + \pi) \\
(R_\kappa, \chi_\kappa) &\to (R_\nu, \chi_\nu) \\
(r_\kappa, \theta_\kappa) &\to (r_\nu, \theta_\nu + \pi)
\end{aligned} \tag{C.2}$$

If we make these substitutions into Eq. C.1 realizing that $\varphi_{j_\lambda}(\theta_\lambda + \pi) = (-1)^{j_\lambda} \varphi_{j_\lambda}(\theta_\lambda)$, and appropriately relabel quantum numbers which serve as summation indices, we obtain:

$$
\begin{aligned}
P_{\nu\kappa}\,\Psi_{p}^{\lambda v_\lambda j_\lambda} \underset{R_\lambda \to \infty}{\sim} & (-1)^{j_\lambda}\, e^{ik^{\lambda}_{j_\lambda v_\lambda} R_\lambda \cos\chi_\lambda}\, \varphi_{j_\lambda}(\theta_\lambda)\, \frac{\phi^{\lambda}_{j_\lambda v_\lambda}(r_\lambda)}{\sqrt{r_\lambda}} \\
& + \sum_{v'_\lambda j'_\lambda} (-1)^{j'_\lambda}\, \frac{e^{ik^{\lambda}_{v'_\lambda j'_\lambda} R_\lambda}}{\sqrt{R_\lambda}}\, f^{\lambda v'_\lambda j'_\lambda}_{\lambda v_\lambda j_\lambda}(\chi_\lambda)\, \varphi_{j'_\lambda}(\theta_\lambda) \\
& \times \frac{\phi^{\lambda}_{v'_\lambda j'_\lambda}(r_\lambda)}{\sqrt{r_\lambda}} \left(\frac{\hbar}{\mu\,|V^{\lambda}_{v'_\lambda j'_\lambda}|}\right)^{\frac{1}{2}} \\
\underset{R_\kappa \to \infty}{\sim} & \sum_{v_\kappa j_\kappa} (-1)^{j_\kappa}\, \frac{e^{ik^{\nu}_{v_\kappa j_\kappa} R_\kappa}}{\sqrt{R_\kappa}}\, f^{\nu v_\kappa j_\kappa}_{\lambda v_\lambda j_\lambda}(\chi_\kappa)\, \varphi_{j_\kappa}(\theta_\kappa) \\
& \times \frac{\phi^{\nu}_{v_\kappa j_\kappa}(r_\kappa)}{\sqrt{r_\kappa}} \left(\frac{\hbar}{\mu\,|V^{\nu}_{v_\kappa j_\kappa}|}\right)^{\frac{1}{2}} \\
\underset{R_\nu \to \infty}{\sim} & \sum_{v_\nu j_\nu} (-1)^{j_\nu}\, \frac{e^{ik^{\kappa}_{v_\nu j_\nu} R_\nu}}{\sqrt{R_\nu}}\, f^{\kappa v_\nu j_\nu}_{\lambda v_\lambda j_\lambda}(\chi_\nu)\, \varphi_{j_\nu}(\theta_\nu) \\
& \times \frac{\phi^{\kappa}_{v_\nu j_\nu}(r_\nu)}{\sqrt{r_\nu}} \left(\frac{\hbar}{\mu\,|V^{\kappa}_{v_\nu j_\nu}|}\right)^{\frac{1}{2}} \qquad \text{(C.3)}
\end{aligned}
$$

The line wave part of C.3 differs only by a factor of $(-1)^{j_\lambda}$ from the corresponding part of C.1. Since the scattering solutions are unique, this implies that the corresponding circular wave parts must be related by the same proportionality constant, i.e.,

$$P_{\nu\kappa}\,\psi_p^{\lambda v_\lambda j_\lambda} = (-1)^{j_\lambda}\,\psi_p^{\lambda v_\lambda j_\lambda} \tag{C.4}$$

Replacement of Eqs. C.1 and C.3 into C.4 and identification of the corresponding outgoing wave parts in channel λ immediately yields

$$f_{\lambda v_\lambda j_\lambda}^{\lambda v'_\lambda j'_\lambda} = (-1)^{j_\lambda + j'_\lambda}\, f_{\lambda v_\lambda j_\lambda}^{\lambda v'_\lambda j'_\lambda} \tag{C.5}$$

which is identical to Eq. 6.4. In order to compare the outgoing wave solutions in channels ν and κ, we first must realize that the $\phi^{\nu}_{v_\kappa j_\kappa}(r_\kappa)$ (and $k^{\nu}_{v_\kappa j_\kappa}$) of Eq. C.3, and the $\phi^{\kappa}_{v_\kappa j_\kappa}(r_\kappa)$ (and $k^{\kappa}_{v_\kappa j_\kappa}$) of Eq. C.1 are identical since these represent vibrational wavefunctions in the two product arrangement channels both of which are the same for a homonuclear target. This allows us to compare the outgoing wave solutions in channels ν and κ in Eq. C.4, obtaining

$$f_{\lambda v_\lambda j_\lambda}^{\nu v_\kappa j_\kappa} = (-1)^{j_\lambda + j_\kappa}\, f_{\lambda v_\lambda j_\lambda}^{\kappa v_\kappa j_\kappa} \tag{C.6}$$

in both cases. Eq. C. 6 is identical to Eq. 6.3.

APPENDIX D: POST ANTISYMMETRIZATION FOR THE $H + H_2$ EXCHANGE REACTION

Although correct expressions for the indistinguishable (antisymmetrized) cross sections in terms of the distinguishable atom reactive and nonreactive amplitudes have been listed by Doll, George and Miller [42], who have obtained their results using the integro-differential equation approach described by Miller [43], there seems to be some confusion in the use of these expressions so we shall derive them here in order to clarify their meanings. We will follow the post-antisymmetrization procedure outlined by Schiff [23] which is somewhat more transparent than Miller's. In all of our treatment below we assume that the interaction potential is not spin-dependent and that there are no external magnetic fields present.

We start by rewriting the asymptotic physical solution (Eq. 5.30) for distinguishable atom scattering (in the mass-scaled coordinate system), using, for notational simplicity, the labels $\lambda = 1$, $\nu = 2$ and $\kappa = 3$:

$$\Psi_p^{1v_1j_1}(1,2,3) \underset{\sim}{\overset{R_1\to\infty}{}} e^{i\underset{\sim}{k}^1_{v_1j_1}\cdot\underset{\sim}{R}_1} W^1_{v_1j_1}(2,3) + \sum_{v_1'j_1'} \frac{e^{ik^1_{v_1'j_1'}R_1}}{\sqrt{R_1}} W^1_{v_1'j_1'}(2,3) \times C^{v_1'j_1'} f^{1v_1'j_1'}_{1v_1j_1}(\chi_1)$$

$$\underset{\sim}{\overset{R_2\to\infty}{}} \sum_{v_2j_2} \frac{e^{ik^2_{v_2j_2}R_2}}{\sqrt{R_2}} W^2_{v_2j_2}(3,1)\, C^{v_2j_2} f^{2v_2j_2}_{1v_1j_1}(\chi_2)$$

$$R_3 \overset{\to}{\sim} \infty \sum_{v_3 j_3} \frac{e^{ik^3_{v_3 j_3} R_3}}{\sqrt{R_3}} W^3_{v_3 j_3}(2,1)\, C^{v_3 j_3}\, f^{3 v_3 j_3}_{1 v_1 j_1}(\chi_3) \tag{D.1}$$

where, for example,

$$W^1_{v_1 j_1}(2,3) = \frac{\varphi_{j_1}(\theta_1)\, \phi^1_{v_1 j_1}(r_1)}{\sqrt{r_1}} \tag{D.2}$$

and

$$C^{v_1' j_1'} = \left(\frac{\hbar}{\mu \left|V_{v_1' j_1'}\right|}\right)^{\frac{1}{2}} \tag{D.3}$$

For simplicity the circumflex on the scattering amplitude $\hat{f}$ of Eq. 5.30 has been omitted. Note that we have used the numbers 1, 2 and 3 as both an arrangement channel label <u>and</u> a particle label. Provided that we always permute particles in a cyclic way in our arrangement channel labeling, the two designations are identical and we will consider this to be the case here. This means that the coordinate $\underset{\sim}{r}_1$ is the internuclear vector from particle 2 to particle 3 (in the $\underset{\sim}{R}_1$, $\underset{\sim}{r}_1$ coordinate system) and therefore the 2,3 diatomic molecule wavefunction is a function of $\underset{\sim}{r}_1$. We should also point out that for $H + H_2$, the separated arrangement channel quantum states are all identical so the labels $v_1 j_1$, $v_2 j_2$ and $v_3 j_3$ are essentially dummy indices and do not imply, for example, that $W^1_{v_1 j_1}$ differs in its functional form from $W^2_{v_2 j_2}$ or $W^3_{v_3 j_3}$ when $j_1 = j_2 = j_3$ and $v_1 = v_2 = v_3$. As a consequence of the symmetry property of Eq. 6.1 for $H + H_2$, and in view of the above discussion, the wavefunction in Eq. D.1 has the property

$$\Psi_p^{1v_1j_1}(1,2,3) = (-1)^{j_1}\,\Psi_p^{1v_1j_1}(1,3,2) \tag{D.4a}$$

This is valid in all three arrangement channels provided that Eqs. 6.3 and 6.4 are satisfied. These two equations also imply that the behavior of the wavefunction $\Psi_p^{2v_1j_1}(2,3,1)$ under the same permutation is:

$$\Psi_p^{2v_1j_1}(2,3,1) = (-1)^{j_1}\,\Psi_p^{3v_1j_1}(3,1,2) \tag{D.4b}$$

Now consider the spin wavefunctions of the separated atom plus diatom system in arrangement channel 1. Since the three hydrogen atoms have spin $\frac{1}{2}$, these wavefunctions are:

$$v_1(1,2,3) = \alpha(1)\,\alpha(2)\,\alpha(3) \tag{D.5a}$$

$$v_2(1,2,3) = \beta(1)\,\alpha(2)\,\alpha(3) \tag{D.5b}$$

$$v_3(1,2,3) = \frac{1}{\sqrt{2}}\,\alpha(1)\,[\alpha(2)\,\beta(3) + \beta(2)\,\alpha(3)] \tag{D.5c}$$

$$v_4(1,2,3) = \frac{1}{\sqrt{2}}\,\beta(1)\,[\alpha(2)\,\beta(3) + \beta(2)\,\alpha(3)] \tag{D.5d}$$

$$v_5(1,2,3) = \alpha(1)\,\beta(2)\,\beta(3) \tag{D.5e}$$

$$v_6(1,2,3) = \beta(1)\,\beta(2)\,\beta(3) \tag{D.5f}$$

$$v_7(1,2,3) = \frac{1}{\sqrt{2}}\,\alpha(1)\,[\alpha(2)\,\beta(3) - \beta(2)\,\alpha(3)] \tag{D.5g}$$

$$v_8(1,2,3) = \frac{1}{\sqrt{2}}\,\beta(1)\,[\alpha(2)\,\beta(3) - \beta(2)\,\alpha(3)] \tag{D.5h}$$

They are eigenfunctions of S_z but not S^2 and have the symmetry property

$$v_i\,(1,3,2) = \begin{cases} v_i\,(1,2,3) & i = 1\text{-}6 \\ -v_i\,(1,2,3) & i = 7,8 \end{cases} \tag{D.6}$$

The correct separated atom plus diatom wavefunctions are then

$$\Phi^{1v_1j_1(i)}\,(1,2,3) = \Psi_p^{1v_1j_1}\,(1,2,3)\; v_i\,(1,2,3) \tag{D.7}$$

where (i) here designates the spin state of the system. Since $\Phi^{1v_1j_1}\,(1,2,3)$ must be antisymmetric with respect to permutation of particles 2 and 3, we have the requirements (in view of Eqs. D.4 and D.6) that

$$j_1 = \begin{cases} \text{odd for } i = 1\text{-}6 & \text{(ortho states)} \\ \text{even for } i = 7,8 & \text{(para states)} \end{cases} \tag{D.8}$$

We now form the completely antisymmetric wavefunction $\Psi^{Av_1j_1(i)}\,(1,2,3)$ by superimposing the functions $\Phi^{\lambda v_1j_1(i)}$ $(\lambda = 1,2,3)$ having the same initial states v_1j_1:

$$\Psi^{Av_1j_1(i)} = \Phi^{1v_1j_1(i)}\,(1,2,3) + \Phi^{2v_1j_1(i)}\,(2,3,1) + \Phi^{3v_1j_1(i)}\,(3,1,2) \qquad i = 1\text{-}8 \tag{D.9}$$

Eqs. D.4, D.6 and D.8 can be used to prove that $\Psi^{Av_1j_1(i)}$ is antisymmetric under a permutation of any two of the three particles in the system. This then is the correct scattering solution, and its asymptotic behavior can be used to determine the correct antisymmetrized scattering amplitudes. This asymptotic behavior can be determined by evaluating $\Psi^{Av_1j_1(i)}$ at large values of R_1 (or R_2 or R_3) which yields:

$$\Psi^{Av_1j_1(i)}(1,2,3) \underset{R_1\sim\infty}{\sim} e^{i\underset{\sim}{k}^1_{v_1j_1}\cdot \underset{\sim}{R}_1} W^1_{v_1j_1}(2,3)\, v_i(1,2,3)$$

$$+ \sum_{v_1'j_1'} \frac{e^{ik^1_{v_1'j_1'}R_1}}{\sqrt{R_1}} W^1_{v_1'j_1'}(2,3)\; C^{v_1'j_1'} \Big\{ f^{1v_1'j_1'}_{1v_1j_1}\, v_i(1,2,3)$$

$$+ f^{1v_1'j_1'}_{2v_1j_1}\, v_i(2,3,1) + f^{1v_1'j_1'}_{3v_1j_1}\, v_i(3,1,2) \Big\} \qquad \text{(D.10)}$$

This has the form of a physical scattering solution, but the expression in brackets must be re-expressed in terms of the $v_j(1,2,3)$ spin functions of the final separated atom-diatom ($j = 1$ to 8). Accordingly, we write

$$f^{1v_1'j_1'}_{1v_1j_1}\, v_i(1,2,3) + f^{1v_1'j_1'}_{2v_1j_1}\, v_i(2,3,1) + f^{1v_1'j_1'}_{3v_1j_1}\, v_i(3,1,2)$$

$$= \sum_{j=1}^{8} f^{A(j)v_1'j_1'}_{(i)v_1j_1}\, v_j(1,2,3) \qquad \text{(D.11)}$$

where $f^{A(j)v_1'j_1'}_{(i)v_1j_1}$ is the antisymmetrized scattering amplitude for scattering from initial state $(i)v_1j_1$ (spin state i) to final state $(j)v_1'j_1'$ (where Eq. D.8 must be satisfied for both of these states). We can solve for the $f_{(i)v_1j_1}^{A(j)v_1'j_1'}$ by multiplying Eq. D.11 by $v_k(1,2,3)$, integrating over all spin variables and then replacing the index k by j in the result. The resulting expressions for $f_{(i)v_1j_1}^{A(j)v_1'j_1'}$ in terms of the distinguishable atom scattering amplitudes are given in Table I. The expressions in that table have been simplified by the use of the relation (see Eqs. 6.3):

$$f_{2v_1j_1}^{1v_1'j_1'} = (-1)^{j_1+j_1'} f_{3v_1j_1}^{1v_1'j_1'} \tag{D.12}$$

In the notation of Doll, George and Miller [42] $f_{1v_1j_1}^{1v_1'j_1'}$ is the direct scattering amplitude while $f_{2v_1j_1}^{1v_1'j_1'}$ is the exchange amplitude.

The state to state cross sections are (from Eq. 5.29):

$$\sigma_{(i)v_1j_1}^{(j)v_1'j_1'} = \frac{1}{\bar{k}_{v_1j_1}} \left| f_{(i)v_1j_1}^{(j)v_1'j_1'} \right|^2 \tag{D.13}$$

and the cross sections of Eq. 6.5 are obtained by summing Eq. D. 13 over final spin states and averaging over initial ones. As an example, the para to ortho cross section (Eq. 6.5b) is given by (dropping the v_1j_1, $v_1'j_1'$ indices but retaining the spin labels)

$$\begin{aligned} \sigma_p^o = {} & \tfrac{1}{2}(\sigma_7^1 + \sigma_7^2 + \sigma_7^3 + \sigma_7^4 + \sigma_7^5 + \sigma_7^6 \\ & + \sigma_8^1 + \sigma_8^2 + \sigma_8^3 + \sigma_8^4 + \sigma_8^5 + \sigma_8^6) = \frac{3}{\bar{k}} \left| f_2^1 \right|^2 \end{aligned} \tag{D.14}$$

$f^{(j)v'_1j'_1}_{(i)v_1j_1}$		final j =	1	2	3	4	5	6	7	8
		j'_1	odd	odd	odd	odd	odd	odd	even	even
initial i	j_1	label \ label	ortho	ortho	ortho	ortho	ortho	ortho	para	para
1	odd	ortho	$f_1^1+f_2^1$	0	0	0	0	0	0	0
2	odd	ortho	0	f_1^1	$\sqrt{2}\,f_2^1$	0	0	0	$\sqrt{2}\,f_2^1$	0
3	odd	ortho	0	$\sqrt{2}\,f_2^1$	$f_1^1+f_2^1$	0	0	0	$-f_2^1$	0
4	odd	ortho	0	0	0	$f_1^1+f_2^1$	$\sqrt{2}\,f_2^1$	0	0	f_2^1
5	odd	ortho	0	0	0	$\sqrt{2}\,f_2^1$	f_1^1	0	0	$-\sqrt{2}\,f_2^1$
6	odd	ortho	0	0	0	0	0	$f_1^1+2f_2^1$	0	0
7	even	para	0	$\sqrt{2}\,f_2^1$	f_2^1	0	0	0	$f_1^1-f_2^1$	0
8	even	para	0	0	0	$-f_2^1$	$\sqrt{2}\,f_2^1$	0	0	$f_1^1-f_2^1$

Table 1. Antisymmetrized scattering amplitudes $f^{(j)v'_1j'_1}_{(i)v_1j_1}$ and their relation to the distinguishable atom amplitudes $f^{1v'_1j'_1}_{1v_1j_1}$ and $f^{1v'_1j'_1}_{2v_1j_1}$.*

---

*The indices v_1j_1 and $v'_1j'_1$ on the $f^{1v'_1j'_1}_{1v_1j_1}$ and $f^{1v'_1j'_1}_{2v_1j_1}$ are omitted.

FOOTNOTES

[*] Work supported in part by the United States Air Force Office of Scientific Research (Grant No. AF05R-73-2539).

[†] Work performed in partial fulfillment of the requirements for the Ph.D. degree in Chemistry at the California Institute of Technology.

[‡] Present address: Soreq Nuclear Center, Yavne, Israel; and Department of Chemical Physics, The Weizmann Institute of Science, P.O. Box 26, Rehovot, Israel.

[§] Contribution No.

REFERENCES

[1] E. M. Mortenson and K. S. Pitzer, 1962, Chem. Soc. (London) Spec. Publ., 16, 57; E. M. Mortenson, 1968, J. Chem. Phys., 48, 4029.

[2] D. J. Diestler and V. McKoy, 1968, J. Chem. Phys., 48, 2951.

[3] C. C. Rankin and J. Light, 1971, J. Chem. Phys., 51, 1701; G. Miller and J. C. Light, 1971, J. Chem. Phys., 54, 1635; 1971, ibid., 54, 1643.

[4] D. J. Truhlar and A. Kuppermann, 1970, J. Chem. Phys., 52, 3841; 1972, ibid., 56, 2232.

[5] Aron Kuppermann, Aug. 1970, Proceedings of the Conference on Potential Energy Surfaces in Chemistry, U.C. Santa Cruz, W. A. Lester, ed., p. 121; 1971, Electronic and Atomic Collisions, Proceedings of VII ICPEAC, North Holland, Amsterdam, p. 3.

[6] D. J. Diestler, 1971, J. Chem. Phys., 54, 4547.

[7] B. R. Johnson, 1972, Chem. Phys. Lett., 13, 172.

[8] S. F. Wu and R. D. Levine, 1971, Mol. Phys., 22, 881.

[9] E. Shipsey, 1973, J. Chem. Phys., 58, 232.

[10] G. C. Schatz, J. Bowman and A. Kuppermann, 1973, J. Chem. Phys., 58, 4023; G. C. Schatz and A. Kuppermann, 1973, J. Chem. Phys., 59, 964; J. M. Bowman, G. C. Schatz and A. Kuppermann, 1974, Chem. Phys. Lett., 24, 378; G. C. Schatz, J. M. Bowman and A. Kuppermann, 1975, J. Chem. Phys., 63, 674, 685.

[11] J. T. Adams, R. L. Smith and E. F. Hayes, 1974, *J. Chem. Phys.*, **61**, 2193.

[12] M. Baer and D. J. Kouri, 1974, *Chem. Phys. Lett.*, **24**, 37; M. Baer, 1974, *J. Chem. Phys.*, **60**, 1057; A. Persky and M. Baer, 1974, *J. Chem. Phys.*, **60**, 133; M. Baer, U. Halavee and A. Persky, 1974, *J. Chem. Phys.*, **61**, 5122.

[13] P. B. Middleton and R. E. Wyatt, 1972, *J. Chem. Phys.*, **56**, 2702; E. A. McCollough and R. E. Wyatt, 1971, *J. Chem. Phys.*, **54**, 3578; 1971, *ibid.*, **54**, 3592.

[14] R. P. Saxon and J. C. Light, 1972, *J. Chem. Phys.*, **56**, 3874; 1972, *ibid.*, **56**, 3885.

[15] A. Altenberger-Siczek and J. C. Light, 1974, *J. Chem. Phys.*, **61**, 4373.

[16] G. Wolken and M. Karplus, 1974, *J. Chem. Phys.*, **60**, 351.

[17] (a) A. B. Elkowitz and R. E. Wyatt, *J. Chem. Phys.*, in press; (b) S. A. Harms and R. E. Wyatt, 1972, *J. Chem. Phys.*, **57**, 2722.

[18] M. Baer and D. J. Kouri, 1971, *Chem. Phys. Lett.*, **11**, 238; 1972, *J. Chem. Phys.*, **56**, 1758; 1972, *ibid.*, **57**, 3991.

[19] A. Kuppermann, G. C. Schatz and M. Baer, 1974, *J. Chem. Phys.*, **61**, 4362.

[20] G. C. Schatz, A. Kuppermann and M. Baer, to be published.

[21] For reactions for which one of the three arrangement channels is energetically inaccessible, the integration needs to be done usually in only the two remaining open arrangement channels and a some-

what different and simpler matching procedure is required. This situation is not described in this paper although it can be handled by a straightforward modification of the theory here presented.

[22] A. Kuppermann and G. C. Schatz, 1975, J. Chem. Phys., 62, 2502.

[23] L. I. Schiff, 1968, Quantum Mechanics, (McGraw-Hill, New York, 3rd Ed.), p. 384-395.

[24] A. M. Lane and R. G. Thomas, 1958, Rev. Mod. Phys., 30, 257; These authors use the term "collision matrix" in lieu of "scattering matrix."

[25] If γ'_λ is the angle between 0 and π defined, by $\cos\gamma'_\lambda = \underset{\sim}{\bar{R}}_\lambda \cdot \underset{\sim}{\bar{r}}_\lambda / |\bar{R}_\lambda| |\bar{r}_\lambda|$ then $\gamma'_\lambda = \gamma_\lambda$ for $0 \leq \gamma_\lambda \leq \pi$ and $\gamma'_\lambda = 2\pi - \gamma_\lambda$ for $\pi \leq \gamma_\lambda \leq 2\pi$. In any case, $\cos\gamma'_\lambda = \cos\gamma_\lambda$.

[26] L. M. Delves, 1959; Nucl. Phys., 9, 391; 1960, 20, 275.

[27] D. Jepsen and J. O. Hirschfelder, 1959, Proc. Nat. Acad. Sci., 45, 249.

[28] This is true because the incident plane ("line") wave solution discussed in Section 5.2 contains a whole spectrum of total angular momenta (corresponding classically to a range of impact parameters), many of which contribute to the reaction.

[29] The angles χ_ν and χ_λ differ by an angle $\Delta\chi_{\nu\lambda}$ which is a function of r_λ, R_λ and γ_λ only as seen in Eqs. A.8 and A.9. Therefore, $\varphi_J(\chi_\lambda)$ is also an eigenfunction of $\hbar/i\,(\partial/\partial\chi_\nu)_{\gamma_\lambda}$ with the same eigenvalue $J\hbar$. The quantum number J is as a result independent of the arrangement channel λ used to obtain it.

[30] A. Kuppermann, (a) Chem. Phys. Lett., in press; (b) J. Chem.

Phys., to be published.

[31] R. N. Porter and M. Karplus, 1964, *J. Chem. Phys.*, **40**, 1105.

[32] Actually, values of ω_{λ_0} smaller than $\pi - \alpha_{\nu\lambda}$ and of ω_{λ_1} greater than $\pi/2$ are also permissible but not needed to determine the wavefunction on the matching half-plane $\pi_{\nu\lambda}$.

[33] *Handbook of Mathematical Functions*, (M. Abramowitz and I. A. Stegun, Eds.), National Bureau of Standards, Washington, D.C., 1964, Chap. 9.

[34] D. G. Truhlar, dissertation, California Institute of Technology, 1970, (unpublished), Appendix 4.

[35] R. Gordon, 1969, *J. Chem. Phys.*, **51**, 14.

[36] We used a version of Gordon's method developed by A. Wagner for inelastic atom-diatom collisions. See A. Wagner and V. McKoy, 1973, *J. Chem. Phys.*, **58**, 5561.

[37] To clarify this concept, let us consider a scattering solution consisting of an incoming wave in arrangement channel λ and outgoing waves in all three arrangement channels λ, ν, κ. There will, in general, be N of these kinds of scattering solutions which are linearly independent (for a close coupling expansion truncated at N terms in each arrangement channel), along with N having incoming waves in channel ν and N with incoming waves in channel κ for a total of 3N. The latter two sets of solutions will have only outgoing waves in channel λ and, in the absence of the inclusion of dissociated states, it will be impossible to linearly combine these latter 2N solutions to

generate the N sets of solutions which have incoming waves in channel λ. Therefore we have 3N scattering solutions which are linearly independent when the entire configuration space is considered although only 2N of them are independent in any one asymptotic arrangement channel.

[38] N. S. F. Mott and H. S. W. Massey, 1965, *The Theory of Atomic Collisions*, 3rd Ed. (Clarendon Press, Oxford).

[39] Note that there are a few differences in phases and signs between the formulas which describe coplanar scattering and those for 3-D [38]. These changes result from the differences between the phases of the cylindrical and spherical Bessel functions [33] and, of course, have no physical significance.

[40] R. B. Walker and R. E. Wyatt, 1974, *J. Chem. Phys.*, **61**, 4839.

[41] This expression is obtained from reference 33, p. 361, Eq. 9.1.41 by setting $t = i\exp(i\chi_{\lambda'})$.

[42] J. D. Doll, T. F. George and W. H. Miller, 1973, *J. Chem. Phys.*, **58**, 1343.

[43] W. H. Miller, 1969, *J. Chem. Phys.*, **50**, 407.

FIGURE CAPTIONS

FIG. 1. Vectors used to specify the location of the three atoms in the A, B, C collision system relative to the center of mass G. G_{BC}, G_{AC} and G_{AB} denote the locations of the centers of mass of the diatomic, BC, AC and AB, respectively. $\underset{\sim}{\overline{R}}_{\alpha}$, $\underset{\sim}{\overline{r}}_{\alpha}$, $\underset{\sim}{\overline{R}}_{\beta}$, $\underset{\sim}{\overline{r}}_{\beta}$, $\underset{\sim}{\overline{R}}_{\gamma}$, $\underset{\sim}{\overline{r}}_{\gamma}$ are defined in text.

FIG. 2. Plot of potential contours for the $H + H_2$ reaction in the $X_\lambda Y_\lambda Z_\lambda$ space defined in the text using the spherical polar coordinate mapping of Eq. 3.1, for six fixed values of the azimuthal angle γ_λ. (a) $\gamma_\lambda = 0°$ and $180°$, (b) $\gamma_\lambda = 45°$ and $225°$, (c) $\gamma_\lambda = 90°$ and $270°$. In (a) we also depict the lines of intersection of the $\gamma_\lambda = 0, 180°$ plane with the half planes $\pi_{\nu\lambda}$, $\pi_{\kappa\nu}$, $\pi_{\lambda\kappa}$ defined by Eq. 3.2, which are used to divide configuration space into three arrangement channel regions λ, ν, κ. For each figure above, OW_λ is the intersection of the half plane determined by OZ_λ and the corresponding smallest γ_λ with the $OX_\lambda Y_\lambda$ plane.

FIG. 3. Division of the R_λ, r_λ space into four regions I, II, III and IV. The contours are equipotentials of the matrix element $V_0^\lambda(r_\lambda, R_\lambda)$ (see Eq. 3.8) in eV for the Porter Karplus $H + H_2$ potential energy function. The dashed line L is the line of steepest ascents and descents for V_0^λ. The locations of the

points P'_0, P_0 and P_1 are discussed in Section 3.3 of the text. Q is the origin of this space.

FIG. 4. The polar coordinates ρ_λ, φ_λ and ζ, η_λ and their interrelationships in R_λ, r_λ space.

FIG. 5. (a) Plot of the matching half planes $\pi_{\nu\lambda}$ and $\pi_{\lambda\kappa}$, and their intersection with a cone of constant ω_λ $(\omega_{\lambda_0} \leqslant \omega_\lambda \leqslant \omega_{\lambda_1})$ showing the straight lines of intersection which occur at two angles $\gamma_\lambda(\omega_\lambda)$ for which $\cot\omega_\lambda = -\cot\alpha_{\nu\lambda}\cos\gamma_\lambda$, and two more for which $\cot\omega_\lambda = -\cot\alpha_{\lambda\kappa}\cos\gamma_\lambda$.

(b) Lines of intersection of $\pi_{\nu\lambda}$ with constant ω_λ cones at intervals of $\Delta\omega_\lambda = 5°$ for $H + H_2$ where $\omega_{\lambda_0} = 60°$ and $\omega_{\lambda_1} = 90°$.

FIG. 6. Plot of equipotential contours on the matching surface $\pi_{\nu\lambda}$ for the $H + H_2$ reaction in the Cartesian coordinate system W_λ, Y_λ where $W_\lambda = (X_\lambda^2 \sin^2\alpha_{\nu\lambda} + Z_\lambda^2 \cos^2\alpha_{\nu\lambda})^{\frac{1}{2}}$ and the system $X_\lambda, Y_\lambda, Z_\lambda$ is the one described in Section 3.1. Because of the symmetry of the H_3 system, Fig. 6 is equivalent to the lower half of Fig. 2c since the $Z_\lambda < 0$ half plane of the $OY_\lambda Z_\lambda$ plane is for this system the same as the $\pi_{\kappa\nu}$ matching plane. The half-lines emanating from the origin correspond to constant values of γ_λ and η_λ, as indicated.

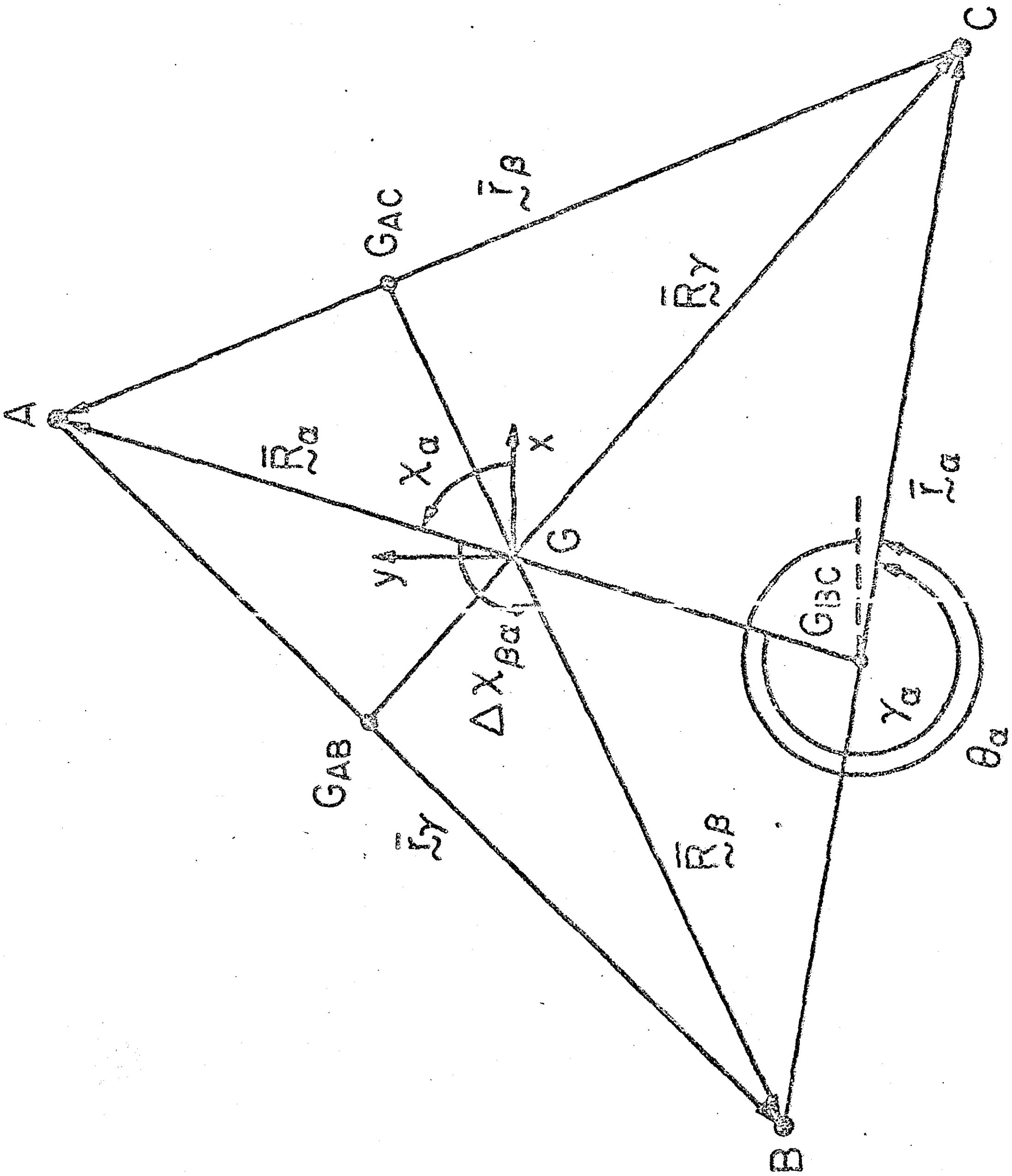
A
B
C
G
G_{AC}
G_{AB}
G_{BC}
x
y
$\bar{\underset{\sim}{R}}_{\alpha}$
$\bar{\underset{\sim}{R}}_{\beta}$
$\bar{\underset{\sim}{R}}_{\gamma}$
$\bar{\underset{\sim}{r}}_{\alpha}$
$\bar{\underset{\sim}{r}}_{\beta}$
$\bar{\underset{\sim}{r}}_{\gamma}$
χ_{α}
$\Delta\chi_{\beta\alpha}$
γ_{α}
θ_{α}

Figure 1

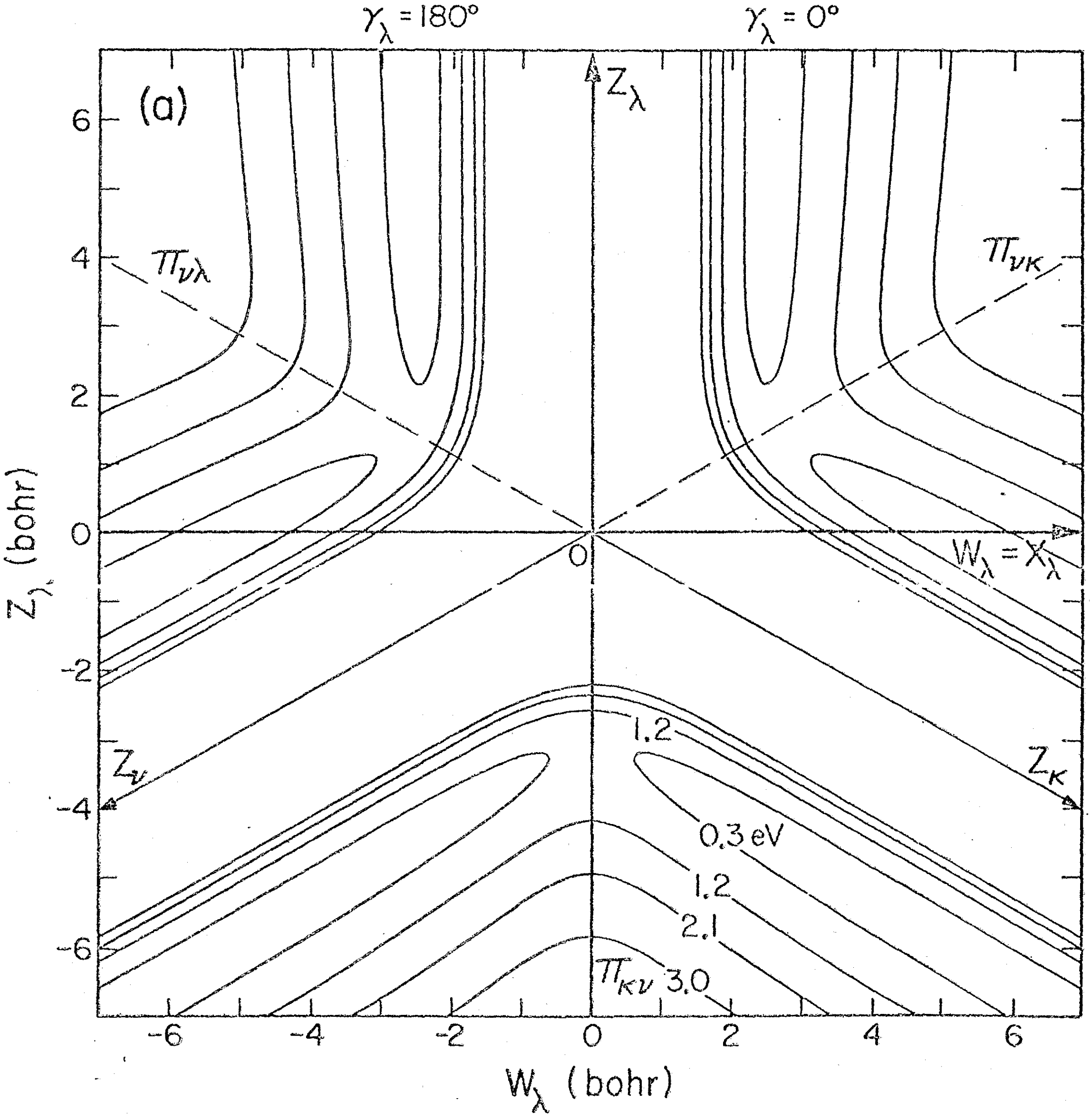
$\gamma_\lambda = 180°$
$\gamma_\lambda = 0°$
(a)
Z_λ
$\pi_{\nu\lambda}$
$\pi_{\nu\kappa}$
$W_\lambda = X_\lambda$
0
Z_ν
Z_κ
1.2
0.3 eV
1.2
2.1
$\pi_{\kappa\nu}$ 3.0
Z_λ (bohr)
W_λ (bohr)
6
4
2
0
-2
-4
-6
-6
-4
-2
0
2
4
6

Figure 2a

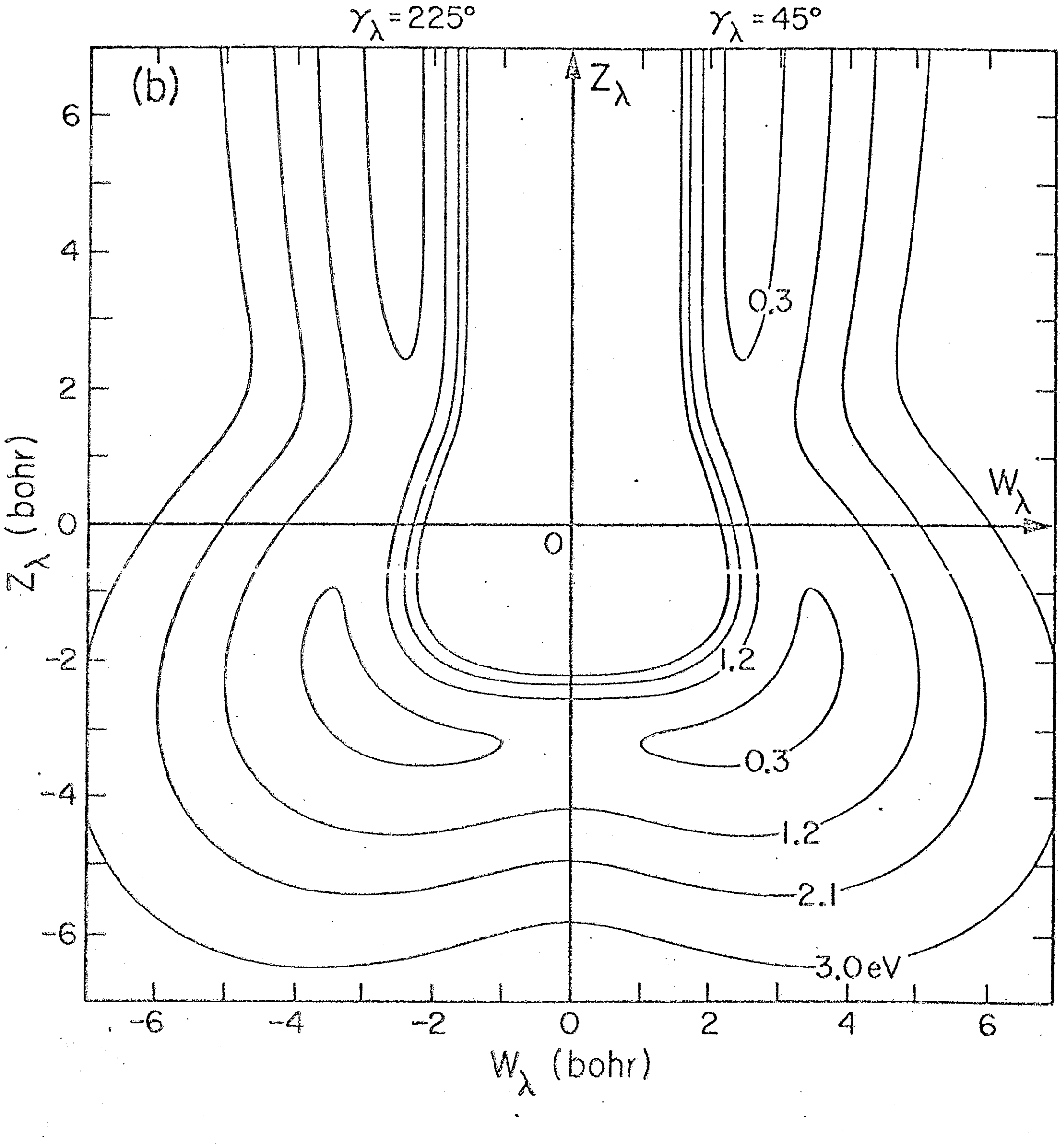
$\gamma_\lambda = 225°$
$\gamma_\lambda = 45°$
(b)
Z_λ
W_λ
0.3
0
1.2
0.3
1.2
2.1
3.0 eV
6
4
2
0
-2
-4
-6
Z_λ (bohr)
-6
-4
-2
0
2
4
6
W_λ (bohr)

Figure 2b

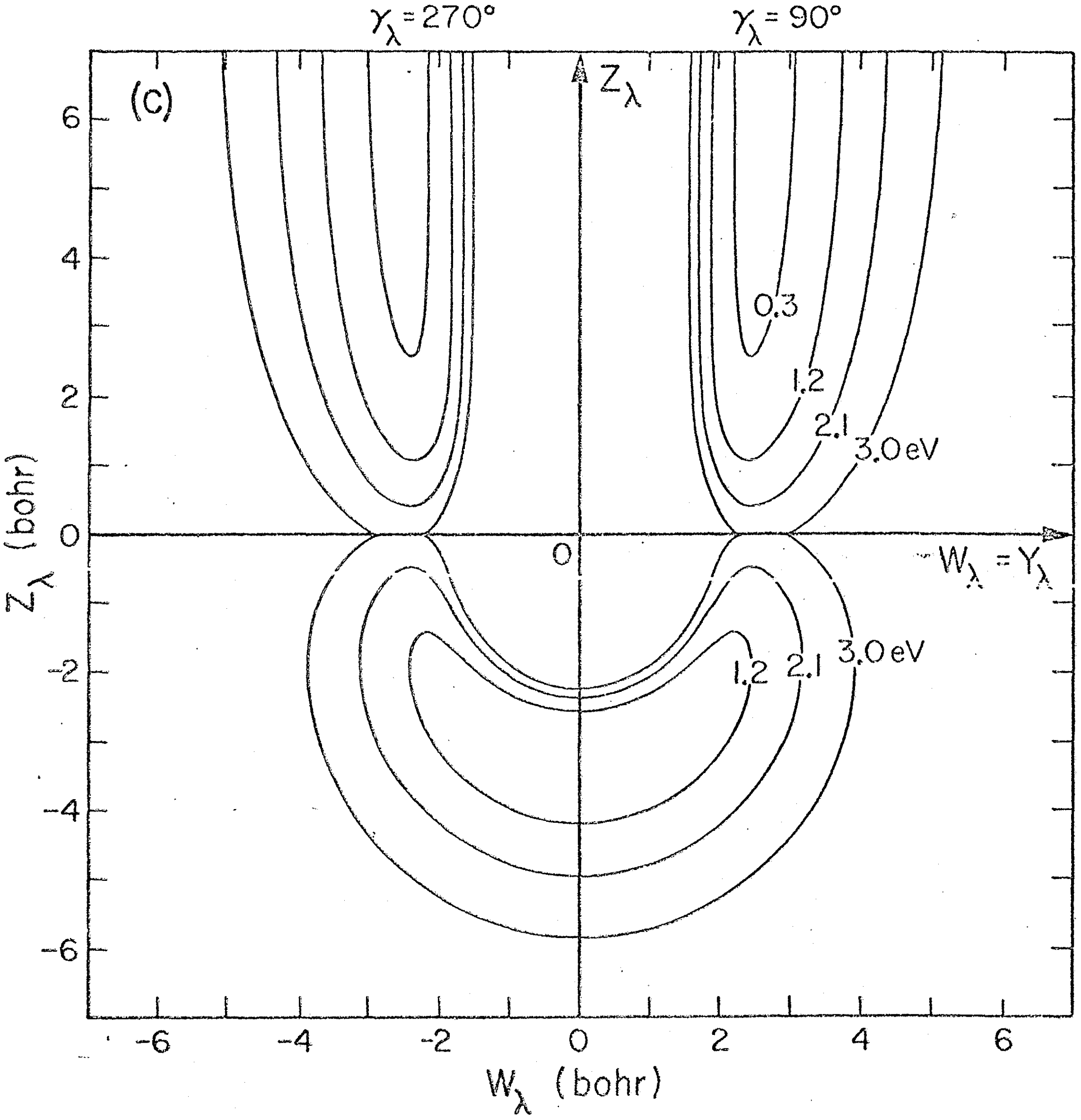
$\gamma_\lambda = 270°$
$\gamma_\lambda = 90°$
(c)
Z_λ
$W_\lambda = Y_\lambda$
0.3
1.2
2.1
3.0 eV
0
1.2
2.1
3.0 eV
Z_λ (bohr)
W_λ (bohr)
-6
-4
-2
0
2
4
6

Figure 2c

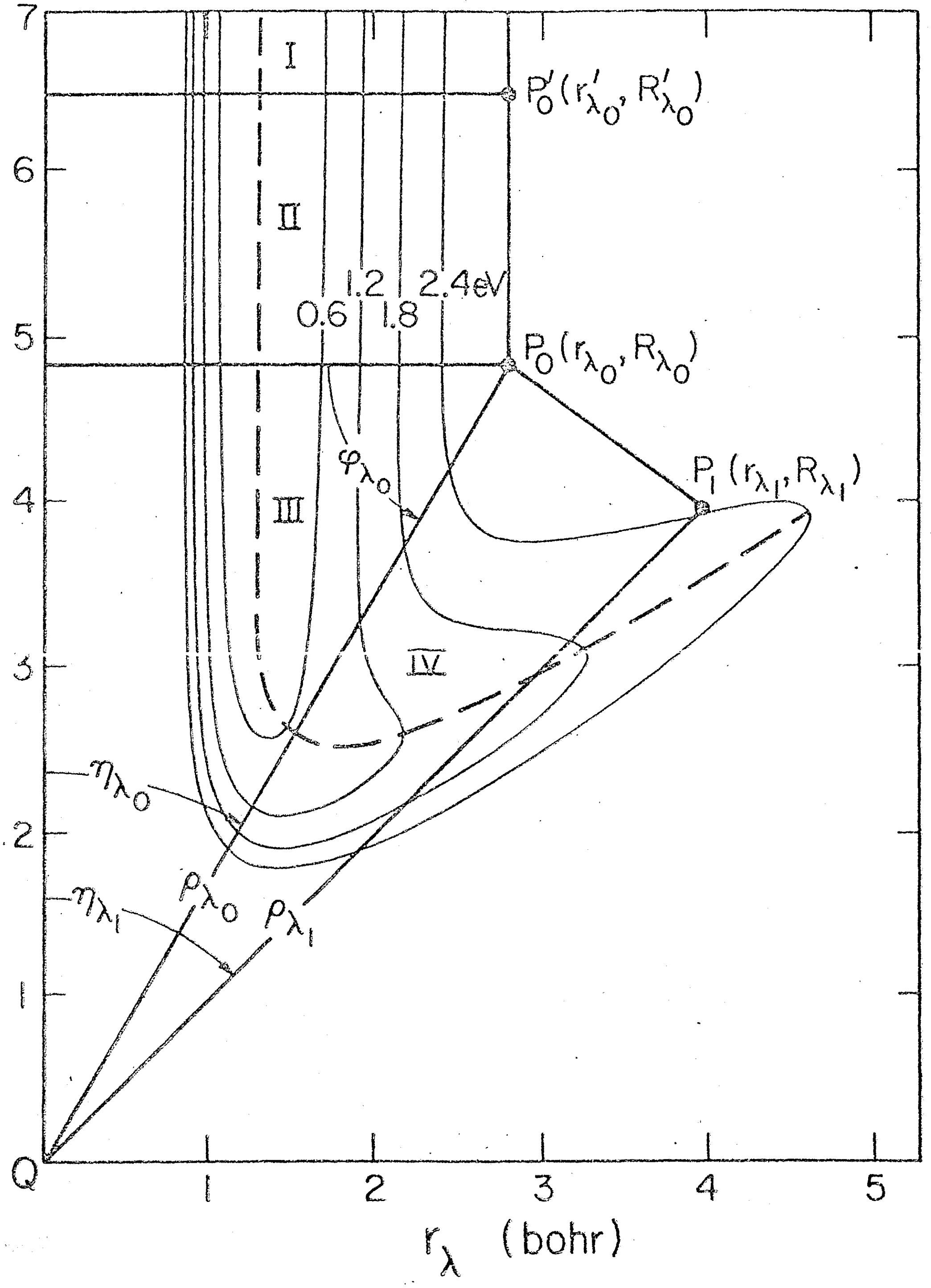
I
II
III
IV
0.6
1.2
1.8
2.4eV
$P'_0(r'_{\lambda_0}, R'_{\lambda_0})$
$P_0(r_{\lambda_0}, R_{\lambda_0})$
$P_1(r_{\lambda_1}, R_{\lambda_1})$
φ_{λ_0}
η_{λ_0}
η_{λ_1}
ρ_{λ_0}
ρ_{λ_1}
Q
R_λ (bohr)
r_λ (bohr)
1
2
3
4
5
6
7

Figure 3

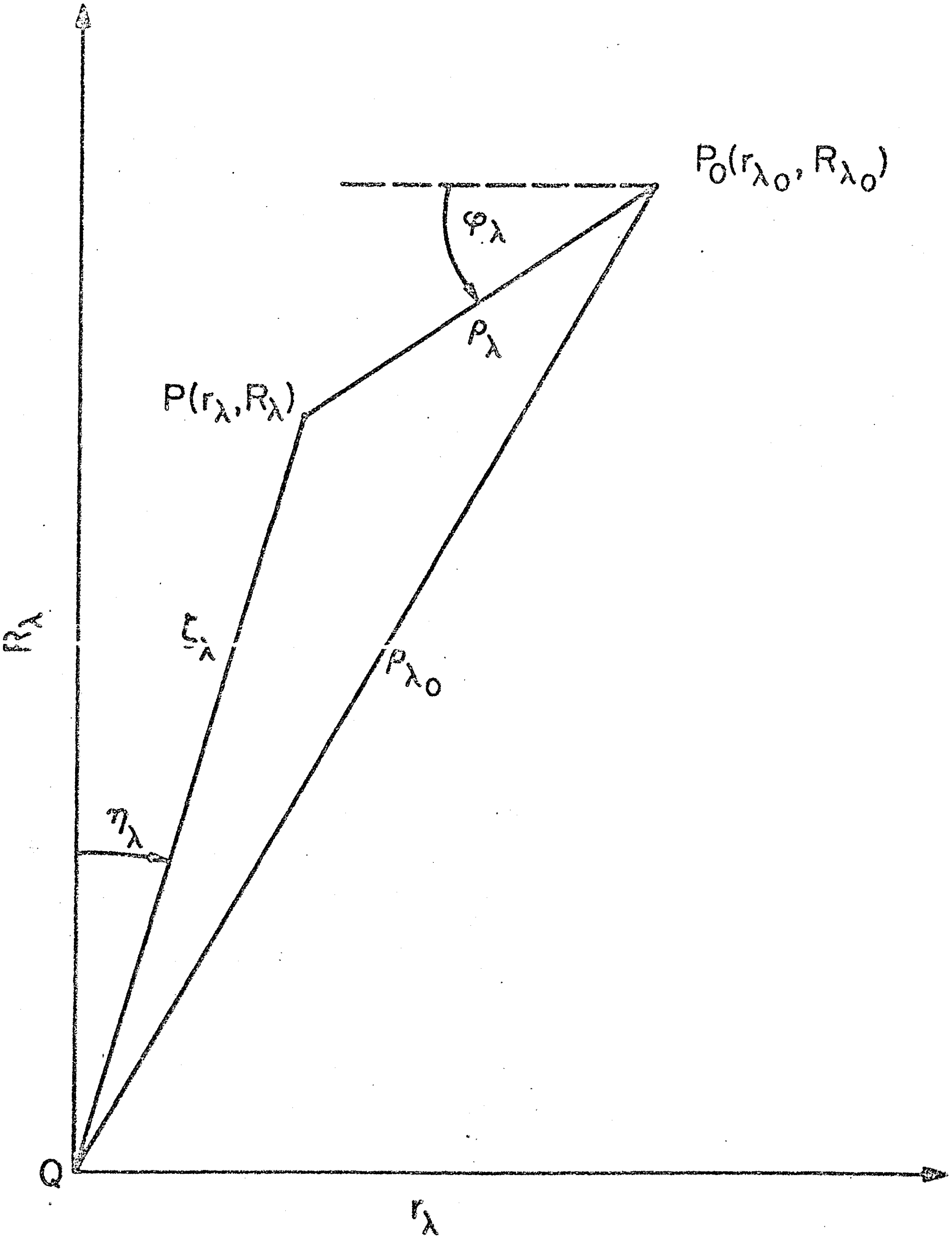
$P_0(r_{\lambda_0}, R_{\lambda_0})$
φ_λ
ρ_λ
$P(r_\lambda, R_\lambda)$
R_λ
ξ_λ
ρ_{λ_0}
η_λ
Q
r_λ

Figure 4

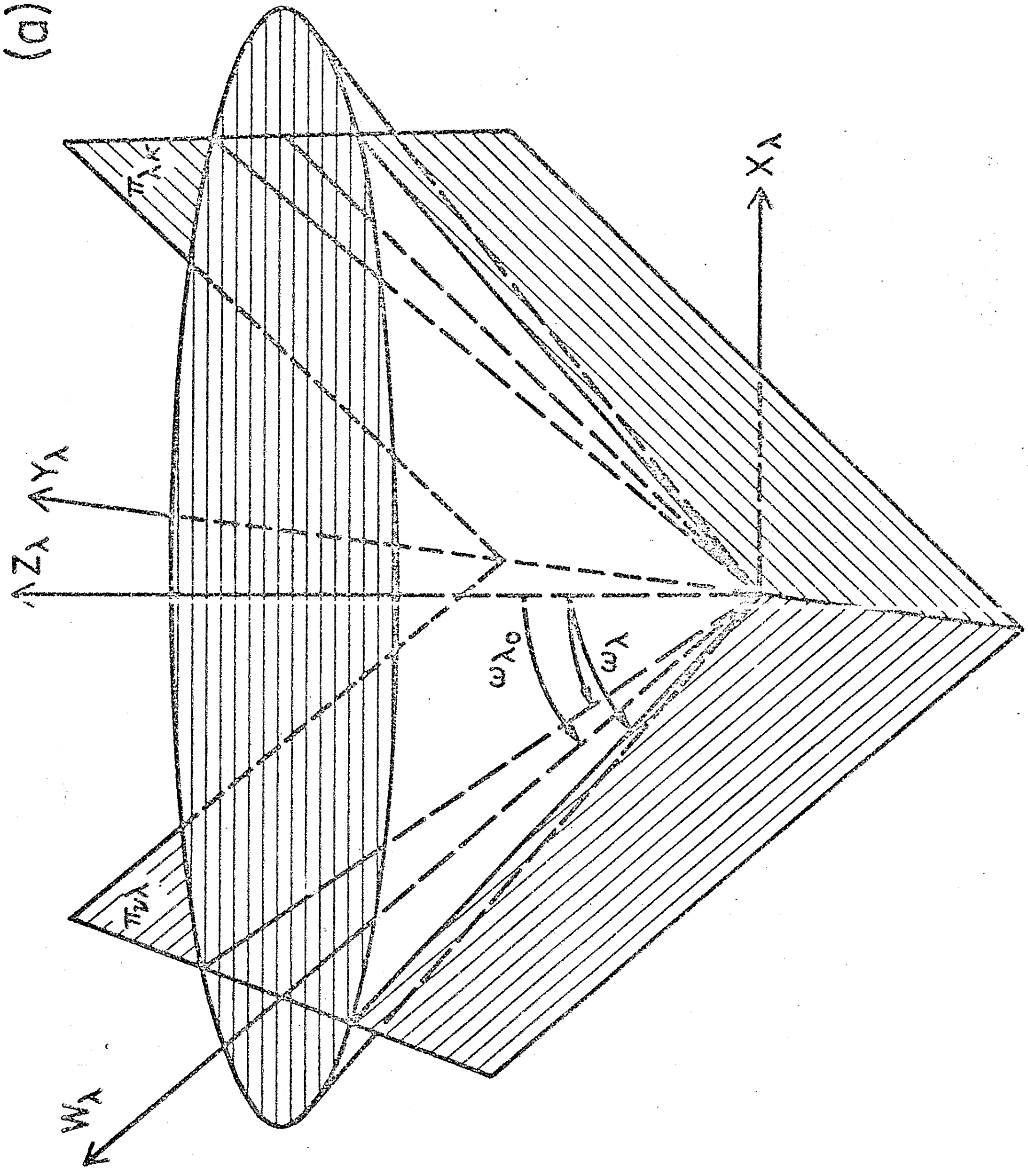

Figure 5a

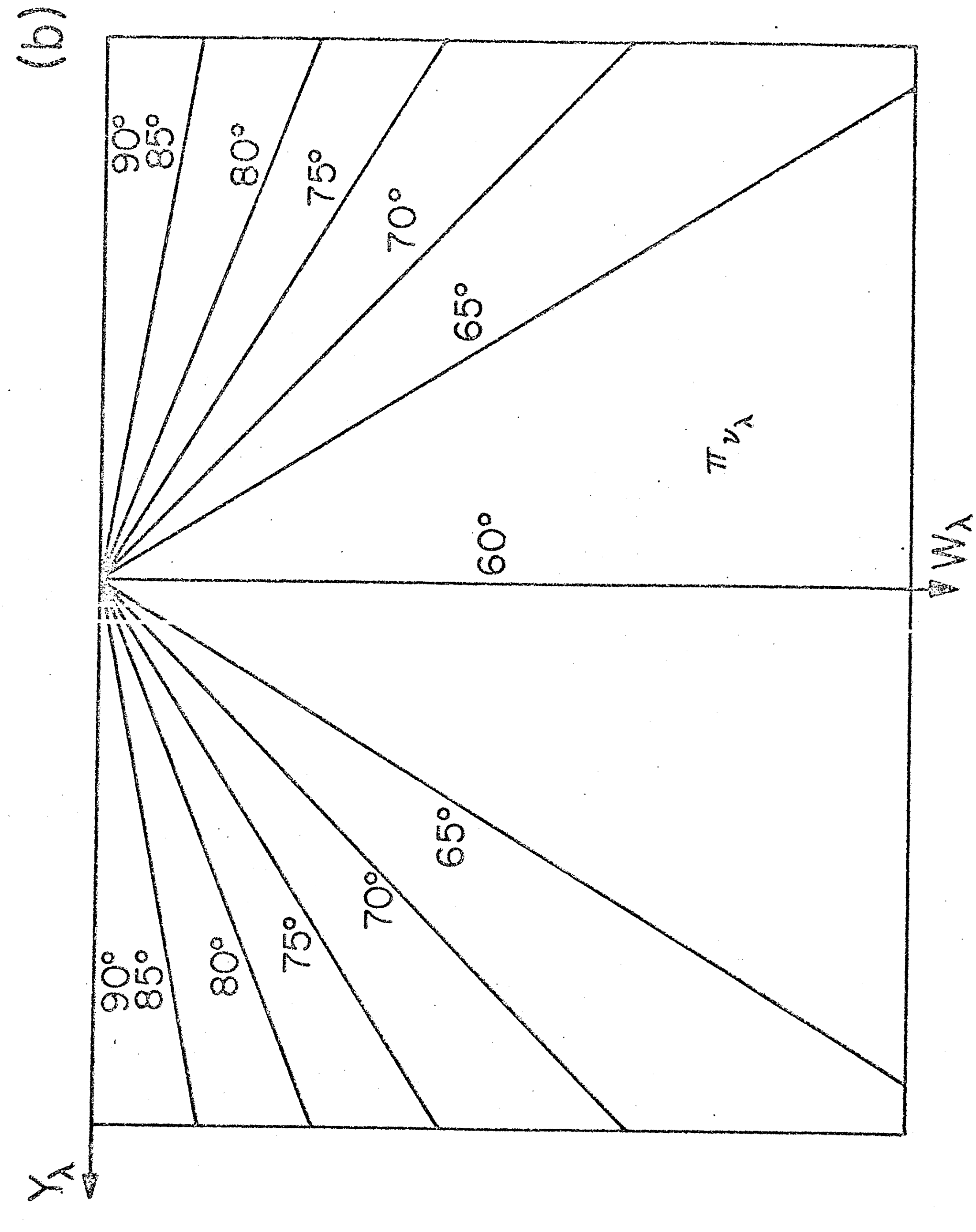
(b)
90°
85°
80°
75°
70°
65°
60°
π_{ν_λ}
W_λ
90°
85°
80°
75°
70°
65°
Y_λ

Figure 5b

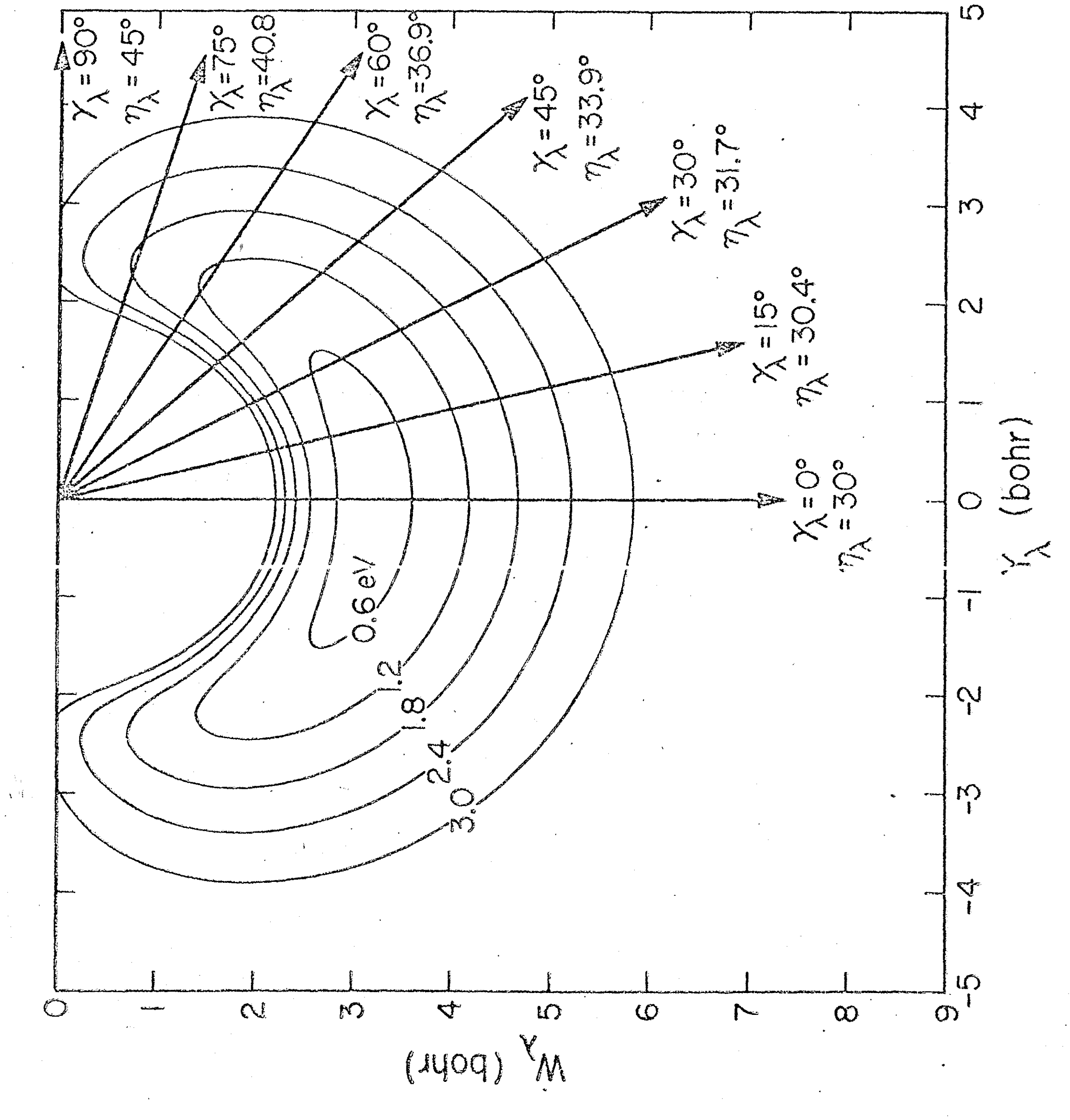
$\chi_\lambda = 90°$ $\eta_\lambda = 45°$
$\chi_\lambda = 75°$ $\eta_\lambda = 40.8$
$\chi_\lambda = 60°$ $\eta_\lambda = 36.9°$
$\chi_\lambda = 45°$ $\eta_\lambda = 33.9°$
$\chi_\lambda = 30°$ $\eta_\lambda = 31.7°$
$\chi_\lambda = 15°$ $\eta_\lambda = 30.4°$
$\chi_\lambda = 0°$ $\eta_\lambda = 30°$
0.6 eV
1.2
1.8
2.4
3.0
W_λ (bohr)
0
1
2
3
4
5
6
7
8
9
Y_λ (bohr)
-5
-4
-3
-2
-1
0
1
2
3
4
5

Figure 6

5. ACCURATE QUANTUM MECHANICAL CROSS SECTIONS FOR PLANAR ATOM DIATOM REACTIONS: II. APPLICATION TO $H + H_2$

Accurate quantum mechanical cross sections for planar atom diatom reactions: II. application to $H + H_2$*

George C. Schatz[†] and Aron Kuppermann
Arthur Amos Noyes Laboratory of Chemical Physics,
Division of Chemistry and Chemical Engineering[‡],
California Institute of Technology, Pasadena, California 91125

(Received

The results of an accurate quantum mechanical treatment of the planar $H + H_2$ exchange reaction on a realistic potential energy surface are presented. Full vibration rotation convergence was achieved in the calculations, and this, together with a large number of auxiliary convergence tests, indicates that the cross sections are accurate to 5% or better. The reactive differential cross sections are always backward peaked over the range of total energies from 0.3 to 0.65 eV. Non-reactive $j = 0$ to $j' = 2$ cross sections are backwards peaked at low energy (0.4 eV) shifting to sidewards peaking for $E > 0.5$ eV. Quantum symmetry interference oscillations are very significant in the $j = 0$ to $j' = 2$ para to para cross sections for $E \geq 0.6$ eV. Reactive integral cross sections show two distinct kinds of energy dependence. At low energy (< 0.5 eV), barrier tunnelling gives them a largely exponential energy dependence while above 0.5 eV (the effective threshold energy) the cross sections are nearly linear. Comparison of collinear and coplanar transition probabilities indicates

similar 1D and 2D energy dependence but with a shift in energy from 1D to 2D due to bending motions in the transition state. An analysis of rotational distributions indicates surprisingly good correspondence with temperature-like distributions. The results of a one vibration approximation calculation are examined, and errors by as much as three orders of magnitude are found with this method at some energies. Shapes of angular distributions are, however, accurately predicted. Additional analyses include comparisons with previous distorted wave and coupled channel results, and calculations of thermal rate constants.

1. INTRODUCTION

A reaction of fundamental interest in the field of chemical dynamics is the $H + H_2$ hydrogen atom exchange reaction. This simplest of chemical reactions has been the subject of numerous dynamical studies by quasi-classical,[1,2] semi-classical[3,4] and quantum mechanical[5-13] methods and has been the focal point for the development of many approximate reaction rate theories.[14] In addition, this system provides the fundamental example for characterizing quantum effects in chemical reactions and determining their importance on experimental observables. For these reasons, the calculation of accurate quantum mechanical cross sections for $H + H_2$ is of great importance. Unfortunately, until recently there existed neither the proper methods for efficiently solving the Schrödinger equation for this system nor adequately powerful computers to handle the computations involved without the introduction of approximations of unknown accuracy.

In a previous paper[15] (hereafter referred to as I) we presented a method for accurately and efficiently solving the Schrödinger equation for reactive collisions of an atom with a diatomic molecule moving on a fixed plane. The planar motion restriction was introduced for computational simplicity only with no fundamental limitations involved in applying a similar procedure to three dimensional collisions as well. In this paper, we present the results of an application of this method to planar $H + H_2$ on a realistic potential energy surface. The results to be discussed include reactive and non-reactive transition probabilities, differential cross sections and integral cross sections, product rotational state distributions and rate constants. In a preliminary communication,[8] we examined the importance of closed vibrational channels in a vibration rotation close coupling expansion and found that the errors associated with an early truncation of the vibrational basis set expansion could be very serious in many cases although qualitative trends obtained with the truncated basis were often properly described. We will examine the one vibrational basis function approximation in somewhat greater detail in this paper, and will, in addition, compare our results with the approximate results of others in which different methods, types of approximations and potential surfaces were used.

As we pointed out in I, the method we have developed for solving the Schrödinger equation for planar atom plus diatomic molecule collisions can be extended to 3D systems without significant conceptual changes, so an additional reason for undertaking the current calculations was to test the feasibility of the method in preparation for its application to 3D reactive systems. These calculations for the 3D $H + H_2$ system are currently in progress and will be presented in detail elsewhere.[16] A preliminary communication of the results of this 3D work and its relationship with the coplanar results presented here has already been published.[9]

In Section 2 we describe the reactive scattering calculations, including convergence tests and computational considerations, and the representation of the potential energy surface. The results of the calculations are presented and discussed in Section 3. Section 4 contains a general summary and discussion.

2. QUANTUM MECHANICAL CALCULATIONS FOR PLANAR REACTIVE H + H_2

2.1 General Description of the Method

The method used to solve the Schrödinger equation for planar reactive and non-reactive H + H_2 collisions has been extensively described in I. As outlined there, the procedure for obtaining the full set of primitive solutions to the partial-wave Schrödinger equation is divided into two stages. In the first one, a close coupling method is used to generate solutions to the Schrödinger equation in each of the three arrangement channel regions of internal configuration space. These solutions are then smoothly matched to one another in the second stage and the resulting primitive solutions, which are everywhere smoothly continuous, are then linearly combined to yield the appropriate reactance and scattering matrix solutions. This procedure is then repeated for a sufficient number of partial waves J to obtain converged reactive, inelastic and (if desired) elastic cross sections. The potential energy surface used in all the calculations was the semi-empirical H_3 surface of Porter and Karplus[17] (all coupling to excited electronic surfaces being neglected). In solving the Schrödinger equation for these reactive collision systems, great care must be exercised to insure adequate invariance of the results with respect to a change in (a) the number of vibration-rotation basis functions used, (b) the reference potential V_{ref} used to generate these functions, (c) the representation of the potential surface (see Section 2.2) and (d) the nature of the functions used to represent the wave function on the matching surface (i.e., the "matching surface basis functions" of I).

As discussed in I, a number of symmetry properties inherent in $H + H_2$ and similar systems may be utilized to reduce the computation time involved in doing these calculations. Most significant in this respect are (a) cyclic permutational symmetry of the three atom system which allows one to consider only one arrangement channel region in doing all calculations, and (b) two atom permutational symmetry, which allows one to decouple the even and odd rotational states throughout most of the calculation. These same symmetry properties allow us to reduce the number of different distinguishable atom scattering amplitudes between a given initial vibration rotation state of the reagent H_2 and a given final state of the product H_2 to just two: one reactive and one non-reactive amplitude. We shall denote the reagent diatomic states by the vibration rotation quantum numbers vj and the product ones by v'j'. Distinguishable atom reactive transitions will be designated by the superscript R, non-reactive ones by N and (indistinguishable) anti-symmetrized ones by A. In this notation, the relation between the antisymmetrized differential cross sections and the distinguishable atom dimensionless scattering amplitudes (Eqs. 6.5 of I) is:

$$\sigma^{A}_{vj \to v'j'} = \begin{cases} \frac{1}{k_{vj}} \left| f^{N}_{vj \to v'j'} - f^{R}_{vj \to v'j'} \right|^{2} \\ \qquad \text{(j, j' even, para} \to \text{para)} \\ \frac{3}{k_{vj}} \left| f^{R}_{vj \to v'j'} \right|^{2} = 3\,\sigma^{R}_{vj \to v'j'} \\ \qquad \text{(j even, j' odd, para} \to \text{ortho)} \\ \frac{1}{k_{vj}} \left| f^{R}_{vj \to v'j'} \right|^{2} = \sigma^{R}_{vj \to v'j'} \\ \qquad \text{(j odd, j' even, ortho} \to \text{para)} \\ \frac{1}{k_{vj}} \left\{ \left| f^{N}_{vj \to v'j'} + f^{R}_{vj \to v'j'} \right|^{2} + 2 \left| f^{R}_{vj \to v'j'} \right|^{2} \right\} \\ \qquad \text{(j, j' odd, ortho} \to \text{ortho)} \end{cases} \qquad (2.1)$$

where k_{vj} is the (unscaled) wave number ($\bar{k}_{vj}$ of I), and $f^{N}_{vj \to v'j'}$ and $f^{R}_{vj \to v'j'}$ were denoted by $\hat{f}^{\lambda v'j'}_{\lambda vj}$ and $\hat{f}^{\nu v'j'}_{\lambda vj}$, respectively in I. For planar systems, the rotational quantum number j is an algebraic integer and may be either positive, negative or zero. For $j \neq 0$, the two states j and -j are degenerate and said to have different polarizations. Cross sections which have been summed over final rotational polarizations and averaged over initial ones will be indicated by the symbols $\bar{\sigma}_{vj \to v'j'}$ and (for the integral cross sections) $\bar{Q}_{vj \to v'j'}$. For example, the integral cross section $\bar{Q}^{R}_{01 \to 02}$ is given by:

$$\bar{Q}^{R}_{01 \to 02} = \frac{1}{2} \left[Q^{R}_{01 \to 02} + Q^{R}_{01 \to 0-2} + Q^{R}_{0-1 \to 02} + Q^{R}_{0-1 \to 0-2} \right] \qquad (2.2)$$

In I (Appendix C and Section 5.2) we found that the symmetry of the Hamiltonian with respect to reflection through the triatom plane leads to the following relations between cross sections within the same rotational manifolds (valid for R, N or A transitions):

$$\sigma_{vj\to v'j'}(\chi) = \sigma_{v-j\to v'-j'}(2\pi - \chi) \qquad (2.3)$$

and

$$Q_{vj\to v'j'} = Q_{v-j\to v'-j'} \qquad (2.4)$$

As defined in I, the scattering angle χ is the angle between the directions of motion of the final and initial H atoms in the center of mass system and spans the range $0 \leq \chi \leq 2\pi$. For reactive differential cross sections, the more customary angle to use is the angle χ_R of the direction of the product H_2 with respect to the direction of the incident H, and is related to χ by

$$\chi_R = \chi + \pi \qquad (\mathrm{Mod}\ 2\pi) \qquad (2.5)$$

Therefore, the backward reactive scattering direction corresponds to $\chi_R = \pi$ and $\chi = 0$.

2.2 Representation of the Potential Energy Surface

In setting up the coupled differential equations which must be solved in each arrangement channel region $\lambda = \alpha, \beta, \gamma$, the potential energy surface $V^\lambda(r_\lambda, R_\lambda, \gamma_\lambda)$ is expanded (see definitions in I) in a cosine Fourier series of the angle γ_λ (Eq. 3.8a of I):

$$V^\lambda(r_\lambda, R_\lambda, \gamma_\lambda) = \sum_{k=0}^{\infty} V_k^\lambda(r_\lambda, R_\lambda) \cos k\gamma_\lambda . \qquad (2.6)$$

In the case of the $H + H_2$ reaction, $V^{\lambda}(r_{\lambda}, R_{\lambda}, \gamma_{\lambda})$ is symmetric about $\gamma_{\lambda} = \pm \pi/2$ (Eq. 6.1 of I) so only even k terms need be included in Eq. 2.6. Once the coefficients $V_k^{\lambda}(r_{\lambda}, R_{\lambda})$ are determined, the rotational coupling in the Schrödinger equation can be analytically evaluated (as in Eq. 3.9 of I) which greatly facilitates the determination of the potential matrix elements needed in the integration procedure. Unfortunately, in general, the $V_k^{\lambda}(r_{\lambda}, R_{\lambda})$ must be calculated numerically from the relation

$$V_k^{\lambda}(r_{\lambda}, R_{\lambda}) = \frac{2}{(1 + \delta_{k_0})\pi} \int_0^{\pi} \cos k\gamma_{\lambda} \, V^{\lambda}(r_{\lambda}, R_{\lambda}, \gamma_{\lambda}) \, d\gamma_{\lambda} \qquad (2.7)$$

and the effort involved in computing this integral negates the advantage of using an analytical expression such as Eq. 2.6. However, for the Porter-Karplus potential surface[17] (and for many others as well), in the regions of internal configuration space sampled in the calculation, the expansion Eq. 2.6 converges very rapidly (after only 3 or 4 terms). We can then redefine the V_k^{λ} by requiring that, instead of satisfying Eq. 2.7, they force Eq. 2.6, with a finite number n of even terms, to be satisfied exactly at n values of γ_{λ}. For example, if 3 terms are included, then we can find V_0^{λ}, V_2^{λ} and V_4^{λ} by solving the three algebraic equations obtained when Eq. 2.6, truncated after three even terms, is evaluated at $\gamma = 0$, $\pi/4$ and $\pi/2$. The result is:

$$\begin{pmatrix} V_0^\lambda(r_\lambda, R_\lambda) \\ V_2^\lambda(r_\lambda, R_\lambda) \\ V_4^\lambda(r_\lambda, R_\lambda) \end{pmatrix} = \begin{pmatrix} \frac{1}{4} & \frac{1}{2} & \frac{1}{4} \\ \frac{1}{2} & 0 & -\frac{1}{2} \\ \frac{1}{4} & -\frac{1}{2} & \frac{1}{4} \end{pmatrix} \begin{pmatrix} V^\lambda(r_\lambda, R_\lambda, \gamma_\lambda = 0) \\ V^\lambda(r_\lambda, R_\lambda, \gamma_\lambda = \pi/4) \\ V^\lambda(r_\lambda, R_\lambda, \gamma_\lambda = \pi/2) \end{pmatrix} \qquad (2.8)$$

For a small number of terms in the potential function expansion, the above interpolative procedure yields a representation of the full potential function $V^\lambda(r_\lambda, R_\lambda, \gamma_\lambda)$ which is computationally more efficient but has about the same accuracy as the one generated using Eq. 2.7. Of course, the goodness of this procedure depends very significantly on the nature of the potential energy surface being considered, but for the Porter-Karplus H_3 surface, it allows an adequate representation of the potential while requiring an exact evaluation of V^λ at only 3 or 4 values of γ_λ (and the use of Eq. 2.6 for all others). In Figure 1, we depict equipotential contours of the potential energy surface at $\gamma_\lambda = 0$, $\pi/4$ and $\pi/2$, the values required in the evaluation of Eq. 2.8.

2.3 Convergence and Accuracy Tests

It is of crucial importance in close-coupling calculations to establish that the resulting reaction probabilities and cross sections have converged adequately. Indeed, we shall see later that premature truncation of the vibration-rotation basis set expansion can result in errors in the final integral cross sections by several orders of magnitude, even though other tests, such as conservation of flux, may be approximately satisfied. Furthermore, many approximate quantum methods involve various kinds of truncations and/or other approximations, and it is highly desirable to obtain fully converged results which are of sufficient accuracy to assess the validity of those methods.

The most obvious criteria which must be satisfied by the results of an accurate quantum calculation are conservation of flux and time reversal invariance. These two principles require that the scattering matrix $\underset{\approx}{S}_J$ be unitary symmetric for each total angular momentum quantum number J and therefore that the corresponding probability matrix $\underset{\approx}{P}_J$ (defined by Eq. 5.20 of I) be symmetric and that the sum of the elements of each of its rows (or columns) should equal unity. These criteria are necessary but not sufficient to insure accurate results.

In the results to be discussed in detail in Section 3, we consider a range of total energies E from 0.30 eV to 0.75 eV (translational energies relative to the $v = 0$, $j = 0$ reagent H_2 state of 0.029 to 0.479 eV). Flux conservation and microscopic reversibility were checked in each calculation, and for $E \leq 0.60$ eV, deviations from flux conservation were never worse than 1% and from symmetry less than about 5% (for non-negligible transitions). For $0.60 \text{ eV} < E \leq 0.75$ eV, deviations from flux conservation were less than 3% and from symmetry less than 10%. In order to insure satisfactory convergence (better than 5%) in the calculation, vibration-rotation basis sets including 40 to 60 terms (channels) were required. For energies less than 0.50 eV, a 40 channel basis consisting of 5 vibrational wave functions combined with 10, 10, 8, 6 and 6 rotational wave functions for $v = 0, 1, 2, 3$ and 4 respectively were used in general. In the 0.50 to 0.60 eV range, a 48 channel basis set of 4 vibrations and 12 rotations per vibration was adequate while for energies above

0.60 eV, a 60 channel basis of 5 vibrations and 12 rotations per vibration was used. Typical probability matrices from these calculations (for a 48 channel calculation at 0.55 eV) are given in Table I. Both the reactive and non-reactive transition probability matrices are highly symmetric and the sums of the probabilities in each row differs from unity by a very small amount in every case. In Table II we examine the convergence behavior of the transition probabilities both as the number of vibrations per rotation is increased and as the number of rotations per vibration is increased (all at 0.6 eV). In part (a) of that table we see that the results change by less than 5% in going from 12 to 14 rotations per vibration and by somewhat larger amounts in going from 10 to 14. With fewer than 10 rotations, errors of 10% to nearly 100% are observed in certain transition probabilities. When vibrational convergence is examined (part B of Table II), we find that 2% convergence is attained with four vibrations and that the use of fewer than that number can lead to errors as large as 50% along with poor flux conservation.

Another important accuracy test in these calculations is the invariance of the results to changes in the character of the vibration rotation basis set. There are two important ways to test this. First, one should be able to change the number of rotations per vibration or the number of vibrations per rotation without changing the results as long as convergence has been attained. Second, the results should be independent of the reference potential $V_{ref}(r_\lambda, R_\lambda)$ (Eq. 3.35 of I) which serves to define the vibrational basis functions as long as V_{ref} becomes equal to the correct diatomic potential $v(r_\lambda)$ in the limit

$R_\lambda \to \infty$. In Table III we present the results of these two kinds of tests. The first column tabulates representative non-reactive and reactive transition probabilities for $E = 0.50$ eV, $J = 0$ calculations with a 48 channel basis (4 vibrations, 12 rotations/vibration) and a reference potential $V_{ref} = V(r_\lambda, R_\lambda, \gamma_\lambda = 0)$ (the one actually used in most of the calculations). In the second column we give the corresponding probabilities obtained when the reference potential $V_{ref} = V_0^\lambda(r_\lambda, R_\lambda)$ is used (Eq. 2.6). Finally, in the last column we give the transition probabilities obtained with the $V_0^\lambda(r_\lambda, R_\lambda)$ reference potential and a 50 channel basis (5 vibrations, 12, 12, 10, 8 and 8 rotations in $v = 0, 1, 2, 3$ and 4, respectively). The deviations between the corresponding probabilities is less than 5%. This result is typical of the accuracy for energies $E \leq 0.60$ eV. Somewhat larger changes are found for $0.6 \text{ eV} < E \leq 0.75$ eV but usually less than 10%.

Two additional accuracy tests are (a) convergence of the results with respect to the number of terms in the expansion of the potential (Eq. 2.6), and (b) invariance of the results with respect to a change in the matching surface basis functions $T^{\nu\lambda}$ (Eq. 4.7 of I). We find that the reaction probabilities change by less than 5% in going from 3 to 4 terms in Eq. 2.6 and virtually not at all in going from 4 to 5 terms. All calculations reported in this paper were done with 3 terms in Eq. 2.6 and using Eq. 2.8 to calculate V_0, V_2 and V_4. The effects of completeness of the expansion of the wave function on the matching surface were studied in two ways. First, several different choices of matching surface basis functions $T^{\nu\lambda}$ were used (different sine and cosine combinations (see I) and Legendre polynomials) and invariance of the results to within 2% was found. Best unitarity of ${}^{J}\underset{\approx}{S}$ was obtained with the basis set (c) of Section 4.1 of I and this choice was used in all further calculations. Second, the degree of completeness of the matching surface basis functions $T^{\nu\lambda}$ determines the degree of orthogonality of the matrix $\underset{\approx}{s}^{J}_{\nu\lambda}$ of Eq. 4.29 in I which transforms the solution in ν coordinates to that in coordinates λ. This property of $\underset{\approx}{s}^{J}_{\nu\lambda}$ determines the unitarity property of the scattering matrix $\underset{\approx}{S}_{J}$ to a certain extent but it is also necessary if the non-reactive transition probabilities between even and odd rotational states are to vanish as required by the symmetry of the H_3 system (see Eq. 6.4 of I). Examples of the effects of a nonorthogonal $\underset{\approx}{s}^{J}_{\nu\lambda}$ are seen in Table I where the nonreactive ortho to para transition probabilities typically have magnitudes of 10^{-7} rather than 10^{-25} which is more typically the case[18] when the orthogonality is built in through the use of Eq. 4.30 of I. In that equation, the matrix $\underset{\approx}{\bar{s}}^{J}_{\nu\lambda}$ (the complex counterpart of $\underset{\approx}{s}^{J}_{\nu\lambda}$ is related to a real symmetric matrix $\underset{\approx}{\Delta}^{\nu\lambda}$ via

$$\underset{\approx}{\bar{s}}^{J}_{\nu\lambda} = \exp iJ\underset{\approx}{\Delta}^{\nu\lambda} \qquad (2.9)$$

This expression is inherently unitary even when a truncated basis is used to calculate $\underset{\approx}{\Delta}^{\nu\lambda}$. It should be apparent that this error is of negligible importance for the example given, but as J increases, deviations from orthogonality of $\underset{\approx}{s}^{J}_{\nu\lambda}$ also increase. Fortunately, the reaction probabilities decrease rapidly as this happens and since a nonorthogonal matching procedure has no effect on inelastic transition probabilities in the absence of reaction[19], the problem with completeness of the matching surface functions disappears at higher J. No artificial orthogonalization procedures were introduced in the calculation (such as were used by Saxon and Light[8]), and therefore unitarity of $\underset{\approx}{S}_J$ and zero-ness of the even to odd reactive transition probabilities are tests of the completeness of $T^{\nu\lambda}$.

We conclude this section by quoting some computation times for these calculations. Both the integration and matching times vary roughly as N^3 for $N > 20$ where N is the number of channels. For 48 channel calculations using an IBM 370-158 computer, about 22 minutes of computation time per partial wave J was required, of which 17 minutes was spent in the integration of the coupled equations and the rest in the matching and asymptotic analysis. About 13 partial waves ($J = 0 - 12$) were required for convergence of the reactive cross sections and 30 partial waves ($J = 0 - 29$) for convergence of the inelastic nonreactive cross sections at energies near $E = 0.50$ eV.

2.4 The One Vibrational Basis Function Approximation (OVA)

An often used[5-7] (but seldom justified) approximation in quantum calculations has been the neglect of closed vibrational channels in the vibration-rotation close coupling expansion. For $H + H_2$ at low energies, only the ground vibrational level is open, so this approximation involves the use of only one vibrational basis function plus a complete set of rotational functions for that vibration. The main reason for using this approximation is the large reduction in computation time (by one to two orders of magnitude for $H + H_2$) compared to a vibrationally converged calculation. One of the objects of this paper is to examine the accuracy of this approximation by comparing the results of its application with the fully converged ones.

The procedure that we have used to perform these one vibration approximation (OVA) calculations is almost identical to that outlined in I. The following modifications are, however, needed:

(a) The overlap matrix $\underset{\approx}{S}_i^\lambda$ between the vibration-rotation basis sets in subregions i and i + 1 (Eq. 3.42 of I) is orthogonalized according to the Schmidt procedure.[20] This is required because otherwise the strongly nonorthogonal overlap matrix associated with this severe truncation of the vibrational expansion results in an excessive lack of flux conservation.

(b) The effective potential matrix in the strong interaction region (and analogously in the matching region) is modified to (see Eq. 3.48 of I):

$$\begin{aligned}(\underset{\approx}{V}_J^{e\lambda(s)})_{v_\lambda j_\lambda}^{v_\lambda' j_\lambda'} = \langle v_\lambda | \rho_\lambda^2 [V_{j_\lambda j_\lambda'}^\lambda + \delta_{j_\lambda j_\lambda'} \{ -V_{\text{ref}}^\lambda + \frac{\hbar^2}{2\mu} \\ \times (\frac{j_\lambda^2 - \frac{1}{4}}{(r_{\lambda_0} - \rho_\lambda \cos\varphi_\lambda)^2} + \frac{(J - j_\lambda)^2 - \frac{1}{4}}{(R_{\lambda_0} - \rho_\lambda \sin\varphi_\lambda)^2} + \frac{1}{4\rho_\lambda^2}) \}] | v_\lambda' \rangle\end{aligned} \tag*{(2.10}$$

For a complete vibration-rotation basis set expansion, this expression is identical to that in Eq. 3.48 of I, but in the OVA it is different with the above expression being the more consistent one.[21]

Even with these modifications, there are still many ambiguities in the application of this procedure. The most serious of these is the lack of invariance of the results to our choice of $V_{\text{ref}}(r_\lambda, R_\lambda)$. In Section 3 we shall examine results for $V_{\text{ref}} = V(r_\lambda, R_\lambda, \gamma_\lambda = 0)$ and for $V_{ref} = V_0^{\lambda}(r_{\lambda}, R_{\lambda})$ with the hope that the range of results provided by these two calculations is representative of what can generally be obtained in this approximation.

3. RESULTS FOR COPLANAR $H + H_2$

3.1 Transition Probabilities

In this section we shall examine the energy and J dependence of the distinguishable atom reactive and inelastic nonreactive transition probabilities. The reactive probabilities for the $v = 0,\ j = 0 \rightarrow v' = 0,\ j' = 1$ transition $P^R_{J,00 \rightarrow 01}$ are plotted in Figures 2 and 3 for several energies as a function of J. The probabilities for negative J are obtained from those for positive J through the use of the relation (Eq. 5.37 of I) (valid for R or N probabilities)

$$P_{J,vj \rightarrow v'j'} = P_{-J,v-j \rightarrow v'-j'} \tag{3.1}$$

Figures 2 and 3 indicate that $P^R_{J,00 \rightarrow 01}$ has a maximum near $J = 0$ for small E with the peak gradually shifting to small positive J as E is increased. Furthermore, the range of J's which must be included, in order that the differential reaction cross sections (see Eq. 5.35 of I) should have converged to approximately 2%, increases with E from about 9 at $E = 0.30$ eV (i.e., $|J| \leq 4$) to about 23 at $E = 0.65$ eV ($|J| \leq 11$). The maximum in the reaction probabilities at small J indicates that only small impact parameter collisions contribute significantly to the reaction cross section. The semi-classical relation between the impact parameter b and the orbital angular momentum l (as derived in I) is:

$$b = l/k_{vj} \tag{3.2}$$

where we define the sign of b to be the same as that of l, and k_{vj} is the wave number associated with the incident state. Since $l = J - j$, and $j = 0$ for the transitions considered in Figures 2 and 3, we see that b is proportional to J, and thus the range of impact parameters which contribute significantly to the reaction cross section increases with E in those figures (from $|b| \leq 1.74$ bohr at 0.45 eV to $|b| \leq 2.22$ bohr at 0.65 eV). In Figure 4 we plot the reaction probabilities versus J at several energies for the transition $v = 0,\ j = 0 \rightarrow v' = 0,\ j' = 0$. Equation 3.1 indicates that this transition probability should be symmetric about $J = 0$ but aside from that restriction, we find that the curves in that figure are otherwise very similar in appearance to those in Figure 3. This conclusion applies quite generally to the reaction probability versus J plots obtained for most other reactive transitions. A discussion of the energy dependence of the reaction probabilities will be given in Section 3.4.

In Figure 5 we compare the converged reaction probabilities $P^R_{J,00\rightarrow 00}$ with the corresponding OVA result for a collinear reference potential $V_{coll} = V^{\lambda}(r_{\lambda}, R_{\lambda}, \gamma_{\lambda} = 0)$ at an energy of 0.60 eV. We see that the OVA result has the correct functional dependence on J but that the magnitudes of the probabilities at each J are nearly a factor of 2 too small. OVA calculations using $V_{ref} = V_0^{\lambda}(r_{\lambda}, R_{\lambda})$ yield probabilities which are only slightly different from the $V_{ref} = V_{coll}$ results in Fig. 5. (For example, the $V_{ref} = V_0^{\lambda}$ reaction probability for $J = 0$ is 0.0397 compared to 0.0420 in Fig. 5). The analogous comparison at other energies between 0.3 and 0.6 eV indicates that the OVA probabilities for the two choices of V_{ref} always have values within 30% of one another. More important, the OVA probabilities and converged results are generally in good agreement in their J dependence, but very poor agreement in energy dependence, and this difference in energy dependence has a dominant influence on the behavior of the reaction cross sections, as will be discussed in Section 3.3.

In Figure 6 we plot the inelastic nonreactive probabilities for the transition $v = 0, j = 0 \rightarrow v' = 0, j' = 2$ versus J for several energies E. The inelastic probabilities are seen to span a much larger range of J's than the reactive ones, indicating that larger impact parameter collisions can contribute significantly to the inelastic processes. At all energies in Fig. 6, the maximum rotational excitation probability occurs for J positive (although some smaller magnitude negative J peaks do appear at the higher energies). The increased likelihood of exciting a positive rotational sublevel in a nonreactive collision with J initially positive is in agreement with the classical picture of the collision shown in Figure 7 (Collision I) in which the incident atom having a positive impact parameter (see Eq. 3.2) impulsively strikes the "bottom" atom of the diatomic molecule in Fig. 7I(a) thus exerting positive torque on that molecule and exciting it into a rotational state with positive j'. Following this collision, one would expect the dominant scattering angle χ to lie between 180° and 360° relative to the x axis in Fig. 7. In the next section we shall see that this is precisely what the differential cross sections indicate. Still unexplained, however, are the double peaked distributions at the higher energies in Fig. 6. Intuitively, one would expect that the positive J peak results from the mechanism described above (Collision I in Fig. 7). The negative J peak must arise from a different collision mechanism, quite possibly that pictured in Collision II of Fig. 7, in which the incident atom, having small negative impact parameter, strikes the bottom atom of the diatom in Fig. 6IIa and rebounds into the $0° \leq \chi \leq 180°$ hemisphere.

3.2 Differential Cross Sections

Figures 8, 9 and 10 depict the differential reactive cross sections corresponding to the same transitions and energy ranges as were used for the reaction probabilities in Figs. 2, 3 and 4, respectively. The $v = 0, j = 0 \rightarrow v' = 0, j' = 1$ distinguishable atom reactive cross sections of Figs. 8 and 9 can be trivially converted to the corresponding antisymmetrized para → ortho quantities by multiplication by 3 (see Eq. 2.1). Because of Eq. 2.3, the curves in Fig. 10 are exactly symmetric about $\chi_R = 180°$. We see that all reactive differential cross sections are strongly backward peaked. This is in agreement with the results of 2 and 3 dimensional quasi-classical calculations[1,2] and with the results of experiments on $D + H_2$[22] and $H + T_2$[23], and is consistent with a rebound-type collision mechanism. The magnitudes of the differential cross sections near $\chi_R = 0°$ are all sufficiently small to allow us to conclude that forward scattering contributions to the reactive angular distributions are negligible. The small amplitude oscillations in some of the higher energy differential cross sections in Figs. 9 and 10 are very likely spurious since they typically result from incomplete interference between different partial waves. This type of oscillatory behavior can be caused by as little as a 5% relative error in the matrix elements of $\underset{\approx}{S}_J$ for a single partial wave, thus pointing out that equally accurate calculations for each partial wave are necessary if spurious effects of this type are to be avoided. Of course, if there were rotational resonances in certain partial waves, then we would correctly expect to see some form of oscillatory behavior in the angular distributions. Rotational resonances have indeed been observed in calculations on nonreactive atom diatom scattering, but these resonances have always been associated with attractive wells in the potential surfaces used.[24] In the case of the purely repulsive Porter-Karplus[17] potential, such wells do not exist and thus purely rotational resonances are unlikely.[25] The full width at half maximum (FWHM) of the backward scattered peak in the differential cross section remains relatively constant over the energy range studied and roughly equal to 70° (i.e., $145° \leq \chi_R \leq 215°$ in Fig. 10). Some broadening does however occur at the higher energies.

The angular distributions for the OVA results previously considered in Fig. 5 are plotted in Fig. 11. As in Fig. 5, we see that the shape of the converged curve is qualitatively well approximated by that of the OVA one, but there is about a factor of two difference in the magnitudes of the cross sections. This similarity and difference continues to exist at other energies as well.

In Fig. 12 we plot the distinguishable atom nonreactive inelastic differential cross sections $\sigma^N_{00\to02}$ at $E = 0.40$, 0.50, 0.60 and 0.70 eV. These angular distributions clearly reflect the one or two peaked nature of the nonreactive probability plots of Fig. 6 and show predominantly backward to sidewards peaking with the position of the maximum shifting gradually to a more forward direction with increasing energy. The maximum value of $\sigma^{N}_{00\to02}$ always occurs for $180° \leq \chi \leq 360°$, in agreement with our qualitative classical ideas of Section 3.1. At higher energies we see double peaked distributions, possibly corresponding to the two mechanisms pictured in Fig. 7. There is little evidence of any high frequency oscillations in any of the cross sections plotted in Fig. 12 which indicates that the collision process is predominantly direct (nonresonant).

Since the $v = 0$, $j = 0 \to v' = 0$, $j' = 2$ transition considered in Fig. 12 corresponds to a para to para transition which can occur by both nonreactive and reactive mechanisms, the correct physically measurable quantity (in a 2D world) to consider is the antisymmetrized para to para cross sections which can be obtained through the use of Eq. 2.1. In Figs. 13, 14 and 15 we plot the resulting antisymmetrized angular distributions $\bar{\sigma}^{A}_{00\to02}$ (summed over degenerate product rotational polarizations) for total energies of 0.5, 0.6 and 0.7 eV, respectively. Also plotted for comparison are the corresponding distinguishable atom nonreactive and reactive cross sections where, for consistency, the angle χ rather than χ_R (see Eq. 2.5) is used for plotting the reactive differential cross sections. In terms of χ, the reactive cross section is forward peaked while the nonreactive one is backward peaked at 0.5 eV shifting to sidewards peaking at the higher energies. At 0.50 eV (Fig. 13), the reactive cross section has a maximum value of 0.0045 bohr/rad which is over 200 times smaller than the maximum value of the nonreactive one, 0.92 bohr/rad. This implies that $f^N_{vj\to v'j'}$ in Eq. 2.1 has a much larger absolute value than $f^R_{vj\to v'j'}$ so that the antisymmetrized and nonreactive differential cross sections are nearly identical. Some small amplitude oscillations are seen in $\bar{\sigma}^A_{00\to 02}$ at small χ in the neighborhood of the region where the reactive cross section has a maximum. These oscillations result from interference between the direct and exchange contributions to the antisymmetrized cross section and are similar in origin to the quantum symmetry oscillations which have been observed in atom-atom elastic and inelastic scattering.[26] As the energy is increased, the reactive cross sections increase much more rapidly than do the nonreactive ones (at all scattering angles), and (as is indicated in Figs. 14 and 15) the oscillations in the antisymmetrized differential cross sections become quite pronounced in the forward direction. The frequency of oscillations in Figs. 13 - 15 seems to decrease with increasing scattering angle although for χ near 180° the differences between the antisymmetrized and nonreactive cross sections are too small to allow an adequate characterization of this property. A small increase in the oscillation frequency with increasing energy is also apparent from the figures.

3.3 Integral Cross Sections

In Fig. 16 we plot the reactive integral cross sections $\bar{Q}^R_{00\to 01}$, $\bar{Q}^R_{00\to 03}$, and $\bar{Q}^R_{00\to 05}$ as a function of the total energy E and translational energy E_0. Both linear and semi-logarithmic scales are used to show the functional dependence of these cross sections over a wide range of energies. If we define the effective threshold energy for a process as being that value of E for which the corresponding integral cross section is 0.01 bohr, then the threshold energies for $\overline{Q}^{R}_{00\to01}$, $\overline{Q}^{R}_{00\to03}$ and $\overline{Q}^{R}_{00\to05}$ are 0.491, 0.546 and > 0.75 eV, respectively. A discussion of the significance of the effective threshold energies will be deferred to Section 3.4 where we will also compare our coplanar results with those of collinear calculations on the same potential energy surface. Above threshold, $\overline{Q}^{R}_{00\to01}$ rises in a nearly linear manner up to about 0.65 eV and achieves a maximum value of 0.31 bohr at about $E = 0.70$ eV. $\overline{Q}^{R}_{00\to03}$ and $\overline{Q}^{R}_{00\to05}$ increase monotonically in the energy range spanned by this figure, but may level off at higher energies. At very low energies, the integral cross sections exhibit approximate exponential behavior. A characterization of the product rotational state distribution implicit in Fig. 16 will be given in Section 3.5. We should finally note that the reactive cross sections in Fig. 16 can be converted to the corresponding para → ortho quantities by multiplication by 3.

In Fig. 17 we compare the reactive cross section $\overline{Q}^{R}_{00}$ (summed over all product states) with the OVA result (using $V_{\text{ref}} = V(r_\lambda, R_\lambda, \gamma_\lambda = 0)$). As mentioned in Section 3.1, the results obtained using $V_{\text{ref}} = V_0^\lambda(r_\lambda, R_\lambda)$ have almost the identical energy dependence. It is apparent from the figure that the vibrationally converged integral cross section differs quite significantly from the OVA result over much of the energy range considered, the difference being about 3 orders of magnitude for total energies below 0.36 eV. The two curves do cross near $E = 0.52$ eV, which is quite interesting, since a previous analysis of the collinear $H + H_2$ system (on a slightly different potential surface) indicated that this reaction is very nearly vibrationally adiabatic at this energy.[27] Since, as we shall see in the next section, collinear and coplanar calculations can be related in a reasonably accurate manner, one might be able to assess the accuracy of OVA calculations in 2 and 3 dimensions by analyzing the extent of vibrational adiabaticity in the corresponding collinear systems.

In Fig. 18 we compare the nonreactive and antisymmetrized integral cross sections $\overline{Q}^{N}_{00\rightarrow 02}$ and $\overline{Q}^{A}_{00\rightarrow 02}$ as a function of E and E_0. The rotationally inelastic cross sections have much larger magnitudes than the reactive ones of Figs. 16 and 17, with a peak value of 3.76 bohr near E = 0.54 eV. Since the $v' = 0$, $j' = 2$ state of H_2 becomes energetically accessible at E = 0.300 eV, we see that there is essentially zero threshold energy for the nonreactive process so that $\overline{Q}^{A}_{00\rightarrow 02}$ coincides almost exactly with its distinguishable atom counterpart $\overline{Q}^{N}_{00\rightarrow 02}$ at all energies below 0.50 eV. Thereafter, $\overline{Q}^{A}_{00\rightarrow 02}$ becomes progressively larger than $\overline{Q}^{N}_{00\rightarrow 02}$ with no apparent oscillatory behavior as a function of energy resulting, in contrast to the angular distributions of Figs. 13 - 15.

3.4 Comparison of Coplanar and Collinear Results

Because planar cross sections have the dimensions of length while collinear ones are dimensionless (i.e., collinear cross section equals collinear reaction probability), a direct comparison of these quantities is not possible. One could devise models for converting collinear results into planar ones by assigning a model impact parameter dependence to the collinear reaction probabilities. A more straightforward comparison can be effected instead by examining the behavior of the corresponding collinear[28,29] and coplanar reaction probabilities (the latter for J = 0) as are plotted in Fig. 19. Probabilities for other J's or different initial states vj could have been used, but those for J = 0 and v = j = 0 were chosen for this comparison because they correspond more closely to the collinear conditions. This choice is furthermore justified by the fact that the form of the energy dependence of the coplanar probabilities for different J or j (for reasonably small values of these quantum numbers)is essentially the same as that of P_{00}^{R} (J = 0) as is demonstrated in Fig. 20 (where P_{00}^{R} (J = 0), P_{00}^{R} (J = 4) and P_{01}^{R} (J = 0) are plotted). Figure 19 indicates that the coplanar results have nearly the same energy dependence with the energy scale shifted upwards by about 0.055 eV in going from the collinear to the coplanar curves. In addition, the maximum value of the collinear reaction probability is 1.0 whereas that of the coplanar one is about 0.6. Both the energy shift and the difference in the maximum probability are explainable in terms of relatively simple concepts. To understand the energy shift, we examine the nature of the triatomic H_3 system in its transition state. In the linear case, this triatomic pseudomolecule has two vibrational degrees of freedom: an asymmetric stretch mode, which is unstable and leads to motion along the reaction coordinate, and a stable symmetric stretch mode. When the reaction occurs and the system passes through the transition state region, the total energy partitions itself between these two vibrational modes. Energy in the symmetric stretch mode is not easily converted into the asymmetric stretch mode making it unavailable to overcome the potential surface barrier. This is a partial physical interpretation of the fact that the collinear threshold energy (the value of E at which the reaction probability is 0.01) is 0.42 eV, which is somewhat larger than the 0.39 eV Porter-Karplus surface barrier height. Collinear threshold phenomena such as this have been analyzed in detail elsewhere.[27,30] In going from a linear to a planar transition state we add one bending degree of freedom to the internal motion of the transition state which also does not contribute to motion along the reaction coordinate and which will also tie up some of the energy needed to overcome the activation barrier. This additional energy in the bending motion is a plausible explanation for the 0.055 eV upward energy shift observed in Fig. 19, and is approximately equal to the zero point bending energy of about 0.06 eV for the surface used.[31] Much of the above explanation has its basis on an approximate statistical theory proposed by Marcus.[32] The difference in the maximum probabilities attained by the collinear and coplanar results can be understood by examining the orientation dependence of the reaction probability. In the planar case with $j = 0$ initially, the diatomic molecule does not rotate and has equal probability of being in any orientation with respect to the direction of approach of the incident atom. Since the barrier height of the potential energy surface is 0.396 eV for collinear collisions and increases to 2.8 eV for perpendicular ones, we would expect that in the energy range being considered, the reaction probability should be greatest for linear collisions and decrease to zero for perpendicular ones. The coplanar probability should represent an average over all initial orientations and if we assume unit reaction probability for $|\gamma_\lambda| \leq 54°$ and, by symmetry, for $|180° - \gamma_\lambda| \leq 54°$ and zero probability elsewhere, we obtain a coplanar reaction probability of 0.60 in agreement with Fig. 19. The 54° cut-off angle is in reasonable agreement with previous estimates of the orientation dependence of the reaction probability obtained from distorted wave results[12] and from classical trajectory results.[2]

3.5 Product State Rotational Distributions

In Fig. 21 we plot the integral cross sections $\overline{Q}^R_{00 \to 0j'}$ (summed over final rotational polarizations) as a function of the product rotational energy and quantum number for several total energies E. We see from the figure that only small j' rotational states are appreciably excited in these reactive collisions. The relative population of final rotational states is not strongly dependent on total energy although some broadening of the distribution does occur at higher E. Not shown in the figure are the final rotational state distributions from initial states $j \neq 0$. The qualitative shapes of these distributions are not strongly dependent on j and look very much like those for $j = 0$ in Fig. 21. However, the magnitudes of the $\overline{Q}^R_{0j \to 0j'}$ decrease monotonically with increasing j for a given j'.[33]

To a large extent, the distributions in Fig. 21 resemble rotational Boltzman-like distributions with a single temperature parameter. Distributions of this type, for a planar system, may be expected to have the form[34]

$$f_{j'}(E) = A(E)(2 - \delta_{j'0})\, e^{-E_{j'}/kT(E)} \quad (3.3)$$

where A(E) and T(E) are energy dependent constants and $2 - \delta_{j'0}$ is a degeneracy factor. In Fig. 22 we plot $\log\left[\frac{2}{2-\delta_{j'0}} \bar{Q}^{R}_{00\to 0j'}\right]$ as a function of the product rotational energy. The resulting curves for different E are approximately linear (most nearly so at the higher energies) in agreement with the predictions of Eq. 3.3, with temperature parameters T(E) in the neighborhood of 250 - 400 K. We should point out that although the rotational distributions are temperature-like, we find no evidence of long lived compound state (i.e., complex) formation in this reaction at the energies being considered.[28] Indeed, the rotational distributions seem to be determined to a large extent by the shape of the potential energy surface in the transition state region of configuration space (see lower half of Fig. 1c). In this transition state, the asymptotic free rotational motion has become a seriously restricted bending motion. This bending motion becomes again a free rotational motion after the reaction, and, at least qualitatively, the distribution of different product rotational states appears to be determined by the overlap of this bending wave function and the asymptotic free rotor wave function. If this reasoning is correct, then the resemblance of the rotational distribution in Figs. 21 and 22 to a thermal distribution is at least partially coincidental. This phenomenon should however be quite common since restricted bending motion in the transition state region is a common feature of the potential energy surfaces for many reactions.

In Fig. 23 we plot the OVA cross sections in a manner analogous to that done for the converged cross sections in Fig. 20. Fig. 23 indicates that the OVA rotational distributions fit the temperature-like distribution given by Eq. 3.3 to about the same accuracy as the converged results. However, the OVA temperature parameters are somewhat higher (450 - 620 K) indicating that this approximate procedure predicts rotational distributions which are much broader than the converged ones.

3.6 Comparisons with Other Coplanar Calculations

In Fig. 24 we plot our $Q^R_{00\to01}$ (SK) along with the corresponding results of two other studies on coplanar $H + H_2$. $Q^R_{00\to01}$ (WW, SE) and $Q^R_{00\to01}$ (WW, WE) are the results of two different applications of the distorted wave approximation by Walker and Wyatt[12] on the Porter-Karplus surface. SE and WE refer respectively to the strong and weak expansion path choices of the nonreactive reference potential used to generate the distorted wave functions. $Q^R_{00\to01}$ (AL) is the close-coupling result (using one variation of the OVA) of Altenberger-Siczek and Light[17] in which an earlier calculation of Saxon and Light[5] is corrected. These calculations were done for an analytical surface fitted to the <u>ab initio</u> SSMK[35] surface. The two approximate calculations of Walker and Wyatt seem to bracket our result at low energies, but for $E > 0.60$ eV, the absence of conservation of flux in the distorted wave calculation results in a gross overestimation of the integral cross sections. Thus, the distorted wave method remains accurate only when the reaction probabilities or cross sections are small. A similar conclusion was also drawn from an analogous collinear comparison.[36]

The distorted wave differential cross sections $\sigma^{R}_{00\to00}$ (Fig. 25) are in good qualitative although not quantitative agreement with the corresponding results of our converged calculations, but a similar comparison of the cross sections $\sigma^{R}_{00\to01}$ in that figure indicates serious disagreement, apparently the result of a much more rapid fall off in the distorted wave reaction probabilities with decreasing J (J < 0) than is the case with our results (as seen in Fig. 25(a)).

The results of Altenberger-Siczek and Light[7] cannot be quantitatively compared with ours because of the difference in potential energy surfaces used in the two calculations but some qualitative observations are nevertheless appropriate. First, the effective threshold energies (defined in Section 3.3) of the integral cross sections are about 0.502 eV for $Q^{R}_{00\to01}$(SK) and 0.531 eV for $Q^{R}_{00\to01}$ (AL). The difference between these two numbers is identical to the 0.029 eV difference between the respective potential barriers (0.396 eV vs. 0.425 eV) in the surfaces used in the calculations. Since the properties of the triatomic activated complexes are similar, one might expect that a small change in barrier height should indeed result in a correspondingly small change in effective threshold energy as observed. The fact that $Q^{R}_{00\to01}$ (AL) is an OVA result should be of little significance in this argument since it was shown in Section 3.3 that our own OVA cross sections have effective threshold energies in good agreement with our converged ones. Second, except for some possibly spurious oscillations, the Altenberger-Siczek and Light angular distributions (Figs. 8 - 10 of Ref. 7) have shapes which are generally similar to ours (Figs. 9, 10 of this paper) for all transitions considered. The dominant peak near 180° in their angular distributions is somewhat narrower than ours and their reaction probabilities fall off more rapidly with increasing $|J|$ than do ours in Figs. 2 - 4. Both of these differences could be a result of the different potential surfaces used, since as seen in Figs. 5 and 11 the OVA does not strongly affect the shapes of σ^R versus χ and P^R versus J curves.

3.7 Rate Constants

In this section we will examine the behavior of the para → ortho thermal rate constant $k_{p\to o}(T)$. The ortho → para rate constant can, of course, be obtained from $k_{p\to o}$ by using the easily calculable equilibrium constant for this reaction,[37] computed for the coplanar world of this paper. To obtain $k_{p\to o}(T)$ we first require the para to ortho cross sections $\bar{Q}^A_{vj}$ (summed over all final ortho states and averaged over initial (para) rotational polarizations). These are listed in Table IV for both the converged and OVA calculations.

The planar para → ortho rate constant is given by

$$k_{p\to o}(T) = \frac{1}{Q} \sum_{v=0}^{\infty} \sum_{\substack{j=0 \\ (j=\text{even})}}^{\infty} (2 - \delta_{j0})\, e^{-E_{vj}/kT} k^A_{vj}(T) \qquad (3.4)$$

where

$$Q = \sum_{v=0}^{\infty} \sum_{\substack{j=0 \\ (j=\text{even})}}^{\infty} (2 - \delta_{j0})\, e^{-E_{vj}/kT} \qquad (3.5)$$

and

$$k^{A}_{vj}(T) = \sqrt{\frac{2}{\mu}} \quad \frac{1}{kT} \quad \int_{0}^{\infty} e^{-E'_{vj}/kT} \quad \overline{Q}^{A}_{vj}(E'_{vj}) \quad \sqrt{E'_{vj}} \quad dE'_{vj} \qquad (3.6)$$

E_{vj} is the vibration-rotation energy of the initial state with quantum numbers vj and E'_{vj} is the translational energy relative to that state ($E'_{vj} = E - E_{vj}$). μ is the reduced mass associated with the relative motion of the reagents and the factor $2 - \delta_{j0}$ is introduced to account explicitly for rotational degeneracy. The initial spin degeneracy is 1 for all para states. The rate constant thus defined has the units cm^2/molec•sec which is appropriate for a planar world in which concentrations are measured in molec/cm^2.

Using Eqs. 3.4 - 3.6 along with the data in Table III, $k_{p \to o}(T)$ has been calculated, and the resulting Arrhenius plots for the vibrationally converged and OVA ($V_{ref} = V(r_\lambda, R_\lambda, \gamma_\lambda = 0)$) results are presented in Fig. 26. As might be expected from the appearance of the integral cross sections in Fig. 17, the OVA rate constant is considerably larger than the converged one at low temperatures with the ratio of the two being 12.4 and 2.83 at 200 K and 300 K, respectively. At high temperatures, the two rate constants approach each other quite closely, a reflection of the similar effective threshold energies of the converged and OVA cross sections. The high temperature portions of the Arrhenius plots in Fig. 26 are nearly linear with resulting Arrhenius activation energies of 5.2 and 5.0 kcal/mole for the converged and OVA results, respectively. The high temperature Arrhenius straight line corresponding to the converged results is represented by the dashed line of Fig. 26. We will defer a detailed comparison of these rate constants with those of accurate 1 and 3 dimensional calculations and with approximate theoretical and experimental ones to a separate paper.[16]

4. CONCLUSION

It should be apparent from the wealth of dynamical information presented in Section 3 that these calculations can be extremely useful to our understanding of chemical dynamics. We would like to stress that these calculations are not overly time consuming but it is unlikely that similar ones will be done on more than the very simplest of chemical systems. Rather, the primary emphasis is to use these results as benchmarks against which approximate theories may be compared, with the hope that these theories may be in turn applied to more complicated systems. The comparisons with approximate calculations presented in Section 3.6 were incomplete in that the results of quasi-classical and semi-classical coplanar calculations on the Porter-Karplus H_3 surface are needed to assess the quantitative accuracy of these important approximate theories. Also requiring further consideration is the use of collinear-type theories to provide approximate coplanar results, and similarly of coplanar theories to describe the three dimensional world.[38] This was discussed briefly in Section 3.4 and will be further investigated in a separate paper.[16]

The coplanar calculations are also important in elucidating what kinds of phenomena are significant in chemical reactions. The quantum symmetry oscillations in the para → para angular distributions

(Section 3.2) but not in the corresponding integral cross sections as a function of energy (Section 3.3) are a good example. Such quantum symmetry effects may eventually be a useful experimental tool for characterizing reactive potential surfaces. Also of great importance is the characterization of the reaction in terms of direct and resonant mechanisms. This was briefly mentioned in Section 3.2 where we remarked that the reaction appeared to be completely dominated by the direct mechanism. A more detailed analysis at energies higher than were considered in this work indicates that in the neighborhood of certain energies (such as $E \sim 0.92$ eV) this no longer seems to be correct as very significant resonant-like effects are observed. The importance of these resonant processes is discussed elsewhere[28].

Finally, as was mentioned in the introduction, these calculations are significant in that they demonstrate the feasibility of the method outlined in paper I for doing quantum 2D scattering calculations. Extension of this method to the 3D problem has recently been accomplished[9] and the results of these 3D calculations and their comparison with 2D and 1D ones should be extremely useful to our understanding of chemical dynamics.

ACKNOWLEDGEMENT

We thank Ambassador College for generous use of their computational facilities.

TABLE I. Nonreactive (N) and reactive (R) probability matrices for E = 0.55 eV, J = 2*.

				N			
(vj)	(v'j') = (00)	(0+1)	(0-1)	(0+2)	(0-2)	(0+3)	(0-3)
(00)	0.0186	0.263(-8)	0.113(-6)	0.404	0.276	0.370(-7)	0.248(-7)
(0+1)	0.287(-7)	0.0134	0.477	0.689(-7)	0.104(-7)	0.199	0.0629
(0-1)	0.337(-7)	0.477	0.0899	0.897(-7)	0.112(-7)	0.129	0.140
(0+2)	0.406	0.204(-7)	0.228(-7)	0.240	0.172	0.289(-7)	0.108(-7)
(0-2)	0.277	0.530(-8)	0.298(-7)	0.171	0.474	0.287(-8)	0.496(-8)
(0+3)	0.633(-8)	0.199	0.129	0.126(-8)	0.343(-8)	0.636	0.651(-2)
(0-3)	0.527(-8)	0.0624	0.140	0.327(-8)	0.468(-8)	0.653(-2)	0.785

				R			
(vj)	(v'j') = (00)	(0+1)	(0-1)	(0+2)	(0-2)	(0+3)	(0-3)
(00)	0.0436	0.0380	0.0265	0.0167	0.0803(-1)	0.0347(-1)	0.911(-3)
(0+1)	0.0380	0.0357	0.0219	0.0178	0.0567(-1)	0.0378(-1)	0.621(-3)
(0-1)	0.0261	0.0220	0.0167	0.0980(-1)	0.0502(-1)	0.0181(-1)	0.664(-3)
(0+2)	0.0174	0.0175	0.0961(-1)	0.0857(-1)	0.0246(-1)	0.0211(-1)	0.232(-3)

TABLE I. (Cont.)

				R			
(vj)	(v'j') = (00)	(0+1)	(0-1)	(0+2)	(0-2)	(0+3)	(0-3)
(0-2)	0.0774(-1)	0.0588(-1)	0.0518(-1)	0.0232(-1)	0.0180(-1)	0.412(-3)	0.243(-3)
(0+3)	0.0356(-1)	0.0373(-1)	0.0184(-1)	0.0206(-1)	0.412(-3)	0.500(-3)	0.407(-4)
(0-3)	0.879(-3)	0.619(-3)	0.655(-3)	0.237(-3)	0.234(-3)	0.398(-4)	0.386(-4)
Sums‡	1.0014	0.9997	1.0003	0.9980	1.0001	0.9999	1.0005

* Not all allowed transitions are shown. Numbers in parentheses indicate power of ten by which number preceding it should be multiplied.

‡ Sum of probabilities from a given initial state over all possible final states and arrangement channels.

TABLE II. Rotational and vibrational convergence of coplanar transition probabilities at E = 0.60 eV, J = 1.

(A) Rotational convergence (with 4 vibrations and N rotations per vibration)

N	U^a	$P^N_{00\to02}$	$P^N_{01\to0-1}$	$P^R_{00\to00}$	$P^R_{00\to01}$	$P^R_{01\to0-1}$
6	1.035	0.293	0.435	0.0738	0.0667	0.0356
8	1.020	0.276	0.339	0.0743	0.0525	0.0380
10	1.010	0.202	0.257	0.0840	0.0706	0.0416
12	1.004	0.194	0.230	0.0829	0.0645	0.0396
14	1.002	0.189	0.221	0.0821	0.0673	0.0397

(B) Vibrational convergence (with M vibrations and 12 rotations per vibration)

M	U^a	$P^N_{00\to02}$	$P^N_{01\to0-1}$	$P^R_{00\to00}$	$P^R_{00\to01}$	$P^R_{01\to0-1}$
1[b]	1.003	0.259	0.260	0.0404	0.0372	0.0295
2	1.063	0.161	0.204	0.0895	0.0738	0.0477
3	1.063	0.238	0.315	0.0749	0.0578	0.0329
4	1.004	0.194	0.230	0.0829	0.0645	0.0396
5	1.007	0.195	0.233	0.0832	0.0646	0.0396

[a] U indicates that sum of all transition probabilities from a specific vj state which differs by the largest amount from unity and hence is a conservative measure of deviations from flux conservation.

[b] The one vibration result was calculated according to the procedure outlined in Section 2.4.

TABLE III. Nonreactive and reactive transition probabilities for $E = 0.50$ eV, $J = 0$.

	$N=48, V_{coll}$[a]	$N=48, V_0$[b]	$N=50, V_0$[c]
$P^{N}_{00 \to 00}$	0.180	0.180	0.183
$P^{N}_{00 \to 0\pm2}$	0.383	0.383	0.383
$P^{N}_{0\pm1 \to 0\pm1}$	0.207	0.207	0.211
$P^{N}_{0\pm1 \to 0\mp1}$	0.583	0.582	0.580
$P^{R}_{00 \to 00}$	$0.787\text{x}10^{-2}$	$0.787\text{x}10^{-2}$	$0.755\text{x}10^{-2}$
$P^{R}_{00 \to 0\pm1}$	$0.580\text{x}10^{-2}$	$0.578\text{x}10^{-2}$	$0.557\text{x}10^{-2}$
$P^{R}_{0\pm1 \to 0\pm1}$	$0.422\text{x}10^{-2}$	$0.419\text{x}10^{-2}$	$0.404\text{x}10^{-2}$
$P^{\bar{R}}_{0\pm1 \to 0\mp1}$	$0.413\text{x}10^{-2}$	$0.410\text{x}10^{-2}$	$0.395\text{x}10^{-2}$

[a] 48 channels ($v = 0$-3; 12 rotations/vibration), $V_{ref} = V_{coll} = V(r_\lambda, R_\lambda, \gamma_\lambda = 0)$.

[b] 48 channels ($v = 0$-3; 12 rotations/vibration), $V_{ref} = V_0{}^{\lambda}(r_\lambda, R_\lambda)$.

[c] 50 channels ($v = 0$-4; 12, 12, 10, 8, 8 vibrations for $v = 0, 1, 2, 3, 4$ respectively), $V_{ref} = V_0{}^{\lambda}(r_\lambda, R_\lambda)$.

TABLE IV. Para to ortho integral cross sections for $H + H_2$[*].

	Converged			OVA		
E	$\overline{Q}^A_{00}$	$\overline{Q}^A_{02}$	$\overline{Q}^A_{04}$	$\overline{Q}^A_{00}$	$\overline{Q}^A_{02}$	$\overline{Q}^A_{04}$
0.30	0.356(-11)	-	-	0.543(-8)	-	-
0.35	0.144(-6)	0.137(-7)	-	0.343(-3)	0.221(-4)	-
0.40	0.499(-4)	0.868(-5)	0.400(-4)	0.280(-2)	0.976(-3)	0.228(-7)
0.45	0.299(-2)	0.721(-3)	0.104(-5)	0.0249	0.958(-2)	0.288(-3)
0.50	0.0543	0.0319	0.127(-3)	0.0918	0.0476	0.336(-2)
0.55	0.391	0.140	0.309(-2)	0.294	0.166	0.0250
0.60	0.841	0.361	0.0233	0.533	0.339	0.0727
0.65	1.025	0.619	0.0724	†	†	†
0.70	1.134	0.877	0.194	†	†	†
0.75	1.204	1.088	0.344	†	†	†

---

[*] In bohr. All cross sections have been summed over final ortho (odd j') states and averaged over initial rotational polarizations. A number in parentheses indicates power of 10 by which number preceding it is multiplied.

TABLE IV. (Cont.)

[†] These cross sections were not calculated but estimates of their values (through various extrapolation procedures) were used in the rate constant calculations. Because they involve higher energy results, their contributions to these rate constants are small as are the errors resulting from the extrapolations.

[*] Work supported in part by the United States Air Force Office of Scientific Research.

[†] Work performed in partial fulfillment of the requirements for the Ph.D. degree in Chemistry at the California Institute of Technology.

[‡] Contribution No.

[1] R. P. Saxon and J. C. Light, J. Chem. Phys. 57, 2758 (1972).

[2] M. Karplus, R. N. Porter and R. D. Sharma, J. Chem. Phys. 43, 3259 (1965);the classical angular distribution is reported in Ref. 25.

[3] J. D. Doll, T. F. George and W. H. Miller, J. Chem. Phys. 58, 1343 (1973).

[4] J. J. Tyson, R. P. Saxon and J. C. Light, J. Chem. Phys. 59, 363 (1973).

[5] R. P. Saxon and J. C. Light, J. Chem. Phys. 56, 3874 (1972); 56, 3885 (1972).

[6] G. Wolken and M. Karplus, J. Chem. Phys. 60, 351 (1974).

[7] A. Altenberger-Siczek and J. C. Light, J. Chem. Phys. 61, 4373 (1974).

[8] A. Kuppermann, G. C. Schatz and M. Baer, J. Chem. Phys. 61, 4362 (1974).

[9] A. Kuppermann and G. C. Schatz, J. Chem. Phys. 62, 2502 (1975).

[10] K. T. Tang and M. Karplus, Phys. Rev. A4, 1844 (1971).

[11] K. T. Tang and B. H. Choi, J. Chem. Phys. 62, 3642 (1975).

[12] R. B. Walker and R. E. Wyatt, J. Chem. Phys. 61, 4839 (1974).

[13] Reference 1 contains an extensive list of collinear studies of this reaction.

[14] H. S. Johnston, *Gas-Phase Reaction Rate Theory*, Ronald Press, New York, 1966, Chap. 10 and references therein.

[15] A. Kuppermann, G. C. Schatz and M. Baer, Mol. Phys., submitted.

[16] G. C. Schatz and A. Kuppermann, in preparation.

[17] R. N. Porter and M. Karplus, J. Chem. Phys. **40**, 1105 (1964).

[18] Double precision (64 bit) arithmetic was used for all calculations.

[19] As J increases, the repulsive centrifugal potential increases, effectively raising the potential in the interaction region and decreasing the reaction probability. As might be expected, the wave function should become smaller in the interaction region as this happens. In the integration procedure, those solutions generated by propagating into the interaction region (the plus solutions) will increase exponentially there (all channels being closed in that region for large J), while those generated by propagating out (the minus solutions) will decrease exponentially (i.e., will increase exponentially in the propagation direction). This occurs because of the dominance of the increasing exponential solution over the decreasing one in the direction of propagation. Only the physically meaningful decreasing solutions (as one penetrates the potential barrier in the strong interaction region) can be smoothly matched at the boundaries of the arrangement channel regions, so the matching procedure gives zero weight to the plus solutions (i.e., $\underset{\approx}{C}_J^+(\underset{\approx}{C}_J^-)^{-1} = \underset{\approx}{0}$ in Eq. 4.44 of I). From Eqs. 5.9 - 5.14 and especially 5.18 of I, we see that $\underset{\approx}{C}_J^+(\underset{\approx}{C}_J^-)^{-1} = \underset{\approx}{0}$ leads to a reactance matrix which is independent of any additional information about the matching, and hence the resulting nonreactive transition probabilities will not be sensitive to the lack of ortho-

gonality of $\underset{\approx}{s}_{\nu\lambda}^{J}$.

[20] For example, see R. Courant and D. Hilbert, *Methods of Mathematical Physics* (Vol. I), Interscience, New York, 1970, p. 4.

[21] We have tested both expressions in doing the OVA calculations, and have found that Eq. 3.48 of I leads to a much poorer approximation to the converged results than does Eq. 2.10 of the present paper, and that use of the former expression can actually lead to spurious resonant-like behavior in some transition probabilities. This could presumably result from the fact that in Eq. 2.10, we have analytically assumed completeness in carrying out the matrix multiplication present in Eq. 3.48 of I, so the effects of a severe basis set truncation might be less important than in Eq. 3.48 of I, where this completeness is neither assumed nor explicitly included.

[22] J. Geddes, H. F. Krause and W. L. Fite, J. Chem. Phys. **56**, 3298 (1972).

[23] G. H. Kwei, V. W. S. Lo and E. A. Entemann, J. Chem. Phys. **59**, 3421 (1973).

[24] D. A. Micha, Phys. Rev. **162**, 88 (1967); D. A. Micha, Chem. Phys. Lett. **1**, 139 (1967); R. D. Levine, B. R. Johnson, J. T. Muckerman and R. B. Bernstein, J. Chem. Phys. **49**, 56 (1968); R. D. Levine and R. B. Bernstein, J. Chem. Phys. **53**, 686 (1970).

[25] This argument does not rule out vibrational Feshbach resonances. These resonances have actually been observed in planar $H + H_2$[28] (at higher energies than are considered in this paper). As one might expect, however, they affect more than one partial wave[28] and thus are probably not responsible for the oscillations observed here.

[26] For examples, see: J. M. Farrer and Y. T. Lee, J. Chem. Phys. 56, 5801 (1972); P. E. Siska, J. M. Parson, T. P. Schafer and Y. T. Lee, J. Chem. Phys. 55, 5762 (1971); J. M. Farrar and Y. T. Lee, J. Chem. Phys. 57, 5492 (1972); H. Haberland, C. H. Chen and Y. T. Lee, Atomic Physics 3, 339 (1973); B. Andresen and A. Kuppermann, *Mol. Phys.*, in press.

[27] J. M. Bowman, A. Kuppermann, J. T. Adams and D. G. Truhlar, Chem. Phys. Letters 20, 229 (1973).

[28] G. C. Schatz and A. Kuppermann, Phys. Rev. Lett., submitted.

[29] D. J. Diestler, J. Chem. Phys. 54, 4547 (1971).

[30] D. G. Truhlar and A. Kuppermann, J. Chem. Phys. 56, 2232 (1972).

[31] A. B. Elkowitz and R. E. Wyatt, J. Chem. Phys., to be published.

[32] R. A. Marcus, J. Chem. Phys. 46, 959 (1967).

[33] The dependence of $\overline{Q}^{R}_{0j\to 00}$ on j can be extracted from the $\overline{Q}^{R}_{00\to 0j}$ in Fig. 21 by multiplying the latter by the ratio $2k_{00}/[k_{02}(1+\delta_{j0})]$ where the wave numbers k_{00} and k_{02} refer to the $v = 0$, $j = 0$ and $v = 0$, $j = 2$ states of H_2, respectively, and $(1+\delta_{j0})/2$ is a degeneracy factor.

[34] The distribution may be derived from an information theoretic formalism [see, for example, A. Ben-Shaul, R. D. Levine and R. B. Bernstein, J. Chem. Phys. 57, 5427 (1972)] by assuming that the surprisal function is linear in the product rotational energy. Note that the 2D translational density of states is independent of E_j, and is therefore omitted from Eq. 3.3.

[35] I. Shavitt, R. M. Stevens, F. L. Minn and M. Karplus, J. Chem. Phys. 48, 2700 (1968).

[36] R. B. Walker and R. E. Wyatt, Chem. Phys. Lett. **16**, 52 (1972).

[37] A. Farkas, *Orthohydrogen, Parahydrogen and Heavy Hydrogen*, (Cambridge University Press, 1935) p. 13.

[38] For a recent paper on this subject, see R. B. Walker and R. E. Wyatt, Mol. Phys. **28**, 101 (1974).

FIG. 1. Plot of potential contours for the H + H_2 reaction in the $x_\lambda y_\lambda z_\lambda$ space having spherical coordinates $\zeta = (R_\lambda^2 + r_\lambda^2)^{\frac{1}{2}}$, $\omega_\lambda = 2\tan^{-1} r_\lambda/R_\lambda$ and γ_λ for $\gamma_\lambda = 0$ and 180° (a), 45° and 225° (b) and 90° and 270° (c). In (a) we also depict the lines of intersection of the $\gamma_\lambda = 0$, 180° plane with the half planes $\pi_{\nu\lambda}$, $\pi_{\kappa\nu}$, $\pi_{\lambda\kappa}$ defined in I which form the matching surfaces of the calculation. For each figure above, OW_λ is the intersection of the half plane determined by OZ_λ and the corresponding smallest γ_λ with the $OX_\lambda Y_\lambda$ plane. Because of arrangement channel permutational symmetry, the lower half of (c) represents contours on the matching plane $\pi_{\kappa\nu}$.

FIG. 2. Converged coplanar reaction probability $P_{J,00\to01}$ (for the v = 0, j = 0 → v' = 0, j' = +1 transition) as a function of the total angular momentum quantum number J for E = 0.30 eV (crosses), 0.35 eV (triangles), 0.40 eV (squares) and 0.45 eV (circles). Smooth curves have been drawn through the points.

FIG. 3. Reaction probability $P^R_{J,00\to01}$ analogous to Fig. 2 at total energies of 0.50 eV (crosses), 0.55 eV (triangles), 0.60 eV (squares), and 0.65 eV (circles).

FIG. 4. Converged coplanar reaction probability $P^R_{J,00\to00}$ (i.e., v = 0, j = 0 → v' = 0, j' = 0) analagous to Fig. 2.

FIG. 5. Coplanar reaction probability $P^R_{J,00\to00}$ for E = 0.60 eV (translational energy E_0 = 0.33 eV) versus the total angular momentum quantum number J. Squares indicate the converged result while circles indicate the OVA probability for collinear reference potential (V_{coll} =

$V(r_\lambda, R_\lambda, \gamma_\lambda = 0))$.

FIG. 6. Coplanar converged inelastic probability $P^N_{J,00 \rightarrow 02}$ as a function of J for total energies E = 0.40 eV (dash-dot), 0.50 eV (dashed), 0.60 eV (solid) and 0.70 eV (solid).

FIG. 7. Schematic representation of dominant collisions contributing to the $j = 0 \rightarrow j' > 0$ collisional (nonreactive) excitation process. Shown are (a) the initial approach of the collision partners in the center of mass coordinate system, (b) the collision itself with the direction of the rotational polarization indicated by curved arrows, and (c) the receding scattered particles. Collision I considers a collision with l (and hence b) initially positive (relative to the coordinate system shown). Collision II considers negative initial l and b. Note that the diatomic rotor with j = 0 is classically motionless with equal probability for any rotational phase. The particular phase chosen was that believed to give significant rotational excitation for each situation pictured.

FIG. 8. Converged coplanar reactive differential cross section σ^R_{00-01} versus the scattering angle χ_R for energies E = 0.30, 0.35, 0.40 and 0.45 eV.

FIG. 9. Reactive differential cross section $\sigma^R_{00 \rightarrow 01}$ analogous to Fig. 6 at total energies E = 0.50, 0.55, 0.60 and 0.65 eV.

FIG. 10. Converged coplanar reactive differential cross section $\sigma^R_{00 \rightarrow 00}$ at same energies as in Fig. 8. These curves are symmetric about $\chi_R = 180°$.

FIG. 11. Vibrationally converged and OVA differential cross section $\sigma^{R}_{00\rightarrow 00}$ at E = 0.600 eV (E_0 = 0.330 eV). OVA cross section was computed with a collinear reference potential ($V_{coll} = V(r_\lambda, R_\lambda, \gamma_\lambda = 0)$). The cross section for this transition is symmetric about $\chi_R = 180°$.

FIG. 12. Inelastic nonreactive (converged) differential cross section for the coplanar v = 0, j = 0 → v' = 0, j' = +2 transition at total energies E = 0.40 eV (dash-dot), 0.50 eV (dashed), 0.60 eV (solid) and 0.70 eV (solid).

FIG. 13. Nonreactive (solid), reactive (dashed) and antisymmetrized (dash-dot) differential cross sections for the coplanar v = 0, j = 0 → v' = 0, $|j'| = 2$ transition (summed over final rotational polarizations) at E = 0.500 eV (E_0 = 0.230 eV). Note that the scattering angle used is χ and $\chi = 0$ corresponds, for reactive scattering, to $\chi_R = 180°$ (see Eq. 2.5).

FIG. 14. Nonreactive, reactive and antisymmetrized differential cross sections analogous to Fig. 13 at E = 0.600 eV (E_0 = 0.330 eV). See remark about χ in the caption for that figure.

FIG. 15. Nonreactive, reactive and antisymmetrized differential cross sections analogous to Fig. 13 at E = 0.700 eV (E_0 = 0.430 eV). See remark about χ in the caption of that figure.

FIG. 16. Converged integral reactive cross sections $\tilde{Q}^{R}_{00\rightarrow 01}$, $\tilde{Q}^{R}_{00\rightarrow 03}$ and $\tilde{Q}^{R}_{00\rightarrow 05}$ versus total energy E and translational energy E_0. (a) linear scale, (b) semi-logarithmic scale.

FIG. 17. Integral reactive cross section $\overline{Q}^{R}_{00}$ (summed over all accessible final states) versus total energy E and relative energy E_0. Circles represent vibrationally converged results and squares the OVA ones using a collinear reference potential.(a) linear scale, (b) semi-logarithmic scale.

FIG. 18. Inelastic nonreactive integral cross sections $\overline{Q}^{N}_{00\to02}$ and $\overline{Q}^{A}_{00\to02}$ (summed over final polarizations) versus the total energy E and relative translational energy E_0.

FIG. 19. Total reaction probabilities P^{R}_{0} (collinear) and P^{R}_{00} (coplanar, J = 0, v = 0, j = 0 and summed over all final states) versus the total energy E and translational energy E_0. (a) linear scale, (b) semi-logarithmic scale.

FIG. 20. Coplanar total reaction probabilities $P^{R}_{00}(J = 0)$ (circles and solid curve), $P^{R}_{00}(J = 4)$ (triangles and dashed curve) and P^{R}_{01} (J = 0) (squares and dash-dotted curve) summed over all final states versus total energy E and translational energy E_0. (a) linear scale. (b) logarithmic scale. Note that the $P^{R}_{00}(J = 1 - 3)$ curves all lie between the solid and dash-dotted curves in the figure.

FIG. 21. Converged coplanar integral reactive cross sections $\overline{Q}^{R}_{00\to0j'}$ versus the final rotational energy at a fixed total energies E = 0.50 eV (crosses), 0.55 eV(triangles), 0.60 eV (squares) and 0.65 eV (circles).

FIG. 22. Semi-logarithmic plot of the integral reactive cross section $\overline{Q}^{R}_{00\rightarrow 0j'}$ (x $2/(2 - \delta_{j'0})$) versus the final rotational energy at a fixed total energy for E = 0.50, 0.55, 0.60 and 0.65 eV (symbols analogous to Fig. 21). A straight line is drawn connecting the nearly linear low j' points.

FIG. 23. Semi-logarithmic plot of the OVA reactive cross section $\overline{Q}^{R}_{00\rightarrow 0j'}$ (x $2/(2 - \delta_{j'0})$) at energies E = 0.50, 0.55 and 0.60 eV analogous to Fig. 22.

FIG. 24. Integral cross section $Q^{R}_{00\rightarrow 01}$ versus E and E_0 for several exact and approximate coplanar calculations. $Q^{R}_{00\rightarrow 01}$ (SK) refers to the present results, $Q^{R}_{00\rightarrow 01}$(WW, WE) and $Q^{R}_{00\rightarrow 01}$ (WW, SE) are the results of distorted wave calculations of Ref. 12, and $Q^{R}_{00\rightarrow 01}$(AL) is the OVA result (on a different potential surface and using a method somewhat different from ours) of Ref. 7.

FIG. 25. Reaction probabilities $P^{R}_{J,00\rightarrow 00}$ and $P^{R}_{J,00\rightarrow 01}$, (a) and differential cross sections $\sigma^{R}_{00\rightarrow 00}$ and $\sigma^{R}_{00\rightarrow 01}$ (b). WW refers to the SE results of Ref. 12 with dashed curves referring to 00 → 00 transitions and dash-dot curves referring to 00 → 01. SK refers to the results of this paper (Figs. 3, 4, 9, and 10) with solid curves for 00 → 00 and short dashed for 00 → 01. WW results are at $E_0 = 0.340$ eV (E = 0.61 eV) while SK results are at $E_0 = 0.330$ eV (E = 0.600 eV).

FIG. 26. Arrhenius plot of the converged and OVA para to ortho coplanar thermal rate constants for H + H_2 for the converged and OVA (collinear reference potential) results. The dashed straight line is tangent to the converged one at high temperatures.

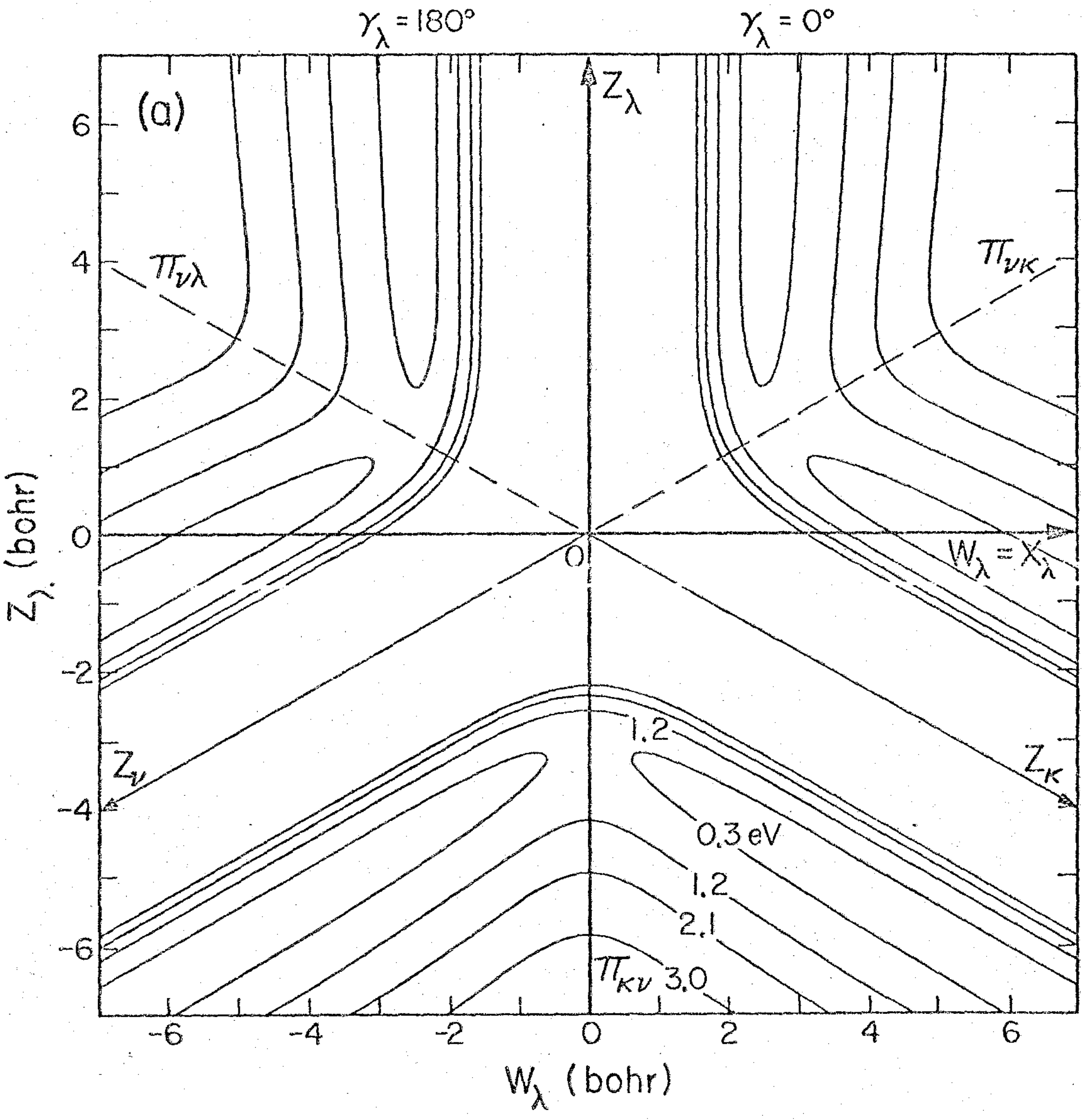
$\gamma_\lambda = 180°$
$\gamma_\lambda = 0°$
(a)
Z_λ
$\pi_{\nu\lambda}$
$\pi_{\nu\kappa}$
$W_\lambda = X_\lambda$
0
Z_ν
Z_κ
1.2
0.3 eV
1.2
2.1
$\pi_{\kappa\nu}$ 3.0
6
4
2
0
-2
-4
-6
Z_λ (bohr)
-6
-4
-2
0
2
4
6
W_λ (bohr)

Figure 1a

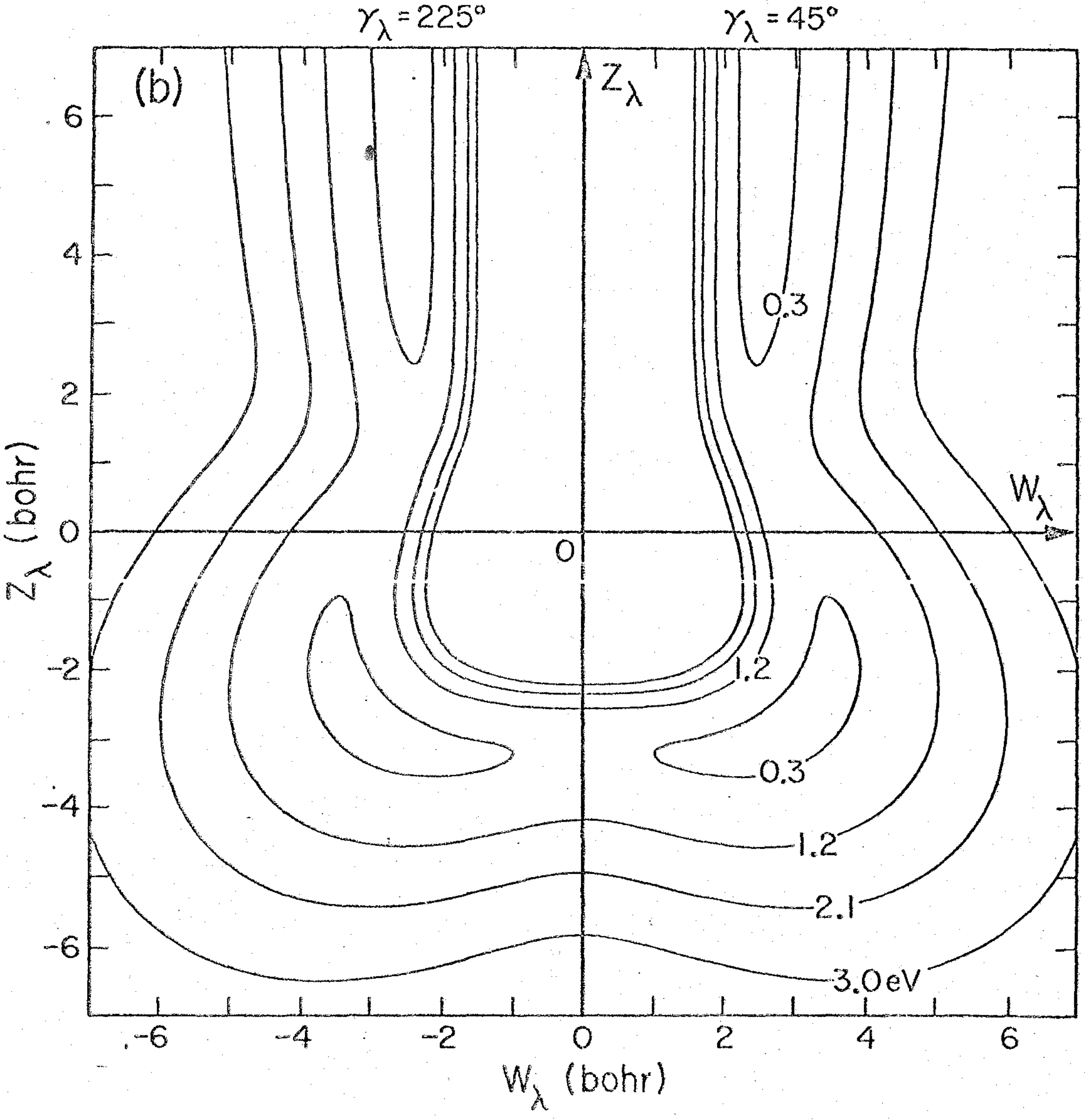
$\gamma_\lambda = 225°$
$\gamma_\lambda = 45°$
(b)
Z_λ
W_λ
0.3
0
1.2
0.3
1.2
2.1
3.0eV
6
4
2
0
-2
-4
-6
-6
-4
-2
0
2
4
6
Z_λ (bohr)
W_λ (bohr)

Figure 1b

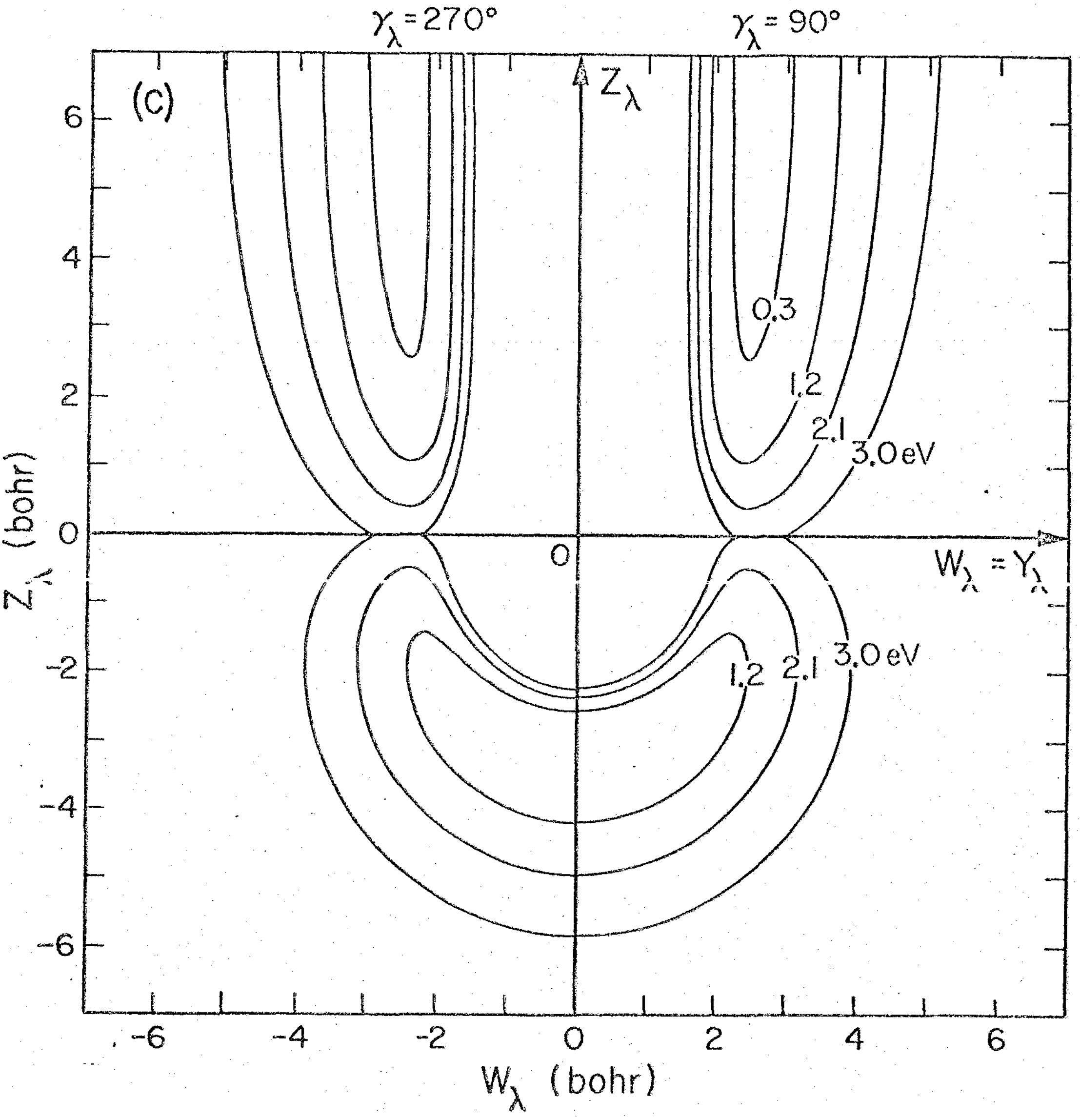

$\gamma_\lambda = 270°$
$\gamma_\lambda = 90°$
(c)
Z_λ
$W_\lambda = Y_\lambda$
0
0.3
1.2
2.1
3.0 eV
1.2
2.1
3.0 eV
Z_λ (bohr)
W_λ (bohr)
6
4
2
0
-2
-4
-6
-6
-4
-2
0
2
4
6

Figure 1c

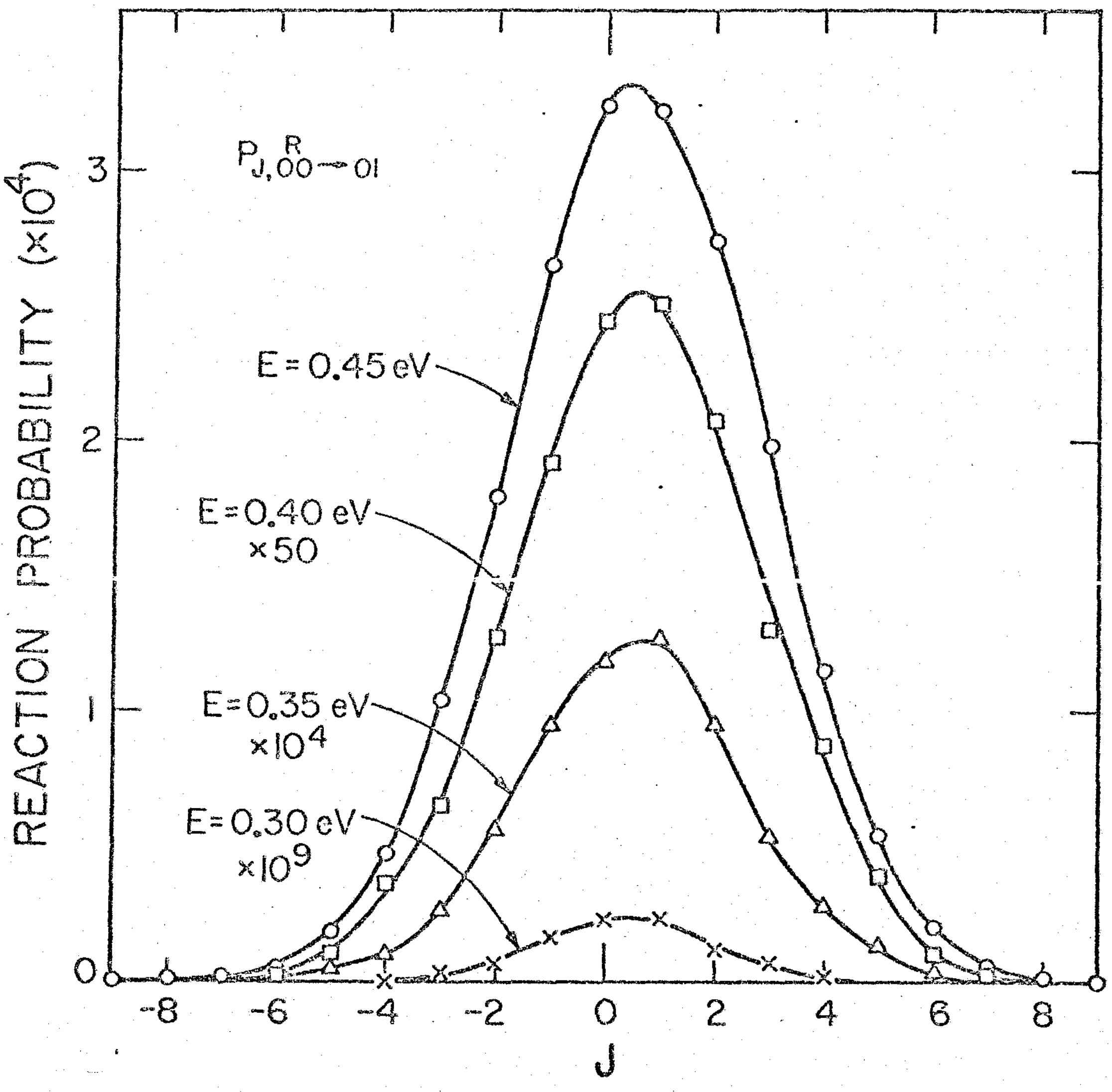
$P^R_{J,00\to01}$
REACTION PROBABILITY ($\times10^4$)
E = 0.45 eV
E = 0.40 eV
×50
E = 0.35 eV
×10^4
E = 0.30 eV
×10^9
0
1
2
3
-8
-6
-4
-2
0
2
4
6
8
J

Figure 2

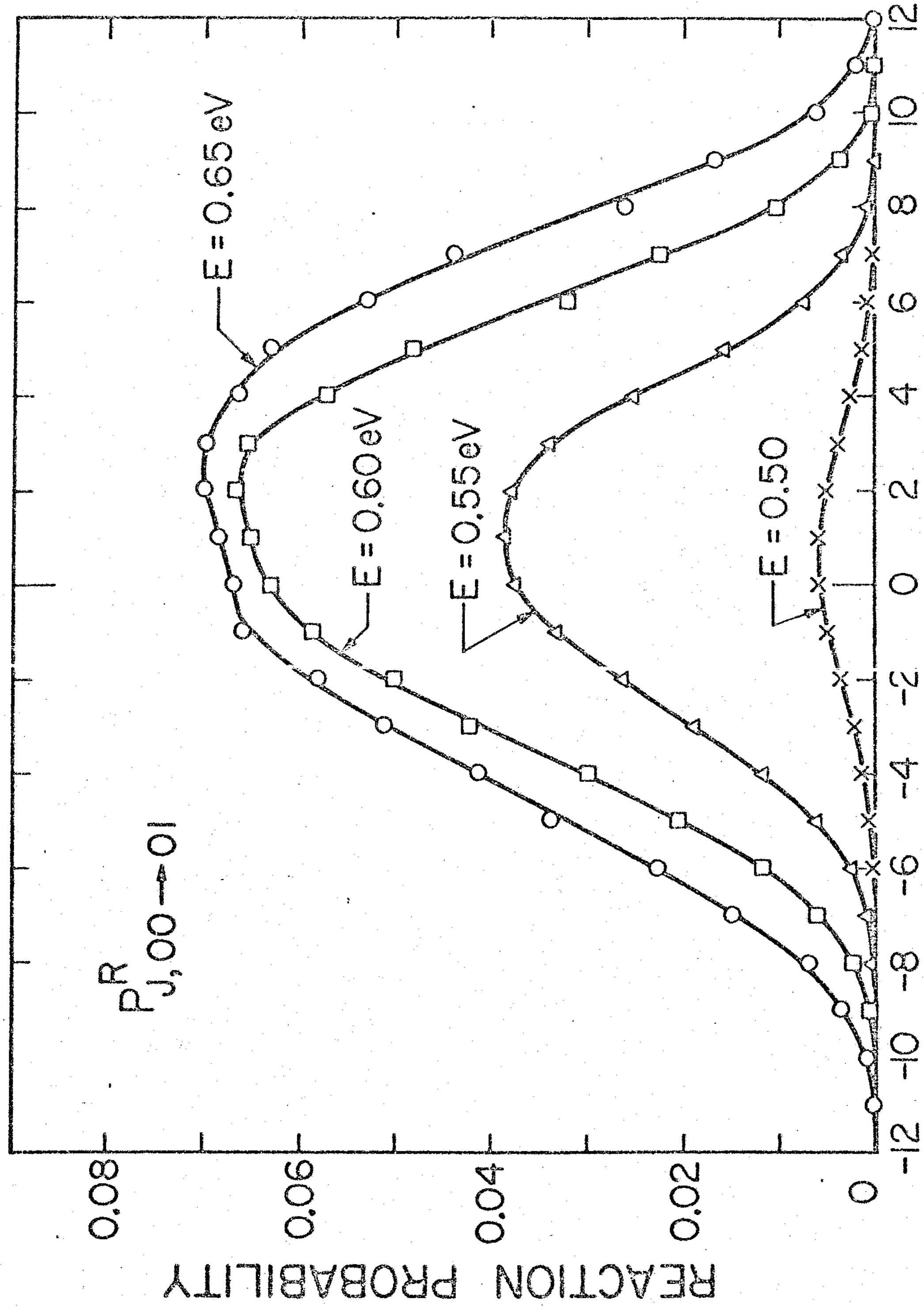
REACTION PROBABILITY
0.08
0.06
0.04
0.02
0
J
-12
-10
-8
-6
-4
-2
0
2
4
6
8
10
12
$P^{R}_{J,00\rightarrow01}$
E = 0.65 eV
E = 0.60 eV
E = 0.55 eV
E = 0.50

Figure 3

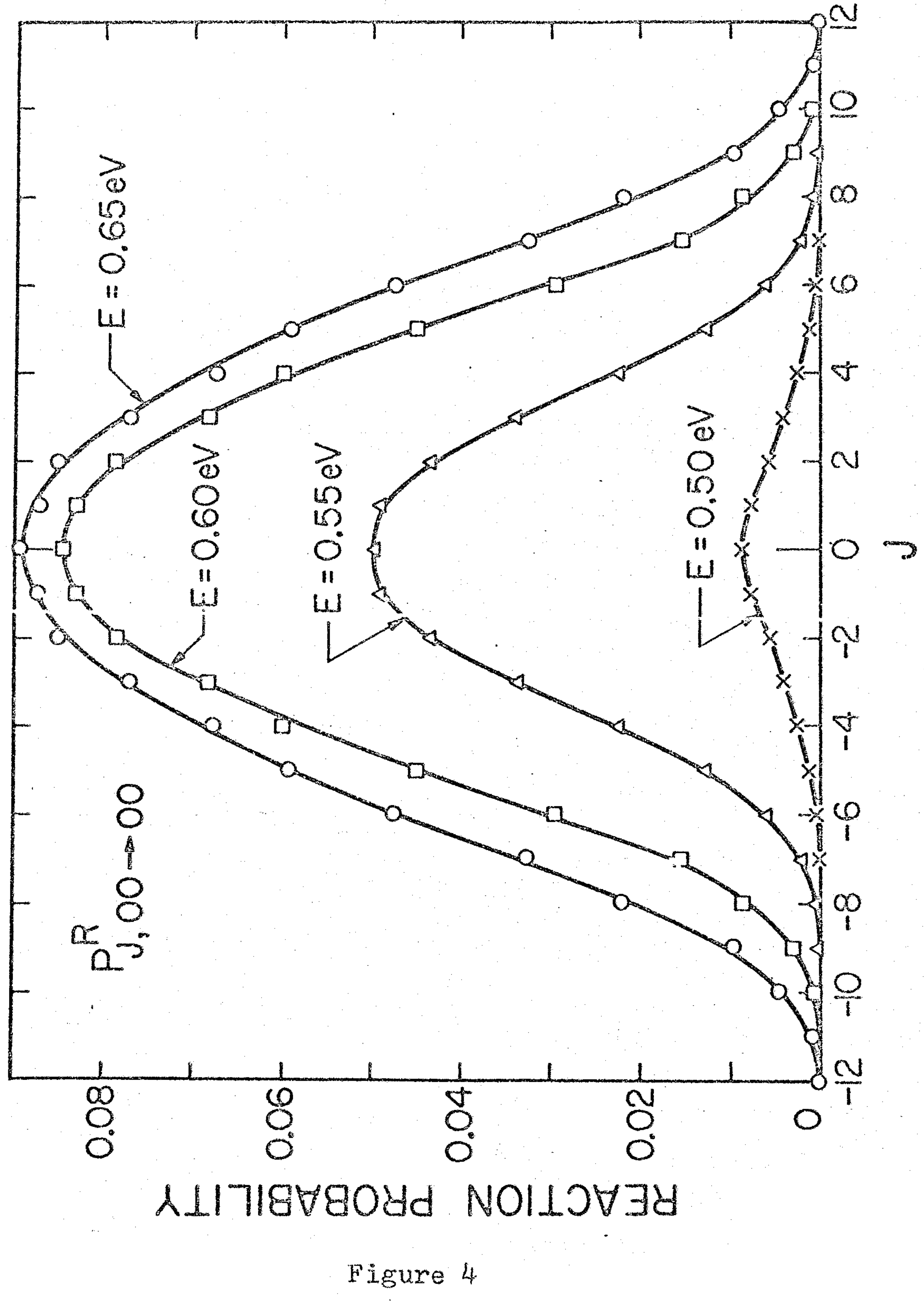
$P^R_{J,00\to00}$
E = 0.65eV
E = 0.60eV
E = 0.55eV
E = 0.50eV
REACTION PROBABILITY
0
0.02
0.04
0.06
0.08
J
-12
-10
-8
-6
-4
-2
0
2
4
6
8
10
12

Figure 4

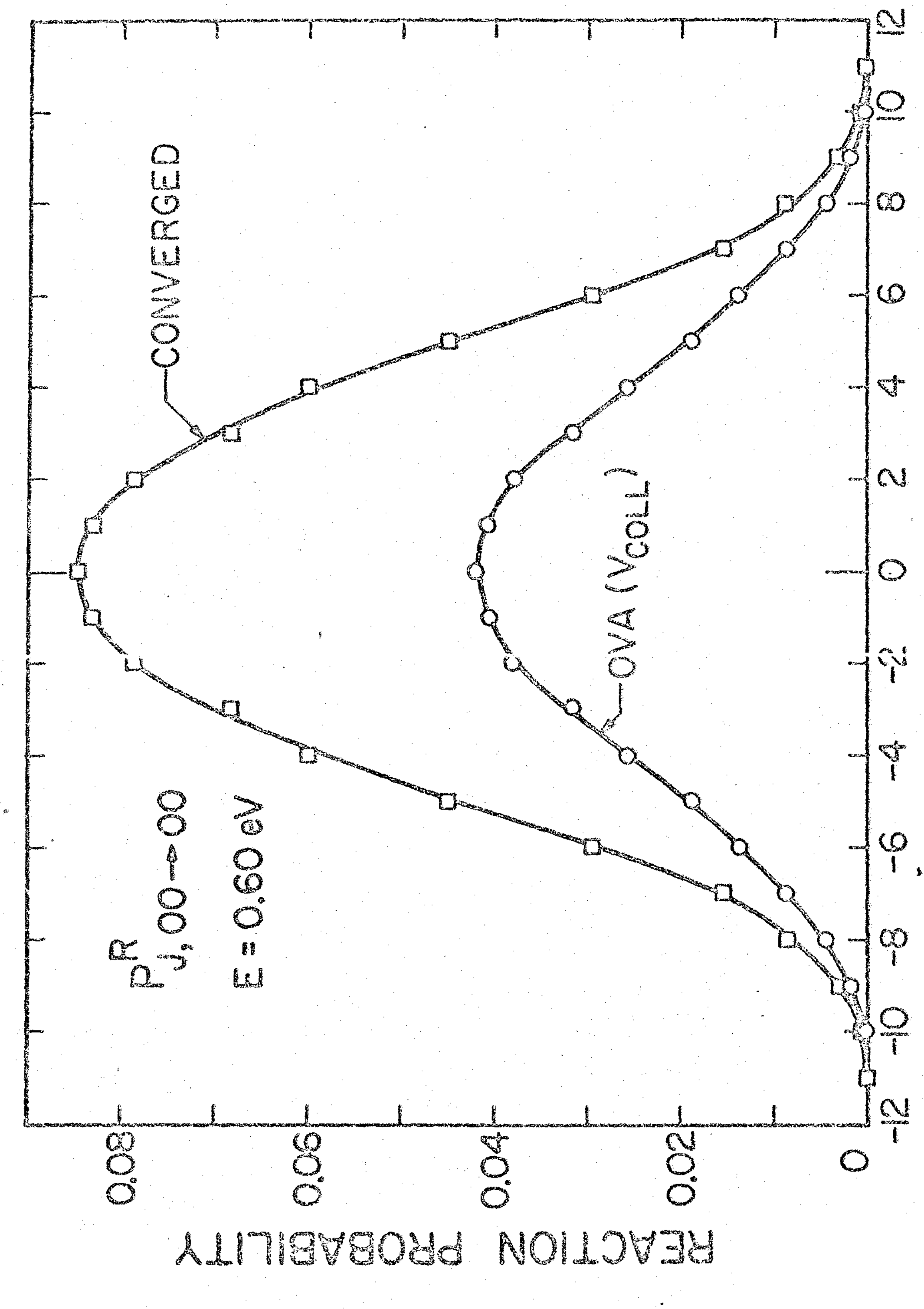
$P^R_{J,00\rightarrow00}$
E = 0.60 eV
CONVERGED
OVA (V_{COLL})
REACTION PROBABILITY
0
0.02
0.04
0.06
0.08
J
-12
-10
-8
-6
-4
-2
0
2
4
6
8
10
12

Figure 5

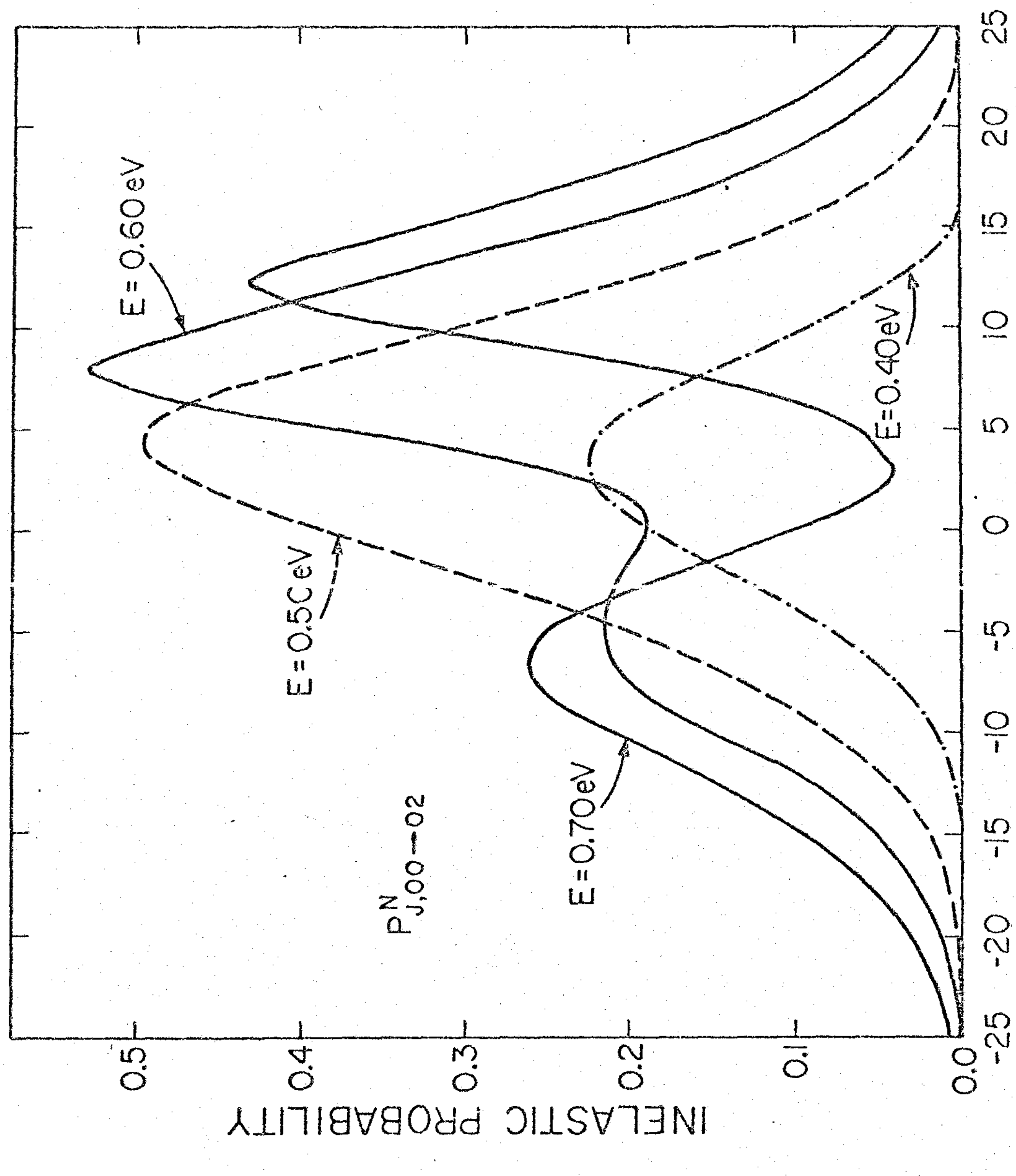
INELASTIC PROBABILITY
0.0
0.1
0.2
0.3
0.4
0.5
J
-25
-20
-15
-10
-5
0
5
10
15
20
25
$P^{N}_{J,00-02}$
E=0.70eV
E=0.50eV
E=0.60eV
E=0.40eV

Figure 6

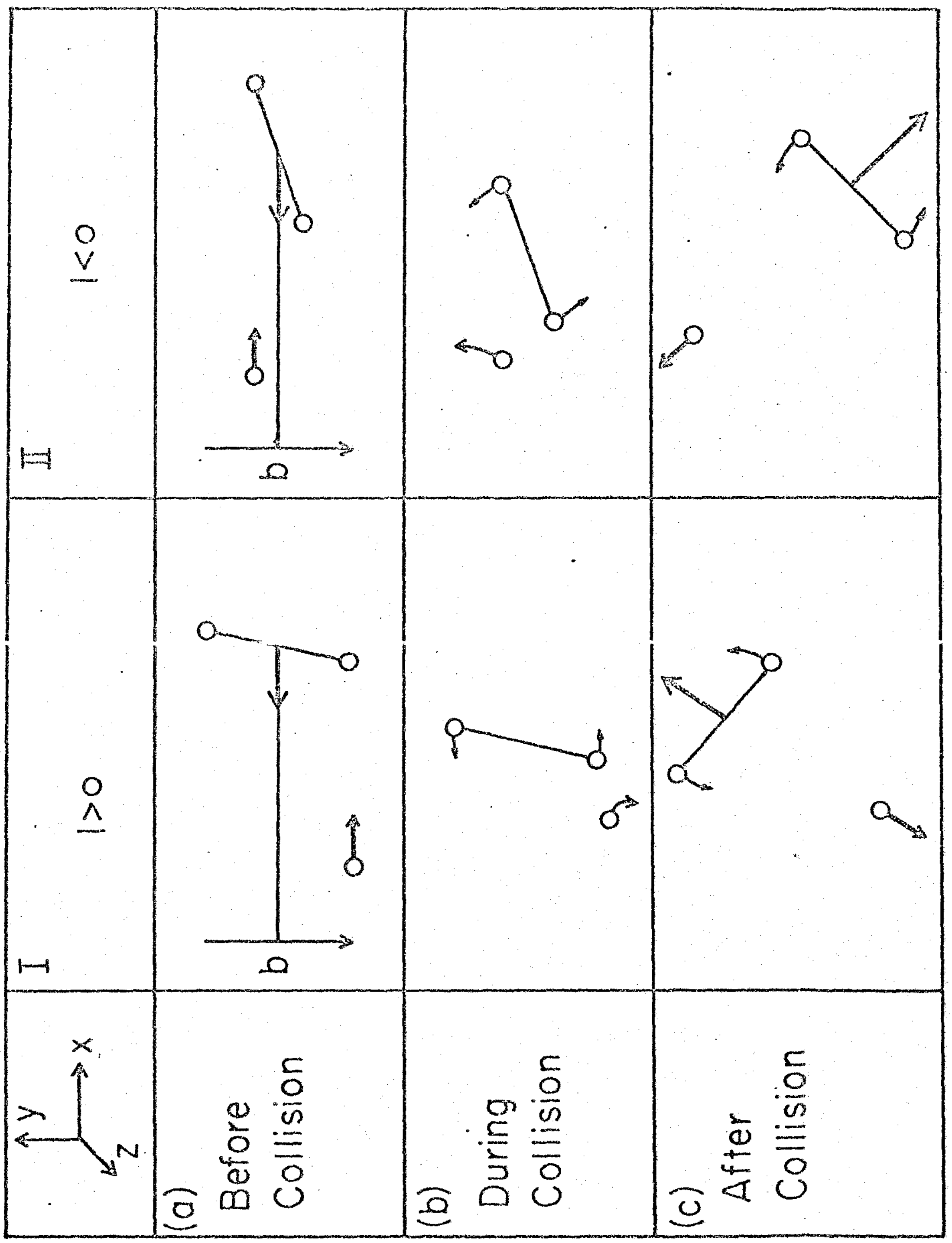
y
x
z
I
l>0
II
l<0
(a) Before Collision
b
b
(b) During Collision
(c) After Collision

Figure 7

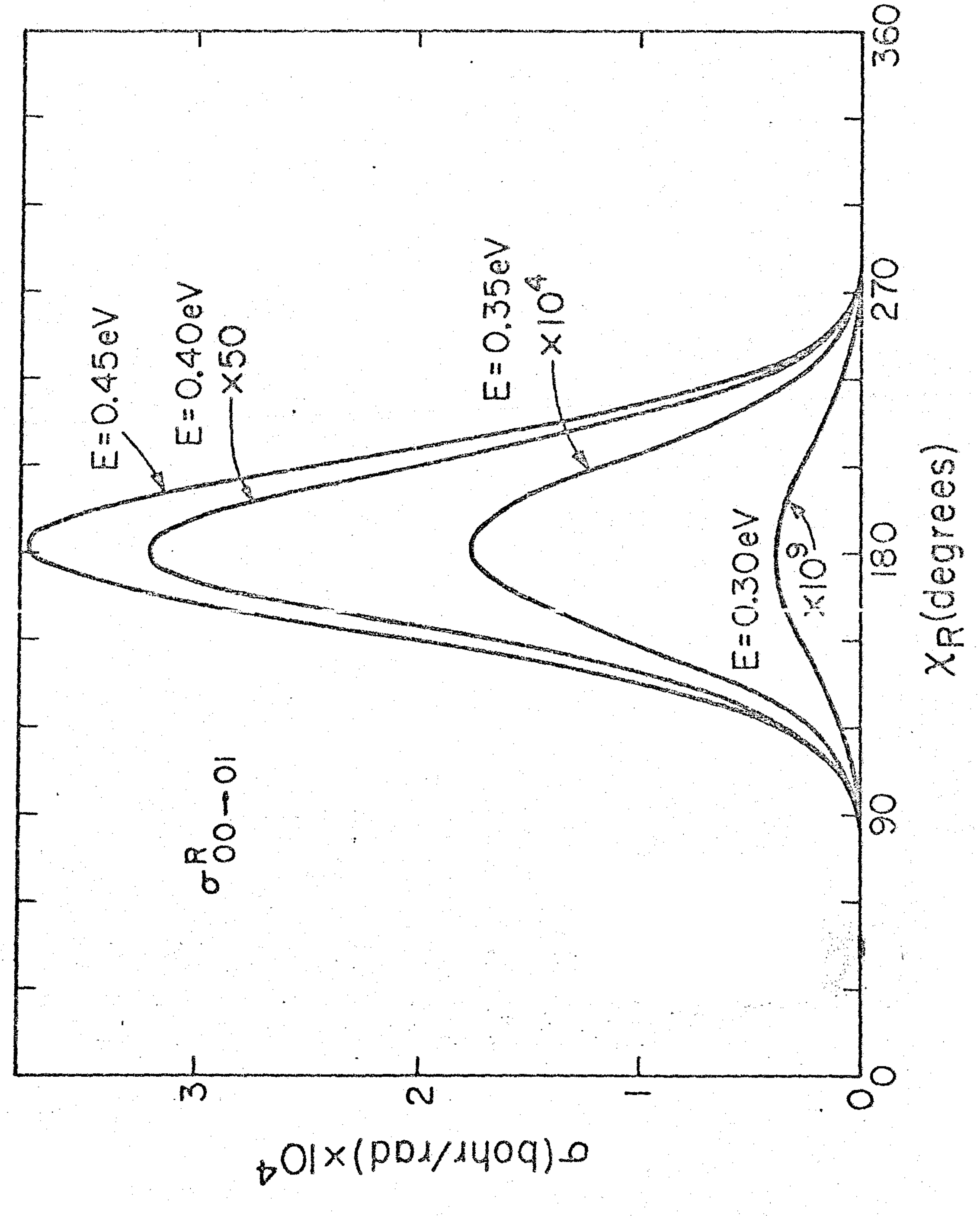

σ^R_00→01
E=0.45eV
E=0.40eV
X50
E=0.35eV
X10^4
E=0.30eV
X10^9
σ(bohr/rad)×10^4
0
1
2
3
0
90
180
270
360
χ_R(degrees)

Figure 8

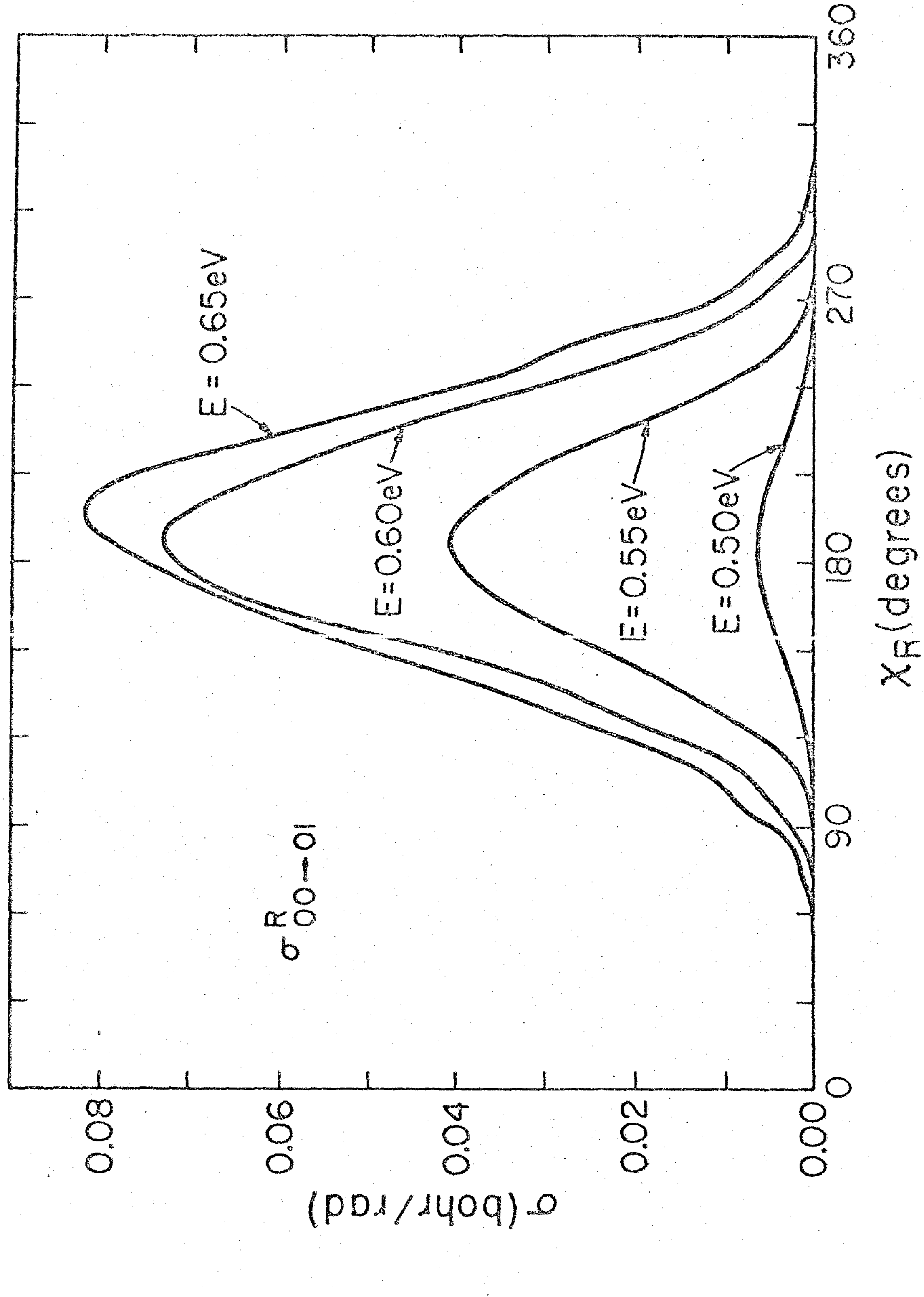

σ(bohr/rad)
0.00
0.02
0.04
0.06
0.08
0
90
180
270
360
χR (degrees)
σ R 00→01
E = 0.65eV
E=0.60eV
E=0.55eV
E=0.50eV

Figure 9

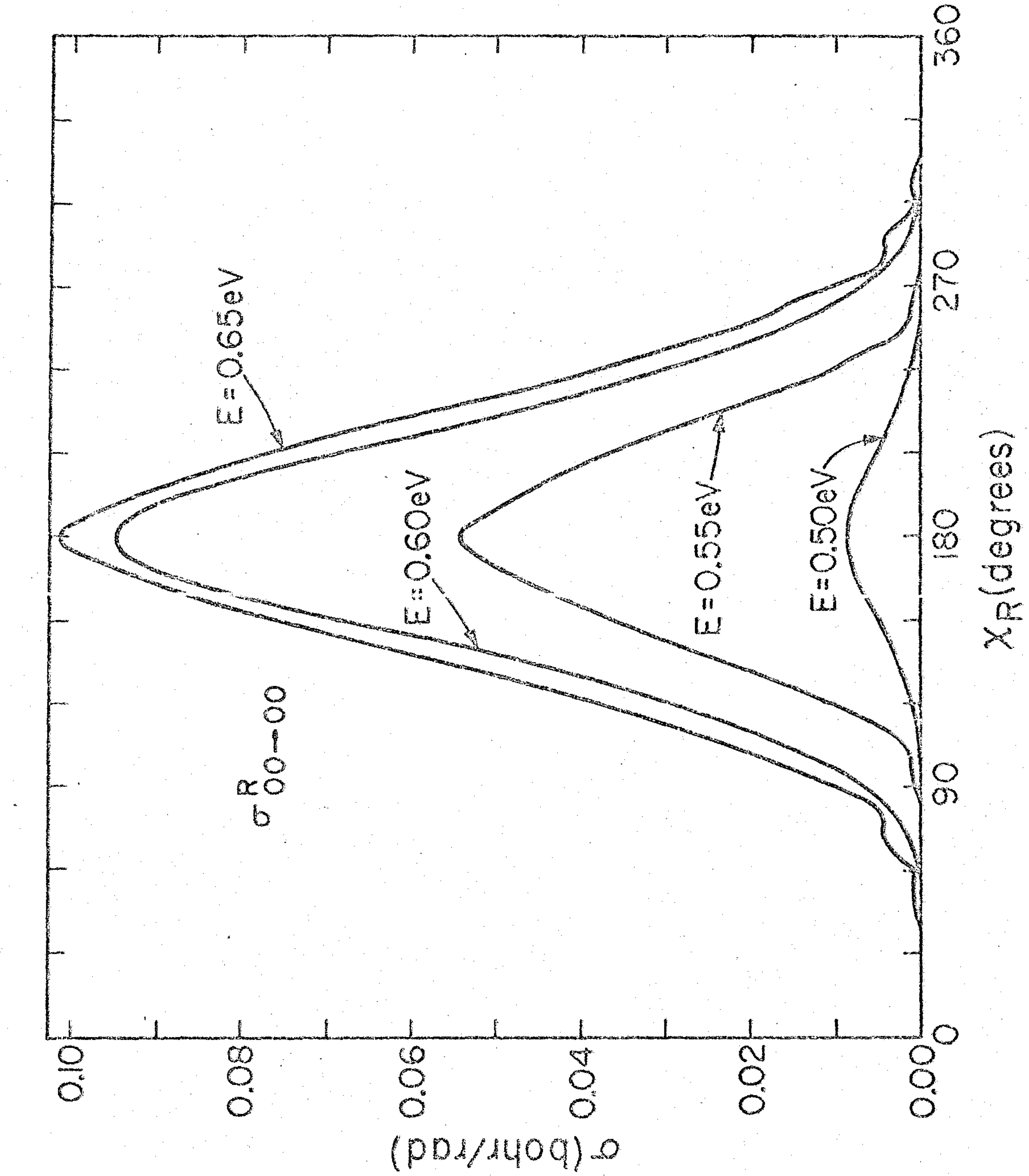
σ(bohr/rad)
0.10
0.08
0.06
0.04
0.02
0.00
0
90
180
270
360
χR(degrees)
σ R 00→00
E=0.65eV
E=0.60eV
E=0.55eV
E=0.50eV

Figure 10

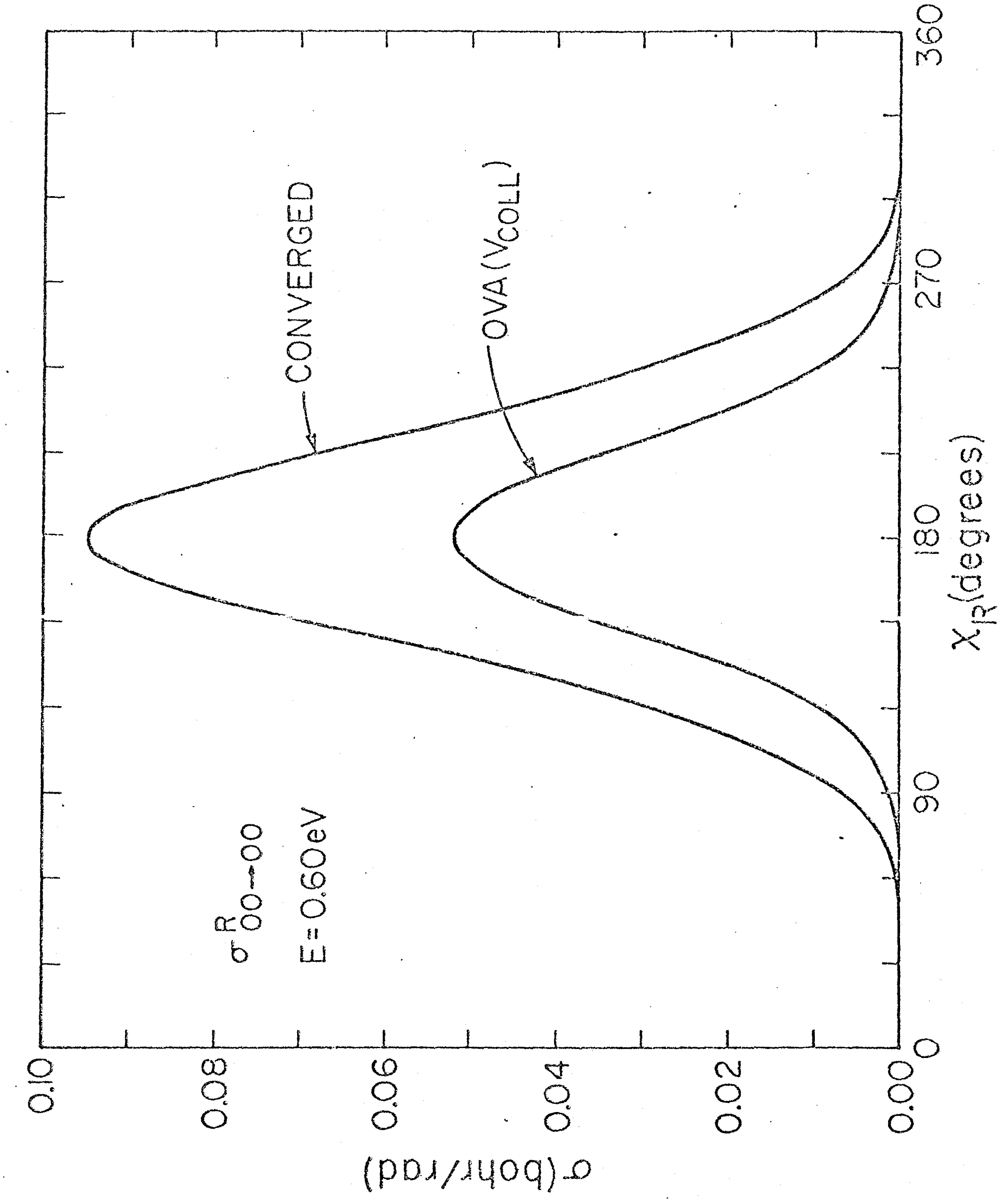
σ$^R_{00\to00}$
E=0.60eV
CONVERGED
OVA (V$_{COLL}$)
σ(bohr/rad)
0.00
0.02
0.04
0.06
0.08
0.10
0
90
180
270
360
X$_P$(degrees)

Figure 11

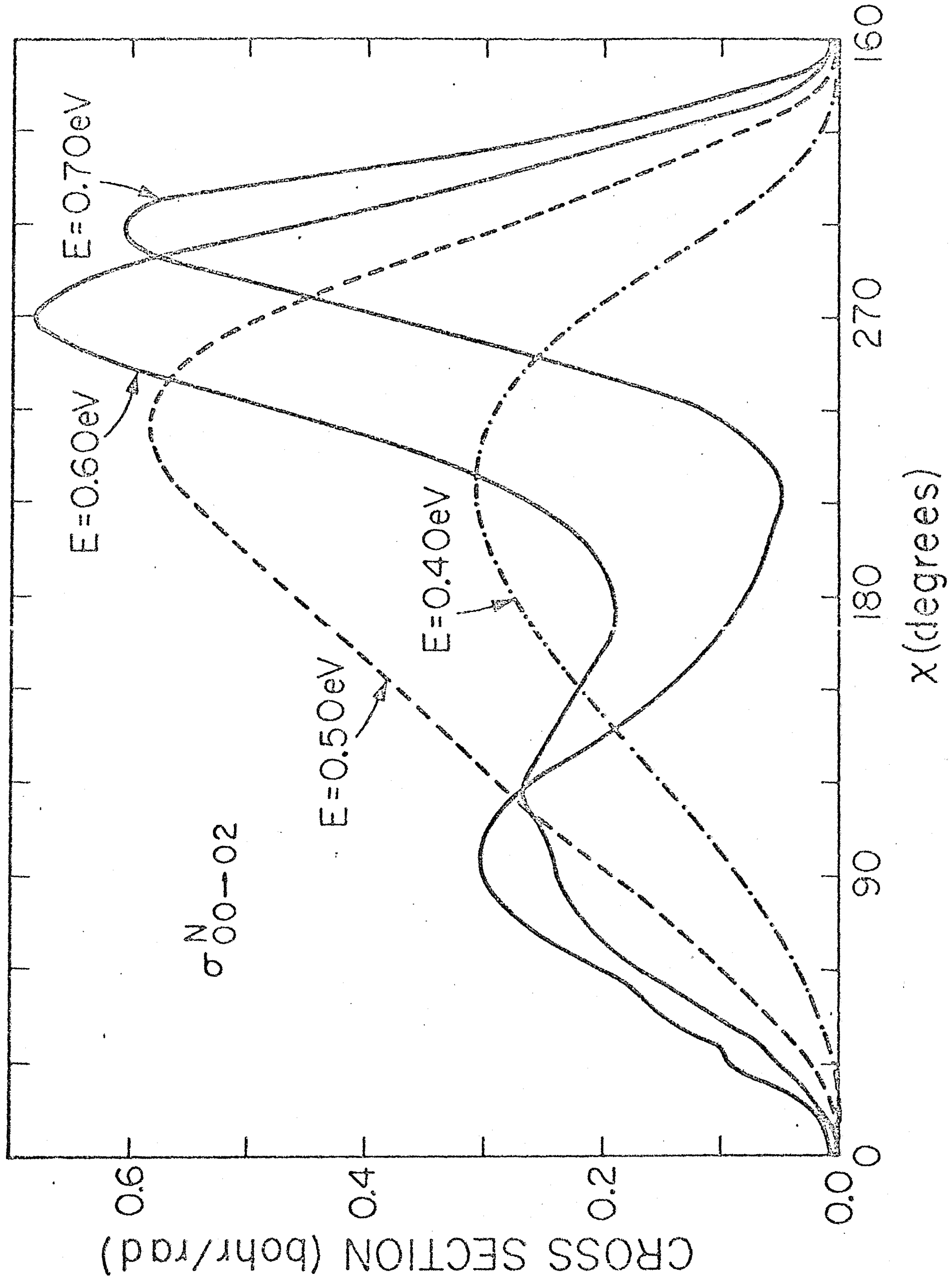
σ^{N}_{00-02}
E=0.70eV
E=0.60eV
E=0.50eV
E=0.40eV
CROSS SECTION (bohr/rad)
0.0
0.2
0.4
0.6
X(degrees)
0
90
180
270
360

Figure 12

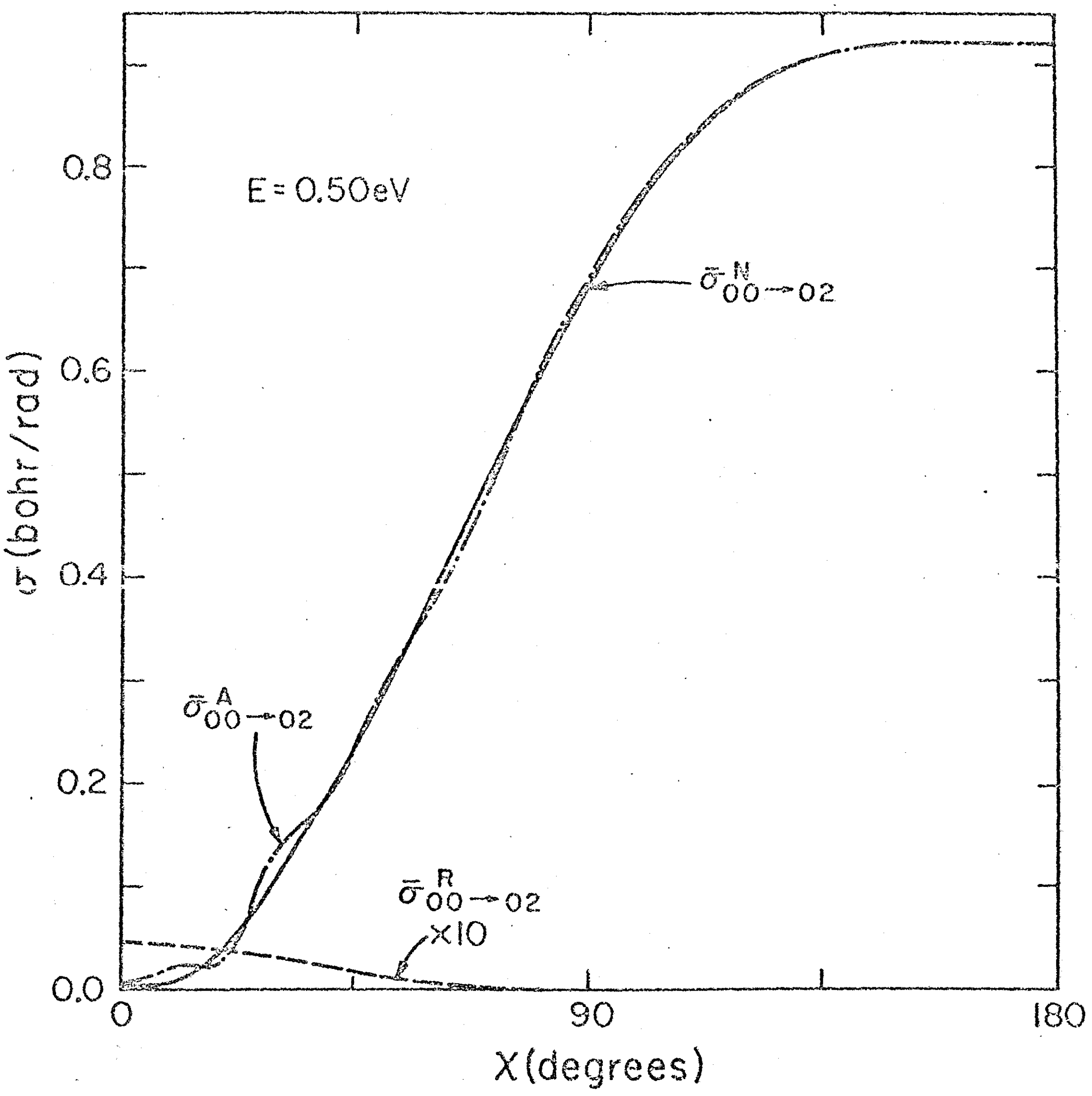
E = 0.50eV
$\bar{\sigma}^{N}_{00\rightarrow02}$
$\bar{\sigma}^{A}_{00\rightarrow02}$
$\bar{\sigma}^{R}_{00\rightarrow02}$
×10
σ (bohr/rad)
0.0
0.2
0.4
0.6
0.8
0
90
180
X(degrees)

Figure 13

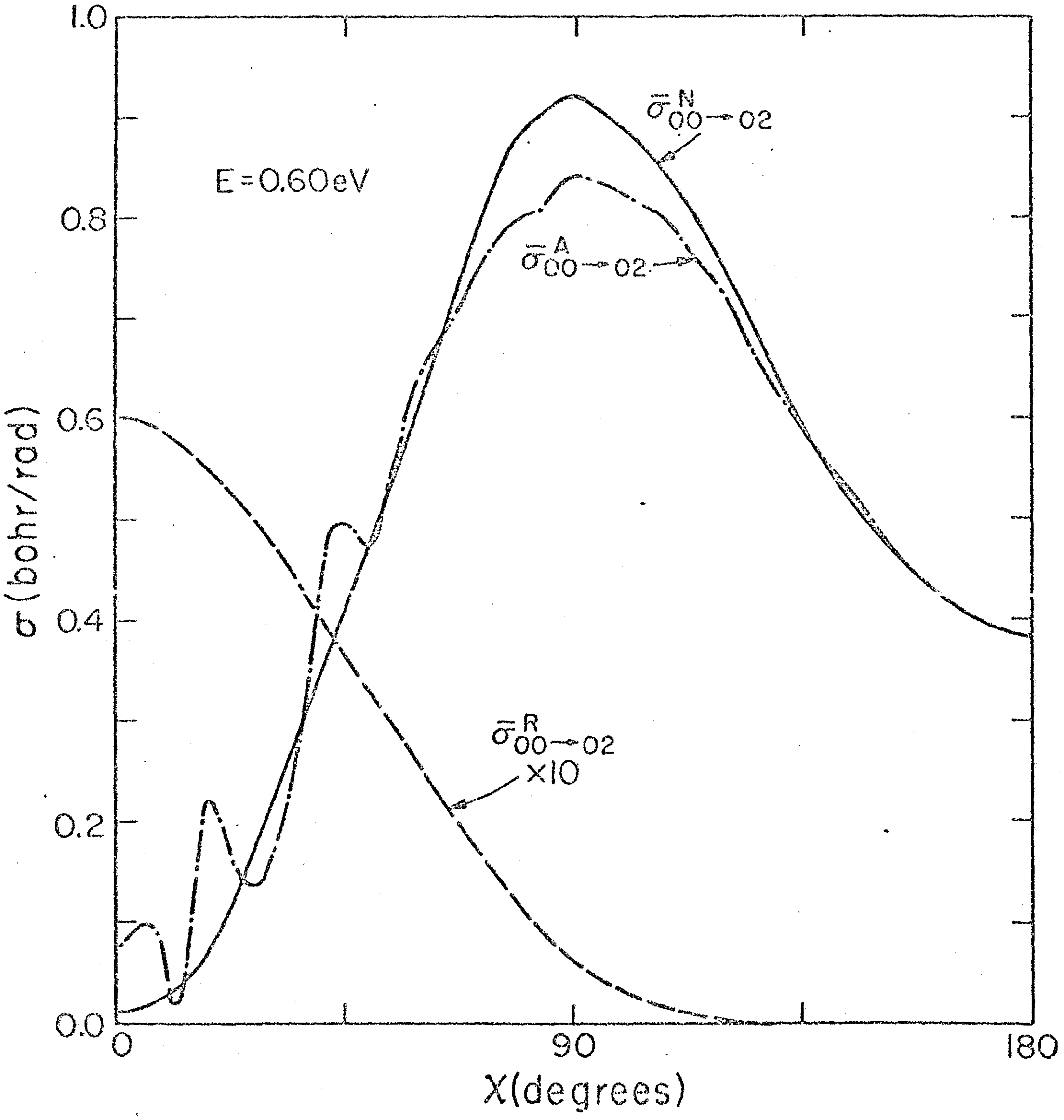
E=0.60eV
$\bar{\sigma}^{N}_{00\to02}$
$\bar{\sigma}^{A}_{00\to02}$
$\bar{\sigma}^{R}_{00\to02}$ ×10
σ (bohr/rad)
1.0
0.8
0.6
0.4
0.2
0.0
0
90
180
χ(degrees)

Figure 14

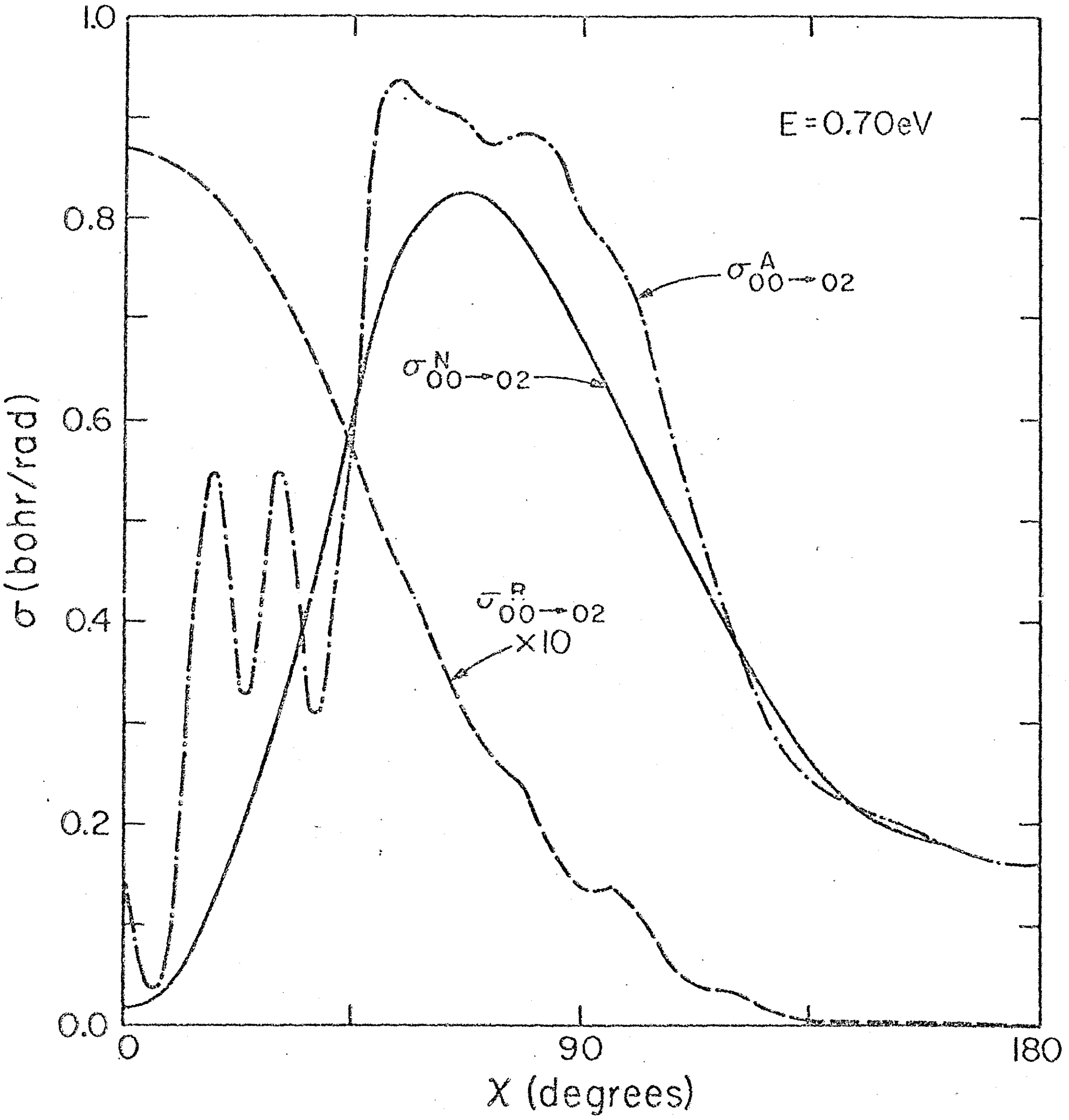
1.0
0.8
0.6
0.4
0.2
0.0
0
90
180
σ (bohr/rad)
X (degrees)
E = 0.70eV
$\sigma^{A}_{00\to02}$
$\sigma^{N}_{00\to02}$
$\sigma^{R}_{00\to02}$
×10

Figure 15

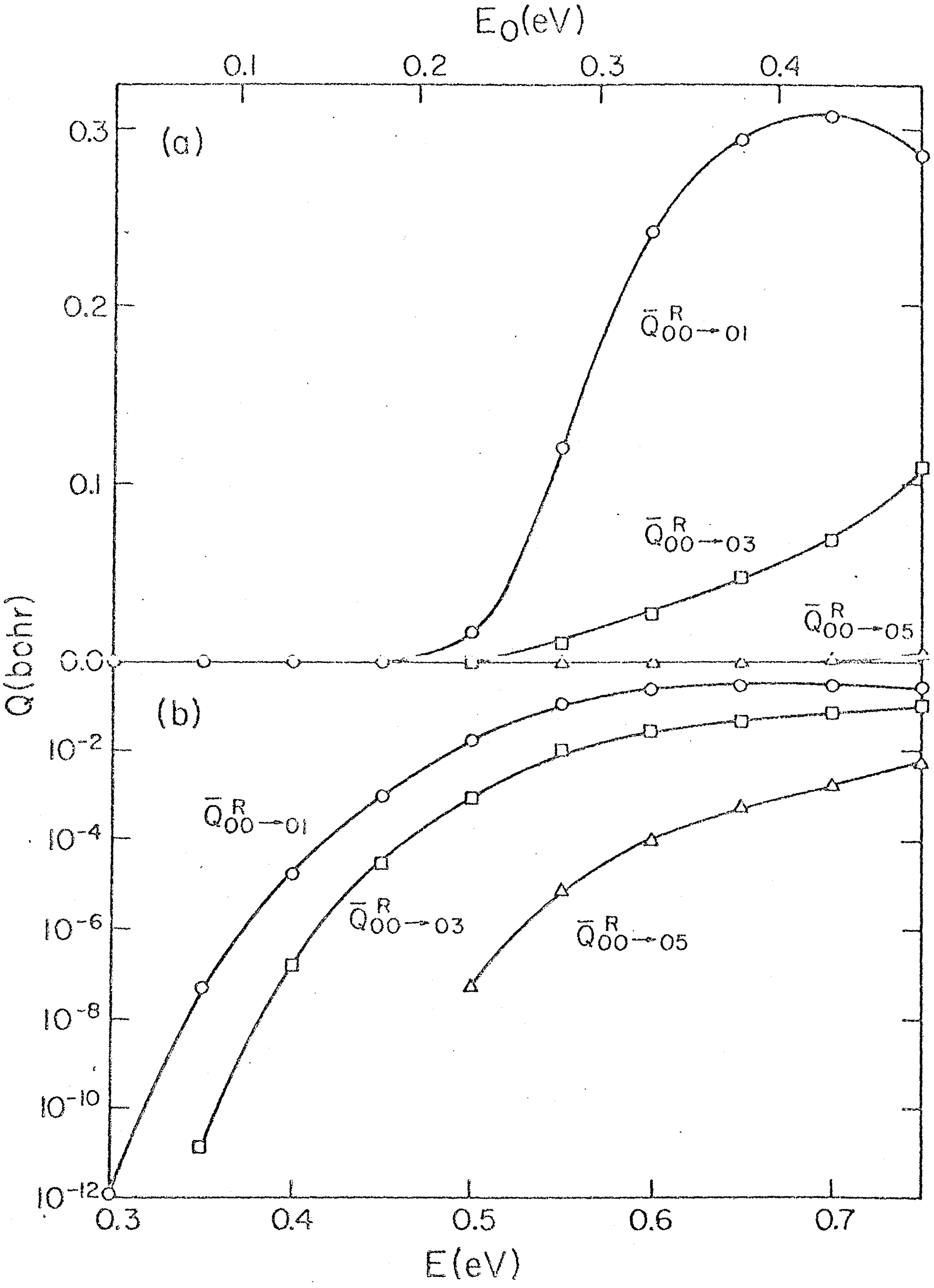
E_0(eV)
0.1
0.2
0.3
0.4
(a)
0.3
0.2
0.1
0.0
$\bar{Q}^R_{00\to01}$
$\bar{Q}^R_{00\to03}$
$\bar{Q}^R_{00\to05}$
Q(bohr)
(b)
10^{-2}
10^{-4}
10^{-6}
10^{-8}
10^{-10}
10^{-12}
$\bar{Q}^R_{00\to01}$
$\bar{Q}^R_{00\to03}$
$\bar{Q}^R_{00\to05}$
0.3
0.4
0.5
0.6
0.7
E(eV)

Figure 16

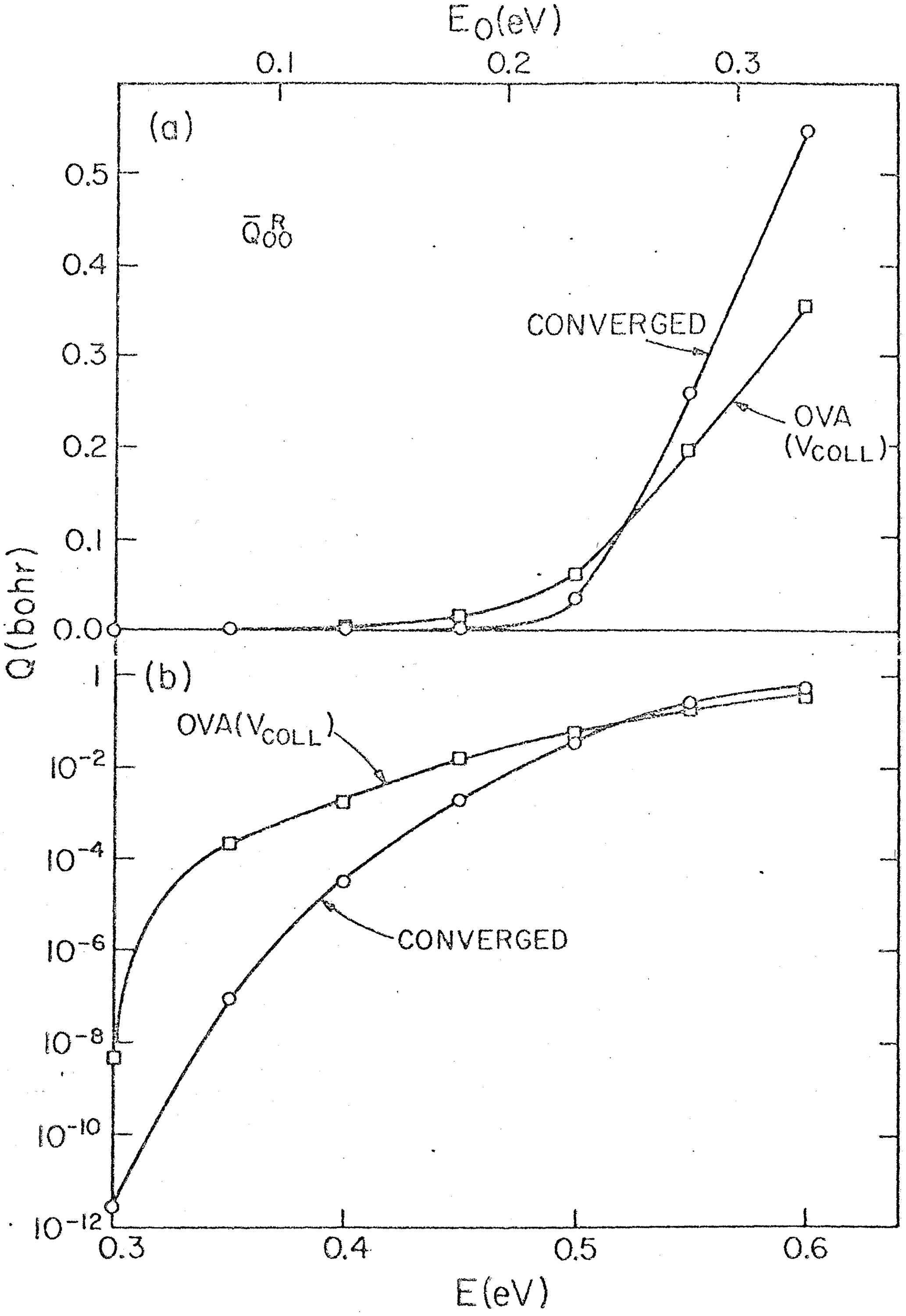

E0(eV)
0.1
0.2
0.3
(a)
$\bar{Q}^R_{00}$
0.5
0.4
0.3
0.2
0.1
0.0
CONVERGED
OVA
(VCOLL)
Q(bohr)
(b)
1
OVA(VCOLL)
10-2
10-4
10-6
10-8
10-10
10-12
CONVERGED
0.3
0.4
0.5
0.6
E(eV)

Figure 17

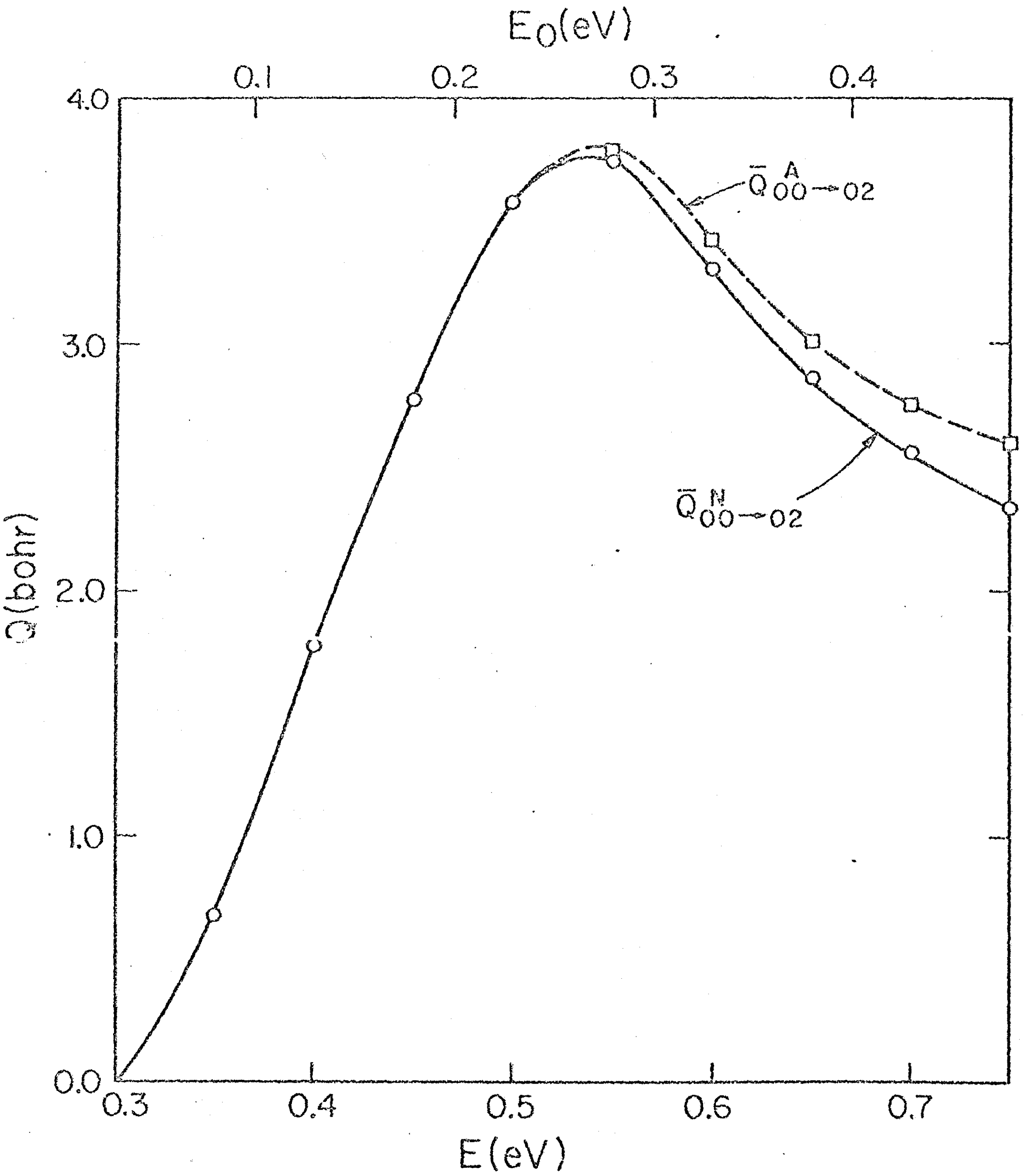
E_0(eV)
0.1
0.2
0.3
0.4
4.0
3.0
2.0
1.0
0.0
Q(bohr)
$\bar{Q}^{A}_{00\rightarrow 02}$
$\bar{Q}^{N}_{00\rightarrow 02}$
0.3
0.4
0.5
0.6
0.7
E(eV)

Figure 18

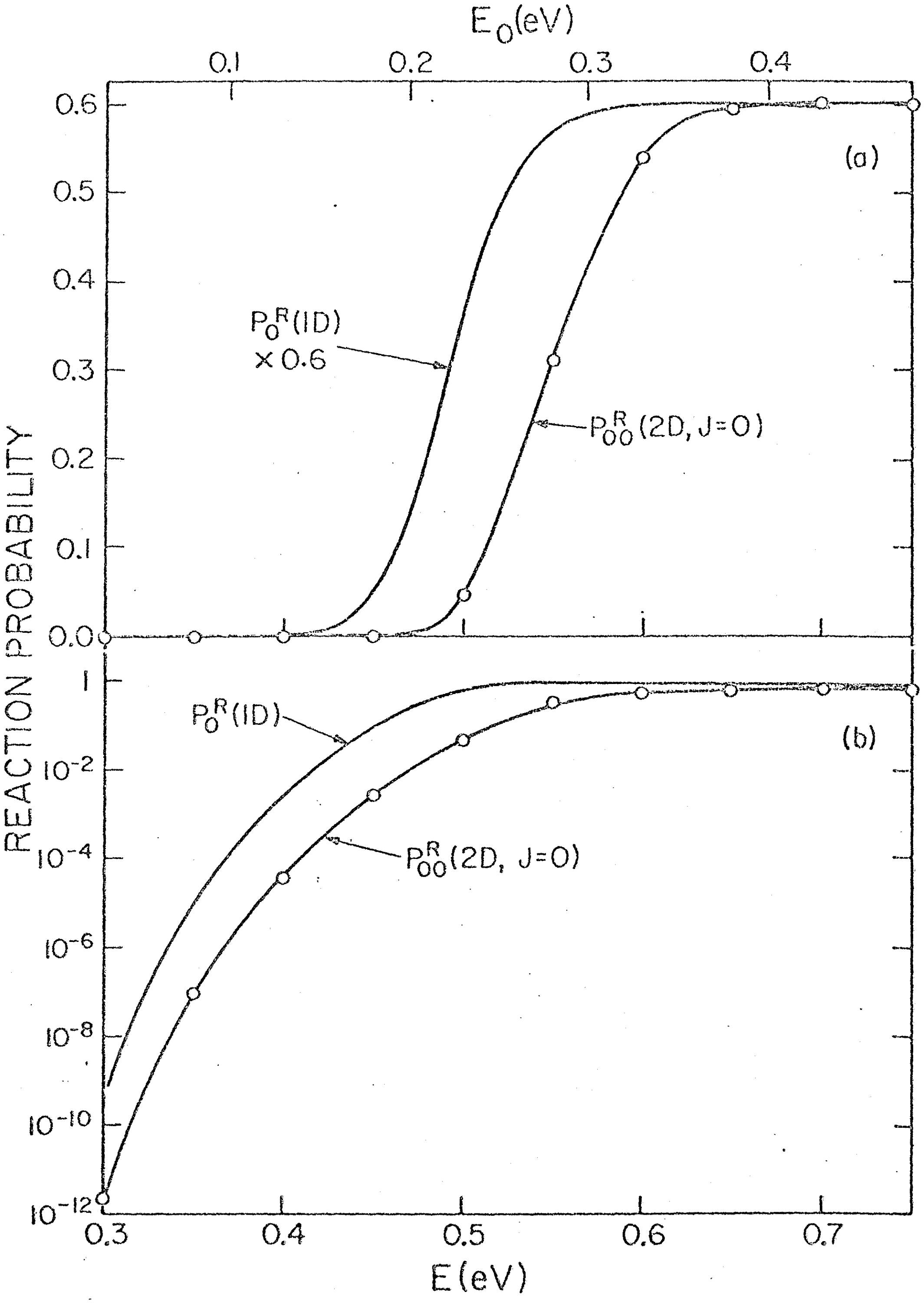
E_0(eV)
0.1
0.2
0.3
0.4
0.6
0.5
0.4
0.3
0.2
0.1
0.0
(a)
P_0^R(1D) × 0.6
P_{00}^R(2D, J=0)
REACTION PROBABILITY
1
10^{-2}
10^{-4}
10^{-6}
10^{-8}
10^{-10}
10^{-12}
(b)
P_0^R(1D)
P_{00}^R(2D, J=0)
0.3
0.4
0.5
0.6
0.7
E(eV)

Figure 19

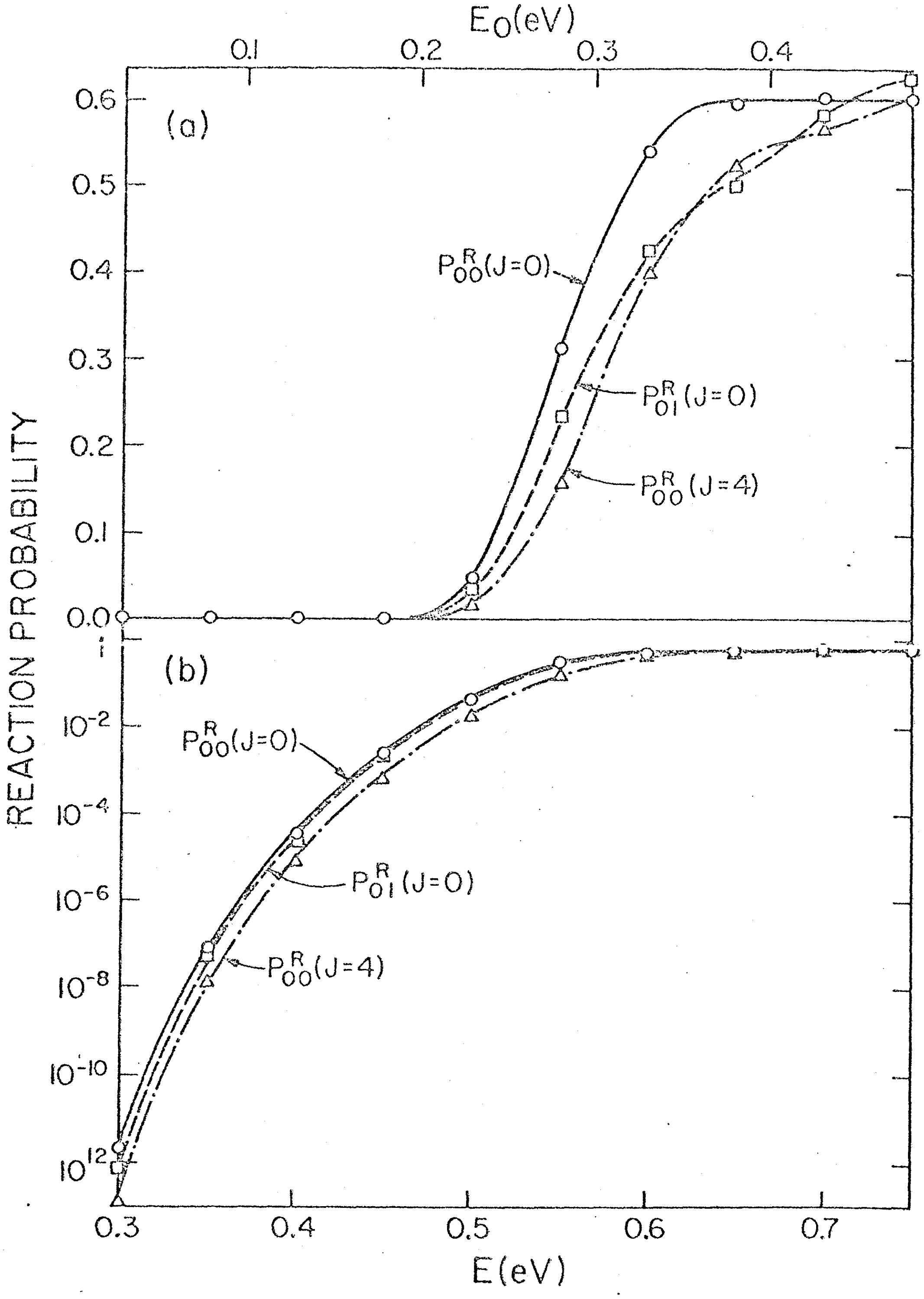
E0(eV)
0.1
0.2
0.3
0.4
REACTION PROBABILITY
(a)
0.0
0.1
0.2
0.3
0.4
0.5
0.6
$P^R_{00}(J=0)$
$P^R_{01}(J=0)$
$P^R_{00}(J=4)$
(b)
1
10-2
10-4
10-6
10-8
10-10
10-12
$P^R_{00}(J=0)$
$P^R_{01}(J=0)$
$P^R_{00}(J=4)$
0.3
0.4
0.5
0.6
0.7
E(eV)

Figure 20

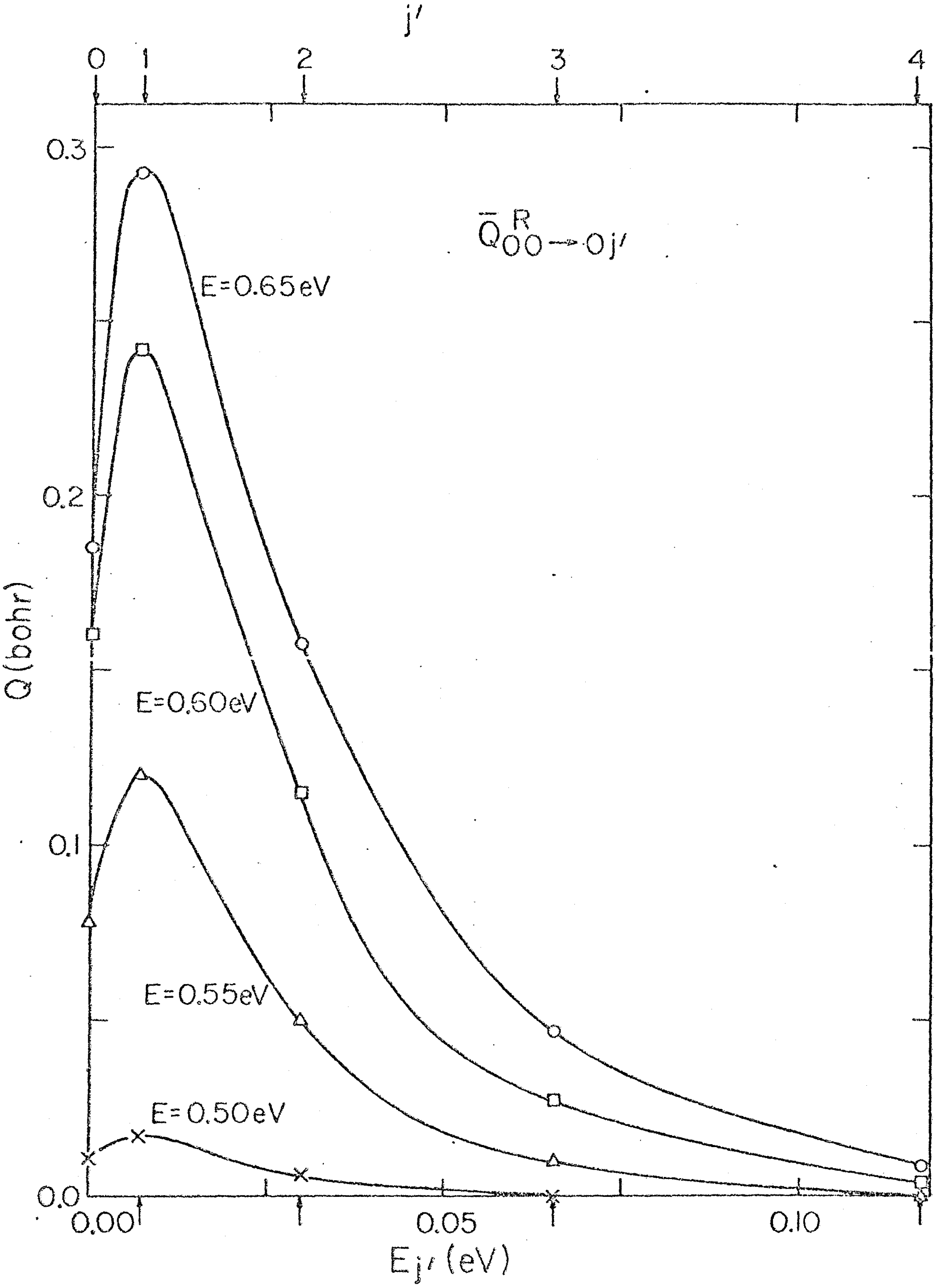
j′
0
1
2
3
4
$\bar{Q}^{R}_{00\rightarrow 0j'}$
E=0.65eV
E=0.60eV
E=0.55eV
E=0.50eV
0.3
0.2
0.1
0.0
Q (bohr)
0.00
0.05
0.10
$E_{j'}$ (eV)

Figure 21

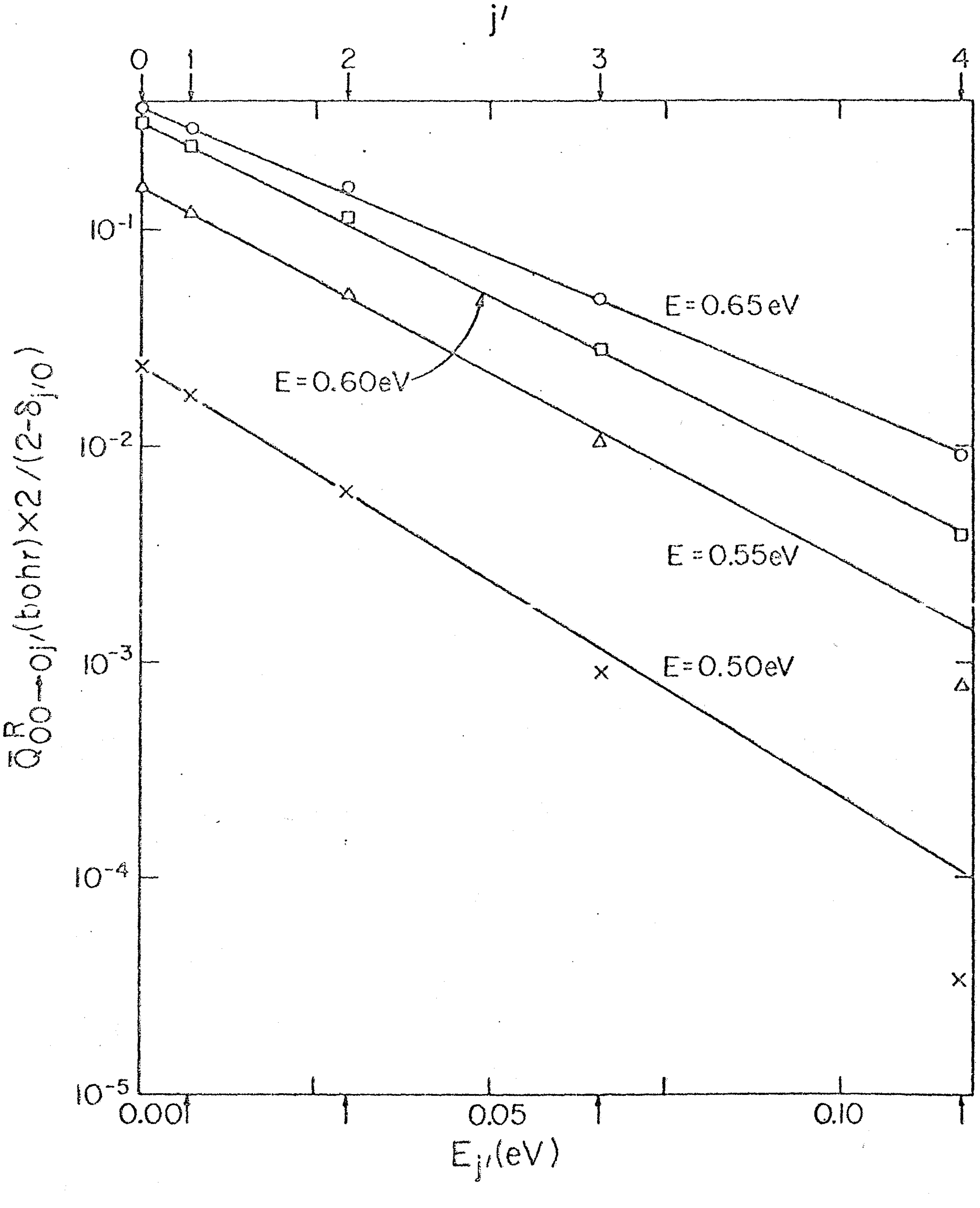
j'
0
1
2
3
4
10^{-1}
10^{-2}
10^{-3}
10^{-4}
10^{-5}
$\bar{Q}^R_{00\to0j'}$(bohr)×2/(2-$\delta_{j'0}$)
E=0.65 eV
E=0.60eV
E=0.55eV
E=0.50eV
0.001
0.05
0.10
$E_{j'}$(eV)

Figure 22

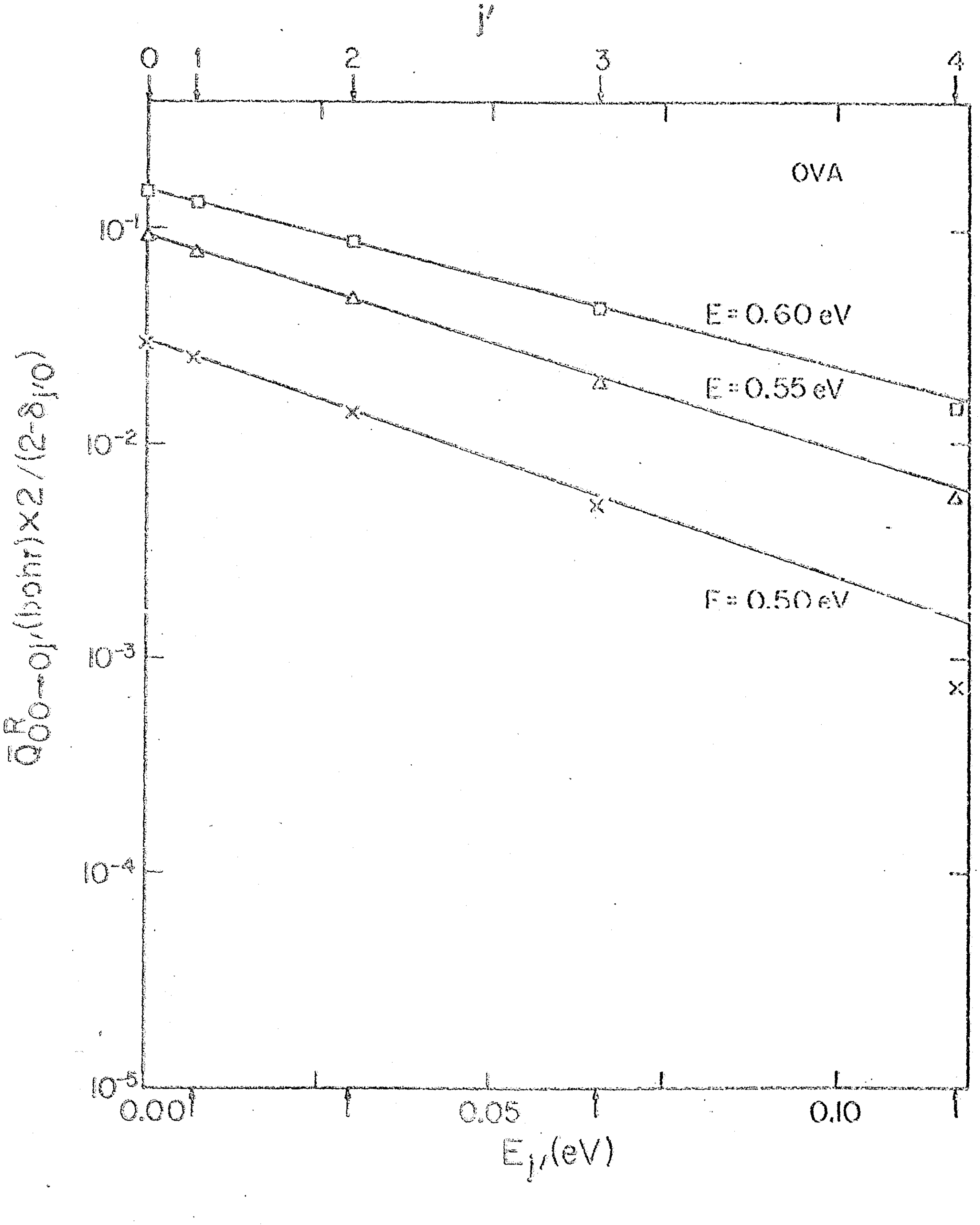
j'
0
1
2
3
4
OVA
E = 0.60 eV
E = 0.55 eV
E = 0.50 eV
10^{-1}
10^{-2}
10^{-3}
10^{-4}
10^{-5}
$\bar{Q}^R_{00\to 0j'}$(bohr)×2/(2-$\delta_{j'0}$)
0.001
0.05
0.10
$E_{j'}$(eV)

Figure 23

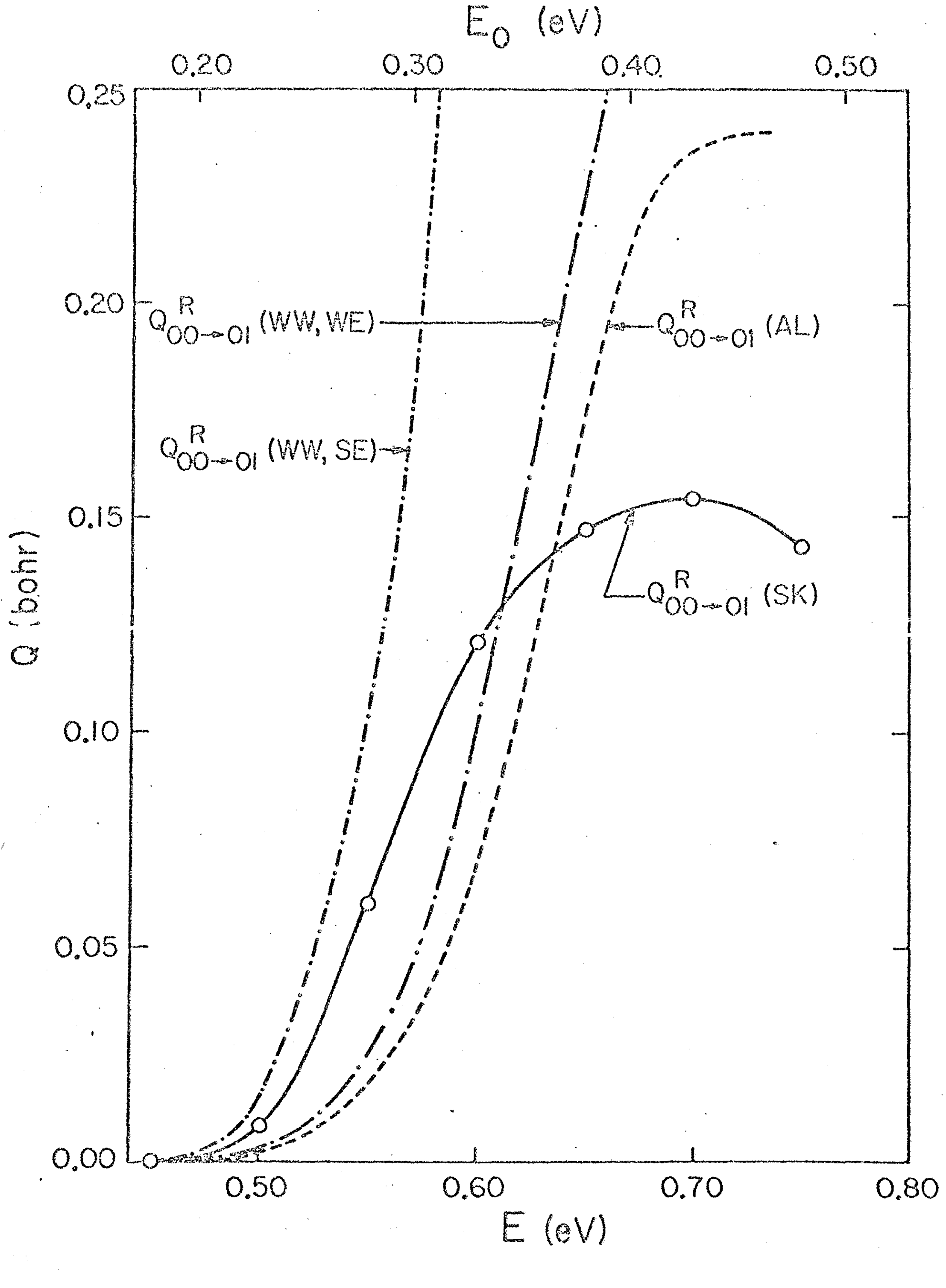
E_0 (eV)
0.20
0.30
0.40
0.50
0.25
0.20
0.15
0.10
0.05
0.00
Q (bohr)
$Q^R_{00\to01}$ (WW, WE)
$Q^R_{00\to01}$ (AL)
$Q^R_{00\to01}$ (WW, SE)
$Q^R_{00\to01}$ (SK)
0.50
0.60
0.70
0.80
E (eV)

Figure 24

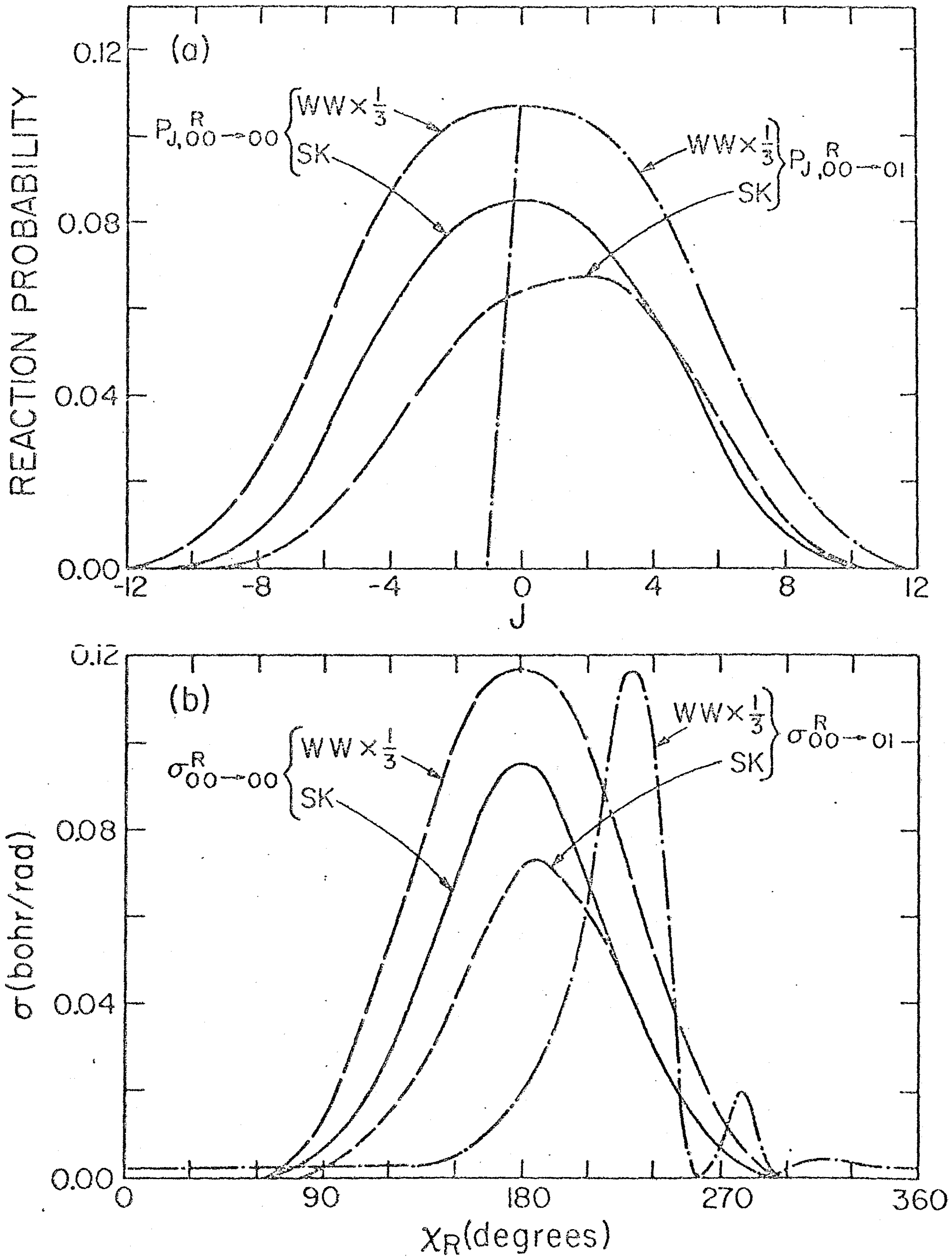
(a)
REACTION PROBABILITY
0.12
0.08
0.04
0.00
-12
-8
-4
0
4
8
12
J
$P^R_{J,00\to00}$
WW × 1/3
SK
WW × 1/3
SK
$P^R_{J,00\to01}$
(b)
σ(bohr/rad)
0.12
0.08
0.04
0.00
0
90
180
270
360
χR(degrees)
$\sigma^R_{00\to00}$
WW × 1/3
SK
WW × 1/3
SK
$\sigma^R_{00\to01}$

Figure 25

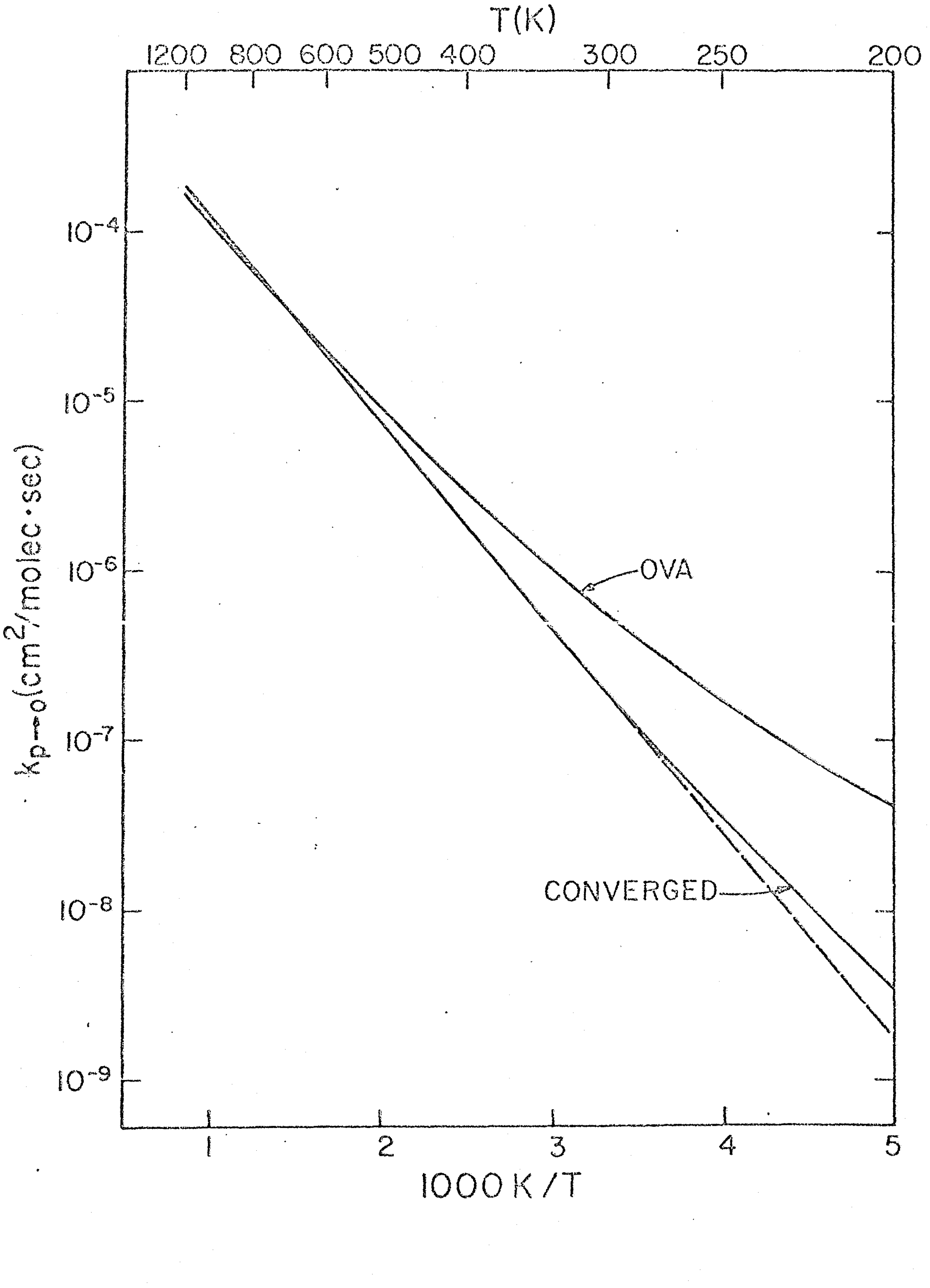
T(K)
1200
800
600
500
400
300
250
200
$k_{p\to o}$(cm^2/molec·sec)
10^{-4}
10^{-5}
10^{-6}
10^{-7}
10^{-8}
10^{-9}
OVA
CONVERGED
1
2
3
4
5
1000 K/T

Figure 26